Rewiring of hippocampal circuits, optogenetic synaptic silencing and optimized two-photon imaging of genetically encoded indicators

DISSERTATION

with the aim of achieving a doctoral degree (Dr. rer. nat.)

at the Faculty of Mathematics, Informatics and Natural Sciences

Department of Biology

University of Hamburg

Submitted by

Mauro Pulin

Hamburg, 2022

This work has been performed at the Institute for Synaptic Physiology, Center for Molecular Neurobiology Hamburg, University Medical Center Hamburg-Eppendorf.

Director: Prof. Dr. Thomas G. Oertner

The following evaluators recommended the admission of the dissertation:

Supervisor: Prof. Dr. Thomas G. Oertner

Institute for Synaptic Physiology
Center for Molecular Neurobiology Hamburg (ZMNH)
University Medical Center Hamburg-Eppendorf

Co-supervisor: Prof. Dr. J. Simon Wiegert

Research Group Synaptic Wiring and Information Processing
Center for Molecular Neurobiology Hamburg (ZMNH)
University Medical Center Hamburg-Eppendorf

Date of disputation: 04.07.2022

Table of Contents

Abstract

Information is transferred between neurons across synapses. It is well accepted that synapses are able to store information as long-lasting changes of their strength, but the lifetime of most excitatory synapses is limited. While synaptic plasticity leads to sustained changes in synaptic efficacy, it is less clear how it influences the lifetime of individual synaptic contacts and whether it contributes to long-lasting changes of synaptic pathways. We have previously shown that LTD reduces the lifetime of Schaffer collateral synapses in an input-specific manner. Here I tested the long-term consequences of LTP on synaptic stability and the interaction of LTP and LTD induced consecutively 24 hours apart. I found that LTP has a long-lasting stabilizing effect on dendritic spines, monitored over one week. Furthermore, in consecutive plasticity experiments (LTD followed by LTP and vice versa), I demonstrated that the last plasticity event fully overrode the effects of the previous one, thus determining synaptic lifetime. These results confirm our hypothesis that initial weight adjustments of synaptic strength are transient but have long-term consequences on synaptic survival.

To better understand how synapses contribute to brain circuit function, their direct optogenetic manipulation is desired. However, optogenetic synaptic silencing has been difficult to achieve. Here I describe eOPN3, a targeting-enhanced mosquito derived type II rhodopsin, for rapid optical control of the $G_{i/o}$ signaling pathway. Activation of eOPN3 leads to only mild somatic inhibition of spiking in pyramidal neurons, whereas local activation at presynaptic terminals leads to efficient and reversible suppression of neurotransmitter release. This robust inhibition of synaptic transmission was also confirmed in head-fixed and freely behaving mice. The mechanisms of synaptic inhibition reflect those of native presynaptic metabotropic $GABA_B$ receptors. Taken together, eOPN3 can be used to selectively suppress neurotransmitter release at synaptic terminals with high spatiotemporal precision, opening new opportunities for functional interrogation of long-range neuronal circuits *in vivo*.

Aside from optically manipulating synaptic transmission, optical read-out of neurotransmitters with genetically encoded sensors is informative about synaptic pathway function. I discovered a strong two-photon polarization excitation bias for a subclass of genetically encoded GPCR-based neuromodulator sensors. Those sensors consist of a fluorescent protein attached to a GPCR-based sensing domain. This particular design orients the fluorescent protein nearly parallel to the cell membrane. The fixed orientation poses a problem under excitation with polarized light as fluorescent proteins are preferentially excited when the polarized light is parallel to the dipole axis of their chromophores. This effect is known as fluorescence-dependent linear dichroism. In dendrites that run parallel to the polarization of the excitation laser, this led to a complete loss of the fluorescence signal. The development of a passive optical device that generates alternating pulses of orthogonal light polarization removed the orientation dependence and allowed unbiased measurements of indicator fluorescence.

Zusammenfassung

Informationen werden zwischen Neuronen über Synapsen übertragen. Es ist allgemein anerkannt, dass Neuronen Informationen als lang anhaltende Änderungen ihrer synaptischen Stärke speichern können, jedoch ist die Lebensdauer der meisten erregenden Synapsen begrenzt. Während synaptische Plastizität zu anhaltenden Veränderungen der synaptischen Stärke führt, ist es noch weitgehend unerforscht, wie synaptische Plastizität die Lebensdauer einzelner synaptischer Kontakte beeinflusst und ob sie zu lang anhaltenden Veränderungen synaptischer Verschaltung beiträgt. Wir haben zuvor gezeigt, dass Langzeitdepression (long term depression, LTD) die Lebensdauer der Synapsen von Schaffer-Kollateralen eingangsspezifisch reduziert. In dieser Arbeit erforschte ich die Folgen von Langzeitpotenzierung (long-term potentiation, LTP) auf die synaptische Stabilität, sowie die Wechselwirkung von LTP und LTD, wenn diese im Abstand von 24 Stunden induziert wurden. Ich fand heraus, dass LTP über den Beobachtungszeitraum von einer Woche eine stabilisierende Wirkung auf dendritische Spines hat. Darüber hinaus habe ich in aufeinanderfolgenden Plastizitätsexperimenten (LTD gefolgt von LTP und umgekehrt) gezeigt, dass das letzte Plastizitätsereignis die Auswirkungen des vorherigen vollständig aufhebt, und somit die synaptische Lebensdauer bestimmt. Diese Ergebnisse bestätigen unsere Hypothese, dass anfängliche Veränderungen der synaptischen Stärke vorübergehend sind, jedoch langfristige Auswirkungen auf die Lebensdauer der Synapsen haben.

Ein einflussreiches Werkzeug um erforschen zu können wie Synapsen zur Funktion neuronaler Schaltkreise beitragen, ist ihre direkte optogenetische Manipulation. Optogenetische Inhibition von Synapsen ist jedoch mit derzeit verfügbaren molekularen Werkzeugen schwierig zu erreichen. Hier beschreibe ich eOPN3, ein in Moskitos exprimiertes Rhodopsin vom Typ II, welches für die Expression und den zellulären Transport in Neuronen verbessert wurde und für schnelle optische Kontrolle des $G_{i/o}$-Signalwegs genutzt werden kann. Während die Aktivierung von eOPN3 nur eine leichte Hemmung der Aktionspotential-Initiation in Somata von Pyramidalzellen zur Folge hatte, führte lokale eOPN3-Aktivierung in der Präsynapse zu einer effizienten und reversiblen Unterdrückung der Neurotransmitterfreisetzung. Diese robuste Hemmung der synaptischen Übertragung wurde in lebenden Mäusen bestätigt. Die Mechanismen dieser Art der synaptischen Hemmung sind vergleichbar zu den Mechanismen nativer präsynaptischer, metabotroper $GABA_B$-Rezeptoren. Zusammengefasst kann eOPN3 verwendet werden, um die Freisetzung synaptischer Neurotransmitter mit hoher räumlicher und zeitlicher Präzision selektiv zu unterdrücken. Dies eröffnet neue Möglichkeiten für die Erforschung der Funktion neuronaler Schaltkreise im lebenden Gehirn.

Neben der optischen Manipulation der synaptischen Übertragung ist auch das optische Auslesen der Neurotransmitterfreisetzung mittels genetisch kodierter Sensoren eine essenzielle Methode um die Funktion synaptischer Kommunikation zu erforschen. Im Rahmen meiner Arbeit entdeckte ich eine starke Polarisationsabhängigkeit der optischen Anregung mittels Zwei-Photonen-Mikroskopie bei einer bestimmten Gruppe genetisch codierter, GPCR-basierter Sensoren für Neuromodulatoren. Diese Sensoren bestehen aus einem fluoreszierenden Protein, welches an eine GPCR-basierte Sensordomäne gebunden ist. Dieses besondere Design bedingt eine Orientierung des fluoreszierenden Proteins nahezu

parallel zur Zellmembran. Diese starre Orientierung stellt bei Anregung mit polarisiertem Licht ein Problem dar, da fluoreszierende Proteine bevorzugt angeregt werden, wenn das polarisierte Licht parallel zur Dipolachse ihrer Chromophore verläuft. Dieser Effekt ist als fluoreszenzabhängiger linearer Dichroismus bekannt. Bei Dendriten, die parallel zur Polarisation des Anregungslasers verlaufen, führte dies zu einem vollständigen Verlust des Fluoreszenzsignals. Durch die Entwicklung eines passiven optischen Elements, welches alternierende Pulse orthogonaler Lichtpolarisation erzeugt, konnten wir die Orientierungsabhängigkeit umgehen und Anregung der Indikatoren unabhängig von der Polarisationsachse erreichen.

Research summary

This thesis is structured in three separate parts, each of them describing the three main projects I was involved in during my PhD, which I will briefly summarize below.

The first project investigated the link between synaptic plasticity and long-term stability of Schaffer collateral synapses in the rodent hippocampus. Several studies explored the information processing capability of individual synapses and their contribution to long-term memory storage. Most excitatory synapses harbor dendritic spines, small protrusions emanating from dendritic branches. Spines provide both an anatomical and functional substrate for synaptic transmission and the basis for the synapse specificity of plasticity. Synaptic plasticity, expressed as long-term potentiation (LTP) and long-term depression (LTD), is thought to drive the remodeling of cortical circuits, and provides a cellular mechanism of learning and information storage in the brain. Although changes in synaptic pathways seem stable over time, it is less clear how plasticity affects individual synapses over time. Here I used a non-invasive, all-optical method to tightly control the activity of individual Schaffer collateral synapses and to follow their fate over a period of seven days using optogenetic stimulation of synaptic transmission and two-photon spine Ca^{2+} imaging. I induced LTP, LTD or both in sequence to investigate the consequences of those plasticity events on the survival of individual synapses. LTP triggered transient spine growth and prolonged synaptic survival over seven days. In contrast, LTD induction at single synapses decreased their chance of survival, confirming previous results. After consecutive plasticity events of opposite polarity (LTD followed by LTP and vice versa), the last event fully determined spine survival. Thus, multiple weight adjustments are not linearly integrated but rather synapse survival is dominated by the most recent plasticity event.

The second part of my thesis describes the development and validation of a novel inhibitory optogenetic tool, aimed at the blocking synaptic transmission when activated directly at presynaptic terminals. Silencing of long-range axonal projections has posed a formidable challenge for modern neuroscience. Existing optogenetic tools suffer from low efficacy and off-target effects when applied to presynaptic terminals, while chemogenetic synaptic silencing approaches lack spatiotemporal precision. Here, I describe eOPN3, a targeting-enhanced type-II mosquito rhodopsin that can effectively suppress presynaptic neurotransmitter release through activation of the $G_{i/o}$ signaling pathway. I show that expression of eOPN3 in CA3 pyramidal cells of organotypic hippocampal slices yields efficient membrane targeting and trafficking to distal axons projecting to area CA1. Activation of eOPN3 in the somatodendritic compartment of CA3 cells leads to mild G protein-coupled inwardly rectifying K^+ (GIRK)-channel mediated hyperpolarization and weak reduction in action potential firing. In contrast, brief activation of eOPN3 at synaptic terminals strongly reduces the amplitude of excitatory postsynaptic currents (EPSCs) between pairs of synaptically connected cells without affecting presynaptic action potential firing. Moreover, similar to natural presynaptic inhibition via $GABA_B$-receptor mediated $G_{i/o}$ signaling, eOPN3 activation reduced action potential evoked calcium influx at presynaptic terminals and displayed high-pass filtering properties during high firing rates. When applied in behaving animals, eOPN3 displayed strong and reliable pathway-specific inhibitory effects. In conclusion, eOPN3 may become a crucial tool for selective silencing of neuronal

terminals, allowing detailed evaluations of their functional contribution to cognitive and behavioral processes.

The third and last part of the thesis describes the discovery and the remedy of a problem when imaging a new class of genetically encoded fluorescent reporters for neuromodulators with linearly polarized light. Here I identified a strong polarization excitation bias when imaging G-protein-coupled receptors (GPCR)-based neuromodulator sensors with two-photon microscopy. The effect likely arises from the orientation of the fluorophore relative to the polarization of the incident beam, such that circularly permuted green fluorescent protein (cpGFP) barrels are preferentially excited when orthogonal to the polarization of light. Depending on the length and rigidity of the linker sections, tethering the cpGFP on both ends to transmembrane domains of GPCRs may orient the barrel in a fixed position, parallel to the membrane. This rigid orientation leads to a complete loss of fluoresce from tubular structures such as dendrites that run parallel to the polarization of the excitation light. To overcome this problem, we developed a passive optical device that generates interleaved pulse trains of orthogonal polarization. Inserted into the beam path of a two-photon microscope, the device removed the strong directional bias from fluorescence images, thus allowing measuring the spatial distribution and dynamics of neurotransmitter release from the relative change in fluorescence.
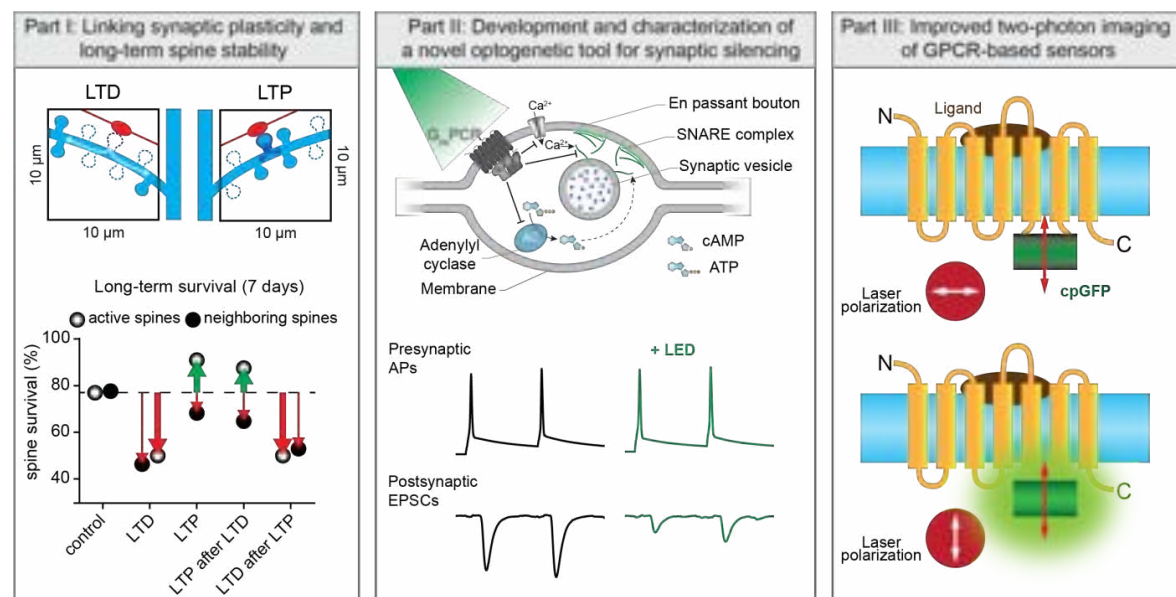
1 Introduction

1.1 Part I

1.1.1 Neuronal transmission at the Schaffer collateral synapse

In the mammalian central nervous system (CNS), neuronal transmission occurs at highly specialized functional connections known as synapses. Synaptic transmission is the primary operational process of the nervous system underlying our cognitive and motor functions. Activity-dependent changes of synaptic transmission and connections are thought to be involved in learning and memory processes. Classically, information between neurons can be transmitted via two types of synapses: electrical and chemical. Electrical synapses conduct electrical impulses (ions) through closely spaced gaps (only a few nanometers) known as gap junctions. Although electrical synapses have the advantage of conducting signals much faster than chemical synapses, they lack dynamic range and gain. Electrical synapses will not be further discussed as this thesis focuses exclusively on chemical synapses, specifically excitatory glutamatergic transmission at the Schaffer collateral synapse.

Probably the best characterized excitatory synapse of the CNS, the Schaffer collateral synapse represents the connection between presynaptic CA3 and postsynaptic CA1 pyramidal neurons of the hippocampus. Here, neuronal transmission occurs in a well-defined laminar organization and due to its distinct pre- and postsynaptic structure, the Schaffer collateral synapse has been extensively investigated in many studies of synaptic physiology. Chemical synapses, where most excitatory neurotransmission occurs, consist of a presynaptic terminal ('pre synapse'), a synaptic cleft, and a postsynaptic compartment ('post synapse'). The basic principle underlying chemical neurotransmission is the release and subsequent postsynaptic sensing of chemical compounds known as neurotransmitters (mostly amino acids), hence its name "chemical" neurotransmission. Excitatory chemical synaptic transmission in the CNS is very fast (<1 ms) (Sabatini and Regehr, 1996). After the generation of an action potential (also known as 'spike') at the axon initial segment (AIS), the depolarization propagates along the axon mainly via ion flux through voltage-sensitive Na^+ channels, eventually reaching the synaptic terminals. The latter, also known as synaptic bouton, is a specialized structure containing neurotransmitter-filled vesicles and a complex release machinery that mediates vesicle fusion. The depolarization generated by the AP induces the opening of voltage gated Ca^{2+} channels (VGCCs) present at synaptic terminals, which allows Ca^{2+} influx from the extracellular space. Ca^{2+} ions thus engage a molecular release machinery, responsible for triggering the fusion of synaptic vesicles with the plasma membrane and the release of their content into the synaptic cleft (Sudhof, 2013). The released neurotransmitter, in this case glutamate, can typically reach concentrations higher than 1 mM in the narrow synaptic cleft (~20-40 nm wide) (Clements et al., 1992). Before quickly diffusing away and being taken up by presynaptic and glial glutamate transporters, glutamate is captured by postsynaptic receptors that then generate a postsynaptic response (depolarization) (Fig. 1). Postsynaptic glutamate receptors can be classified into two main categories: ionotropic and metabotropic. Ionotropic glutamate receptors, namely α-amino-3-hydroxy-5-methyl-4-isoxazolepropionic acid receptors (AMPARs), the N-methyl-D-aspartate

receptors (NMDARs) and kainate receptors, mediate fast synaptic transmission. They are ligand-gated, non-selective cation channels that open upon binding of glutamate and conduct positive charges into the postsynapse, causing a depolarization. If enough ionotropic glutamate receptors are activated at the same time, they may cause a depolarization big enough to trigger an action potential in the postsynaptic neuron. AMPA-type glutamate receptors provide most of the postsynaptic depolarization under resting membrane potential, since they do not display a voltage-dependent Mg^{2+} block of their channel pore as NMDARs. Most AMPARs in the CNS are heterotetramers comprised of four receptor subunits, GluA1-GluA4. At the Schaffer collateral synapses, most AMPARs are heteromers comprised of GluA2 with either GluA1 or GluA3. AMPARs are mainly permeable to the monovalent cations Na^+ and K^+. When glutamate binds to AMPARs, opening of the channel leads to a strong influx of Na^+ and only a small efflux of K^+, such that the net effect is a depolarization of the postsynaptic membrane. NMDARs are heteromeric tetramers typically consisting of two obligatory GluN1 subunits and two accessory GluN2 subunits. They are non-selective cation channels permeable for Na^+, K^+, and Ca^{2+}, with the latter corresponding approximately to 15% of the current flow (Jahr and Stevens, 1993; Schneggenburger et al., 1993). Activation of NMDARs requires the binding of two molecules of glutamate (to the GluN2 subunit) and two molecules of glycine (to the GluN1 subunit) and a depolarization to remove the Mg^{2+} block from the channel pore, thus acting as "coincidence detectors". However, even at resting membrane potentials, Mg^{2+} block is incomplete and NMDARs are able to conduct at ~15 % of peak conductance (Sabatini et al., 2002). Consistent with depolarization-dependent Mg^{2+} block and the ionic electrochemical gradient, NMDA receptor-dependent ionic current increases with increasing neuronal depolarization, reaching a reversal potential around 0 mV. Compared to AMPARs, NMDARs have much slower glutamate binding kinetics. Although they have a higher affinity for glutamate, NMDARs activate more slowly (having a peak conductance long after the AMPA peak current) and remain open for longer (hundreds of milliseconds) than AMPARs. Unlike ionotropic receptors, metabotropic glutamate receptors (mGluRs) are not ion channels (but can indirectly activate them). Upon binding of glutamate, mGluRs couple to heterotrimeric G-proteins (part of the G-protein coupled receptors or GPCRs) and mediate a slower signal transduction cascade. Depending on which type of G-protein they couple to, mGluRs can either have excitatory or inhibitory effects on neuronal function.
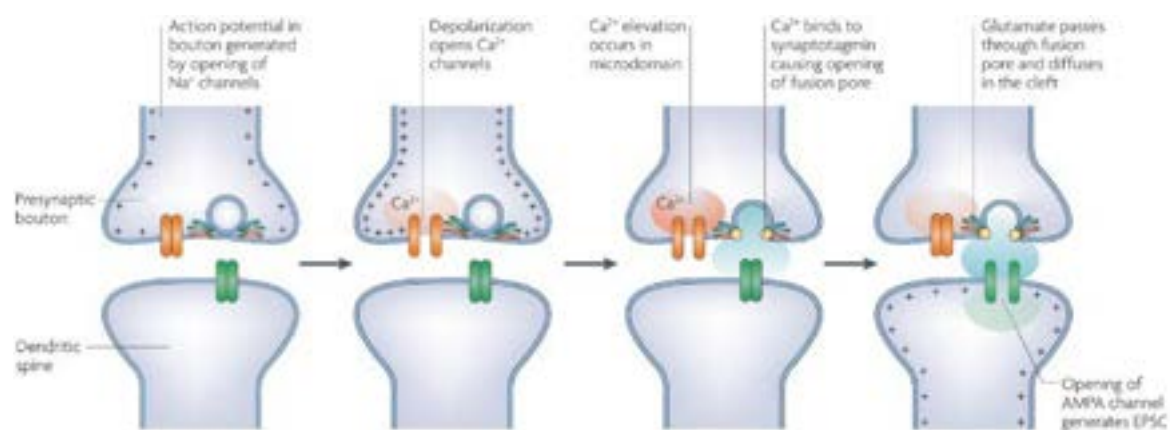
Figure 1. Sequence of events during chemical transmission at a central glutamatergic synapse. Figure from Lisman et al., 2007.

1.1.2 Postsynaptic structure and function

1.1.2.1 Composition and morphology of dendritic spines

Towards the end of the 19th century, the Spanish histologist Santiago Ramón y Cajal first discovered and described the presence of dendritic spines in the mammalian CNS. In his pioneering work, he proposed that those tiny "espinas" might serve as contact points between neurons (Yuste, 2015). It took more than 50 years after their first discovery, thanks to the emergence of electron microscopy, to confirm that dendritic spines are the main postsynaptic sites of excitatory neurotransmission. When visualized under an electron microscope, excitatory spine synapses are often referred to as 'asymmetric', considering their prominent postsynaptic area compared to the less electron-dense presynaptic side. To the contrary, inhibitory synapses display similar pre- and postsynaptic membrane densities and are referred to as symmetric synapses. Estimates indicate that more than 90% of excitatory synapses terminate on spines, with the human brain roughly containing 100 trillion of them. Dendritic spines are tiny protrusions (ranging from ~0.01-1 μm^3) arising from a parent dendrite (and sometimes from the soma or even from the axon hillock), consisting of a spine head (~0.5 μm in diameter) and a smaller spine neck (~0.1 μm in diameter) (Bourne and Harris, 2008). The spine cytoskeletal organization is enriched with actin proteins, which can undergo activity-driven remodeling, making them highly dynamic in shape and size (Bosch et al., 2014; Okamoto et al., 2004). The spine head contains an electron-dense region known as the postsynaptic density (PSD) (Fig. 2B). The PSD consists of receptors, ion channels, scaffold proteins, cytoskeletal proteins, and signaling enzymes all involved in synaptic transmission and activity-dependent plasticity. In addition to its molecular composition, the morphology of the spine is thought to be critical for synaptic function, as spine head size correlates with synaptic strength. In the rodent hippocampal region, the area of PSD has been correlated to the size of the spine head, the number of postsynaptic receptors (AMPARs) and to the number of presynaptic vesicles (the ready-releasable pool of transmitters) (Harris and Stevens, 1989; Holderith et al., 2012; Knott et al., 2006; Nusser et al., 1998), suggesting that bigger spines correspond to stronger synapses. The density of dendritic spines varies in the brain depending on the cell type, although on average, it does not exceed five spines/μm of dendrite (Harris and Kater, 1994). Based on the morphology and dimension of their head and neck, dendritic spines are classically categorized as mushroom spines (large head and narrow neck), thin spines (small head and narrow neck) and stubby spines (with no apparent separation between the spine head and spine neck) (Fig.2A). However, due to their dynamic changes in shape and size, this classical categorization of spine types is considered by many unprecise and artificial. The morphology of dendritic spines received particular attention over the past few decades. As I will discuss later, spine size is often correlated with synaptic strength. Therefore, on one hand, big mushroom spines are likely close to the limit of synaptic size and strength, hence have no further potential for strengthening (but quite some range for weakening). On the other hand, thin spines, possibly representing small or immature synapses, would possess great potential for growth and strengthening, and may be the preferential sites for potentiation. This has led

to the view of mushroom spines representing 'memory' spines and thin spines representing 'learning' spines (Bourne and Harris, 2007). Another member of this classification, dendritic filopodia, described as very thin, headless filamentous protrusions of the plasma membrane, are often considered precursors of mature spines, involved in synaptogenesis and spine formation (Fiala et al., 1998; Portera-Cailliau et al., 2003; Zuo et al., 2005). However, in the brain of young mice, only a tiny percentage of filipodia turns into spines (Majewska et al., 2006; Zuo et al., 2005).
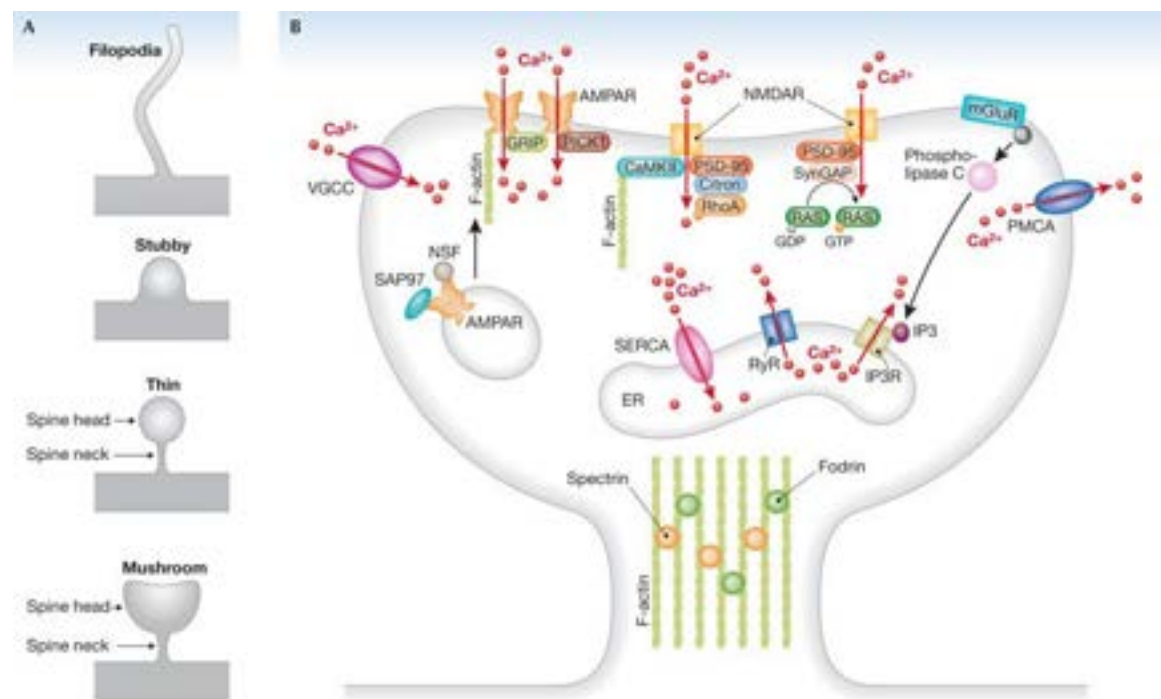
Figure 2. Structural and molecular organization and Ca²⁺ signaling in dendritic spines. (a) Classic view of most common type of spines and filopodia. **(b)** Molecular organization of the players involved in Ca²⁺ signaling in spines. Synaptic stimulation produces postsynaptic depolarization through AMPA- and NMDA-type glutamate receptors located on the postsynaptic density (PSD), enriched with actin, scaffold proteins and signaling molecules. Synaptic Ca²⁺ influx is mediated by NMDARs and voltage-gated Ca²⁺ channels (VGCCs), gated by the depolarization of AMPARs. Spines containing an endoplasmic reticulum (ER) have an addition source of Ca²⁺, which can amplify excitatory postsynaptic Ca²⁺ transients (EPSCaTs) in a mechanism known as Ca²⁺-induced Ca²⁺-release (CICR). CICR is mediated through the activation of ryanodine receptors (RyRs), downstream of Ca²⁺ entry via NMDARs. Alternatively, strong synaptic stimulation can trigger the activation of metabotropic glutamate receptors (mGluRs) and stimulate Ca²⁺ release from internal stores by activating inositol triphosphate receptors (IP₃Rs). Upon entry, most Ca²⁺ ions are either buffered or extruded from the spine cytosol through the plasma membrane Ca²⁺ ATP-ase (PMCA) outside the cell or inside the ER by the sarcoplasmic/endoplasmic reticulum Ca²⁺ ATP-ase (SERCA) pump. Figure from Rochefort and Konnerth, 2012.

Spines were originally considered as purely isolated diffusional compartments from the parent dendrite (Sabatini et al., 2002; Svoboda et al., 1996), given by the fact that diffusional exchange of cytosolic molecules between spine and its parent dendrite is in the range of 20-200 ms, and therefore much slower than the time constant of free diffusion. Follow-up studies proved that their three-dimensional structure can also function as biochemical and electrical compartments (Araya et al., 2006a; Araya et al., 2006b; Cornejo et al., 2021; Grunditz et al., 2008; Lee et al., 2009; Murakoshi et al., 2011). Activity-dependent tuning of

the spine neck morphology can further regulate chemical and electrical compartmentalization. For instance, it was shown that strong synaptic activation or step depolarization increase spine compartmentalization (narrowing the spine neck), a mechanism which can amplify synaptic excitatory postsynaptic potentials (EPSPs) and possibly boosting plasticity induction and local dendritic integration at the expense of somatic voltage depolarization (Bloodgood and Sabatini, 2005; Grunditz et al., 2008). Other studies propose a widening and shortening of the spine neck following LTP-inducing protocols, pushing the synapses to work in a more linear regime by decreasing the voltage amplification in spines, (and therefore preventing further potentiation) while at the same time producing bigger somatic amplitudes. This might classify "stubby" spines as recently potentiated synapses. The reduction of the spine neck resistance might also facilitate the transport of resources from the parent dendrite into the spine undergoing potentiation (Araya et al., 2014; Tonnesen et al., 2014).

1.1.2.2 Ca^{2+} sources and signaling in dendritic spines

It was only after the development and application of two-photon laser scanning microscopy (2PLSM) (Denk et al., 1990), that synaptic transmission could be visualized and studied in greater detail at the level of individual synapses in intact tissue (Svoboda and Yasuda, 2006). 2PLSM combined with Ca^{2+} imaging has revealed that spines function as isolated Ca^{2+} compartments and may represent the basic functional units of neuronal integration (Yuste and Denk, 1995). Ca^{2+} has proven to be a universal signaling agent that plays many pivotal roles in different cellular processes, even so in neurons and dendritic spines (Berridge et al., 1998). The rise in local spine Ca^{2+} concentration activates signal-transduction pathways underlying adaptive neuronal responses. Ca^{2+} regulates diverse synapse-specific functions, including synaptic transmission, local biochemical signaling, protein synthesis, growth, as well as functional and structural plasticity (Bloodgood and Sabatini, 2007a; Higley and Sabatini, 2012; Zucker, 1999). Under resting conditions, Ca^{2+} concentration inside the cell is very low (nanomolar range), while outside the cell, it is 100,000 times higher (millimolar range), creating a strong electrochemical gradient between the two compartments. Depending on the input source, Ca^{2+} can enter in spines through three main pathways: 1) NMDA-type glutamate receptors, 2) Voltage gated Ca^{2+} channels (VGCCs) and 3) release from intracellular Ca^{2+} stores such as the endoplasmic reticulum (ER) (Figure 2B) (Kovalchuk et al., 2000; Oertner et al., 2002; Sabatini et al., 2002; Yuste et al., 1999).

1.1.2.3 NMDAR-dependent Ca^{2+} influx in dendritic spines

In spines of CA1 pyramidal neurons of the hippocampus, the main sources of excitatory postsynaptic Ca^{2+} transients (EPSCaTs) during synaptic activity are NMDARs, with a smaller contribution of VGCCs (Kovalchuk et al., 2000; Mainen et al., 1999; Oertner et al., 2002; Yuste et al., 1999). Consistent with their role as "coincidence detectors", NMDA-mediated spine Ca^{2+} transients reach higher concentrations inside spine heads at more depolarized potentials than resting states, possibly explaining the different Ca^{2+} concentrations involved in plasticity induction. AMPARs also play a fundamental role in NMDAR activation. More than direct Ca^{2+} influx through the channel, AMPAR activation

results in depolarization of the spine membrane facilitating the unblocking of NMDARs. This is a particularly efficient mechanism in diffusionally isolated spines, which results in EPSCaTs amplification (Grunditz et al., 2008; Holbro et al., 2010). The local spine depolarization further activates VGCCs that contribute to additional Ca^{2+} entry. In addition, transient depolarization may occur when back-propagating action potentials invade the dendritic arbor, amplifying NMDAR-mediated Ca^{2+} influx. This enhancement contributes to Ca^{2+}-dependent spike-timing dependent plasticity. (Kampa et al., 2007; Nevian and Sakmann, 2006). Ca^{2+} influx through VGCCs is also involved in a negative feedback loop, where R-type Ca^{2+} channels activate small conductance, Ca^{2+} activated-K^+ channels (SK channels) in their close proximity, repolarizing the spine and terminating NMDAR signaling (Bloodgood and Sabatini, 2007b; Ngo-Anh et al., 2005).

NMDAR-mediated Ca^{2+} transients were also used to probe short-term synaptic plasticity properties at individual synapses. Optical quantal analysis at single glutamatergic synapses suggested that small CNS synapses can release more than one vesicle per action potential and that the probability of multivesicular release events increases with synaptic release probabilities (Oertner et al., 2002). Two-photon Ca^{2+} imaging combined with synaptic stimulation further showed that NMDARs are not saturated by the release of a single vesicle (Mainen et al., 1999; Oertner et al., 2002) and that on average less than five receptors are open upon glutamate release and in some cases only one or none (Nimchinsky et al., 2004). Although rare, failures in the probability of NMDARs activation can contribute to the synaptic noise during synaptic transmission (the other source of noise being the stochastic release of neurotransmitters). Notably, the number of NMDARs does not scale with spine volume, so that smaller spines experience larger Ca^{2+} transients during synaptic transmission. The spine neck-geometry can also influence the Ca^{2+} influx through NMDARs. The narrow neck, typical for small spines, allows larger and more confined increases in Ca^{2+} concentration in the spine head, promoting LTP induction. Contrary, large spines with wider neck results in smaller increases in spine Ca^{2+} and greater outflow of Ca^{2+} into the dendritic shaft. This suggests that spines with different sizes and shapes might be differentially tuned during synaptic plasticity, with small spines being the preferential sites for the induction of long-term potentiation (Matsuzaki et al., 2004; Noguchi et al., 2005).

The Ca^{2+} permeability of NMDARs was shown to be regulated by their subunit composition. Indeed, in CA1 pyramidal cells, GluN2B-containing NMDARs display higher fractional Ca^{2+} permeability (the fraction of total current carried by Ca^{2+} ions) and higher glutamate affinity. This has been shown to account for the Ca^{2+} transients heterogeneity found on a synapse-by-synapse basis and hypothesizes to be a selective way underlying synapse-specific plasticity (Sobczyk et al., 2005; Sobczyk and Svoboda, 2007). NMDARs have been linked with a developmental change in subunit composition from GluN2B to GluN2A and shown to be rapidly regulated in response to plasticity-inducing stimuli (Bellone and Nicoll, 2007). The Ca^{2+} permeability through NMDARs is also regulated by the phosphorylation status mediated by metabotropic signaling. For instance, PKA phosphorylation increases the Ca^{2+} permeability while dephosphorylation by phosphatase-1 reduces Ca^{2+} influx (Skeberdis et al., 2006).

1.1.2.4 Other sources of Ca²⁺ influx and clearance of Ca²⁺ in dendritic spines

VGCCs make up a second class of contributors to Ca^{2+} influx within dendritic spines (Fig. 2B). If enough depolarization is provided during synaptic stimulation, VGCCs will open, amplifying the Ca^{2+} influx mediated by NMDARs. Ca^{2+} can also enter spines during back-propagation of action potentials, which trigger an almost immediate rise in spine Ca^{2+} (<2 ms). The latter is primarily mediated by the opening of VGCCs expressed on the spine membrane, with little contribution of Ca^{2+} release from internal stores (Sabatini et al., 2002; Sabatini and Svoboda, 2000; Yasuda et al., 2003). On average, a typical dendritic spine of a CA1 pyramidal neuron contains between 1-20 VGCCs (mainly R and T-type), of which more than half open during a backpropagating AP, displaying stochastic behavior with an open probability of ~0.5. Metabotropic signaling, specifically $G_{i/o}$, can further reduce the channel open probability of those VGCCs. The morphology of the spine impacts Ca^{2+} transient amplitudes and dynamics. Spines have high surface-to-volume ratios (SVR), which decreases with increasing spine size since the SVR ratio of a sphere (as the spine head) is inversely proportional to the radius. Therefore, if the density of Ca^{2+} channels would be independent of spine size, the spine Ca^{2+} transients should be smaller in larger spines than in smaller ones (because of the dilution effect). However, the number of VGCCs per spine is proportional to the spine volume, so that Ca^{2+} accumulation per AP is constant in spines with vastly different SVR ratios (Yasuda et al., 2003). It was also reported that strong activation of spine VGCCs by trains of somatically fired APs (but not strong synaptic activation) induces a spine-specific, long-lasting depression of R-type Ca^{2+} channels (>30 min). This activity-dependent mechanism is part of a self-compensatory negative-feedback that individual spines utilize to counter the excessive Ca^{2+} experience, which can have functional implications in plasticity induction and expression (Yasuda et al., 2003).

In some cases, strong glutamatergic release can lead to the synaptic activation of metabotropic glutamate receptors (mGluRs), triggering a phospholipase-C (PLC) and inositol trisphosphate (IP3) receptors-dependent Ca2+ release from internal stores (Fig. 2B & 3) (Dudman et al., 2007). In addition, putative calcium-induced-calcium-release (CICR) from internal stores by activation of ryanodine receptors, may also contribute to synaptically-evoked spine Ca^{2+} transients (Emptage et al., 1999). However, considering that only a small subset of spines (mostly large, mature synapses) contains an ER (~20%) (Holbro et al., 2009; Perez-Alvarez et al., 2020b), the relative contribution of spine Ca^{2+} transients released from internal stores during low-frequency synaptic activation is low.

Dendritic spines are equipped with endogenous Ca^{2+} buffers (i.e., Ca^{2+}-binding proteins) such as calmodulin and calbindin, and efficient Ca^{2+} extrusion mechanisms to rapidly clear Ca^{2+} from the cytoplasm. This rapid clearance is essential to maintaining spatially and temporally localized Ca^{2+} signals that can mediate synapse-specific forms of plasticity. Those include the sarco-endoplasmic reticulum ATP-ase (SERCA) which sequesters Ca^{2+} ions inside the lumen of intracellular organelles such as the ER, while the plasma membrane Ca^{2+} ATP-ase (PMCA), the Na^+-Ca^{2+} (NCX) and Na^+-Ca^{2+}-K^+ exchangers (NCKX), move Ca^{2+} ions from the cytosol to the extracellular space. Notably, the extrusion mediated by the

PMCA and NCX slows down in an activity and Ca^{2+}-dependent manner, providing a positive feedback mechanism for Ca^{2+} signaling in dendritic spines (Scheuss et al., 2006).
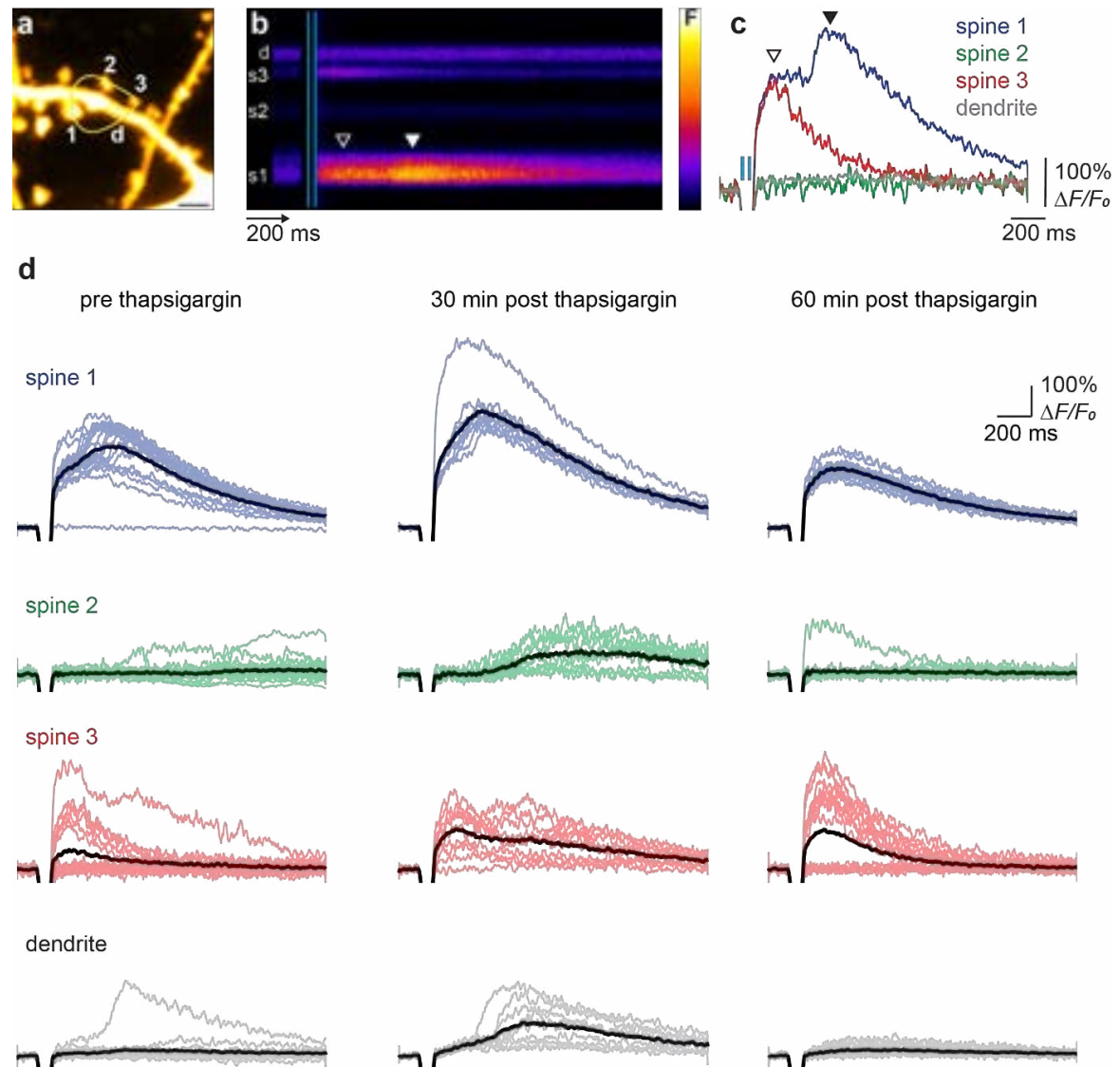
Figure 3. Delayed Ca^{2+} release events from internal store at single spines following synaptic stimulation. (a) Two-photon maximum intensity projection of a dendritic stretch of a CA1 pyramidal neuron in an organotypic hippocampal slice culture expressing the Ca^{2+} indicator GCaMP6s. Yellow line indicates the arbitrary line scan path used to sample Ca^{2+} transients. Numbers indicate spines, d=dendrite. Scale bar: 2 microns. **(b)** Fluorescence signal across time from arbitrary line scan on dendrite shown in (a) in response to paired presynaptic optical stimulation (vertical blue lines) of ChR2-expressing CA3 neurons. **(c)** Plotted traces of the transients shown in (b). Empty and filled triangles correspond to direct, synaptic Ca^{2+} influx through NMDARs and delayed Ca^{2+} release from internal stores, respectively, also indicated in (b). **(d)** Temporally matched traces from multiple trials across multiple spines and parent dendrite, before, 30 minutes and 60 minutes after the application of the non-competitive inhibitor of the sarco/endoplasmic reticulum Ca^{2+} ATP-ase (SERCA) pump thapsigargin. Block of Ca^{2+} refilling by inhibition of the SERCA pump followed by Ca^{2+} depletion from internal stores by repetitive synaptic stimulation removes the delayed Ca^{2+} transients while preserving the direct one (color: individual trials; black: average trials) (Unpublished data, M. Pulin).

1.1.3 Synaptic plasticity and stability

Synaptic plasticity refers to the ability of synaptic connections to modify their strength and efficacy in response to activity. Modification of synaptic transmission at pre-existing synapses has been proposed to play a central role in the capacity of the brain to incorporate new experiences into persistent memory traces. Activity-driven synaptic plasticity can either increase or decrease the strength of synaptic transmission and those changes can occur at different temporal domains, ranging from milliseconds to hours or longer, each with different functional implications. Over the last few decades, multiple forms and functions of synaptic plasticity have been extensively studied and characterized (Citri and Malenka, 2008; Magee and Grienberger, 2020). For instance, classical Hebbian plasticity postulates that correlative activity between presynaptic and postsynaptic neurons strengthens their connections following the detection of two coincident events (Hebb, 1949). This form of correlative plasticity, which can be quickly induced but its effects are often long-lasting, has been widely accepted to represent the neural basis of associative learning. Conversely, non-Hebbian forms of synaptic plasticity, such as homeostatic plasticity, operates on a much slower time scale, do not require coincident activity of two (or more) neurons and generally affect the strength of all synapses in response to global perturbation of activity. This thesis will focus on Hebbian-type long-term synaptic plasticity, namely long-term potentiation and long-term depression of synaptic strength.

1.1.3.1 Long-term plasticity of excitatory synaptic transmission

Integration of new experiences (i.e., learning) is thought to cause activity-dependent, long-lasting modification of synaptic strength. First postulated by Santiago Ramon y Cajal and later reformulated by Canadian psychologist Donald Hebb (Hebb, 1949), the proposed idea of synaptic plasticity in strengthening synaptic connections was experimentally proven only in the early 1970s with the discovery of long-term potentiation (LTP) by Bliss and Lomo (Bliss and Lomo, 1973). After this groundbreaking discovery, extensive research has been dedicated on the function and possible implications of LTP as cellular and molecular mechanisms underlying learning and memory. Its functional counterpart, long-term depression (LTD) was first reported almost 20 years later, as an activity-mediated decrease in synaptic transmission (Dudek and Bear, 1992), demonstrating that changes in synaptic strength could be bi-directionally modulated (Fig. 4B) (Mulkey and Malenka, 1992). When considering both forms of plasticity, this supports the idea that memory formation and storage is not a simple gain of strength (i.e., LTP) but rather the result of a balanced distribution of synaptic weights.

Experimentally, those two classical forms of plasticity have been shown to both occur in response to different activity-patterns and to require Ca^{2+} signaling via NMDARs, although with different concentrations and dynamics. Both LTP and LTD maintain input specificity at spiny synapses, given by localized Ca^{2+} accumulation and biochemical signaling restricted to activated synapses (homosynaptic plasticity) without influencing adjacent spines. However, interactions between nearby active and non-active synapses have been reported, such that potentiation of a single synapse lowers the threshold for subsequent potentiation of neighboring synapses (Fig. 5E) (Harvey and Svoboda, 2007; Harvey et al., 2008).

At the Schaffer collateral synapse (Fig. 4A), one of the most studied and characterized models of NMDAR-dependent plasticity, LTP induction requires simultaneous activation of both pre- and postsynaptic neurons (presynaptic glutamate release and postsynaptic receptor activation), which lead to a strong postsynaptic depolarization and full activation of NMDARs. Consequently, Ca^{2+} influx through NMDARs is now maximal and necessary to activate the biochemical signaling processes responsible for potentiation. Experimentally, this is usually achieved by applying high-frequency stimulation (HFS) to the afferent fibers or by artificial depolarization of the postsynaptic neuron during concomitant presynaptic stimulation. Conversely, LTD can be induced by prolonged repetitive low-frequency stimulation (LFS) which causes only a modest postsynaptic depolarization (Fig 4B). Like LTP, LTD requires the activation of NMDARs, but a more moderate Ca^{2+} influx. This is possible because, even at resting membrane potential NMDARs can be activated due to incomplete Mg^{2+} block, allowing sufficient Ca^{2+} influx (Malenka and Bear, 2004). In summary, it is now well accepted that modest activation of NMDARs leads to a modest Ca^{2+} influx in dendritic spines, which is an optimal trigger for LTD (Cummings et al., 1996), while strong NMDARs activation result in much larger postsynaptic Ca^{2+} concentrations, beyond some critical threshold, necessary to induce LTP (Bliss and Collingridge, 1993).
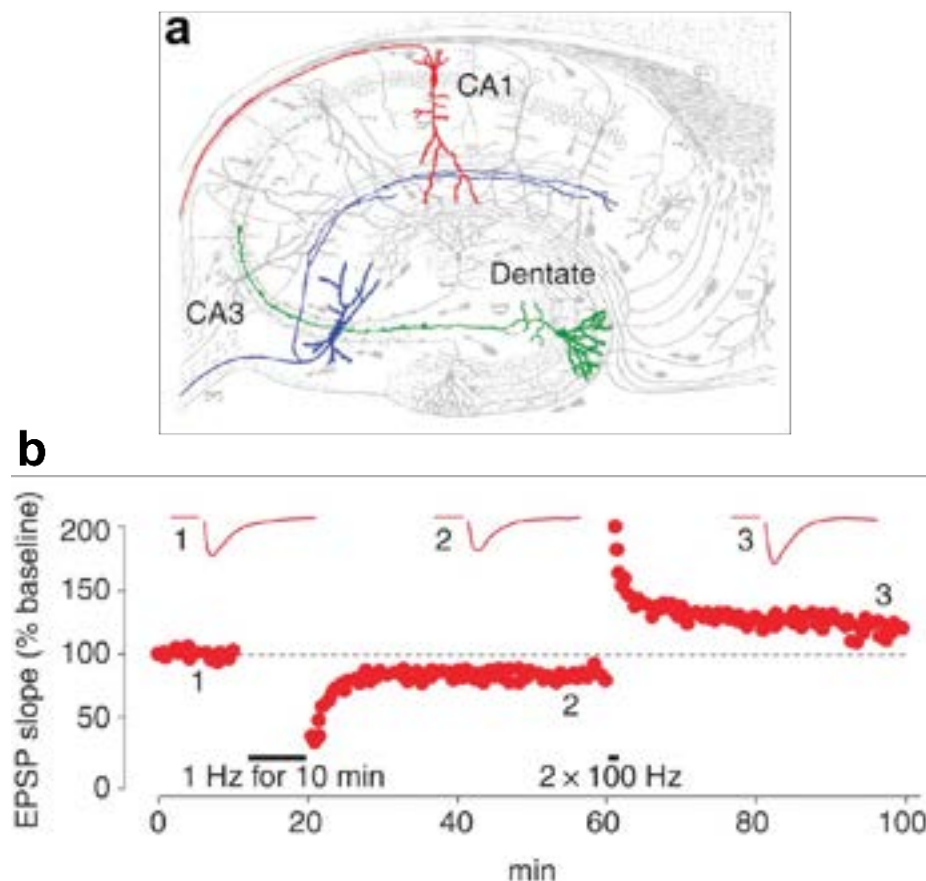
Figure 4. NMDAR-dependent LTD and LTP in the hippocampus. (a) Illustration by Ramon y Cajal (1909) of the trisynaptic pathway in the hippocampus. LTP and LTD are induced by activation of NMDARs at synapses between CA3 and CA1 (red) pyramidal neurons. **(b)** Bidirectional change in CA3-CA1 synaptic efficacy induced by low-frequency stimulation (LFS) or high-frequency stimulation (HFS), to generate LTD and LTP, respectively, in the same synapses monitored by extracellular field recordings in an acute hippocampal slice preparation. Figure and legend adapted from Luscher and Malenka, 2012.

1.1.3.2 NMDAR-dependent LTP and LTD

Multiple events underlie the strengthening of synaptic transmission following LTP induction. Large Ca^{2+} influx through NMDARs triggers a variety of intracellular signaling cascades, most importantly the translocation to the PSD and activation of the Ca^{2+}/calmodulin-dependent protein kinase (CaMKII). The latter is believed to be an essential player in many of the downstream events necessary for expression and maintenance of LTP (Lisman et al., 2012). One of the hallmarks of enhancing synaptic strength during LTP is the alteration in the number, composition and biophysical properties of postsynaptic AMPARs (Derkach et al., 2007; Diering and Huganir, 2018; Huganir and Nicoll, 2013). As the number and organization of AMPARs set the efficacy of glutamatergic synaptic transmission, it is not surprising that modification of AMPAR dynamics occurs during synaptic plasticity (Choquet, 2018). In initial studies, an increase in single-channel conductance of AMPARs has been associated with successful potentiation as a result of CaMKII phosphorylation of the GluA1 receptor subunit (Benke et al., 1998; Derkach et al., 1999; Kristensen et al., 2011). Shortly thereafter, evidence for delivery and accumulation of AMPARs at synaptic sites (PSD) started to emerge (Hayashi et al., 2000; Shi et al., 1999). Although CaMKII is an established major player for the induction of LTP, the signaling cascades underlying the expression and maintenance of LTP are extremely complex, and the link between CaMKII activation (and other kinases and effectors) and insertion of new AMPARs is still not fully understood. It is now well accepted that LTP leads to a mobilization and diffusion-trapping of AMPARs from perisynaptic/extrasynaptic to synaptic sites (Penn et al., 2017) followed by the exocytosis and incorporation of new receptors at potentiated synapses (Granger et al., 2013; Makino and Malinow, 2009; Wu et al., 2017). Modifications of AMPARs auxiliary subunits such as transmembrane AMPAR regulatory proteins (TARPs) are also involved in the translocation of AMPAR into the PSD following LTP induction. Newly inserted AMPARs are then stabilized through their TARP-mediated interaction with PDZ domain-containing scaffold proteins such as PSD-95 that supports the localization of AMPARs at synapses (Opazo et al., 2010; Tomita et al., 2005). More recent evidence suggests that a subpopulation of AMPARs are not randomly distributed within the PSD, but rather organized in clusters or "nanodomains" (Fukata et al., 2013; MacGillavry et al., 2013; Nair et al., 2013) which are themselves co-aligned with presynaptic release sites in so-called "nanocolumns" (Tang et al., 2016). Interestingly, synaptic potentiation has been associated with an increased recruitment and number of those synaptic nanoarchitectures, which ultimately improves synapse efficacy and reliability, providing a new way of fine-tuning synaptic strength (Hruska et al., 2018). Taken together, all those modifications (and others not described here) contribute to the activity-dependent functional potentiation of synaptic transmission.

Although less characterized compared to its counterpart LTP, LTD is described as a weakening of synaptic efficacy, mediated by an activity-dependent loss of AMPARs from the PSD. Similar to LTP, NMDAR-dependent Ca^{2+} influx activates signaling effectors that in the case of LTD, initiate the processes of AMPARs removal (Carroll et al., 1999; Luscher et al., 1999). However, contrary to activation of protein kinases characteristic for LTP, LTD stimuli preferentially trigger the activation of protein phosphatases (primarily calcineurin and protein phosphatase 1) (Mulkey et al., 1994; Mulkey et al., 1993). Those enzymes display higher affinities for Ca^{2+} and are more likely activated by modest increase in Ca^{2+}, which are typical

for LTD stimuli. Transient dephosphorylation of AMPARs themselves or their auxiliary subunits is thought to be the first step towards their dissociation from the PSD (Lee et al., 2000; Morishita et al., 2005). The removed receptors then supposedly first diffuse outside the synaptic sites while later getting trapped at endocytic zones before entering the endocytic cycle (Groc et al., 2004). Very recent work identified Synaptotagmin-3 to be responsible for activity- and Ca^{2+}-dependent removal of AMPARs from synapses during LTD and decay of LTP, even though the precise molecular mechanism mediating this process remain elusive (Awasthi et al., 2019).

Thus, it is generally believed that trafficking of AMPARs in and out of the synapse during LTP and LTD, respectively, account for bidirectional changes in synaptic strength. All the above summarized modifications (and many more) are commonly referred to as functional plasticity.

1.1.3.3 Locus of plasticity expression at the Schaffer collateral synapse

The locus of expression of LTP and LTD has long been a matter of debate. Changes in synaptic strength could be due to more (or less) neurotransmitters being released and/or due to changes in the postsynaptic sensitivity to the released neurotransmitter (Bliss and Collingridge, 2013). It is now widely accepted that synaptic modifications after LTP at the Schaffer collateral synapse are largely postsynaptic, although a presynaptic component has also been described (Bekkers and Stevens, 1990; Emptage et al., 2003; Enoki et al., 2009; Malinow and Tsien, 1990; Padamsey et al., 2017b; Ward et al., 2006). The discovery of silent synapses and their ability to become unsilenced after LTP, together with the proof that glutamate uncaging at single spines (which bypasses the presynaptic release of glutamate) is sufficient to induce LTP, further solidified the concept of LTP being mainly a postsynaptic modification (Busetto et al., 2008; Kerchner and Nicoll, 2008; Matsuzaki et al., 2004). Long-term depression, in addition to the reduction of postsynaptic sensitivity to glutamate, displays a strong presynaptic component, usually observed as a decrease in release probability (P_r) (Padamsey et al., 2017b; Wiegert and Oertner, 2013).

1.1.3.4 Structural plasticity of dendritic spines

Considering the tight correlation between spine head volume, the PSD area, the number of postsynaptic AMPARs and the presynaptic active zone, it is not surprising that synaptic structure is tightly coupled to synaptic function. Thus, it is now well accepted that functional changes in synaptic strength are usually accompanied with changes in synapse structure. In other words, changes in the size of dendritic spines are the structural correlate of changes in synaptic efficacy.
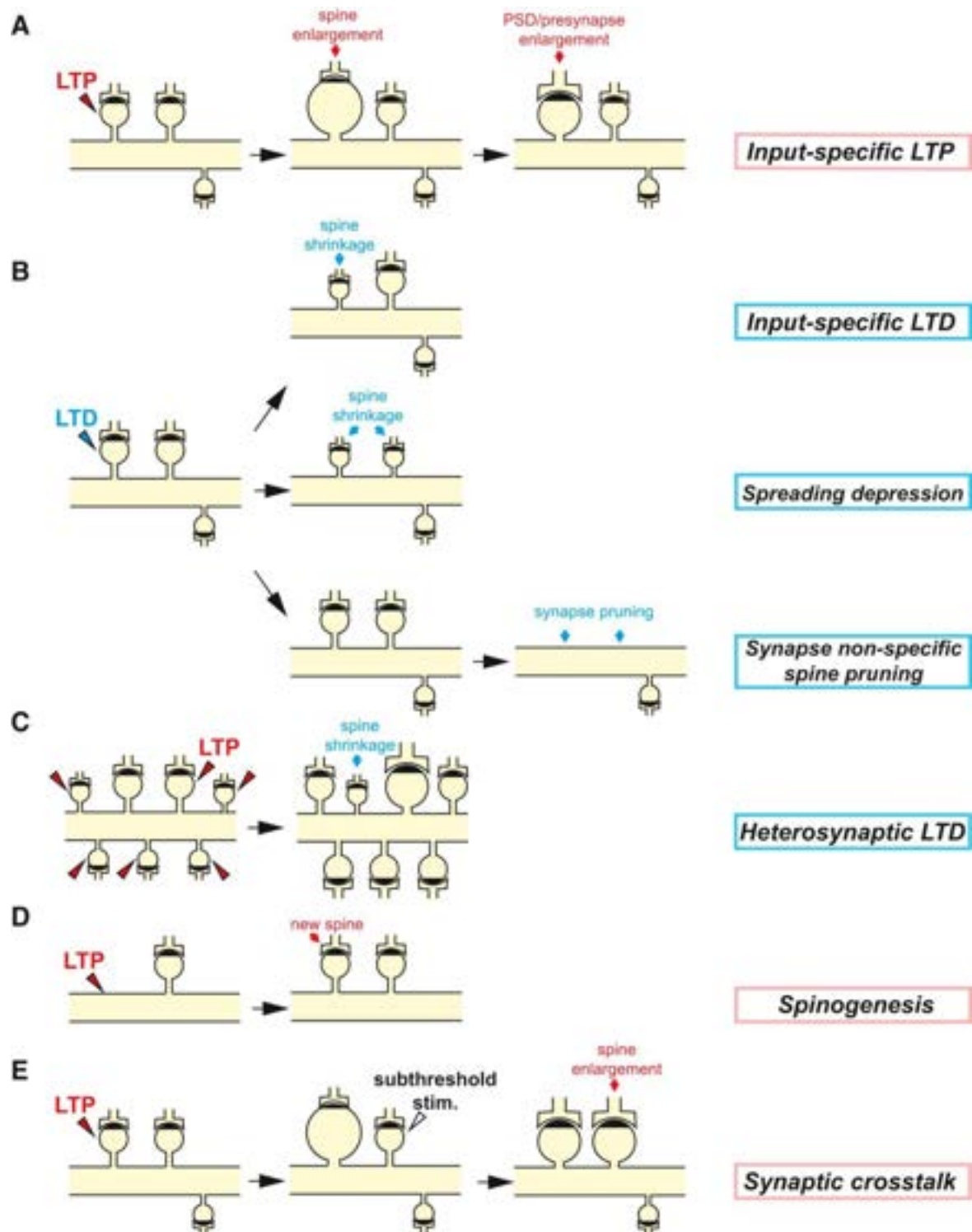
Figure 5. Multiple forms of spine structural plasiticity. (a) Structural plasticity at single spines during input specific LTP. **(b)** Structural plasticity during LTD can result in input-specific spine shrinkage *(top)*, spreading of depression to neighboring, non-stimulated spines *(middle)* or in a non-specific delayed spine pruning *(bottom)*. **(c)** Spine shrinkage can also occur through LTP-induced heterosynaptic LTD. **(d)** Spinogenesis can be induced by glutamate uncaging. **(e)** Structural LTP of neighboring unstimulated spines as a result of synaptic crosstalk. Figure and legend from Nishiyama and Yasuda, 2015.

Right after the discovery of LTP, early EM studies reported a "swelling" of dendritic spines following LTP-inducing stimulation compared to non-stimulated preparation (Fifkova and Van Harreveld, 1977; Van Harreveld and Fifkova, 1975). However, those studies (and others), did not directly prove that pre-existing spines were enlarging following LTP. Pioneering work by the Kasai lab, thanks to the development of two-photon glutamate uncaging (Matsuzaki et al., 2001), finally demonstrated the correlation between functional potentiation and structural enlargement of stimulated spines (Matsuzaki et al., 2004). Repetitive photolysis of caged glutamate induced a persistent expansion of the stimulated spine, which required the activation of NMDARs and CaMKII, and a significant increase in AMPAR-mediated responses. This physical enlargement was later termed structural LTP (sLTP) (Fig. 5A). The massive but transient initial spine structural expansion is ultimately stabilized at a level higher than the original one and sustained for hours. Several studies by a number of different labs, confirmed the correlation between function and structural LTP at single spines (Bosch et al., 2014; Harvey and Svoboda, 2007; Lang et al., 2004; Lee et al., 2009; Okamoto et al., 2004), suggesting that spine enlargement potentially allows synapses to accommodate more AMPARs, thus increasing the postsynaptic sensitivity to glutamate. Spine growth and the insertion of new AMPAR are followed by a delayed increase in the PSD (Bosch et al., 2014; Meyer et al., 2014). The initial rapid structural expansion is thought to be mediated by the rearrangement of actin cytoskeleton within the spine (Bosch et al., 2014; Honkura et al., 2008; Matsuzaki et al., 2004; Okamoto et al., 2004). Technical advances in imaging techniques found that actin polymerization and its subsequent stabilization is responsible for the spine enlargement, downstream of a CaMKII-dependent activation of small GTPases within individual spines (Harvey et al., 2008; Hedrick et al., 2016; Murakoshi et al., 2011). It is believed that these small GTPases (Cdc42, Rac1, RhoA and Ras among others) regulate the activity of several actin-binding proteins (ABPs) such as the actin depolymerizing factor (ADF), cofilin and profilin, promoting actin polymerization after LTP induction. Of note, inhibition of these G-proteins also abolishes functional LTP, further linking functional and structural changes necessary for successful potentiation. In addition to intracellular spine structural remodeling, extracellular factors can also contribute to the structural plasticity of dendritic spines. Those include autocrine signaling by the brain-derived neurotrophic factor (BDNF), remodeling of the extracellular matrix and proteolytic cleavage of neuronal cell adhesion molecules (NCAMs) (Harward et al., 2016; Hedrick et al., 2016; Padamsey et al., 2017a; Wang et al., 2008). Ultimately, activity-driven protein synthesis may be required for sustained structural remodeling and maintenance of long-term plasticity-induced synaptic changes (Govindarajan et al., 2011; Hafner et al., 2019; Tanaka et al., 2008).

Conversely, a decrease in synaptic strength following LTD induction is associated with spine shrinkage and often even with their disappearance (Fig. 5B) (Bastrikova et al., 2008; Nagerl et al., 2004; Okamoto et al., 2004; Zhou et al., 2004). Similar to the spine enlargement observed after LTP, this process involves the remodeling of actin cytoskeleton, although the two mechanisms seem to be regulated by parallel but separate downstream intracellular signaling pathways. LTD stimuli are thought to activate calcineurin that presumably dephosphorylate p-cofilin, and by doing so, the latter acts as a severing enzyme which depolymerizes F-actin. Calcineurin and dephosphorylated cofilin were shown to diffuse over several micrometers (as far as 15 μm from the stimulated spine), acting as a spreading

shrinkage factor necessary and sufficient for shrinkage of neighboring spines (Oh et al., 2015). Interestingly, compared to the almost immediate spine growth following LTP, spine shrinkage seems to occur over longer time periods, probably owing to the slower dismantling of the PSD. However, spine shrinkage is not always observed after LTD (Nagerl et al., 2004; Wiegert and Oertner, 2013; Zhou et al., 2004), showing that functional plasticity can be dissociated from structural plasticity. This would suggest that, although the two mechanisms share the same initial triggering stimulation, they might be differentially regulated distinct downstream pathway.

In conclusion, it is believed that tight coordination of functional changes in synaptic efficacy with structural synaptic changes induced by plasticity, can guide the reorganization of synaptic networks to be structurally maintained for long time periods. However, we still do not know precisely how stable changes in synaptic strength are or where and when synaptic plasticity comes into play to encode learning paradigms in a given neuronal network.

1.1.3.5 Spine dynamics and activity-dependent circuit rewiring

The development of two-photon microscopy and the introduction of genetically encoded fluorescent probes opened the door for visualizing neuronal structures within scattering tissue such as the brain. Using the combination of those two techniques, small cellular substructures such as dendritic spines were visualized in situ in slice cultures (Dunaevsky et al., 1999; Engert and Bonhoeffer, 1999; Maletic-Savatic et al., 1999), and their long-term dynamics and stability could later be monitored even *in vivo* (Grutzendler et al., 2002; Holtmaat et al., 2005; Lendvai et al., 2000; Trachtenberg et al., 2002). Some of those studies, for instance, report a rapid turnover of small filopodia-like spines, which occurs within hours, while bigger, more mature spines usually remain stable for longer time periods (months or even years).

Changes in spine dynamics are thought to be responsible for shaping brain function during postnatal development but also in an experience-dependent fashion during adulthood (Holtmaat and Svoboda, 2009). In addition to the mere scaling of synaptic strength, changes in synaptic connections are considered essential for learning and memory formation (Caroni et al., 2012). Notably, learning paradigms were shown to promote the stabilization and clustering of newly formed spines in the motor cortex that persisted long after training (Fu et al., 2012; Xu et al., 2009). The evidence provided by those studies suggests that neuronal activity is responsible to drive the remodeling of circuits in the mammalian brain through mechanisms of synapse formation, stabilization and elimination (Fig. 6).
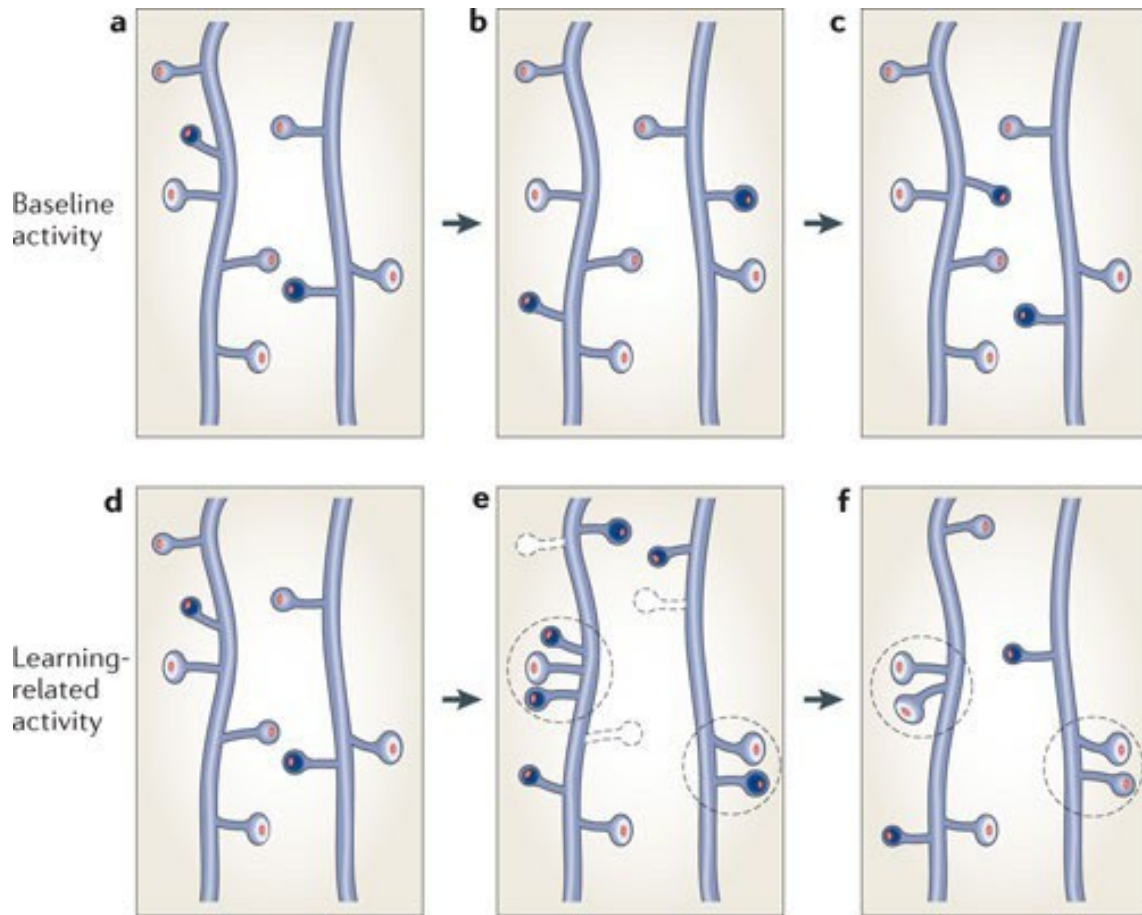
Figure 6. Spine dynamics and learning-induced structural rewiring of synaptic networks. (a-c) Spine turnover under baseline activity, showing gain and loss of transient spines (small black heads) and persistence of stable ones (white heads). **(d-f)** Enhanced turnover od dendritic spines after learning, leading to loss of pre-existing, non-active ones (dashed spines) and formation of new spines (small black heads). Newly formed spines tend to occur in clusters (dashed circles), often in the proximity of pre-existing stable ones, with high chance to persist and integrated in the newly formed synaptic circuit. Figure and legend adapted from Caroni et al., 2012.

1.1.3.6 Plasticity-driven spine dynamics

A prevailing theory is that graded changes in synaptic strength persist as a memory trace of former activity. Synapses in the brain are thought to store information through long-lasting changes in strength but the lifetime of individual synaptic contacts is limited. While spontaneous fluctuations of spines volumes are often observed in the cortex *in vivo* (Holtmaat et al., 2005; Trachtenberg et al., 2002), reflecting the dynamic remodeling of synapses, this opens the question of whether information storage in the brain relies on the analog strength of synapses. Alternatively, on a more behaviorally relevant time scale, information could rather be stored in the rearrangement of the connectivity pattern, which would ultimately be translated as changes in synapse lifetime. In fact, long-term spine stability has been observed, suggesting that life-long memories could potentially be stored in synaptic networks with stable synaptic connectivity (Grutzendler et al., 2002; Yang et al., 2009; Zuo et al., 2005). Given that LTP and LTD are associated with structural changes, they might mediate a precise selection of defined synapses by affecting, for instance, the turnover of dendritic

spines. However, to what extent synaptic plasticity or activity contributes to synapse lifetime remains unknown.

Direct evidence for an activity-dependent spine dynamic regulation comes from *in vitro* studies. Using brain slice preparations, it was shown the LTP-inducing stimuli cause enlargement and stabilization of stimulated spines and that stabilization can last up to three days (De Roo et al., 2008; Hill and Zito, 2013; Yang et al., 2008). In addition to the structural change of pre-existing spines, it was shown that LTP induction in hippocampal slices stimulates the growth of new spines and filopodia (Engert and Bonhoeffer, 1999; Maletic-Savatic et al., 1999; Nagerl et al., 2004; Toni et al., 1999) and that newly formed spines preferentially grow in proximity to activated synapses and become functional (De Roo et al., 2008). Additional studies demonstrated that glutamate uncaging is sufficient to induce *de novo* growth of spines (Fig. 5D) (Kwon and Sabatini, 2011) (Fig. 5D) but also that further potentiation of those newly grown spines helps to stabilize them (Hill and Zito, 2013). Moreover, results from hippocampal slice cultures point also to a long-time lag between early spinogenesis and late synaptogenesis following high-frequency stimulation, indicating a delayed spine maturation into new putative synapses (Nagerl et al., 2007), in accordance with *in vivo* observations (Knott et al., 2006).

Conversely, LTD induction has been associated with destabilization and removal of dendritic spine (Bastrikova et al., 2008; Nagerl et al., 2004; Oh et al., 2013; Wiegert and Oertner, 2013; Zhou et al., 2004) (Fig. 5B). A previous study from our lab investigated the long-term consequences of LTD at individual synapses: By combining presynaptic optogenetic manipulation with functional and structural two-photon imaging of individual Schaffer collateral synapses, Wiegert and Oertner showed that depression leads to a delayed removal of these depressed synapses along with their neighbors (heterosynaptic LTD) (Wiegert and Oertner, 2013). Thus, temporary changes in the connectivity strength in synaptic networks induced by LTD or LTP could be made permanent through synapse elimination and stabilization.

A long-lasting hypothesis posits that synapses can store information through long-lasting changes in synaptic strength, but it is still unknown if and how these functional changes are permanently integrated at the level of individual synapses. While much of the mechanisms of changes in synaptic transmission have been elucidated, it remains unclear what are the long-term consequences of synaptic plasticity and how they affect synapse stability in a functional neuronal network. Throughout life, our brain is constantly exposed to new experiences, which at the level of individual synapses, might be translated into multiple plasticity events. Therefore, the persistence of synapses may directly depend on the precise sequence of potentiation and depression. Previous results from our lab reporting a direct link between induction of LTD and synapses elimination, points in that direction. However, we do not know how potentiation and depression are integrated over time at individual synapses to regulate their lifetime. Does LTP induction results in long-lasting changes in synapse lifetime like LTD by perhaps stabilizing the potentiated spine? If so, can LTP rescue the synapses depressed by LTD and reverse the elimination fate that awaited them? Conversely, can LTD destabilize the otherwise stabilized synapses following LTP? To answer those

questions, in this study, we investigated whether single or sequential plasticity inducing events of opposite polarity cause rewiring of neuronal networks, using the well-characterized CA3-CA1 Schaffer collateral synapse in organotypic hippocampal slice cultures.

1.2   Part II

1.2.1   Optogenetic control of neuronal activity

To elucidate the function of a brain region in the behavior or cognition of an organism, one does require precise and controlled manipulation of its activity. Historically, this has been achieved with rather invasive manipulations to alter the structure and function of the brain. Those include electrical stimulation and pharmacology or even more crude approaches such as lesions or tissue cooling for loss-of-function studies (Wiegert et al., 2017). However, although sometimes efficient, those approaches often lack region specificity and temporal precision. Meeting these criteria has been quite challenging in living organisms, but a breakthrough was made when the advances in genetic engineering were combined with the discovery of light-sensitive proteins. This combination allowed to achieve an unprecedented spatial precision via cell-type specific expression combined with high temporal resolution. This new technology, which utilizes the expression of a light-sensitive protein to control neuronal activity, is known as optogenetics (Deisseroth, 2011; Hausser, 2014).

Optogenetics allows precise control over the activity of genetically defined neuronal cell types while leaving the others unperturbed. Over the past two decades, optogenetic actuators have revolutionized experimental approaches to tackle major neuroscientific questions. As a result, optogenetics has become a widely applied technique and is used in a wide range of studies. Those include investigation of basic neuronal physiology at the single-cell level, up to dissecting complex circuit functions and recently, even reaching the stage of clinical trials in vision restoration (Liu et al., 2012; Packer et al., 2013; Sahel et al., 2021; Scanziani and Hausser, 2009; Yizhar et al., 2011b).

1.2.1.1   Type I (microbial) rhodopsins

The most prominent family of optogenetic tools are microbial rhodopsins (Yizhar et al., 2011a; Zhang et al., 2011). They originate from various organisms, such as prokaryotes (archaea and bacteria) and eukaryotes (algae and fungi). Also known as type-I opsins, microbial rhodopsins are single-component transmembrane proteins that transport various ions across the membrane in response to light. Rhodopsins consist of a light-sensitive chromophore (retinal) covalently bound to a heptahelical transmembrane protein (opsin). Upon light absorption, the rhodopsin enters a cyclic reaction (known as photocycle), where the retinal undergoes isomerization of its protonated Schiff base (it transitions from all-*trans* to 13-*cis* configuration in the case of type-I rhodopsin), leading to conformation rearrangements of the opsin, while still preserving its covalent bond. Thus, the cyclic photoreaction of type-I opsins enables repeated activation, limited by the time required by the rhodopsin to complete its photocycle. Ion-transporting microbial rhodopsins include light-activated ion pumps and channels, but some rhodopsins are also found to be linked to enzymatic activity (Gao et al., 2015; Scheib et al., 2018).

Electrogenic rhodopsins, such as ion pumps and channelrhodopsins, when expressed on the plasma membrane of neurons, can change neuronal excitability through their ionic conductance (Boyden et al., 2005; Chow et al., 2010; Li et al., 2005; Zhang et al., 2007). However, ion pumps, including the proton pumps archaerhodopsin (Arch) and bacteriorhodopsin (BR) and the Cl⁻ pump halorhodopsin (NpHR), conduct a single ion selectively in one direction per photon absorbed, making them relatively inefficient. Thus, pumps require a high expression level at the plasma membrane and high light irradiances for sufficient performance in optogenetic experiments. Further genetic optimizations by the addition of the ER export motif and a neurite trafficking sequence (ts) from the inward rectifying K^+ channel Kir2.1 led to better membrane localization of those pumps, resulting in bigger photocurrents (Gradinaru et al., 2008; Gradinaru et al., 2010; Mattis et al., 2011). Insertion of additional membrane trafficking sequences to the opsin transgene is now a common practice applied to almost every optogenetic tool. In contrast to pumps, light-gated channels pass several ions through their pore per absorbed photon, with the ionic flux being dependent on the electrochemical gradient of the conducted ions and the duration of the conducting state after absorption of a photon.

Light-gated channels, commonly known as Channelrhodopsins (ChRs) (Nagel et al., 2002), represent the most widely used class of microbial rhodopsins so far. ChRs can further be divided into cation-conduction ChRs (CCRs), commonly used for neuronal excitation and anion-conducting ChRs (ACRs), used for inhibition of neuronal spiking (Deisseroth and Hegemann, 2017). Possibly the best-known microbial rhodopsin is the blue-light activated, nonselective cation channel Channelrhodopsin-2 (ChR2) from the green algae *Chlamydomonas reinhardtii* (Nagel et al., 2003). ChR2 has been the first single-component opsin to be expressed in mammalian neurons, allowing millisecond-precise control of neuronal spiking (Boyden et al., 2005; Li et al., 2005).

1.2.1.2 Type II (animal) rhodopsins

The second group of the rhodopsin superfamily is comprised of animal (type-II) opsins, also known as optoGPCRs. Usually found in higher eukaryotes, type-II opsins are associated with visual functions (visual opsins, such as rods and cones) but can also play roles in circadian rhythms and pigment regulation (non-visual opsins) (Shichida and Matsuyama, 2009). Despite sharing no detectable sequence homology, microbial type-I rhodopsins and animal type-II rhodopsins have a similar structural design. The photoreceptor of animal type-II rhodopsins also consist of a seven transmembrane protein, acting as a specialized light-gated G-protein coupled receptor (GPCR) that binds retinal in the 11-*cis* configuration. Retinal isomerizes to all-*trans* when struck by a photon, initiating the GPCR-mediated phototransduction signaling cascade. Type-I rhodopsins can be repetitively activated due to their ability to retain the covalent bond with the retinal upon light absorption. Here the retinal thermally reverts to the all-*trans* configuration, thus allowing the rhodopsin to re-enter a second photocycle. Unlike type-I rhodopsin, the covalent bond in type-II visual opsins is broken following light absorption, a phenomenon known as photobleaching (Fig. 7A). To enter the next photocycle, a new 11-*cis* retinal needs to bind the opsin. On the contrary, non-visual type II rhodopsins, which are found both in vertebrates and invertebrates, retain the

covalent bond between the retinal and the opsin upon illumination and are thus termed bistable (Fig. 7B-C) (Tsukamoto and Terakita, 2010).

Type-II rhodopsins can be evolutionary and functionally classified in two main groups: cyclic-nucleotide signaling (cAMP and cGMP-mediated) and phosphoinositol signaling. Cyclic-nucleotide signaling type II rhodopsins are commonly found in ciliary-type photoreceptors, where the phototransduction is coupled to G_t, $G_{i/o}$ and G_s signaling pathways and commonly act to regulate cyclic nucleotide-gated (CNG) channels. Phosphoinositol signaling type II rhodopsins are found in rhabdomeric-type photoreceptor, where the phototransduction is mediated via G_q signaling (Shichida and Matsuyama, 2009).

Vertebrate type II rhodopsins (vRhs), naturally present in the rods of the retina, were one of the first optogenetic tools heterologously expressed in mammalian neurons to control their activity (Li et al., 2005). Pioneering work by the Herlitze lab first demonstrated that a vertebrate rat rhodopsin 4 (RO4), which naturally couples to the $G_{i/o}$ pathway, can modulate neuronal excitability and synaptic transmission in cultured hippocampal neurons through different signaling cascades of the same G-protein. However, the slow deactivation kinetics and rapid response rundown due to photoceptor bleaching of vRhs, limited their use. An alternative to rod-based vRhs, are vertebrate cone opsins, reported to bleach slower, enabling sustained activation of G-protein signaling pathways. For instance, the fusion of vertebrate cone opsin to the 5-HT$_{1A}$ receptor was sufficient to optically modulate anxiety behavior in mice through repetitive activation of the $G_{i/o}$ pathway (Masseck et al., 2014).

An alternative hybrid optogenetic approach to optically control intracellular signaling via G-proteins, consisting of a chimeric fusion between vertebrate rhodopsin and conventional ligand-gated GPCR, gained popularity over the past few years. Those fusion proteins are referred to as optoXRs (reviewed in Tichy et al., 2019). This hybrid approach allowed optical modulation of the G_q and G_s signaling pathways of the alpha-1 and beta-2 adrenergic receptors (Airan et al., 2009; Kim et al., 2005), respectively and the modulation of the $G_{i/o}$ coupled GPCR pathway of the 5-HT$_{1A}$ receptor (Oh et al., 2010) in behaving animals. However, like vRhs, widespread use of rod-based optoXRs has so far been limited due to their tendency to bleach upon repetitive irradiation.

Of particular interest for optogenetic manipulations of neuronal activity are bistable, non-visual type-II rhodopsins, that couple to a variety of heterotrimeric G-protein complexes (Koyanagi and Terakita, 2014). As previously mentioned, those type II rhodopsins are bleach resistant, thus potentially applicable for repetitive activation, even in non-photoreceptive tissue where the presence of 11-*cis* retinal is limited (Tsukamoto and Terakita, 2010). Several bistable optoGPCRs have been described so far, originating from various organisms. They are able to couple to endogenous G-proteins with potent and prolonged activation of the signaling cascade. Some bistable optoGPCRs further display spectrally distinct stable states that enable photochromic switching between the active and inactive states (Koyanagi et al., 2004), making them promising candidates for precise activation and inactivation of the phototransduction cascade (Fig. 7C).
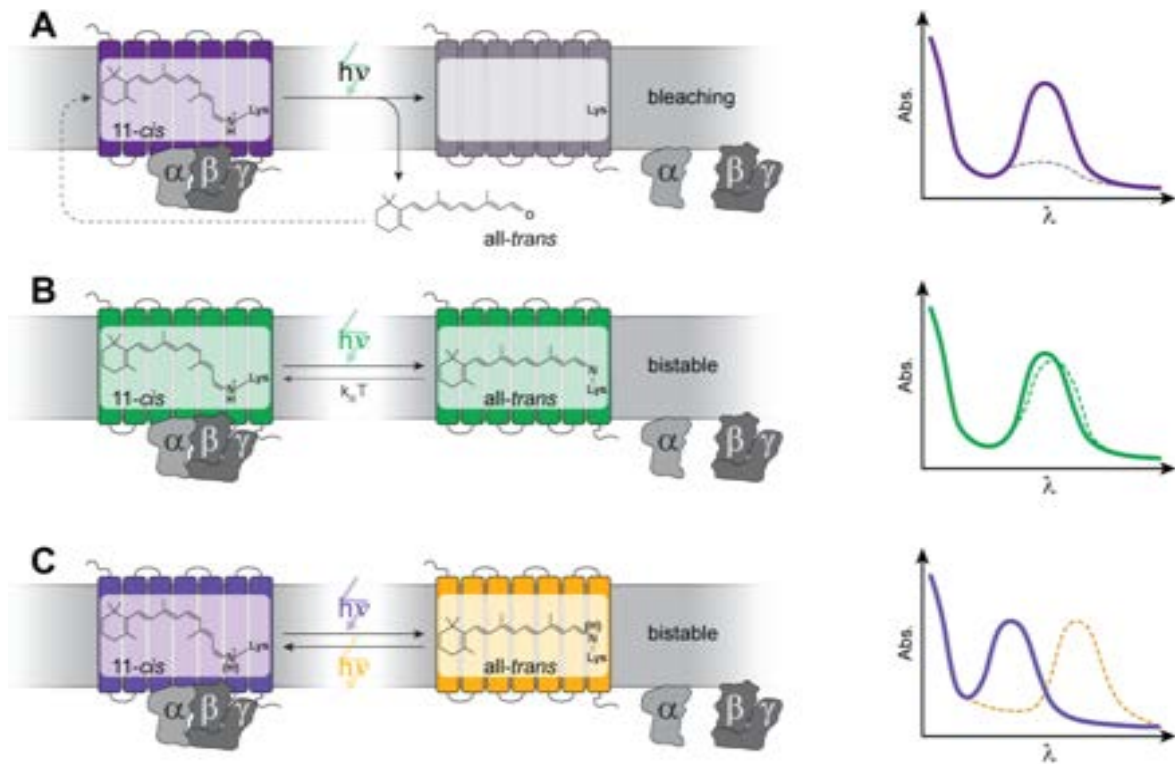
Figure 7. Photocycle properties of bleaching and bistable animal (type II) rhodopsins. Left: schematic diagram of distinct retinal binding mechanisms in bleaching (a) and bistable (b-c) rhodopsins. Righ column: opsins absorbance as a function of wavelength. Tick and dashed lines represent abosrbance of the inactive and active state, respectively. **(a)** Bleaching rhodopsins release all-*trans*-retinal following photon absorption (h*v) and need to bind a new 11-*cis*-retinal before being able to enter the next photocycle. **(b-c)** Bistable rhodopsins retain their covalent bond with retinal independent of its configuration, removing the influence of 11-*cis*-retinal tissue availability. In bistable rhodopsins, all-trans-retinal switches back to 11-*cis*-retinal either by absorbing another photon or spontaneously in the dark with a probability depending on the kinetic energy of the molecule (k_B*T). Photoswitchable bistable optoGPCRs (c) can be interconverted between active and inactive states by absorbing light of different wavelengths. k_B = Boltzmann constant; T = thermodynamic temperature; h = Planck constant; n = photon frequency. Figure kindly provived by Dr. Jonas Wietek and legend adapted from Mahn et al., 2021.

1.2.2 Optogenetic approaches for somatic inhibition of neuronal activity

When studying the function of a neuronal cell type or population in a specific circuit or behavior, loss-of-function approaches are essential for assessing their necessity for the particular parameter of interest (Wiegert et al., 2017). For this reason, inhibitory optogenetic tools became an irreplaceable tool for silencing neuronal activity with high spatiotemporal precision and reversibility. While excitatory optogenetic actuators were used to trigger neuronal firing, inhibitory optogenetic actuators were designed with the intention to suppress neuronal firing. Some of the early tools were based on the light-activated Cl^- pump halorhodopsin (Zhang et al., 2007), which pumps Cl^- ions into the cell, and the H^+ pump archaerhodopsin (Chow et al., 2010), which pumps protons out of the cell. Thus, both tools can be used to hyperpolarize the neuronal cell membrane and thereby suppress APs (Fig. 8A). However, due to their inefficient ion transport (one ion per absorbed photon transported across the membrane), pumps require generally dense membrane expression and

high amounts of light to operate efficiently which can lead to tissue heating and photodamage. In addition, because they actively pump ions regardless of the electrochemical gradient, local changes in ion gradients should be considered to avoid rebound spikes or alterations in the reversal potential of endogenous ionotropic receptors (Mahn et al., 2016; Raimondo et al., 2012).

Engineered ACRs (eACRs), developed by targeted mutagenesis of existing CCRs and their more potent naturally occurring counterparts (nACRs) became the gold standard for optogenetic inhibition neuronal spiking (Berndt et al., 2014; Govorunova et al., 2015; Wietek et al., 2014) (Fig. 8). ACRs are mostly permeable to anions, and unlike inhibitory pumps, ACRs conduct several ions through their channel pore per photon absorbed. The ionic flux exclusively depends on the driving force of the conducted ions. In the case of Cl^-, being the prevalent anion in the brain, this results in "shunting" inhibition of APs in mature neurons, comparable to the action of endogenous $GABA_A$ receptors. Although very efficient, the use of ACRs should be avoided in situations where the flux of Cl^- is depolarizing, such as during development, some specific cell types or subcellular compartments (Kaila et al., 2014; Mahn et al., 2018; Mahn et al., 2016).

In conditions that do not allow the use of ACRs, light-gated K^+ conducting channels might be considered as an alternative approach (Fig. 8). Inhibitory optogenetic tools utilizing K^+ efflux have considerably evolved over the past few years. Some of the complex approaches to make a K^+ channel sensitive to light include K^+ channels coupled to photoswitched tethered ligands (PTL) (Banghart et al., 2004), a chimeric K^+-selective glutamate receptor containing the PTL binding site (Janovjak et al., 2010), light-oxygen-voltage (LOV)-domain-activated K^+ channels (Alberio et al., 2018; Cosentino et al., 2015) and cyclic nucleotide-gated K^+ channels coupled to the photoactivated adenylyl cyclase bPAC (Beck et al., 2018; Bernal Sierra et al., 2018). However, none of these approaches have found wide application in the neuroscience community, mainly due to poor expression in mammalian neurons or other side effects such as altered cAMP levels when using bPAC-based methods. Just recently, naturally occurring light-sensitive K^+ channels have been reported (Govorunova et al., 2021), that may very well outperform all the human attempts in creating a K^+-conducting light-sensitive channel, similarly to ACRs.
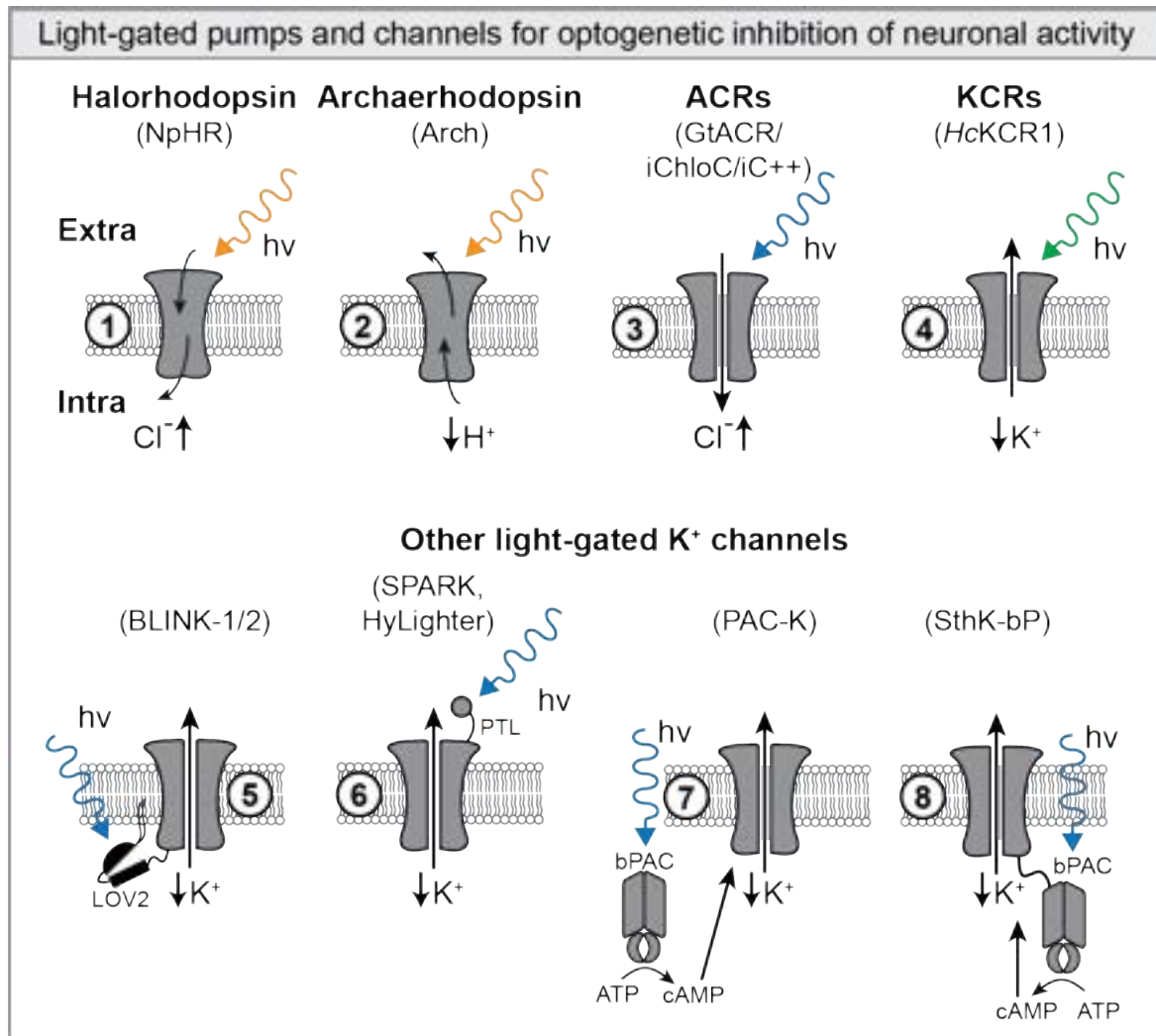
Figure 8. Optogenetic silencing tools for somatic inhibition. Commonly used optogenetic silencers for inhibition of AP firing comprise the inward light-driven pumps halorhodopsin (1) and archaeorhodopsin (2) and light-gated anion channels (3). Halorhodopsin and archaerhodopsins have been also extensively used for presynaptic inhibition of transmitter release (but see Fig. 9). KCRs represent the first class of naturally occurring K^+-conducting channelrhodopsins (4). Other K^+-based approaches comprise indirectly light-activated K^+ channels coupled to the LOV2 domain (5), K^+ channels coupled to photoswitched tethered ligands (PTL) (6) and cyclic nucleotide-gated K^+ channels coupled to the photoactivated adenylyl cyclase (7 and 8). Image adapted from Wiegert et al., 2017.

Additional strategies to reduce somatic excitability would include the use of optoGPCRs that couple to the $G_{i/o}$ pathway. As mentioned in the previous section, VRhs have been employed by several labs to decrease neuronal activity (Li et al., 2005; Masseck et al., 2014), given their higher light sensitivity compared to standard ChRs and their ability to activate the signaling pathway of heterotrimeric $G_{i/o}$-coupled G-proteins. Conventionally, somatic activation of the latter results in decreased production of the second messenger cAMP through inhibition of adenylyl cyclase activity, hyperpolarization mediated by the activation of G-protein coupled inward rectifying K^+ (GIRK) channels and inhibition of several VGCCs.

An alternative strategy for somatic inhibition would be via an optogenetic excitation of inhibitory GABAergic neurons, also known as "ChR-assisted photoinhibition" or indirect photoinhibition. The idea behind this approach is to express excitatory ChRs into inhibitory interneurons either through transgenic lines or viral vectors with high specificity for interneurons (Guo et al., 2014; Zhao et al., 2011). Photostimulation of the GABAergic neurons potently inhibits local pyramidal neurons and thereby removes excitatory output from the optically targeted brain region. However, the different connectivity onto pyramidal neurons that diverse interneurons possess, the strong coupling within cortical circuits and the subsequent uncontrolled spatial spread of inactivation must be considered when designing such optogenetic loss-of-function experiment (Babl et al., 2019; Li et al., 2019).

1.2.3 Presynaptic optogenetic inhibition of neurotransmitter release

Optogenetic manipulation of long-range projecting axons has proven to be a valuable method to study the functional connectivity of genetically defined neurons. For instance, CRACM ("ChR-2-assisted circuit mapping") allowed the spatial mapping of functional synaptic input converging on dendritic branches of postsynaptic targets by optical stimulation of presynaptic ChR2-expressing axons (Martinetti et al., 2021; Petreanu et al., 2007; Petreanu et al., 2009). However, although much more selective than electrical stimulation, optical depolarization of synaptic terminals comes with the expense of an increased release probability (Jackman et al., 2014; Zhang and Oertner, 2007). This artifact leads to a more reliable and efficient synaptic transmission, which presents some advantages if the functional connectivity between two neuronal partners is assessed but complicates the interpretation of physiological synaptic release properties (Martinetti et al., 2021).

Analogous to synaptic circuit investigation by direct optical synaptic stimulation approaches, synaptic silencing could provide a selective approach for studying the contribution of a defined neuronal projection pathway to a function while leaving the upstream bodies and other collaterals untouched. Theoretically, optogenetic silencing of synaptic transmission can be achieved by either blocking the propagation of the AP or by direct suppression of neurotransmitter release. While optogenetic stimulation of synaptic transmission is relatively straightforward to achieve, optogenetic synaptic silencing appears to be much more challenging. Several caveats oppose the use of optogenetic silencing tools at presynaptic terminals. First, like for excitatory ChRs, expression of inhibitory optogenetic tools to the axonal terminal is particularly challenging due the long distance from the soma. Because of the lack of targeting sequences to enhance axonal localization of membrane proteins, opsins must travel and overcome the barrier imposed by the axonal initial segment (AIS) and passively reach axonal terminals over longer time periods (Watanabe et al., 2012). Second, particular attention must be given to the unique physiology of this neuronal compartment.

1.2.3.1 Light-driven pumps and anion channels

The axon possesses different ionic gradients compared to the somatodendritic region (Pugh and Jahr, 2011; Szabadics et al., 2006; Turecek and Trussell, 2001). Therefore, hyperpolarization or shunting inhibition attempts through electrogenic light-driven ion

pumps and channels might not always work or sometimes even display paradoxical side effects (Mahn et al., 2016) (Fig. 9). Meticulous work by Mahn et al., characterized these effects in detail: while evoked presynaptic release was attenuated by optogenetic inhibition with the improved light-gated proton and Cl^- pumps eArch3.0- and eNpHR3.0, respectively, during brief light pulses, light cessation was always followed by unwanted rebound spikes. The latter is most likely a consequence of hyperpolarization-mediated recovery from inactivation of voltage-gated Na^+ (removal of the ball-and-chain inactivation) and low-voltage activated T-type Ca^{2+} channels. Additional hyperpolarization-activated cation channels might open and contribute to the fast depolarization and firing of APs following abrupt cessation of illumination. The authors suggest that this unwanted effect can be avoided by gradually fading the light off with ramp-like light termination. While instantaneous silencing at axonal terminals can be achieved with optogenetic pumps, due to their one-to-one photon-ion stoichiometry type of activity mechanisms, light-driven pumps must constantly be illuminated to maintain a hyperpolarizing state of the membrane potential. This can involuntarily shift the Cl^- reversal potential in the case of halorhodopsin (Raimondo et al., 2012) or alkalize the intracellular compartment when pumping out proton with archaerhodopsin. Such effects would be even more pronounced in small compartments such as the axon with high surface-to-volume ratios. Indeed, the authors observed an even more stunning side-effect on synaptic activity during prolonged illumination. While evoked release was still decently decreased, spontaneous synaptic transmission was massively upregulated during prolonged activation of eArch3.0- but not eNpHR3.0, both in dissociated hippocampal cultures and thalamocortical brain slices. This effect was mediated by the increase of intracellular pH and subsequent activation of pH-dependent Ca^{2+} channels at presynaptic terminals, resulting in an AP-independent increase in spontaneous glutamate release. Interestingly, another study showed that the mechanism of action of eArch3.0 in suppressing transmitter release is mediated through alkalization of the cytosol and not hyperpolarization (El-Gaby et al., 2016). Lastly, Mahn and co-authors tested the ability of a Cl^--conducting ChR to suppress neurotransmission. Activation of GtACR1 at synaptic terminals did not abolish electrically evoked release, but rather enhanced release itself, suggesting that synaptic terminals were being depolarized by the GtACR1 conductance. Such effect could be explained by an increase Cl^- concentration in those thalamic projections (Mahn et al., 2018; Szabadics et al., 2006) which results in a more depolarized Cl^- reversal potential compared to the somatic one.
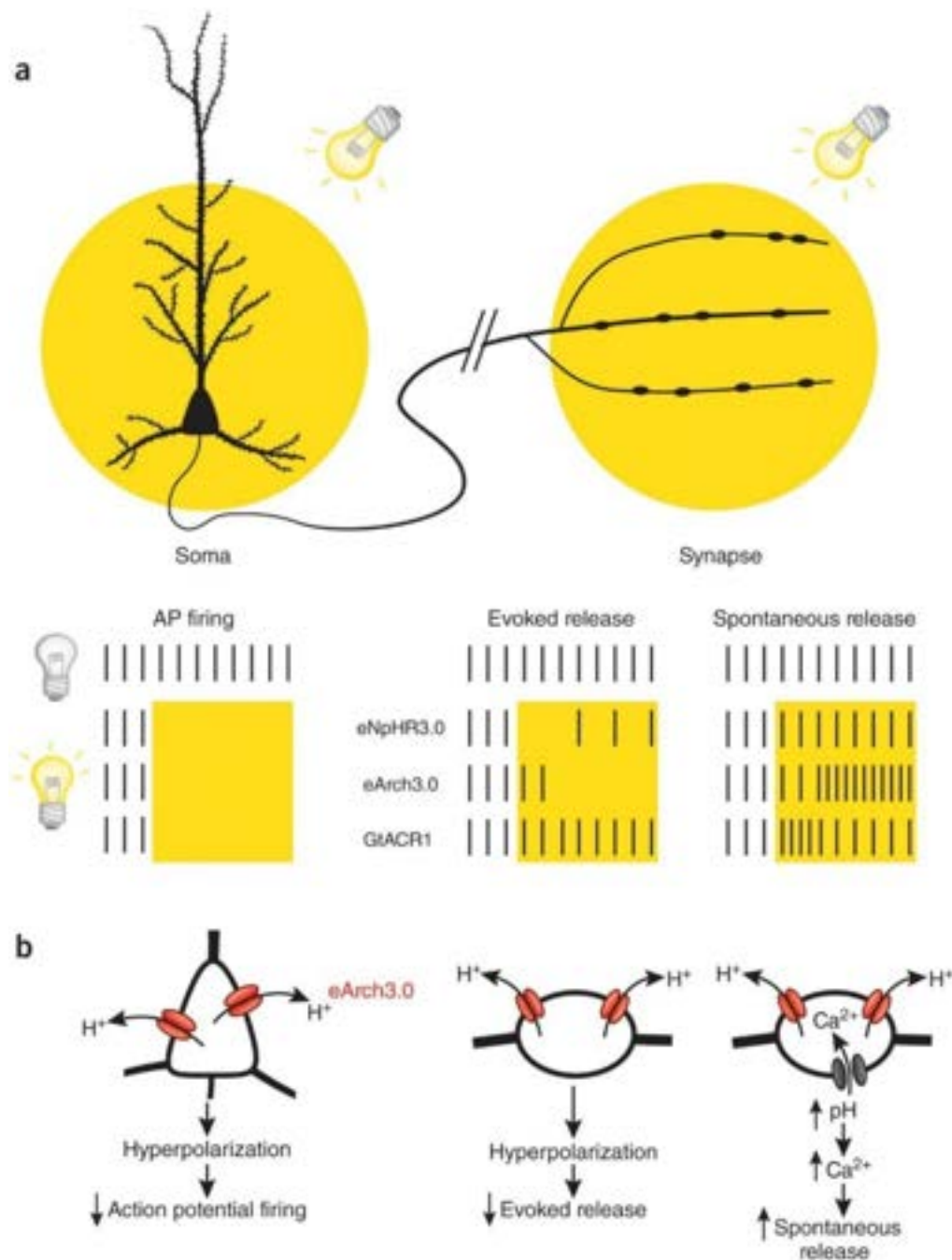
Figure 9. Caveats of presynaptic optogenetic inhibition with light-driven Cl⁻ and H⁺ pumps and ACRs. **(a)** The chloride pump eNpHR3.0 suppresses release evoked by action potentials and has no effect on spontaneous release. The proton pump eArch3.0 suppresses evoked release, but strongly enhances spontaneous release, making the net result difficult to predict. The chloride channel GtACR1 does not affect evoked release, but it directly stimulates release—not the desired outcome if inhibition is the goal. **(b)** Proposed mechanism for the inhibitory and excitatory actions of eArch3.0. During prolonged illumination, alkalization of the cytoplasm leads to activation of pH dependent Ca^{2+} channels, increasing spontaneous release of glutamate. Figure and legend from Wiegert and Oertner, 2016.

A way to reduce axonal excitation and antidromic propagation of spikes induced by activation of potent Cl⁻-conducting ChRs at presynaptic terminals, would be to restrict the expression of those optogenetic tools to the somatodendritic region. This strategy was achieved by adding a soma-targeting motif of voltage-gated K^+ channel Kv2.1 to the opsin,

which restricts its expression to the somatodendritic compartment and even enhanced its potency (Mahn et al., 2018). To achieve silencing at synaptic terminals by local illumination one could in principle employ light-gated K$^+$-channels. The K$^+$ reversal potential at presynaptic terminals would lead to potent hyperpolarization upon opening of K$^+$-channels. However, to date, K$^+$-based presynaptic optogenetic inhibition has not been achieved, mainly because of localization inefficiencies at axonal terminals.

In summary, optogenetic silencing of synaptic transmission with current electrogenic light-driven pumps and channels remains challenging. Applying optogenetic tools at presynaptic terminals requires careful consideration of both the biophysical property of the tool and the specific physiology of the subcellular compartment. All those aspects should be considered when designing an optogenetic silencing experiment and avoid possible side effects, in addition to appropriate controls.
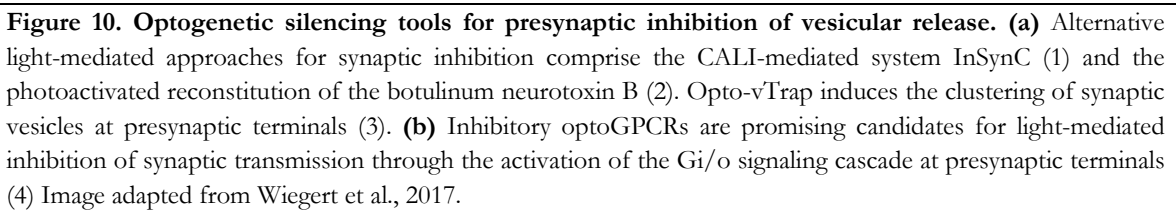
1.2.3.2 Alternative light-activated approaches for synaptic inhibition

Due to the above-mentioned drawbacks, other light-mediated approaches have been developed to achieve the long-persuaded goal of direct silencing at synaptic terminals. Instead of trying to fight the AP propagation by optogenetic hyperpolarization or alkalization, several approaches aimed at directly destroying the presynaptic release machinery. The first of its kind was InSynC, for "Inhibition of Synapses with CALI" (Lin et al., 2013) (Fig 10A). Here, a genetically encoded flavoprotein photosensitizer miniSOG (mini–Singlet Oxigen Generator), is attached to presynaptic proteins synaptobrevin/VAMP-2 or synaptophysin and generates reactive oxygen species (ROS) in response to blue light, disrupting the presynaptic release machine function by protein oxidation in a mechanism coined "chromophore assisted light inactivation" (CALI). InSynC resulted in efficient long-term inhibition of synaptic transmission in dissociated and organotypic neuronal cultures and impaired locomotion in *C. elegans*.

A second approach took advantage of the photoswitching ability of the *Avena sativa* derived light-oxygen-voltage 2 domain (AsLOV2). The fusion of the two naturally binding bacterial peptides to the AsLOV2 domain, created the "improved light-induced dimer" (iLID) system. In the dark, one of the two bacterial peptides is masked by the C-terminal helix of the AsLOV2 domain, which, upon blue light illumination, unbinds from the protein, allowing the two peptides to dimerize (Guntas et al., 2015). Fused to a split Botulin neurotoxin B, the AsLOV2-derived iLID photodimerization system, allows a tight, light-controlled reconstitution of the split Botulinum neurotoxin B (Liu et al., 2019) (Fig 10A). The photoactivated Botulinum neurotoxin B (PA-BoNT), once reconstituted, specifically cleaves the vesicle-associated membrane protein 2 (VAMP2), a member of the presynaptic SNARE proteins complex responsible for vesicle fusion and neurotransmitter release. Blue light illumination at synaptic terminals expressing PA-BoNT or vPA-BoNT (a version of the PA-BoNT attached to the presynaptic vesicle protein synaptophysin), strongly impaired neurotransmission in mouse brain slices and decreased swimming in transgenic *C.elegans*.

If chronic synaptic silencing is desired, both InSynC and vPA-BoNT might be preferentially used, as they do not require repetitive light stimulation. Also, both approaches are in principle applicable to virtually any type of synapse. However, both strategies have a prolonged onset effect requiring several minutes of illumination. Their recovery is even slower (hours) since it depends on the synthesis of new synaptic proteins or by lateral trafficking of intact proteins. Thus, the poor time resolution of those tools has limited applicability. Also, the PA-BoNT system shows residual dark activity and, if virally delivered, requires the application of two AAVs. In addition, long-term consequences of protein destruction or unspecific protein damage, due to ROS spread for instance, should be considered and carefully evaluated.

Just recently, a new flavoprotein-based optogenetic tool to control neurotransmitter release with improved temporal resolution (and no destructive mechanisms of action) was reported. This tool employs the "light-activated reversible inhibition by assembled trap" (LARIAT) technique (Lee et al., 2014), targeting it directly at synaptic vesicles to block their exocytosis. Briefly, LARIAT utilizes the blue-light induced photodimerization between the photosensitive *Arabidopsis thaliana*-derived cryptochrome 2 (CRY2) and its binding partner cryptochrome-interacting basic-helix-loop-helix 1 (CIB1), forming a CRY2-CIB1 multimeric complex (Kennedy et al., 2010). Importantly, CRY2 can form light-induced homooligomers of CRY2:CRY2 via interactions of their photolyase homology regions (PHRs). When conjugated to synaptic vesicles by fusing the CIB1 peptide to VAMP2, blue light illumination produces heteromeric dimers of CRY2:CIB1-VAMP2 and homomeric oligomers of CRY2:CRY2, thus sequestering transmitter-containing vesicle into clusters and inhibiting vesicular release. This approach was named Opto-vTrap (Won et al., 2021) (Fig 10A). Light activation of Opto-vTrap was shown to induce a significant reduction of synaptic- and gliotransmission in acute brain slices, which recovered within 30 minutes. Opto-vTrap was further used to reversibly inhibit hippocampal contextual fear memory retrieval in behaving mice. Opto-vTrap could in principle have a much broader application than trapping neurotransmitter-filled vesicles and could potentially be applied to any type of secreted vesicles and cell type with adequate subcellular targeting. However, despite displaying much better recovery kinetics than InSynC and PA-BoNT, Opto-vTrap requires relative long periods of light exposures (minutes) for activation, much slower than the millisecond precision of microbial rhodopsins.

Figure 10. Optogenetic silencing tools for presynaptic inhibition of vesicular release. (a) Alternative light-mediated approaches for synaptic inhibition comprise the CALI-mediated system InSynC (1) and the photoactivated reconstitution of the botulinum neurotoxin B (2). Opto-vTrap induces the clustering of synaptic vesicles at presynaptic terminals (3). **(b)** Inhibitory optoGPCRs are promising candidates for light-mediated inhibition of synaptic transmission through the activation of the Gi/o signaling cascade at presynaptic terminals (4) Image adapted from Wiegert et al., 2017.

1.2.3.3 Presynaptic inhibition through GPCR signaling

The ideal presynaptic inhibitory optogenetic tool should have a fast onset, an efficient effect and be fully reversible. To date, chemogenetic approaches are probably the most reliable tools for reversible silencing of synaptic transmission. In particular, the inhibitory "designer receptor exclusively activated by designer drugs" (DREADDs) hM4D, has proven to be particularly effective in inhibiting neurotransmitter release (Armbruster et al., 2007; Roth, 2016; Stachniak et al., 2014; Zhu and Roth, 2014). Upon delivery of its cognate ligand clozapine-N-oxide (CNO), this engineered GPCR activates the $G_{i/o}$ signaling pathway and inhibits synaptic transmission similarly to native inhibitory ligand-gated GPCRs (Wu and Saggau, 1997). This inhibitory presynaptic effect is presumably mediated through the suppression of presynaptic VGCCs-mediated Ca^{2+} influx and interference with the presynaptic release machinery (Bean, 1989; Blackmer et al., 2001; Gerachshenko et al., 2005; Hamid et al., 2014; Herlitze et al., 1996; Zamponi and Currie, 2013; Zurawski et al., 2019). However, even this effective approach suffers from low temporal control due to slow drug onset and offset kinetics. This depends on ligand clearance and pharmacokinetics, which can greatly vary between preparations and experimental conditions. Chemogenetic approaches also suffer from poor spatial specificity, as the infusion and diffusion of CNO are hard to control, often leading to potential off-site effects. As previously mentioned, vRhs were shown to couple and activate the $G_{i/o}$ signaling pathway and partially suppress neurotransmitter release (Li et al., 2005) (Fig 10B). Nonetheless, given the fact that they undergo rapid photobleaching, this casts doubts as to whether they can be used for sustained and efficient presynaptic inhibition. Inspired by the potent presynaptic effect of hM4D and supported by the evidence provided by vRhs, we reasoned that members of the $G_{i/o}$-coupled, bistable type II rhodopsin family might function as potent and sustained inhibitors of presynaptic release (Koyanagi and Terakita, 2014; Tsukamoto and Terakita, 2010). The mosquito-derived homolog of the mammalian encephalopsin protein (OPN3) (Koyanagi et al., 2013), which upon light illumination allows efficient and specific activation of the $G_{i/o}$ signaling cascade, appeared as a promising candidate for light-mediated inhibition of neurotransmitter release at presynaptic terminals. We therefore went on to characterize in detail its functional properties and investigate its potential as a novel optogenetic tool for synaptic silencing.

1.3 Part III

1.3.1 Principles of linear dichroism in biological systems

Light is described as a propagating electromagnetic wave whose electric field oscillates perpendicular to the direction of propagation. When the direction of the electric field is well defined, light is referred to as polarized. If the direction of the electric field oscillates in a single plane along the direction of light propagation, it is defined as being 'linearly polarized'. Optical excitation of a molecule depends on the orientation of the dipole moment of the chromophore relative to the linear polarization of the excitation light, a property known as linear dichroism (LD) or anisotropy of excitation. In the case of fluorescence, when the excitation intensity depends on the direction of the excitation light polarization, this is commonly referred to as fluorescence-dependent linear dichroism (FDLD) (Dafforn and Rodger, 2004). Polarization can also be detected in the emitted photons in a process termed fluorescence anisotropy. Measurements of FDLD, which contains information about the orientation of the fluorophore, can be useful to study the movements of fluorescently labeled molecules in a particular environment, such as the rotational speed of molecules in solutions or protein-protein interactions (Hess et al., 2003; Lazar et al., 2011).

This anisotropic optical property of molecules can be particularly exploited when the rotational flexibility of fluorescent molecules is limited, as in membrane proteins (Benninger et al., 2005; Lazar et al., 2011). The cellular plasma membrane is a dynamic but ordered environment, where the molecules and transmembrane proteins can have anisotropic orientations. To investigate the anisotropic properties of membrane-anchored proteins, the excitation light should be linearly polarized such as in lasers used for confocal and two-photon microscopy. However, in conventional confocal microscopy, the incoming laser beam travels through optic fibers that lead to randomized excitation light polarization at the sample. On the contrary, common two-photon microscopes are suitable for FDLD measurements, since the excitation laser beam preserves the linear polarization state of light. Two-photon microscopes use near-infrared lasers that generate femtosecond pulses at high repetition rates, allowing a high photon density and flux required to achieve the near-simultaneous absorption of two photons by a molecule necessary for the two-photon excitation effect (Denk et al., 1990). Single linearly polarized microscopes can be equipped with simple polarization modules, such as rotating half-wave plates, allowing flexible FDLD imaging of different orientations of labeled proteins (Gasecka et al., 2009). Indeed, two-photon polarization microscopy was used to study the activation and subunit interactions of heterotrimeric G-proteins (Lazar et al., 2011), movements of membrane lipid domains (Gasecka et al., 2009) and the effects of cholesterol depletion on the cell membrane organization (Benninger et al., 2005). Furthermore, it was reported that a "doubly-lipidated" GFP (dlGFP), a genetically encoded construct consisting of a GFP anchored to the plasma membrane at both barrel ends, displays strong FDLD properties. This is because the tethering on both sides of the barrel anchors the fluorescent protein in a rigid position, with the chromophore dipole nearly orthogonal to the cell membrane (Roorda et al., 2004). This confers optimal properties to the construct to study anisotropic effects in living cells (Lazar et al., 2011).

1.3.2 Design principles of genetically encoded sensors for neurotransmitters and neuromodulators

Over the last decades, numerous genetically encoded neurotransmitter and neuromodulator fluorescent sensors have been developed (Feng et al., 2019; Jing et al., 2020; Marvin et al., 2013; Marvin et al., 2019; Patriarchi et al., 2018; Sun et al., 2018; Wan et al., 2021). Their introduction and applications in neuroscience has allowed to directly measure neurotransmitter and neuromodulator dynamics with high spatiotemporal resolution and specificity via fluorescence imaging (Sabatini and Tian, 2020). This class of protein-based neurotransmitter and neuromodulator sensors (similar to Ca^{2+} and some voltage sensors) consists of a reporter element, typically a fluorescent protein, attached to a ligand-binding or sensing domain. The design of genetically encoded neurotransmitter and neuromodulator indicators can be generally categorized in two sub-classes, based on their ligand-binding scaffold: bacterial periplasmic binding proteins (PBPs) and G-protein coupled receptors (GPCRs). GPCR-based neuromodulator sensors, originate by inserting a circularly permuted GFP into the third intracellular loop (between transmembrane helices 5 and 6) of native neuromodulatory seven-transmembrane receptors (Wang et al., 2018). Such sensor design removes the G-protein signaling cascade that the binding of the ligand would otherwise trigger. Instead, conformational changes of the receptor upon ligand binding are mechanically transmitted to the fluorescent protein, thereby modulating its fluorescent properties (deprotonation of the chromophore and shift in absorbance). Here, binding of the ligand initiates a cascade of conformational changes within the transmembrane helices, where the largest motions occur at the transmembrane helix 6 after which brings the third intracellular loop from a disordered to an ordered state, a crucial step when recruiting G proteins. Therefore, as for neurotransmitter sensors, in GPCR-based neuromodulators sensors, extracellular changes in ligand concentration are translated into changes in fluorescence. Although granting high molecular specificity and large dynamic range, such sensor design might be sensitive to the polarization of light. This is due to the insertion of the cpGFP by tethering it at both sides of the barrel to the receptor domain, which may orient it parallel to the membrane. Thus, similar to the dlGFP, this orientation may confer a strong polarization dependence of excitation of GPCR-based sensors. Here, we explored this possibility by imaging several GPCR-based fluorescent sensor and other membrane-bound fluorescent reporters with two-photon microscopy in organotypic hippocampal slice cultures. To our surprise, we found strong excitation dependence on light polarization of a subclass of GPCR-based fluorescent reporters. This effect was strikingly visible in tubular structures of well-defined orientation such as the apical dendrites of CA1 pyramidal neurons. From there on, we went to characterize this effect in more details and turn it around in our favor by developing an optical device able to overcome this limitation.

2 Included publications

2.1 Publication I

The full article can be found at the end of this thesis. Please refer to the manuscript for additional information and detailed description of the methods and results.

2.1.1 The fate of hippocampal synapses depends on the sequence of plasticity-inducing events

J. Simon Wiegert[1,2], **Mauro Pulin**[1,2], Christine Elizabeth Gee[1], Thomas G. Oertner[1]

[1]Institute for Synaptic Physiology, Center for Molecular Neurobiology Hamburg, University Medical Center Hamburg-Eppendorf, Hamburg, Germany

[2]Research Group Synaptic Wiring and Information Processing, Center for Molecular Neurobiology Hamburg, University Medical Center Hamburg-Eppendorf, Hamburg, Germany.

2.1.2 Abstract – publication I

Synapses change their strength in response to specific activity patterns. This functional plasticity is assumed to be the brain's primary mechanism for information storage. We used optogenetic stimulation of rat hippocampal slice cultures to induce long-term potentiation (LTP), long-term depression (LTD), or both forms of plasticity in sequence. Two-photon imaging of spine calcium signals allowed us to identify stimulated synapses and to follow their fate for the next 7 days. We found that plasticity-inducing protocols affected the synapse's chance for survival: LTP increased synaptic stability, LTD destabilized synapses, and the effect of the last stimulation protocol was dominant over earlier stimulations. Interestingly, most potentiated synapses were resistant to depression-inducing protocols delivered 24 hr later. Our findings suggest that activity-dependent changes in the transmission strength of individual synapses are transient, but have long-lasting consequences for synaptic lifetime.

2.1.3 Personal contribution – publication I

My contribution to this publication was the following: investigation, formal analysis, data curation and interpretation of the results. In more detail, I conducted experiments, combining different transgene delivery techniques such as single-cell electroporation and viral injections of genetically encoded actuators, indicators and morphology markers in organotypic hippocampal slice cultures with optogenetics, patch-clamp electrophysiology and two-photon microscopy. I measured the function and chronically monitored the structure of individual dendritic spines by two-photon imaging of genetically encoded calcium indicators and morphology markers, respectively, in intact tissue. My results are included in Figures 2 and 3. In addition, I solely conducted the experimental investigation during the revision process that resulted in an additional figure (Figure supplement 1 of Figure 2). Following data acquisition, I analyzed, displayed and interpreted the results and integrated them in the manuscript.

Hamburg, __23.02.2022____.

Mauro Pulin	Prof. Dr. Thomas Oertner	Prof. Dr. Simon Wiegert

2.2   Publication II

The full article can be found at the end of this thesis. Please refer to the manuscript for additional information and detailed description of the methods and results.

2.2.1   Efficient optogenetic silencing of neurotransmitter release with a mosquito rhodopsin

Mathias Mahn[1,2,*], Inbar Saraf-Sinik[1,*], Pritish Patil[1,*], **Mauro Pulin[3,*]**, Eyal Bitton[1], Nikolaos Karalis[2], Felicitas Bruentgens[5], Shaked Palgi[1], Asaf Gat[1], Julien Dine[1], Jonas Wietek[1], Ido Davidi[1], Rivka Levy[1], Anna Litvin[1], Fangmin Zhou[3], Kathrin Sauter[3], Peter Soba[3,4], Dietmar Schmitz[5,6,7,8,9,10], Andreas Lüthi[2], Benjamin R. Rost[6], J. Simon Wiegert[3] and Ofer Yizhar[1]

[1]Department of Neurobiology, Weizmann Institute of Science, Rehovot 76100, Israel

[2]Friedrich Miescher Institute for Biomedical Research, Basel, 4058, Switzerland

[3]Center for Molecular Neurobiology Hamburg, Hamburg 20251, Germany

[4]LIMES Institute, University of Bonn, Bonn 53115, Germany

[5]Charité-Universitätsmedizin Berlin, Berlin 10117, Germany

[6]German Center for Neurodegenerative Diseases (DZNE), Berlin 10117, Germany

[7]Bernstein Center for Computational Neuroscience, Berlin 10115, Germany

[8]Cluster of Excellence NeuroCure, Berlin 10117, Germany

[9]Einstein Center for Neurosciences Berlin, Berlin 10117, Germany

[10]Max-Delbrück Center for Molecular Medicine, Berlin 13125, Germany

*These authors have equally contributed to this work

2.2.2   Abstract – publication II

Information is carried between brain regions through neurotransmitter release from axonal presynaptic terminals. Understanding the functional roles of defined neuronal projection pathways requires temporally precise manipulation of their activity. However, existing inhibitory optogenetic tools have low efficacy and off-target effects when applied to presynaptic terminals, while chemogenetic tools are difficult to control in space and time. Here, we show that a targeting-enhanced mosquito homolog of the vertebrate encephalopsin (eOPN3) can effectively suppress synaptic transmission through the $G_{i/o}$ signaling pathway. Brief illumination of presynaptic terminals expressing eOPN3 triggers a lasting suppression of synaptic output that recovers spontaneously within minutes in vitro and in vivo. In freely moving mice, eOPN3-mediated suppression of dopaminergic nigrostriatal afferents induces a

reversible ipsiversive rotational bias. We conclude that eOPN3 can be used to selectively suppress neurotransmitter release at presynaptic terminals with high spatiotemporal precision, opening new avenues for functional interrogation of long-range neuronal circuits in vivo.

2.2.3 Personal contribution – publication II

My contribution to this publication was the following: investigation, methodology, formal analysis, data curation, interpretation of the results, figures preparation, writing of the original draft, review and editing. I designed and independently conducted essential experiments to characterize and validate the morphological and functional performances of a novel inhibitory optogenetic protein in intact brain tissue. In more detail, after preparing the organotypic hippocampal slice cultures, I used different techniques such as single-cell electroporation and viral injections to deliver the transgenes in rodent neurons. Later, the experiments were performed using a combination of patch-clamp electrophysiology, two-photon microscopy, optogenetic stimulation and pharmacology. The results are displayed in panel G of Figure 1 and in Figures 4, 5, S5 and S7. Data analysis, data curation and interpretation of the results were done by me. In addition, I had a major contribution in writing of the first draft of the manuscript and even more during the revision process, giving valuable input to the discussion section. Of note, this study was a joint project among five different groups, in which I was the only contributing author from my group (not considering my supervisor) and the only shared first author not belonging to the lead group of Prof. Ofer Yizhar.
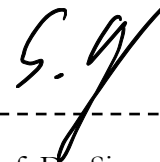
Hamburg, 23.02.2022 .

Mauro Pulin   Prof. Dr. Thomas Oertner   Prof. Dr. Simon Wiegert

2.3   Publication III

The full article can be found at the end of this thesis. Please refer to the manuscript for additional information and detailed description of the methods and results.

2.3.1   Orthogonally-polarized excitation for improved two-photon and second-harmonic-generation microscopy, applied to neurotransmitter imaging with GPCR-based sensors

Mauro Pulin[1,2], Kilian E. Stockhausen[3], Olivia A. Masseck[4], Martin Kubitschke[4], Björn Busse[3,5], J. Simon Wiegert[2] and Thomas G. Oertner[1]

[1]Institute for Synaptic Physiology, Center for Molecular Neurobiology Hamburg, University Medical Center Hamburg-Eppendorf, Hamburg, Germany

[2]Research Group Synaptic Wiring and Information Processing, Center for Molecular Neurobiology Hamburg, University Medical Center Hamburg-Eppendorf, Hamburg, Germany.

[3]Department of Osteology and Biomechanics, University Medical Center Hamburg-Eppendorf, Hamburg, Germany

[4]Synthetic Biology, University of Bremen, Leobener Str. 5, Bremen, Germany

[5]Interdisciplinary Competence Center for Interface Research (ICCIR), University Medical Center Hamburg-Eppendorf, Hamburg, Germany

2.3.2   Abstract – publication III

Fluorescent proteins are excited by light that is polarized parallel to the dipole axis of the chromophore. In two-photon microscopy, polarized light is used for excitation. Here we reveal surprisingly strong polarization sensitivity in a class of genetically encoded, GPCR-based neurotransmitter sensors. In tubular structures such as dendrites, this effect led to a complete loss of membrane signal in dendrites running parallel to the polarization direction of the excitation beam. To reduce the sensitivity to dendritic orientation, we designed an optical device that generates interleaved pulse trains of orthogonal polarization. The passive device, which we inserted in the beam path of an existing two-photon microscope, removed the strong direction bias from fluorescence and second-harmonic (SHG) images. We conclude that for optical measurements of transmitter concentration with GPCR-based sensors, orthogonally polarized excitation is essential.

2.3.3 Personal contribution – publication III

My contribution to this publication was the following: discovery of the two-photon polarization effect on GPCR-based sensor, investigation, formal analysis, data curation, interpretation of the results, figure preparation, review and editing of the manuscript. In more detail, here I prepared organotypic hippocampal slice cultures and transfected individual pyramidal neurons by single-cell electroporation with different genetically encoded GPCR-based fluorescent sensors. Later, I used two-photon polarization microscopy to first discover and then characterize their polarization-dependent excitation properties. My data is displayed in Figure 1, 2, 3 and 5. Moreover, my discovery of the two-photon polarization properties of GPCR-based sensors led to the development of the 'X-pol' device by Prof. Dr. Thomas G. Oertner, with whom I share the patent on it.
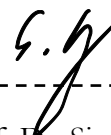
Hamburg, _____23.02.2022_____.

_____   _____   _____
Mauro Pulin   Prof. Dr. Thomas Oertner   Prof. Dr. Simon Wiegert

3 Discussion

3.1 Part I

3.1.1 LTP promotes the stabilization of spiny synapses

Our group showed that optical theta frequency stimulation (oTFS) can induce LTP at individual Schaffer collateral synapses. I confirmed these findings with my own experiments. I measured synaptic transmission by imaging spine calcium influx through NMDA receptors (EPSCaTs), thereby detecting functional synapses. The functional and structural strengthening of those connections, reported as an increase in EPSCaTs amplitude and spine volume, respectively, reflects mainly a postsynaptic adjustment to the presynaptic activity pattern. EPSCaTs failure analysis allowed me also to measure the presynaptic release properties before and after plasticity. While optical low frequency stimulation (oLFS), a protocol our lab used to induce LTD at the Schaffer collateral synapse, was shown to have a strong presynaptic component (decreased release probability) (Wiegert and Oertner, 2013), oTFS did not modify transmitter release probability at individual potentiated synapses. Those finding could be explained by the initial high release probability of synapses I probed in my experiments, which would therefore leave no further space for a presynaptic form of potentiation at those synaptic contacts. However, for direct measurements of vesicular glutamate release probabilities and estimates of quantal content, fluorescent glutamate indicators should be used as a benchmark, as they report direct cleft glutamate release (Durst et al., 2019; Dürst et al., 2021; Helassa et al., 2018).

During the LTP protocol, the synchronous stimulation of presynaptic CA3 cells often produced regenerative calcium transients outside of the stimulated spine that invaded the entire dendrite. I found that the occurrence of those dendritic calcium spikes during the oTFS induction protocol was highly predictive of successful potentiation and spine cluster stabilization. Local dendritic calcium spikes can invade spines and boost cooperativity between active and non-active synapses, promoting synergistic LTP. Consistent with my results, it was found that in the developing hippocampus, temporally correlated synaptic inputs drive local cooperative spine plasticity. Those synaptic events require NMDARs and CICR activity, to induce propagating, regenerative dendritic calcium transients and promote clustered synapses on dendritic branches of CA1 neurons (Lee et al., 2016). Furthermore, several studies also highlight the location-dependent differences in synaptic learning rules. It was shown that at distal dendritic branches, cooperative LTP can be induced by subthreshold and suprathreshold local synaptic inputs (Kim et al., 2015; Losonczy and Magee, 2006; Weber et al., 2016). On the contrary, potentiation on proximal dendritic segments, such as the one occurring on spines located on oblique dendrites relatively close to the soma, probed in my experiments, necessitates strong suprathreshold synaptic inputs to induce dendritic spikes (Mago et al., 2020). Thus, for LTP at proximal dendritic segments, regenerative dendritic nonlinearities seem essential. The need of stronger input patterns at proximal dendrites could partially be attributed to the higher threshold that those low-resistance (due to their large diameter) dendritic segments need to overcome to generate dendritic spikes, compared to the (small diameter) high-impedance distal tuft dendrites (Losonczy and Magee,

2006; Mago et al., 2020). Thus, the likelihood that proximal synapses potentiate increases with an increasing number of coactive inputs distributed throughout the dendrite. Co-active inputs are necessary to elicit dendritic spikes or, more globally, back-propagating APs.

However, the potentiation that I observed was not long-lasting, as 24 hours later, EPSCaTs amplitudes and spine volume returned to baseline levels, in accordance with previous results (De Roo et al., 2008). Nevertheless, successful potentiation left a long-lasting memory tag of formed activity: Once potentiated spines were more likely to be retained in the circuit in the days following LTP (Figure 3 in Wiegert et al., 2018). However, how these activity-dependent potentiation events confer spines with increased stability is still unclear. One possible explanation is that potentiated spines became enriched with adhesion and cross-linking molecules that strengthen the physical connection between pre- and post-synaptic structures (Tang et al., 2016). For instance, it was shown that inter-synaptic competition for neuronal cell adhesion molecules (NCAMs) is a mechanism used by the developing brain to selectively stabilize some spines while pruning others in an activity-dependent manner (Bian et al., 2015). Alternatively, reinforcement of the actin cytoskeleton or insertion of new scaffold proteins in the PSD could provide the spine with improved stability (Cane et al., 2014; Kramar et al., 2006). One potential candidate is the scaffold protein PSD-95. Although the exact mechanism by which PSD-95 provides stability is not entirely clear. Its role in spine stabilization is supported by *in vivo* imaging studies revealing that spines of pyramidal neurons in layer 2/3 of the visual cortex lacking PSD-95 (roughly 20%) are shorter lived (Villa et al., 2016). Interestingly, as mentioned in the introductory section 3.2.1, reorganization and enrichment of the PSD do not occur immediately after plasticity-induced spine growth but is follow with a delay. Although PSD-95 is not necessary for the induction and early expression of long-term potentiation (LTP), its knockdown increases spine turnover, suggesting that proper levels of the protein are necessary for activity-dependent synapse stabilization after initial phases of synaptic potentiation (Ehrlich et al., 2007; El-Husseini et al., 2000; Lambert et al., 2017). Enrichment of stabilizing factors such as polymerized actin filaments, PSD scaffold or trans-synaptic proteins, might be a consequence of enhanced local protein translation after potentiation. Recruitment of the ER and spine apparatus has been observed at highly active spines (Perez-Alvarez et al., 2020b). The presence of the protein synthesis machinery at the root of potentiated spines has been reported and it was shown that local protein synthesis is involved in the maintenance of potentiated spines (Bosch et al., 2014; Govindarajan et al., 2011; Ostroff et al., 2002; Tanaka et al., 2008). Furthermore, it has been demonstrated that the induction of late-phase LTP in one spine facilitates late-phase LTP in nearby spines of the same dendrite in a protein synthesis-dependent manner, suggesting that potentiated spines can share their synthesis products within the same dendritic branch (Govindarajan et al., 2011).

Considering LTP as the cellular substrate for learning and memory, one might speculate that the link between LTP and spine stabilization I describe here might explain *in vivo* studies showing clustering and stabilization of newly formed spines that persisted for months after learning. This interpretation was supported by experiments in which an optogenetic probe was used to selectively shrink recently potentiated spines in the mouse motor cortex following a motor learning task, resulting in the inability to learn the new task

(Hayashi-Takagi et al., 2015). A similar approach was recently used by Goto et al., who developed a reversible optogenetic probe to selectively erase LTP without affecting basal synaptic transmission by optically interfering and disrupting cofilin-mediated sLTP at single spines (Goto et al., 2021). Using this strategy, they were able to decipher the precise spatiotemporal dynamics of LTP contribution in the formation and consolidation of hippocampal episodic memory. In support of the idea that increased spine stability is advantageous for learning, a very recent study has shown that the degree of survival of newly formed spines correlates with performance of learned motor task (Albarran et al., 2021). They further propose the paired immunoglobulin receptor B (PirB) to be involved in spine stabilization. Under physiological conditions, PirB is thought to be required for NMDA receptor-dependent spine shrinkage. Indeed, deletion or acute inhibition of PirB promotes the formation and stabilization of learning-induced spines and generally improves the learning skills of mice compared to control animals (Albarran et al., 2021). This suggests that learning (at least motor learning) is limited by the number of stable spines formed during the acquisition of the skill and this limit can potentially be extended. As my results show, stabilization of spines in not exclusively limited at newly formed spines but is a process also occurring at pre-existing ones. This is supported by a study showing that song learning in juvenile zebra finches is associated with rapid stabilization, accumulation, and enlargement of dendritic spines in the hyperstriatumventrale pars caudalis (HVC), a forebrain nucleus necessary for sensorimotor integration (Roberts et al., 2010). However, learning- and activity-mediated spine formation and stabilization are often accompanied by destabilization and elimination of pre-existing, non-active synapses, thus allowing the circuit to maintain a balanced state (Holtmaat and Svoboda, 2009).

These studies, together with my work, suggest that the stabilization of spine dynamics, best reflect the integration and long-term storage of newly acquired information. Thus, the presence of stable dendritic spines might provide a physical substrate for learning and long-term memory.

3.1.2 Synaptic clustering following plasticity: memory persistence via multisynaptic connections

A previous study from our lab has shown that optical low frequency stimulation (oLFS) triggers a delayed but selective elimination of weakly integrated synapses (Wiegert and Oertner, 2013). The depression seemed to combine a presynaptic and postsynaptic component as both, the release probability and postsynaptic potency were reduced. However, the delayed elimination of depressed synapses seemed not to be correlated with the magnitude of LTD. Still, it occurred preferentially in weakly integrated synapses that showed an initial low probability of neurotransmitter release (Wiegert and Oertner, 2013). This suggests that the initial "analog" adjustment of synaptic strength is eventually translated in a "digital" refinement of the connectivity matrix. However, the depression was not exclusive to the stimulated spine, as the lifetime of their inactive neighbors was also affected. Although neighboring spines did not display any detectable calcium transients during the optical stimulation, they were eliminated from the circuit in the days following LTD, thus displaying a heterosynaptic form of depression. Here, I show that optical theta frequency stimulation

(oTFS) triggers a delayed increase in synaptic strength and spine size, along with a prolonged lifetime of the potentiated spine. However, the increased spine volume and stabilization was not confined only to the potentiated spine but, although to a smaller degree, included also its closest neighbors (<5 μm from the potentiated spine). It is tempting to speculate that those close neighbors became functional in the days following LTP and active participants in the newly formed synaptic cluster, making them more likely to persist in the circuit. Indeed, earlier studies in slice preparations have shown that close-by synapses are more likely to be synchronously coactive than synapses located far away, and the prevalence of co-active synapses decreases as the inter-synaptic distance increases (Kleindienst et al., 2011; Takahashi et al., 2012).

What is the mechanism underlying this synaptic crosstalk and clustering? Previous studies have shown that plasticity at a single synapse influences its neighbors. A notorious study from Harvey and Svoboda showed that the induction of LTP at one spine decreases the threshold for plasticity at nearby spines on the same dendrite, facilitating their potentiation by subthreshold stimuli within a short period (<10 min) (Fig. 5E) (Harvey and Svoboda, 2007). Molecularly, this synaptic crosstalk is likely explained by the activity and spread of signaling molecules such as RhoA, Rac1 and Ras (Yasuda, 2017). Depending on the balance between their diffusion and inactivation rate, some signaling molecules can spread out from the stimulated spine into the dendritic shaft and facilitate plasticity of neighboring synapses (heterosynaptic plasticity) (Colgan et al., 2018; Harvey et al., 2008; Harward et al., 2016; Hedrick et al., 2016). This cooperativity of synaptic plasticity among adjacent spines might be the molecular basis underlying clustering of synaptic inputs observed *in vitro* and *in vivo* (Chen et al., 2012; El-Boustani et al., 2018; Fu et al., 2012; Kerlin et al., 2019; Kleindienst et al., 2011; Takahashi et al., 2012) and would support the notion that spatially close spines encode functionally related information. Indeed, functional clustering of synapses along dendritic branches leads to nonlinear integration of synaptic inputs to promote dendritic spikes, which translates to more potent and longer-lasting responses compared to individual EPSPs (Harnett et al., 2012; Lee et al., 2016). Dendritic spikes may increase the likelihood to fire the postsynaptic neuron or act locally to facilitate synaptic plasticity, thus greatly expanding the computing and storage power of individual neurons (Major et al., 2013). This view suggests that dendritic branches rather than individual synapses are the primary functional units for neuronal computation and perhaps also for long-term memory storage (Branco and Hausser, 2010; Golding et al., 2002; Govindarajan et al., 2006; Losonczy et al., 2008).

My chronic imaging experiments point to a center-surround profile of spine stabilization around the potentiated spine resembling a Mexican hat wavelet. Interestingly, more distant spines (>5 μm from the potentiated spine) did not display any acute structural change but a destabilized lifetime. What determines the borders of the newly formed synaptic cluster? The destabilization of spines further away from the potentiated synapse (>5 μm) likely reflects a mechanism that the local synaptic cluster adopts to set the boundary and prevents other heterosynaptic inputs to become part of the cluster. An elegant study by Niculescu et al., proposed BDNF and its precursor, proBDNF, to play major roles in regulating synapse cluster stabilization through antagonistic modulation of synaptic

transmission. BDNF stabilizes clustered synapses while proBDNF downregulates out-of-sync synapses (synapses not synchronously active) in a matrix-metalloprotease-9 (MMP-9)-dependent fashion. MMP-9 converts proBDNF to BDNF downstream of NMDAR activation, thus efficiently sorting synaptic inputs into correlated clusters along the dendrite (Niculescu et al., 2018). Another recent study identified the immediate early gene Arc as a "synaptic tag" responsible for both, homo- and heterosynaptic plasticity. The strengthening of synaptic inputs in the mouse visual cortex was followed by a delayed heterosynaptic depression at nearby inactive spines. Both forms of plasticity involved AMPAR redistribution among potentiated and depressed synapses, orchestrated by target expression of Arc (El-Boustani et al., 2018). Neuronal activity is therefore responsible for circuit rewiring and competition between active and inactive synapses is a key parameter regulating synaptic lifetime. This supports the notion that, if all synapses are inactive, no competition is taking place, therefore elimination does not occur. On the contrary, if only a small subset of synapses is inactive, those synapses will be eliminated (Yasuda et al., 2011). Recently, Yasuda et al., identified the tyrosine kinase JAK2 as an "elimination signal" to drive removal of inactive synapses. JAK2 was found to be activated at inactive synapses in response to "punishment signals" from nearby active synapses, thereby regulating synapse refinement in an activity-dependent manner (Yasuda et al., 2021).

As opposed to the single synapse approach that I and others used to induce and investigate the effect of synaptic plasticity, other groups examined the role of activity-mediated competitive interactions in regulating spine dynamics by activating a cluster of synapses on the same dendritic branch. Interestingly, two independent studies described that potentiation of multiple neighboring spines leads to a distance and activity-dependent bi-directional restructuring of synaptic strength along the dendrite (Fig. 5C) (Oh et al., 2015; Tong et al., 2021). While both studies report a heterosynaptic spine shrinkage and functional depression of the closest unstimulated spines from the stimulated cluster (within 4 μm), Tong et al. additionally found that spines located between 3.8-7 μm from the center of mass of the stimulated cluster grew significantly in size. What might be the causes of the differences observed on heterosynaptic plasticity after stimulation of single (as in my study) versus multiple synapses? A likely interpretation would be that the different stimulation patterns used to induce LTP might cause distinct spatiotemporal patterns of calcium transients along the dendrites. This would ultimately lead to differential molecular activation patterns and spread of intracellular signaling factors such as CaMKII and calcineurin along the parent dendrite to bias the plasticity outcome at individual synapses. In fact, blocking LTP-induced enlargement at stimulated spines did not prevent spine shrinkage at adjacent ones, pointing to an active process involving shrinking rather than depletion of resources by the potentiated spines (Oh et al., 2015).

In summary, my study supports the concept that activity-dependent competition among synapses occurs on the same dendritic stretch and unused synapses are likely to be removed for fine-tuning of the neuronal circuit. Furthermore, unlike homeostatic plasticity that globally affects all synaptic connection within a cell, this competition mediated by input-specific synaptic plasticity may be responsible for selective optimization of synaptic connections along a dendrite.

3.1.3 Interaction of LTP- and LTD-inducing stimuli

There is extensive evidence that neuronal pathways can undergo bi-directional modifications of their strength (Bear, 2003). However, little is known whether plasticity of different polarities can be induced in succession at the same synapse and the functional and structural consequences of such manipulations remain elusive. A previous study from Lang et al. found that induction of LTD immediately after LTP has no effect on spine size (Lang et al., 2004), while a study from Zhou et al. reports that induction of LTD 30 minutes after LTP, reverses the LTP effect and shrinks the spine head (Zhou et al., 2004). In addition, it was shown that high-frequency glutamate uncaging counters the spine shrinkage effect of low-frequency glutamate uncaging and promotes spine growth (Oh et al., 2013). A major drawback of those studies is that they rely exclusively on structural modifications of the monitored synapses, which, although an accepted correlate of synaptic strength, are not directly reporting functional changes in synaptic efficacy. Moreover, the reported morphological changes were monitored only on a short time scale (max 90 minutes), while the effects on spine stability on longer time scales are unknown. Considering the stabilizing and destabilizing effect of LTP and LTD, respectively, I asked whether sequential plasticity events could be induced 24 hours apart and thus possibly override the likely fate that awaited those spines from the prior manipulation. I show that both types of plasticity could be induced 24 hours after the first round of plasticity of opposite polarity, measured by successful changes in EPSCaTs amplitudes. Interestingly, while LTP was relatively likely to occur one day after LTD, the induction of the latter was a much harder to achieve after the first successful round of potentiation 24 hours earlier, suggesting that previously potentiated synapses were much more resilient to depression. This finding is supported by previous studies showing that, while spine expansion produced by LTP-inducing stimuli could be reliably reversed 10 minutes later by LTD, this was not the case when LTD was applied ~30 minutes after LTP (Kramar et al., 2006; Yang et al., 2008). This suggests that the temporal precision of subsequent plasticity events determines the structural outcome. In addition, Hayama et al., showed that spines stimulated with a glutamate uncaging LTP protocol are 'protected' against spine shrinkage that may otherwise spread from surrounding synapses (Hayama et al., 2013). However, the factors responsible for this newly acquired protection against elimination remain elusive and a matter of further investigation.

Looking at the long-term survival of spines in my study, I found that the last plasticity event, if successful, completely overwrote the previous one, thus determining synaptic lifetime. In that regard, of particular interest is an *in vivo* study showing that mice subject to learning paradigms with opposite behavioral phenotypes (fear conditioning and extinction), display opposite consequences on spine dynamics, namely disappearance and appearance, respectively, at a virtually identical location on the dendrite. Moreover, reconditioning of fear memory promoted the selective elimination of the spines formed after extinction (Lai et al., 2012). Thus, these and my findings suggest that subsequent opposite forms of learning and manipulation of opposite polarities, lead to opposing changes at the levels of individual synapses promoting selective circuit rewiring.

In conclusion, my work links the structure-function relationship of plasticity and long-term spine survival, and it complements structural *in vivo* spine dynamics studies. Although it

is now possible to measure synaptic activity *in vivo* (Chen et al., 2011; Scholl et al., 2021; Wilson et al., 2016), the sparse and often unpredictable pattern of synaptic inputs poses great challenges in efficiently mapping and measuring synaptic changes to correlate them with learning-related behaviors. The future improvements of imaging methods with better single synapse resolution (Kazemipour et al., 2019; Lu et al., 2017), combined with the constant development of fluorescent reporters of synaptic activity (Aggarwal et al., 2022; Marvin et al., 2018; Perez-Alvarez et al., 2020a), will help us in our understanding of how synapses help the brain to compute, store and retrieve information.

3.2 Part II

3.2.1 Functional characterization of eOPN3-mediated presynaptic inhibition

In this work I characterized eOPN3, a targeting-enhanced, mosquito-derived bistable rhodopsin for optical control of the $G_{i/o}$-signaling pathway. I demonstrated that illumination of eOPN3-expressing presynaptic terminals triggers a rapid and reversible inhibition of synaptic transmission. This is most likely mediated by the activation of the $G_{\beta/\gamma}$ signaling that inhibits the activity of voltage gated Ca^{2+} channels (VGCCs) and interferes with the presynaptic release machinery complex (Blackmer et al., 2001; Herlitze et al., 1996). Moreover, activation of the G_{α} might decrease vesicle priming by reducing cAMP levels at the presynapse, similar to $GABA_B$ receptors (Sakaba and Neher, 2003). Our collaborators showed that eOPN3 activation induced an immediate suppression of glutamatergic and GABAergic synaptic transmission in autaptic neuronal cultures. Treatment of the neurons with pertussis toxin occluded the inhibitory effects, confirming again that the mechanism is mediated through the activation of the $G_{i/o}$-signaling pathway. The synaptic inhibitory effect was similar to the activation of $GABA_B$ receptors by baclofen, which is a well-characterized metabotropic modulator of presynaptic release (Wu and Saggau, 1995). Further synaptic recordings in autaptic cultures showed that the eOPN3-mediated synaptic inhibition was not affected by blocking the β/γ subunits-dependent GIRK channels activation, demonstrating that the silencing effect is primarily mediated by a hyperpolarization-independent mechanism at presynaptic terminals. A decrease in the frequency but not amplitude of AP-independent miniature EPSCs upon eOPN3 activation further confirmed its effect on the release probability but not the quantal content.

We showed that the addition of the Kir2.1 ER export and the Golgi trafficking (ts) signals improved the membrane localization of the opsin. I could confirm in CA3 pyramidal neurons of organotypic hippocampal cultures that eOPN3 expresses at distal Schaffer collateral axons: Proper axonal targeting is a prerequisite for effective opsin action at projecting terminals. A brief light pulse, locally applied to presynaptic terminals, significantly decreased synaptic transmission (~80% reduction) in intact tissue without affecting AP firing. The effect lasted for several minutes and recovered spontaneously at a time range of 10 minutes. Furthermore, the recovery time constant measured in slice cultures ($\tau=4.57$ min) matched the one at thalamocortical synapses of the visual pathway measured in awake, head-fixed mice ($\tau=5.17$ min), indicating the reliability of eOPN3 across different systems and preparations.

In line with a presynaptic site of action, eOPN3 activation increased the paired-pulse ratio (PPR) responses of closely time-spaced evoked stimuli, similar to some canonical GPCR-modulators of presynaptic activity (Chalifoux and Carter, 2011a). Interestingly, different neuromodulators are known to decrease release probability without necessarily changing the PPR (Burke et al., 2018). This has been attributed to their different mechanisms of action on presynaptic VGCCs. For instance, metabotropic $GABA_B$ and dopamine receptors D1 (DRD1) regulate presynaptic release in a graded or all-or-none manner, respectively (Burke et al., 2018). While $GABA_B$ receptors engage the $G_{i/o}$-signaling cascade to mediate a net reduction in Ca^{2+} influx per AP, DRD1 receptors engage the $G_{\alpha s}$-signaling cascade modulating the open probability of VGCCs in a PKA-dependent fashion, acting as a gain modulator of synaptic transmission. Thus, regulation of short-term plasticity (STP) properties is mediated by the distinct effects of the corresponding receptor signaling pathways that in turn regulate different biophysical properties of presynaptic VGCCs. In addition, the GPCR-mediated modulation of VGCCs depends also on the nanodomain architecture of presynaptic VGCCs, particularly at synapses where release is driven by only a handful of channels responsible for the influx of Ca^{2+} (Burke et al., 2018; Scimemi and Diamond, 2012).

3.2.2 Mechanisms of action of eOPN3-mediated presynaptic inhibition

$G_{i/o}$-coupled G proteins are known to interfere with VGCC-dependent Ca^{2+} entry by either shifting the voltage-dependent activation or delay the time of first opening via the induction of "reluctant state" of the channel (Zamponi and Currie, 2013). This inhibition is mediated by the binding of the $G_{i/o}$-βγ-dimer to the intracellular loop I–II of the channel's pore-forming α-subunit. Interestingly, strong depolarization or artificial "pre-pulse" depolarization steps can induce the uncoupling of the βγ subunits from the binding site of the intracellular loop, thus relieving the inhibition (Brody and Yue, 2000). The intracellular loop I–II of the VGCC functions as the voltage sensor of the channel and it has been proposed that its movement during membrane depolarization might promote the βγ subunits dissociation (Sandoz et al., 2004). My single-bouton Ca^{2+} imaging experiment demonstrates a GIRK-independent reduction in Ca^{2+} influx at presynaptic terminals after local eOPN3 activation by green light, pointing to direct inhibition of presynaptic VGCCs. Although effect size might have appeared small - probably due to the nonlinear relationship between Ca^{2+} influx and vesicle release - the reduction in Ca^{2+} will significantly decrease neurotransmitter release (Schneggenburger and Neher, 2000). Additional evidence pointing to a direct effect on presynaptic VGCCs by eOPN3 activation was given by the short-term facilitation bias introduced by eOPN3 during high firing rates. Canonical GPCR-mediated presynaptic modulation of release probability at terminals acts as high-pass filter and become less effective during bursts of activity. While classical facilitation occurs through mechanisms of Ca^{2+} accumulation of presynaptic Ca^{2+} concentrations (Jackman and Regehr, 2017), the eOPN3-mediated "artificial" facilitation observed throughout trains of activity is presumably a result of depolarization-mediated relief of β/γ subunit-mediated inhibition of the Ca^{2+} channels (discussed above). Thus, eOPN3 engages a similar $G_{i/o}$-coupled signaling pathway as $GABA_B$ receptors in modulating VGCCs activity (Burke et al., 2018). It imposes a high-pass filter on synaptic transmission during prolonged, high-frequency activity. Therefore, transmission properties should be considered when applying eOPN3 to different synapses.

3.2.3 eOPN3 properties and practical considerations

eOPN3 displays a very broad single-photon activation spectrum (Fig. 1 in Mahn et al., 2021), which peaks at around 500 nm, allowing efficient activation with different wavelengths and commonly available light sources. However, this limits its combination with other optical probes or actuators due to overlapping spectra and potential cross-activation. Like other type-II rhodopsins, eOPN3 is highly light sensitive, with an EC_{50} of ~3 μW mm^{-2} s^{-1}, requiring several orders of magnitude less light than previously developed/commonly used light-gated Cl^- and H^+ pumps and channels. Its broad spectrum and high light sensitivity allow optogenetic inhibition of large tissue volumes at longer wavelengths of moderate intensities, minimizing tissue heating. At the same time, this might impose constraints in experiments where a specific subset of postsynaptic targets needs to be silenced without off-target effects. Therefore, light irradiance should be minimized to prevent inadvertent inhibition. An additional concern regarding the eOPN3 light sensitivity is its unintended activation by ambient light which might occlude its effects in *in vitro* preparations or in transparent organisms. Therefore, the experiments should be conducted in light-shielded conditions or allow the spontaneous recovery of the opsin in the dark before activating the tool for synaptic silencing.

Another feature of eOPN3 is its minimal two-photon activation, thus allowing crosstalk-free imaging of neuronal activity with green indicators. The minimal two-photon activation will allow seamless large field-of-view two-photon raster scanning, which effectively minimizes the irradiance per illuminated area. Any residual eOPN3-activation by two-photon excitation will be limited to the imaging plane, as the probability of two-photon excitation decays with the fourth power of the distance from the focal point. However, eOPN3 activation might occur during prolonged subcellular two-photon imaging due to its slow inactivation rate and subsequent accumulation in the activated state. An additional consideration when combining eOPN3 with imaging of blue-green indicators is the potential indirect eOPN3 activation by the emitted green photons of the fluorophores. Therefore, the eOPN3 experimental conditions should be carefully tested while optimizing the imaging parameters to minimize unintended cross-activation.

3.2.4 Comparison to the photoswitchable lamprey parapinopsin PPO

In parallel to our work on eOPN3, three independent groups were exploiting the potential of another bistable non-visual rhodopsin, parapinopsin, for optogenetic control of intracellular signaling (Copits et al., 2021; Eickelbeck et al., 2020; Rodgers et al., 2021). Of particular interest is the study of Copits et al., which characterized the optogenetic potential of the lamprey parapinopsin (PPO) for light-mediated inhibition of synaptic release. Like eOPN3, PPO couples to the $G_{i/o}$- pathway to mediate its downstream signaling, including GIRK channel activation, inhibition of adenylyl cyclase and of VGCCs. However, unlike eOPN3, PPO is a photoswitchable opsin with less overlapping activation and inactivation spectra. PPO is preferentially switched to a stable active state by UV light and inactivated by amber light, although Copits et al., reported that PPO can also be activated by pulsed blue light. However, blue light is most likely absorbed by both the inactive and active opsin state. While it appears to favor activation, absorption of blue light likely produces an intermediate

unstable photostate that is quickly prone to spontaneous relaxation in the dark, as reported in Copits et al. Nevertheless, PPO was shown to inhibit synaptic transmission effectively and reversibly at thalamocortical projections and to modulate motived behaviors in mice.

Considering its photoinactivation by amber light, PPO can be combined with red fluorescent indicators in single-photon experiments without inadvertent activation, as shown in combination with the red dopamine indicator RdLight1. Because of the same reason, PPO does not suffer from unintentional activation by ambient light, making it easier to use with *in vitro* preparations or transparent organisms. eOPN3 and PPO also differ in respect to their two-photon activation. While eOPN3 is relatively insensitive to two-photon excitation, with only modest activation at wavelengths beyond 1000 nm, PPO is effectively activated by short wavelength ranging from 700 to 900 nm, thus potentially allowing two-photon-mediated optogenetic silencing but also limiting its combination with two-photon imaging.

In summary, both PPO and eOPN3 represent a major upgrade to the optogenetic synaptic silencing toolkit. Both opsins offer complementary options for projection-specific inhibition of synaptic transmission with good temporal resolution. The choice of the opsin will depend on their spectral properties and switching kinetics that are most appropriate for a given experimental paradigm. Bistable type-II rhodopsins such as eOPN3 offer new opportunities for targeted optogenetic suppression of neurotransmitter release at presynaptic terminals. Although eOPN3 was very reliable in different preparations and synapses tested (glutamatergic, GABAergic and dopaminergic), one potential caveat of using GPCR-based optogenetic silencers is the possibility that some cell types lack the proper G-protein signaling machinery at presynaptic terminals or exhibit low coupling and/or sensitivity to $G_{i/o}$ signaling cascade at some synapses. Therefore, the user is advised to consider and test those possibilities and confirm the efficacy of the tool before using it in more complex experimental paradigms.

3.2.5 Outlook and future directions

Presynaptic optogenetic inhibition has come a long way in the last few years. Given the variety of tools at hand, the user might base their preference on factors such as the temporal precision of inhibition, reversibility, spectral properties and the physiology of the synapse under investigation. Presynaptic optogenetic inhibition with microbial type-I ion pumps is still advantageous if a millisecond temporal precision is required. However, they are not effective if prolonged inhibition is desired (Mahn et al., 2016). Although bistable optoGPCRs, such as eOPN3, might be too slow for ultrafast suppression of release, they seem ideal for experiments that require efficient synaptic inhibition in the seconds to minutes range. The user should consider further approaches with slower reversibility for even longer inhibition periods, such as the photoactivated Botulinum neurotoxin B (PA-vBoNT) or the cryptochrome 2-based vesicular trapping approach Opto-vTrap. Alternative chemogenetic approaches such as DREADDs are also suitable for prolonged inhibition. An optogenetic silencer that allows for presynaptic inhibition at a specific synapse between genetically defined and synaptically connected neurons ("trans-synaptic optogenetics") is yet not available and represents an important future goal for optical investigation of synaptic

functions (Prakash et al., 2022). Such an approach might require a strategy where an opsin is reconstituted across the synaptic cleft between pre- and postsynaptic partners, similar to what has been achieved with reconstitution of genetically encoded fluorescent proteins to mark synaptic contacts (Choi et al., 2018; Feinberg et al., 2008; Kim et al., 2011). This would allow modulation of activity at exclusive synaptic connections without interference with other, opsin-free collateral synaptic contacts.

At this stage of the optogenetic technological advancements, the development of an optogenetic actuator for bi-directional control of synaptic transmission represents an apparent next step. Such a tool would resemble the recently published single-vector, tandem construct BiPOLES, used for dual-color modulation of somatic excitability (Vierock et al., 2021). The proposed bi-directional synaptic optogenetic actuator would consist of an inhibitory optoGPCR (preferentially a photoswitchable one, like PPO) and an excitatory ChR. Given crosstalk-free spectral overlap, the combination would elicit neurotransmitter release by ChR-mediated axonal depolarization and inhibit vesicular release with an optoGPCR, similar to what has been achieved by combining the inhibitory DREADD hM4D and the excitatory opsin ChR2 (Stachniak et al., 2014). However, the proposed optogenetic tool would combine both opsin transgenes in a single tandem construct (gene-fusion strategy) to allow for matched expression stoichiometry and co-localization (Kleinlogel et al., 2011). In addition, future improvements in genetic engineering and targeting strategies might optimize trafficking and localization to desired subcellular compartments.

Another potential application of eOPN3 and other $G_{i/o}$-coupled optoGPCRs, could be their use as selective modulators of cAMP levels. The bacterial rhodopsin, bPAC (Stierl et al., 2011) and its recently improved version PACmn (Yang et al., 2021), stimulate the activity of adenylyl cyclase and raise cAMP levels in a light-dependent manner. As opposed to bPAC and PACmn, the signal transduction of the activated G_α subunit of $G_{i/o}$-coupled GPCRs inhibits adenylyl cyclase activity and hence decreases cAMP production. Thus, as opposed to bPAC and PACmn, eOPN3 could be used as a tool to suppress cAMP elevation. cAMP is a ubiquitous second messenger that transduces extracellular signals into many vital cells signaling processes, including gene transcription and ion-channel modulation in neurons. It acts either through direct interactions with its downstream effectors or via the activation of protein kinase A (PKA) and other cyclic nucleotide-binding proteins (Sassone-Corsi, 2012). Our G_sX assay showed strong coupling of eOPN3 to the $G_{i/o}$ signaling pathway and modulation of cAMP production. Thus, selective expression of eOPN3 in diverse cell types (even non-excitable cells) could provide potential new approaches for light-mediated investigation of cAMP-dependent mechanisms.

An additional application of eOPN3 in modulating neuronal physiology could include inhibition of dendritic Ca^{2+} influx. There is abundant evidence that activation of $G_{i/o}$ signaling inhibits VGCC-mediated Ca^{2+} entry in spines and dendrites, as shown by activation of $GABA_B$ receptors and dopamine receptor D2 (DRD2) (Chalifoux and Carter, 2010, 2011b; Higley and Sabatini, 2010; Palmer et al., 2012; Perez-Garci et al., 2013; Sabatini and Svoboda, 2000). Moreover, it was shown that postsynaptic metabotropic $G_{i/o}$ signaling

decreases NMDAR-mediated spine Ca^{2+} influx in cortical and striatal neurons (Chalifoux and Carter, 2010; Higley and Sabatini, 2010). This effect is dependent on the activation of the G_α subunit, which decreases cAMP and the activity of its downstream targets. One of those, protein kinase A (PKA), normally phosphorylates NMDARs, increasing their Ca^{2+} permeability and conductance (Skeberdis et al., 2006). Activation of the $G_{i/o}$ signaling cascade would therefore decrease NMDARs activity. Thus, cellular excitability is decreased via two routes upon activation of the $G_{i/o}$ signaling cascade: through GIRK-channels-mediated hyperpolarization and by the inhibition of VGCCs and NMDARs, which influence postsynaptic Ca^{2+}-dependent signaling in spines and dendrites. Additionally, reduced cAMP levels could lead a decreased activity of hyperpolarization-activated cyclic nucleotide–gated (HCN) channels, which would overall result in reduced neuronal excitability (Noam et al., 2010). Inhibition of Ca^{2+} signaling can have a major impact on neuronal physiology and computation since dendritic NMDAR and Ca^{2+} activities are considered to mediate local, branch-specific non-linear processes underlying higher brain functions such as learning and memory and sensory perception (Bittner et al., 2015; Doron et al., 2020; Sheffield et al., 2017; Takahashi et al., 2020; Takahashi et al., 2016). For instance, "NMDA spikes", local dendritic regenerative potentials originating from the synchronous activation of several glutamatergic synapses, provide the substrate for branch specific causal interactions of synaptic inputs, promoting synaptic plasticity through their strong and long-lasting depolarization (Larkum et al., 2009; Nevian et al., 2007; Schiller et al., 2000). Understanding the role of non-linear dendritic integration and its inhibition by modulating voltage-dependent ion channels in dendrites would be key to understand the transformation of synaptic inputs to AP output.

In the distal apical dendrites of neocortical pyramidal neurons *in vivo*, dendritic "Ca^{2+} spikes" are modulated by the synaptic release of GABA from local interneurons acting on dendritic $GABA_B$ receptors (Perez-Garci et al., 2006). Several studies aimed at perturbing dendritic excitability and Ca^{2+} nonlinearities to study their computational functions. Experimentally, this has been so far achieved by pharmacological activation of $GABA_B$Rs. Indeed, local application of the $GABA_B$R agonist baclofen has been shown to suppress Ca^{2+} spikes in tuft dendrites of layer 5 (L5) pyramidal neurons of the somatosensory cortex (Perez-Garci et al., 2006; Perez-Garci et al., 2013; Takahashi et al., 2016) and in the entire dendritic arbour of layer 2/3 (L2/3) pyramidal neurons in the prefrontal cortex (Chalifoux and Carter, 2011b). Baclofen application mainly affects high-voltage dependent (L-type) Ca^{2+} channels in L5 pyramidal neurons (Perez-Garci et al., 2013), which constitute the predominant conductance activated during the plateau potential of the dendritic Ca^{2+} spike but influences almost every dendritic VGCCs in L2/3 pyramidal neurons (Chalifoux and Carter, 2011b). However, when applied *in vivo*, local baclofen injections can activate pre- and postsynaptic $GABA_B$Rs, thus not allowing to discriminate between a presynaptic decrease in neurotransmitter release and a direct postsynaptic action on dendritic Ca^{2+} sources. Other strategies to reduce regenerative dendritic Ca^{2+} events *in vivo* have employed the activation of Cl^--conducting ChRs in apical tuft dendrites or ChR2-photoactivation of dendritic-targeting somatostatin (SST) interneurons (Doron et al., 2020; Takahashi et al., 2020; Takahashi et al., 2016). However, both approaches carry limitations. On one hand, ACR-mediated dendritic hyperpolarization is Ca^{2+} independent and as it counters the integration of any input, it will not reveal whether the dendritic activity is Ca^{2+} mediated or not. On the other hand,

optogenetic activation of SST interneurons is spatially unspecific, since they do not exclusively target the apical dendrites of L5 pyramidal neurons (Gentet et al., 2012; Wang et al., 2004). A recent paper from the Larkum lab states: "*At present, there is no method to specifically block dendritic Ca^{2+} actively*" (Doron et al., 2020). Here, an optoGPCR that couples to G$_{i/o}$ signaling pathway, such as eOPN3, would overcome those limitations by previous approaches. Targeted expression of those opsins would allow genetic specificity and precise spatio-temporal control of their signaling cascades to modulate synaptic and dendritic Ca^{2+} dynamics (subthreshold synaptic responses, suprathreshold dendritic spikes and even the induction of synaptic plasticity). Thus, when combined with two-photon imaging of activity sensors, the use of optoGPCRs could allow for unprecedented all-optical investigation of active dendritic integration.

3.3 Part III

3.3.1 Mixed light polarization as the new standard in multiphoton imaging

Polarization microscopy has been widely used in biological studies for imaging the structural organization of proteins and lipids in cell membranes (Hess et al., 2003; Kress et al., 2013; Lazar et al., 2011). Still, polarization effects are often ignored or overlooked in fluorescence imaging in biological sciences. To the best of my knowledge, I reported here for the first time the strong polarization-dependence of two-photon excitation of the recently developed GPCR-based neuromodulator sensors. When expressed in pyramidal neurons, the fluorescence signal of the sensors was completely lost in dendrites aligned parallel to the polarization of the excitation beam, while orthogonal dendrites displayed maximal intensity. This is likely explained by the rigid tethering of the cpGFP to the GPCR, orienting the GFP barrel approximately parallel to cell membrane. Thus, in conditions where the transition dipole of the fluorophore is parallel to the incident polarization direction, light absorption is optimal. The more the diploe of the fluorophore orients towards an orthogonal position, the less efficient the two-photon excitation becomes. Indeed, I confirmed this experimentally by rotating the polarization of light by 90° with a half-wave plate. Interestingly, this effect did not occur in all the GPCR-based sensors tested: the family of "G-protein-coupled receptor-activation-based" (GRAB) sensors did not display apparent polarization-dependent excitation. This is most likely attributed to the slightly different sensor design compared to dLight1.2 and sDarken, where the entire third intracellular loop was replaced by a cpGFP. The GRAB family of sensors, instead, retains a considerable portion of the third intracellular loop of the original receptor, which might provide sufficient orientational flexibility to avoid strong polarization excitation bias (Ravotto et al., 2020). I reported a similar polarization-free behavior for the glutamate sensor iGluSnFR and the glycosylphosphatidylinositol-tethered GFP (GPI-GFP). We reasoned that the single-ended membrane anchoring of those fluorescent proteins guarantees sufficient degrees of freedom to randomize the distribution of transition dipoles of the fluorophore with respect to the membrane plane. Our interpretation is supported by a previous study showing that GFP attached to the plasma membrane through flexible, single membrane-targeting tags are less susceptible to FDLD than "doubly-lipidated" GFP (Lazar et al., 2011). In addition, a very recent report highlights the importance of linearly polarized excitation on signals obtained from genetically encoded

fluorescent voltage indicators (Bloxham et al., 2021). In this study, the authors report single-photon FDLD for numerous membrane-bound voltage indicators. It is interesting to note that some of them display polarization-dependent effects of opposite signs. For instance, the voltage sensor ASAP1 and the Archaerhodopsin 3 (Arch)-derived voltage indicator QuasaAr3 display FDLD signals of opposite signs, likely attributed to the different orientation of the chromophore with respect to the plasma membrane. Indeed, the GFP chromophore of ASAP1 is attached to the transmembrane voltage sensing domain in a nearly perpendicular orientation relative to the membrane. Instead, retinal, the light-sensing chromophore of QuasaAr3, has presumably a fixed orientation close to the plane of the membrane, confirming the dependence of the light absorption on the orientation of the dipole relative to the direction of polarization. As we proposed in our study, the fixed retinal orientation in opsins could be exploited for targeting polarized light to optimize the two-photon excitation of ChRs.

To solve the imaging polarization bias of GPCR-based fluorescent sensors, we developed a passive optical device that creates alternating pulses of orthogonal polarization. This simple device uses two polarizing beam splitting cubes to split and then reconstitute the incoming beam into two collinear sub-beams of orthogonal polarization. When inserted into the beam path of the microscope and tilted by 45° around its optical axis to output the two orthogonal pulse trains, the device completely removed the polarization-sensitivity bias of GPCR-based sensors. Because of splitting the incoming beam into two sub-beams, the device doubles the pulse repetition rate at the expense of the pulse energy, which in this case is cut in half. While this effect should require an increase in average laser power to achieve the same image intensity for fluorescent proteins with a fixed orientation, it might not be necessary for some conditions, such as when imaging randomly oriented fluorophores. In the latter condition, more fluorophores can be simultaneously excited by the two orthogonal pulse trains. Recruitment of additional fluorophores - freely diffusible fluorophores in living tissue or randomly oriented fluorophores in fixed samples - should maintain the same signal intensity while photobleaching should be reduced due to the decreased power carried by the two individual pulse trains (Ji et al., 2008).

The constant development of new optical sensors calls for urgent testing of their polarization properties since the degree of the chromophore orientation cannot be known *a priori*. For quantitative optical measurements of extracellular neuromodulator concentrations with GPCR-based sensors, the use of orthogonal pulse trains seems essential and, considering its broader advantages, should be set as the new default imaging mode in multiphoton microscopy.

3.4   Concluding remarks

In the first part of my studies, I investigated the activity mechanisms underlying the rewiring of synaptic connections, focusing on dendritic spines in organotypic hippocampal slice cultures. In particular, I explored the long-term consequences of synaptic plasticity on synaptic stability and the interaction between different plasticity forms at the level of individual synapses. My results suggest the synaptic weight adjustments, made through

strengthening or weakening of synaptic efficacy by LTP and LTD, respectively, directly affect synaptic lifetime, leading to an activity-dependent circuit rewiring. Thus, temporary changes in the connectivity strength of synaptic networks induced by LTP or LTD can be made permanent through synapse stabilization and elimination. In contrast, additional preliminary results not displayed in this thesis, suggest that decreasing synaptic activity itself has no effect on synaptic lifetime. While synaptic survival is strongly biased by synaptic plasticity, reduction of basal synaptic transmission seems not to influence the persistence of individual, functional synaptic contacts. In the future, it would be very informative to link different synaptic transmission patterns to obtain a clear picture of the rules governing synaptic wiring.

In parallel to studying synaptic lifetime, I also worked on the development of optogenetic synaptic silencing tools. This was motivated by the fact that it is still highly challenging to inhibit synaptic transmission with high-spatiotemporal precision. Therefore, much of my PhD was dedicated to the characterization of a novel optogenetic tool to suppress neurotransmission by acting directly at synaptic terminals. In this thesis, I presented eOPN3, a $G_{i/o}$-coupled rhodopsin for rapid and reversible light-mediated suppression of synaptic release. This novel optogenetic tool developed in this project may become crucial for selective silencing of neuronal terminals, especially in the context of dissecting long-range neuronal projection pathways, allowing detailed evaluation of their functional contribution to cognitive and behavioral processes.

Lastly, I presented the discovery of a previously undetected problem concerning the use of a new generation of genetically encoded fluorescent indicators. Some of those recently developed GPCR-based neuromodulator sensors display a significant imaging bias when excited with linearly polarized light. Since the purpose of those fluorescent reporters is to draw conclusions about the spatial distribution of neuromodulators, this assumption is put in jeopardy when imaging them with linearly polarized light, as done with conventional two-photon microscopy. While one remedy would be to design sensors with isotropic fluorescence, here I reported a simple, immediate solution for this problem, by alternating pulses of orthogonal polarization with a passive optical device. The 'X-pol device' allows unbiased quantitative measurements of neuromodulator release and might represent an easy implementation for the neuroscience community when polarized light sources are used for neuromodulator imaging.

4 Acknowledgments

This work would not have been possible without the involvement of many people, whom I would like to acknowledge here.

First and foremost, I would like to express my gratitude to my supervisor, Prof. Dr. J. Simon Wiegert, for giving me the opportunity to join his lab at the very beginning of his independent career and obtain my PhD. His dynamic supervision and thorough guidance have been instrumental for my scientific career and development. Throughout his experience and broad knowledge, I developed my own passion and curiosity for science. I appreciate the faith he had in my abilities, and I am also very grateful for the many opportunities he gave me to attend conferences and meetings, as well as the teaching opportunities at the Cajal courses. Most importantly, if he would not have hired me, I would have never met all the wonderful people I met throughout those years, one in particular!

Many thanks go also to Prof. Dr. Thomas G. Oertner for the opportunity he gave to be part of his group and allowing me to continue being part of it even after the mitosis event. I really appreciate the freedom and trust he gave me to conduct my research in his laboratory and I am grateful for all the support he gave me during this time. His deep technical knowledge and bright ideas have always been very valuable and helpful.

I would also like to thank Dr. Christine E. Gee for always sharing her knowledge and for very helpful discussion and constant availability throughout those years. I always learned a lot through her useful inputs.

Special thanks also go to Iris Ohmert, Sabine Graf, Jan Schröder, Kathrin Sauter and Stefan Schillemeit for excellent technical support and assistance throughout the years. Stefan became a sincere friend and has been very supportive inside and outside the lab.

I would also like to express my gratitude to all the members, past and present, of the Wiegert and Oertner labs, who has taken part of this journey and with whom I shared many unforgettable moments.

Thanks also to all the fantastic collaborators, Prof. Ofer Yizhar, Dr. Mathias Mahn and Dr. Jonas Wietek in particular, with whom I had the pleasure to work with and learned a lot from over the past few years.

Outside of the lab, but still part of the ZMNH community, I would like to express my deepest gratitude to Franco, who has been a lifeline during this time. I am extremely lucky to have found such a friend! Shoot out to Tomas as well, for always keeping up the good and all the fun moments and to Lukas, for keeping me in shape!

I am very grateful to my family for their unconditional love and support I was always getting. The fact that I could always count on them, regardless of the situation gave me constant strength. Thanks also to all the friends who have been close and supported me over the years.

Finally, I would like to thank my mentor, my idol, my best friend and my soul mate, Céline, who always brought sunshine in my life since we met. I wish everyone to find their own 'Céline' in life. Thank you for all the love and support, without you, nothing of that would have been possible.

5 Declaration on oath – Eidesstattliche Versicherung

Declaration on oath

I hereby declare, on oath, that I, Mauro Pulin, have written the present dissertation by my own and have not used other than the acknowledged resources and aids.

Hamburg, __23.02.2022__   Signature: _____

Eidesstattliche Versicherung

Hiermit erkläre ich, Mauro Pulin, an Eides statt, dass ich die vorliegende Dissertationsschrift selbst verfasst und keine anderen als die angegebenen Quellen und Hilfsmittel benutzt habe.

Hamburg, den __23.02.2022__   Unterschrift: _____

6 References

[1]   Aggarwal, A., Liu, R., Chen, Y., Ralowicz, A.J., Bergerson, S.J., Tomaska, F., Hanson, T.L., Hasseman, J.P., Reep, D., Tsegaye, G.*, et al.* (2022). Glutamate indicators with improved activation kinetics and localization for imaging synaptic transmission. bioRxiv, 2022.2002.2013.480251.

[2]   Airan, R.D., Thompson, K.R., Fenno, L.E., Bernstein, H., and Deisseroth, K. (2009). Temporally precise in vivo control of intracellular signalling. Nature *458*, 1025-1029.

[3]   Albarran, E., Raissi, A., Jaidar, O., Shatz, C.J., and Ding, J.B. (2021). Enhancing motor learning by increasing the stability of newly formed dendritic spines in the motor cortex. Neuron.

[4]   Alberio, L., Locarno, A., Saponaro, A., Romano, E., Bercier, V., Albadri, S., Simeoni, F., Moleri, S., Pelucchi, S., Porro, A.*, et al.* (2018). A light-gated potassium channel for sustained neuronal inhibition. Nat Methods *15*, 969-976.

[5]   Araya, R., Eisenthal, K.B., and Yuste, R. (2006a). Dendritic spines linearize the summation of excitatory potentials. Proc Natl Acad Sci U S A *103*, 18799-18804.

[6]   Araya, R., Jiang, J., Eisenthal, K.B., and Yuste, R. (2006b). The spine neck filters membrane potentials. Proc Natl Acad Sci U S A *103*, 17961-17966.

[7]   Araya, R., Vogels, T.P., and Yuste, R. (2014). Activity-dependent dendritic spine neck changes are correlated with synaptic strength. Proc Natl Acad Sci U S A *111*, E2895-2904.

[8]   Armbruster, B.N., Li, X., Pausch, M.H., Herlitze, S., and Roth, B.L. (2007). Evolving the lock to fit the key to create a family of G protein-coupled receptors potently activated by an inert ligand. Proc Natl Acad Sci U S A *104*, 5163-5168.

[9]   Awasthi, A., Ramachandran, B., Ahmed, S., Benito, E., Shinoda, Y., Nitzan, N., Heukamp, A., Rannio, S., Martens, H., Barth, J.*, et al.* (2019). Synaptotagmin-3 drives AMPA receptor endocytosis, depression of synapse strength, and forgetting. Science *363*.

[10]   Babl, S.S., Rummell, B.P., and Sigurdsson, T. (2019). The Spatial Extent of Optogenetic Silencing in Transgenic Mice Expressing Channelrhodopsin in Inhibitory Interneurons. Cell Rep *29*, 1381-1395 e1384.

[11]   Banghart, M., Borges, K., Isacoff, E., Trauner, D., and Kramer, R.H. (2004). Light-activated ion channels for remote control of neuronal firing. Nat Neurosci *7*, 1381-1386.

[12]   Bastrikova, N., Gardner, G.A., Reece, J.M., Jeromin, A., and Dudek, S.M. (2008). Synapse elimination accompanies functional plasticity in hippocampal neurons. Proc Natl Acad Sci U S A *105*, 3123-3127.

[13]   Bean, B.P. (1989). Neurotransmitter inhibition of neuronal calcium currents by changes in channel voltage dependence. Nature *340*, 153-156.

[14]   Bear, M.F. (2003). Bidirectional synaptic plasticity: from theory to reality. Philos Trans R Soc Lond B Biol Sci *358*, 649-655.

[15]   Beck, S., Yu-Strzelczyk, J., Pauls, D., Constantin, O.M., Gee, C.E., Ehmann, N., Kittel, R.J., Nagel, G., and Gao, S. (2018). Synthetic Light-Activated Ion Channels for Optogenetic Activation and Inhibition. Front Neurosci *12*, 643.

[16]   Bekkers, J.M., and Stevens, C.F. (1990). Presynaptic mechanism for long-term potentiation in the hippocampus. Nature *346*, 724-729.

[17]   Bellone, C., and Nicoll, R.A. (2007). Rapid bidirectional switching of synaptic NMDA receptors. Neuron *55*, 779-785.

[18]   Benke, T.A., Luthi, A., Isaac, J.T., and Collingridge, G.L. (1998). Modulation of AMPA receptor unitary conductance by synaptic activity. Nature *393*, 793-797.

[19] Benninger, R.K., Onfelt, B., Neil, M.A., Davis, D.M., and French, P.M. (2005). Fluorescence imaging of two-photon linear dichroism: cholesterol depletion disrupts molecular orientation in cell membranes. Biophys J *88*, 609-622.

[20] Bernal Sierra, Y.A., Rost, B.R., Pofahl, M., Fernandes, A.M., Kopton, R.A., Moser, S., Holtkamp, D., Masala, N., Beed, P., Tukker, J.J.*, et al.* (2018). Potassium channel-based optogenetic silencing. Nat Commun *9*, 4611.

[21] Berndt, A., Lee, S.Y., Ramakrishnan, C., and Deisseroth, K. (2014). Structure-guided transformation of channelrhodopsin into a light-activated chloride channel. Science *344*, 420-424.

[22] Berridge, M.J., Bootman, M.D., and Lipp, P. (1998). Calcium--a life and death signal. Nature *395*, 645-648.

[23] Bian, W.J., Miao, W.Y., He, S.J., Qiu, Z., and Yu, X. (2015). Coordinated Spine Pruning and Maturation Mediated by Inter-Spine Competition for Cadherin/Catenin Complexes. Cell *162*, 808-822.

[24] Bittner, K.C., Grienberger, C., Vaidya, S.P., Milstein, A.D., Macklin, J.J., Suh, J., Tonegawa, S., and Magee, J.C. (2015). Conjunctive input processing drives feature selectivity in hippocampal CA1 neurons. Nat Neurosci *18*, 1133-1142.

[25] Blackmer, T., Larsen, E.C., Takahashi, M., Martin, T.F., Alford, S., and Hamm, H.E. (2001). G protein betagamma subunit-mediated presynaptic inhibition: regulation of exocytotic fusion downstream of Ca2+ entry. Science *292*, 293-297.

[26] Bliss, T.V., and Collingridge, G.L. (1993). A synaptic model of memory: long-term potentiation in the hippocampus. Nature *361*, 31-39.

[27] Bliss, T.V., and Collingridge, G.L. (2013). Expression of NMDA receptor-dependent LTP in the hippocampus: bridging the divide. Mol Brain *6*, 5.

[28] Bliss, T.V., and Lomo, T. (1973). Long-lasting potentiation of synaptic transmission in the dentate area of the anaesthetized rabbit following stimulation of the perforant path. J Physiol *232*, 331-356.

[29] Bloodgood, B.L., and Sabatini, B.L. (2007a). Ca(2+) signaling in dendritic spines. Curr Opin Neurobiol *17*, 345-351.

[30] Bloodgood, B.L., and Sabatini, B.L. (2007b). Nonlinear regulation of unitary synaptic signals by CaV(2.3) voltage-sensitive calcium channels located in dendritic spines. Neuron *53*, 249-260.

[31] Bloxham, W., Brinks, D., Kheifets, S., and Cohen, A.E. (2021). Linearly polarized excitation enhances signals from fluorescent voltage indicators. Biophys J *120*, 5333-5342.

[32] Bosch, M., Castro, J., Saneyoshi, T., Matsuno, H., Sur, M., and Hayashi, Y. (2014). Structural and molecular remodeling of dendritic spine substructures during long-term potentiation. Neuron *82*, 444-459.

[33] Bourne, J., and Harris, K.M. (2007). Do thin spines learn to be mushroom spines that remember? Curr Opin Neurobiol *17*, 381-386.

[34] Bourne, J.N., and Harris, K.M. (2008). Balancing structure and function at hippocampal dendritic spines. Annu Rev Neurosci *31*, 47-67.

[35] Boyden, E.S., Zhang, F., Bamberg, E., Nagel, G., and Deisseroth, K. (2005). Millisecond-timescale, genetically targeted optical control of neural activity. Nat Neurosci *8*, 1263-1268.

[36] Branco, T., and Hausser, M. (2010). The single dendritic branch as a fundamental functional unit in the nervous system. Curr Opin Neurobiol *20*, 494-502.

[37] Brody, D.L., and Yue, D.T. (2000). Relief of G-protein inhibition of calcium channels and short-term synaptic facilitation in cultured hippocampal neurons. J Neurosci *20*, 889-898.

[38] Burke, K.J., Jr., Keeshen, C.M., and Bender, K.J. (2018). Two Forms of Synaptic Depression Produced by Differential Neuromodulation of Presynaptic Calcium Channels. Neuron *99*, 969-984 e967.

[39] Busetto, G., Higley, M.J., and Sabatini, B.L. (2008). Developmental presence and disappearance of postsynaptically silent synapses on dendritic spines of rat layer 2/3 pyramidal neurons. J Physiol *586*, 1519-1527.

[40] Cane, M., Maco, B., Knott, G., and Holtmaat, A. (2014). The relationship between PSD-95 clustering and spine stability in vivo. J Neurosci *34*, 2075-2086.

[41] Caroni, P., Donato, F., and Muller, D. (2012). Structural plasticity upon learning: regulation and functions. Nat Rev Neurosci *13*, 478-490.

[42] Carroll, R.C., Lissin, D.V., von Zastrow, M., Nicoll, R.A., and Malenka, R.C. (1999). Rapid redistribution of glutamate receptors contributes to long-term depression in hippocampal cultures. Nat Neurosci *2*, 454-460.

[43] Chalifoux, J.R., and Carter, A.G. (2010). GABAB receptors modulate NMDA receptor calcium signals in dendritic spines. Neuron *66*, 101-113.

[44] Chalifoux, J.R., and Carter, A.G. (2011a). GABAB receptor modulation of synaptic function. Curr Opin Neurobiol *21*, 339-344.

[45] Chalifoux, J.R., and Carter, A.G. (2011b). GABAB receptor modulation of voltage-sensitive calcium channels in spines and dendrites. J Neurosci *31*, 4221-4232.

[46] Chen, J.L., Villa, K.L., Cha, J.W., So, P.T., Kubota, Y., and Nedivi, E. (2012). Clustered dynamics of inhibitory synapses and dendritic spines in the adult neocortex. Neuron *74*, 361-373.

[47] Chen, X., Leischner, U., Rochefort, N.L., Nelken, I., and Konnerth, A. (2011). Functional mapping of single spines in cortical neurons in vivo. Nature *475*, 501-505.

[48] Choi, J.H., Sim, S.E., Kim, J.I., Choi, D.I., Oh, J., Ye, S., Lee, J., Kim, T., Ko, H.G., Lim, C.S.*, et al.* (2018). Interregional synaptic maps among engram cells underlie memory formation. Science *360*, 430-435.

[49] Choquet, D. (2018). Linking Nanoscale Dynamics of AMPA Receptor Organization to Plasticity of Excitatory Synapses and Learning. J Neurosci *38*, 9318-9329.

[50] Chow, B.Y., Han, X., Dobry, A.S., Qian, X., Chuong, A.S., Li, M., Henninger, M.A., Belfort, G.M., Lin, Y., Monahan, P.E.*, et al.* (2010). High-performance genetically targetable optical neural silencing by light-driven proton pumps. Nature *463*, 98-102.

[51] Citri, A., and Malenka, R.C. (2008). Synaptic plasticity: multiple forms, functions, and mechanisms. Neuropsychopharmacology *33*, 18-41.

[52] Clements, J.D., Lester, R.A., Tong, G., Jahr, C.E., and Westbrook, G.L. (1992). The time course of glutamate in the synaptic cleft. Science *258*, 1498-1501.

[53] Colgan, L.A., Hu, M., Misler, J.A., Parra-Bueno, P., Moran, C.M., Leitges, M., and Yasuda, R. (2018). PKCalpha integrates spatiotemporally distinct Ca(2+) and autocrine BDNF signaling to facilitate synaptic plasticity. Nat Neurosci *21*, 1027-1037.

[54] Copits, B.A., Gowrishankar, R., O'Neill, P.R., Li, J.N., Girven, K.S., Yoo, J.J., Meshik, X., Parker, K.E., Spangler, S.M., Elerding, A.J.*, et al.* (2021). A photoswitchable GPCR-based opsin for presynaptic inhibition. Neuron *109*, 1791-1809 e1711.

[55] Cornejo, V.H., Ofer, N., and Yuste, R. (2021). Voltage compartmentalization in dendritic spines in vivo. Science, eabg0501.

[56] Cosentino, C., Alberio, L., Gazzarrini, S., Aquila, M., Romano, E., Cermenati, S., Zuccolini, P., Petersen, J., Beltrame, M., Van Etten, J.L.*, et al.* (2015). Optogenetics. Engineering of a light-gated potassium channel. Science *348*, 707-710.

[57] Cummings, J.A., Mulkey, R.M., Nicoll, R.A., and Malenka, R.C. (1996). Ca2+ signaling requirements for long-term depression in the hippocampus. Neuron *16*, 825-833.

[58] Dafforn, T.R., and Rodger, A. (2004). Linear dichroism of biomolecules: which way is up? Curr Opin Struct Biol *14*, 541-546.

[59] De Roo, M., Klauser, P., and Muller, D. (2008). LTP promotes a selective long-term stabilization and clustering of dendritic spines. PLoS Biol *6*, e219.

[60] Deisseroth, K. (2011). Optogenetics. Nat Methods *8*, 26-29.

[61] Deisseroth, K., and Hegemann, P. (2017). The form and function of channelrhodopsin. Science *357*.

[62] Denk, W., Strickler, J.H., and Webb, W.W. (1990). Two-photon laser scanning fluorescence microscopy. Science *248*, 73-76.

[63] Derkach, V., Barria, A., and Soderling, T.R. (1999). Ca2+/calmodulin-kinase II enhances channel conductance of alpha-amino-3-hydroxy-5-methyl-4-isoxazolepropionate type glutamate receptors. Proc Natl Acad Sci U S A *96*, 3269-3274.

[64] Derkach, V.A., Oh, M.C., Guire, E.S., and Soderling, T.R. (2007). Regulatory mechanisms of AMPA receptors in synaptic plasticity. Nat Rev Neurosci *8*, 101-113.

[65] Diering, G.H., and Huganir, R.L. (2018). The AMPA Receptor Code of Synaptic Plasticity. Neuron *100*, 314-329.

[66] Doron, G., Shin, J.N., Takahashi, N., Druke, M., Bocklisch, C., Skenderi, S., de Mont, L., Toumazou, M., Ledderose, J., Brecht, M.*, et al.* (2020). Perirhinal input to neocortical layer 1 controls learning. Science *370*.

[67] Dudek, S.M., and Bear, M.F. (1992). Homosynaptic long-term depression in area CA1 of hippocampus and effects of N-methyl-D-aspartate receptor blockade. Proc Natl Acad Sci U S A *89*, 4363-4367.

[68] Dudman, J.T., Tsay, D., and Siegelbaum, S.A. (2007). A role for synaptic inputs at distal dendrites: instructive signals for hippocampal long-term plasticity. Neuron *56*, 866-879.

[69] Dunaevsky, A., Tashiro, A., Majewska, A., Mason, C., and Yuste, R. (1999). Developmental regulation of spine motility in the mammalian central nervous system. Proc Natl Acad Sci U S A *96*, 13438-13443.

[70] Durst, C.D., Wiegert, J.S., Helassa, N., Kerruth, S., Coates, C., Schulze, C., Geeves, M.A., Torok, K., and Oertner, T.G. (2019). High-speed imaging of glutamate release with genetically encoded sensors. Nat Protoc *14*, 1401-1424.

[71] Dürst, C.D., Wiegert, J.S., Schulze, C., Helassa, N., Török, K., and Oertner, T.G. (2021). Vesicular release probability sets the strength of individual Schaffer collateral synapses. bioRxiv, 2020.2008.2002.232850.

[72] Ehrlich, I., Klein, M., Rumpel, S., and Malinow, R. (2007). PSD-95 is required for activity-driven synapse stabilization. Proc Natl Acad Sci U S A *104*, 4176-4181.

[73] Eickelbeck, D., Rudack, T., Tennigkeit, S.A., Surdin, T., Karapinar, R., Schwitalla, J.C., Mucher, B., Shulman, M., Scherlo, M., Althoff, P.*, et al.* (2020). Lamprey Parapinopsin ("UVLamP"): a Bistable UV-Sensitive Optogenetic Switch for Ultrafast Control of GPCR Pathways. Chembiochem *21*, 612-617.

[74] El-Boustani, S., Ip, J.P.K., Breton-Provencher, V., Knott, G.W., Okuno, H., Bito, H., and Sur, M. (2018). Locally coordinated synaptic plasticity of visual cortex neurons in vivo. Science *360*, 1349-1354.

[75] El-Gaby, M., Zhang, Y., Wolf, K., Schwiening, C.J., Paulsen, O., and Shipton, O.A. (2016). Archaerhodopsin Selectively and Reversibly Silences Synaptic Transmission through Altered pH. Cell Rep *16*, 2259-2268.

[76] El-Husseini, A.E., Schnell, E., Chetkovich, D.M., Nicoll, R.A., and Bredt, D.S. (2000). PSD-95 involvement in maturation of excitatory synapses. Science *290*, 1364-1368.

[77] Emptage, N., Bliss, T.V.P., and Fine, A. (1999). Single Synaptic Events Evoke NMDA Receptor–Mediated Release of Calcium from Internal Stores in Hippocampal Dendritic Spines. Neuron *22*, 115-124.

[78] Emptage, N.J., Reid, C.A., Fine, A., and Bliss, T.V. (2003). Optical quantal analysis reveals a presynaptic component of LTP at hippocampal Schaffer-associational synapses. Neuron *38*, 797-804.

[79] Engert, F., and Bonhoeffer, T. (1999). Dendritic spine changes associated with hippocampal long-term synaptic plasticity. Nature *399*, 66-70.

[80] Enoki, R., Hu, Y.L., Hamilton, D., and Fine, A. (2009). Expression of long-term plasticity at individual synapses in hippocampus is graded, bidirectional, and mainly presynaptic: optical quantal analysis. Neuron *62*, 242-253.

[81] Feinberg, E.H., Vanhoven, M.K., Bendesky, A., Wang, G., Fetter, R.D., Shen, K., and Bargmann, C.I. (2008). GFP Reconstitution Across Synaptic Partners (GRASP) defines cell contacts and synapses in living nervous systems. Neuron *57*, 353-363.

[82] Feng, J., Zhang, C., Lischinsky, J.E., Jing, M., Zhou, J., Wang, H., Zhang, Y., Dong, A., Wu, Z., Wu, H.*, et al.* (2019). A Genetically Encoded Fluorescent Sensor for Rapid and Specific In Vivo Detection of Norepinephrine. Neuron *102*, 745-761 e748.

[83] Fiala, J.C., Feinberg, M., Popov, V., and Harris, K.M. (1998). Synaptogenesis via dendritic filopodia in developing hippocampal area CA1. J Neurosci *18*, 8900-8911.

[84] Fifkova, E., and Van Harreveld, A. (1977). Long-lasting morphological changes in dendritic spines of dentate granular cells following stimulation of the entorhinal area. J Neurocytol *6*, 211-230.

[85] Fu, M., Yu, X., Lu, J., and Zuo, Y. (2012). Repetitive motor learning induces coordinated formation of clustered dendritic spines in vivo. Nature *483*, 92-95.

[86] Fukata, Y., Dimitrov, A., Boncompain, G., Vielemeyer, O., Perez, F., and Fukata, M. (2013). Local palmitoylation cycles define activity-regulated postsynaptic subdomains. J Cell Biol *202*, 145-161.

[87] Gao, S., Nagpal, J., Schneider, M.W., Kozjak-Pavlovic, V., Nagel, G., and Gottschalk, A. (2015). Optogenetic manipulation of cGMP in cells and animals by the tightly light-regulated guanylyl-cyclase opsin CyclOp. Nat Commun *6*, 8046.

[88] Gasecka, A., Han, T.J., Favard, C., Cho, B.R., and Brasselet, S. (2009). Quantitative imaging of molecular order in lipid membranes using two-photon fluorescence polarimetry. Biophys J *97*, 2854-2862.

[89] Gentet, L.J., Kremer, Y., Taniguchi, H., Huang, Z.J., Staiger, J.F., and Petersen, C.C. (2012). Unique functional properties of somatostatin-expressing GABAergic neurons in mouse barrel cortex. Nat Neurosci *15*, 607-612.

[90] Gerachshenko, T., Blackmer, T., Yoon, E.J., Bartleson, C., Hamm, H.E., and Alford, S. (2005). Gbetagamma acts at the C terminus of SNAP-25 to mediate presynaptic inhibition. Nat Neurosci *8*, 597-605.

[91] Golding, N.L., Staff, N.P., and Spruston, N. (2002). Dendritic spikes as a mechanism for cooperative long-term potentiation. Nature *418*, 326-331.

[92] Goto, A., Bota, A., Miya, K., Wang, J., Tsukamoto, S., Jiang, X., Hirai, D., Murayama, M., Matsuda, T., McHugh, T.J.*, et al.* (2021). Stepwise synaptic plasticity events drive the early phase of memory consolidation. Science *374*, 857-863.

[93] Govindarajan, A., Israely, I., Huang, S.Y., and Tonegawa, S. (2011). The dendritic branch is the preferred integrative unit for protein synthesis-dependent LTP. Neuron *69*, 132-146.

[94] Govindarajan, A., Kelleher, R.J., and Tonegawa, S. (2006). A clustered plasticity model of long-term memory engrams. Nat Rev Neurosci *7*, 575-583.

[95] Govorunova, E.G., Gou, Y., Sineshchekov, O.A., Li, H., Wang, Y., Brown, L.S., Xue, M., and Spudich, J.L. (2021). Kalium rhodopsins: Natural light-gated potassium channels. bioRxiv, 2021.2009.2017.460684.

[96] Govorunova, E.G., Sineshchekov, O.A., Janz, R., Liu, X., and Spudich, J.L. (2015). NEUROSCIENCE. Natural light-gated anion channels: A family of microbial rhodopsins for advanced optogenetics. Science *349*, 647-650.

[97] Gradinaru, V., Thompson, K.R., and Deisseroth, K. (2008). eNpHR: a Natronomonas halorhodopsin enhanced for optogenetic applications. Brain Cell Biol *36*, 129-139.

[98] Gradinaru, V., Zhang, F., Ramakrishnan, C., Mattis, J., Prakash, R., Diester, I., Goshen, I., Thompson, K.R., and Deisseroth, K. (2010). Molecular and cellular approaches for diversifying and extending optogenetics. Cell *141*, 154-165.

[99] Granger, A.J., Shi, Y., Lu, W., Cerpas, M., and Nicoll, R.A. (2013). LTP requires a reserve pool of glutamate receptors independent of subunit type. Nature *493*, 495-500.

[100] Groc, L., Heine, M., Cognet, L., Brickley, K., Stephenson, F.A., Lounis, B., and Choquet, D. (2004). Differential activity-dependent regulation of the lateral mobilities of AMPA and NMDA receptors. Nat Neurosci *7*, 695-696.

[101] Grunditz, A., Holbro, N., Tian, L., Zuo, Y., and Oertner, T.G. (2008). Spine neck plasticity controls postsynaptic calcium signals through electrical compartmentalization. J Neurosci *28*, 13457-13466.

[102] Grutzendler, J., Kasthuri, N., and Gan, W.B. (2002). Long-term dendritic spine stability in the adult cortex. Nature *420*, 812-816.

[103] Guan, H., Middleton, S.J., Inoue, T., and McHugh, T.J. (2021). Lateralization of CA1 assemblies in the absence of CA3 input. Nat Commun *12*, 6114.

[104] Guntas, G., Hallett, R.A., Zimmerman, S.P., Williams, T., Yumerefendi, H., Bear, J.E., and Kuhlman, B. (2015). Engineering an improved light-induced dimer (iLID) for controlling the localization and activity of signaling proteins. Proc Natl Acad Sci U S A *112*, 112-117.

[105] Guo, Z.V., Li, N., Huber, D., Ophir, E., Gutnisky, D., Ting, J.T., Feng, G., and Svoboda, K. (2014). Flow of cortical activity underlying a tactile decision in mice. Neuron *81*, 179-194.

[106] Hafner, A.S., Donlin-Asp, P.G., Leitch, B., Herzog, E., and Schuman, E.M. (2019). Local protein synthesis is a ubiquitous feature of neuronal pre- and postsynaptic compartments. Science *364*.

[107] Hamid, E., Church, E., Wells, C.A., Zurawski, Z., Hamm, H.E., and Alford, S. (2014). Modulation of neurotransmission by GPCRs is dependent upon the microarchitecture of the primed vesicle complex. J Neurosci *34*, 260-274.

[108] Harnett, M.T., Makara, J.K., Spruston, N., Kath, W.L., and Magee, J.C. (2012). Synaptic amplification by dendritic spines enhances input cooperativity. Nature *491*, 599-602.

[109] Harris, K.M., and Kater, S.B. (1994). Dendritic spines: cellular specializations imparting both stability and flexibility to synaptic function. Annu Rev Neurosci *17*, 341-371.

[110] Harris, K.M., and Stevens, J.K. (1989). Dendritic spines of CA 1 pyramidal cells in the rat hippocampus: serial electron microscopy with reference to their biophysical characteristics. J Neurosci *9*, 2982-2997.

[111] Harvey, C.D., and Svoboda, K. (2007). Locally dynamic synaptic learning rules in pyramidal neuron dendrites. Nature *450*, 1195-1200.

[112] Harvey, C.D., Yasuda, R., Zhong, H., and Svoboda, K. (2008). The spread of Ras activity triggered by activation of a single dendritic spine. Science *321*, 136-140.

[113] Harward, S.C., Hedrick, N.G., Hall, C.E., Parra-Bueno, P., Milner, T.A., Pan, E., Laviv, T., Hempstead, B.L., Yasuda, R., and McNamara, J.O. (2016). Autocrine BDNF-TrkB signalling within a single dendritic spine. Nature *538*, 99-103.

[114] Hausser, M. (2014). Optogenetics: the age of light. Nat Methods *11*, 1012-1014.

[115] Hayama, T., Noguchi, J., Watanabe, S., Takahashi, N., Hayashi-Takagi, A., Ellis-Davies, G.C., Matsuzaki, M., and Kasai, H. (2013). GABA promotes the competitive selection of dendritic spines by controlling local Ca2+ signaling. Nat Neurosci *16*, 1409-1416.

[116] Hayashi-Takagi, A., Yagishita, S., Nakamura, M., Shirai, F., Wu, Y.I., Loshbaugh, A.L., Kuhlman, B., Hahn, K.M., and Kasai, H. (2015). Labelling and optical erasure of synaptic memory traces in the motor cortex. Nature *525*, 333-338.

[117] Hayashi, Y., Shi, S.H., Esteban, J.A., Piccini, A., Poncer, J.C., and Malinow, R. (2000). Driving AMPA receptors into synapses by LTP and CaMKII: requirement for GluR1 and PDZ domain interaction. Science *287*, 2262-2267.

[118] Hebb, D.O. (1949). The organization of behavior; a neuropsychological theory (Oxford, England: Wiley).

[119] Hedrick, N.G., Harward, S.C., Hall, C.E., Murakoshi, H., McNamara, J.O., and Yasuda, R. (2016). Rho GTPase complementation underlies BDNF-dependent homo- and heterosynaptic plasticity. Nature *538*, 104-108.

[120] Helassa, N., Durst, C.D., Coates, C., Kerruth, S., Arif, U., Schulze, C., Wiegert, J.S., Geeves, M., Oertner, T.G., and Torok, K. (2018). Ultrafast glutamate sensors resolve high-frequency release at Schaffer collateral synapses. Proc Natl Acad Sci U S A *115*, 5594-5599.

[121] Herlitze, S., Garcia, D.E., Mackie, K., Hille, B., Scheuer, T., and Catterall, W.A. (1996). Modulation of Ca2+ channels by G-protein beta gamma subunits. Nature *380*, 258-262.

[122] Hess, S.T., Sheets, E.D., Wagenknecht-Wiesner, A., and Heikal, A.A. (2003). Quantitative analysis of the fluorescence properties of intrinsically fluorescent proteins in living cells. Biophys J *85*, 2566-2580.

[123] Higley, M.J., and Sabatini, B.L. (2010). Competitive regulation of synaptic Ca2+ influx by D2 dopamine and A2A adenosine receptors. Nat Neurosci *13*, 958-966.

[124] Higley, M.J., and Sabatini, B.L. (2012). Calcium signaling in dendritic spines. Cold Spring Harb Perspect Biol *4*, a005686.

[125] Hill, T.C., and Zito, K. (2013). LTP-induced long-term stabilization of individual nascent dendritic spines. J Neurosci *33*, 678-686.

[126] Holbro, N., Grunditz, A., and Oertner, T.G. (2009). Differential distribution of endoplasmic reticulum controls metabotropic signaling and plasticity at hippocampal synapses. Proc Natl Acad Sci U S A *106*, 15055-15060.

[127] Holbro, N., Grunditz, A., Wiegert, J.S., and Oertner, T.G. (2010). AMPA receptors gate spine Ca(2+) transients and spike-timing-dependent potentiation. Proc Natl Acad Sci U S A *107*, 15975-15980.

[128] Holderith, N., Lorincz, A., Katona, G., Rozsa, B., Kulik, A., Watanabe, M., and Nusser, Z. (2012). Release probability of hippocampal glutamatergic terminals scales with the size of the active zone. Nat Neurosci *15*, 988-997.

[129] Holtmaat, A., and Svoboda, K. (2009). Experience-dependent structural synaptic plasticity in the mammalian brain. Nat Rev Neurosci *10*, 647-658.

[130] Holtmaat, A.J., Trachtenberg, J.T., Wilbrecht, L., Shepherd, G.M., Zhang, X., Knott, G.W., and Svoboda, K. (2005). Transient and persistent dendritic spines in the neocortex in vivo. Neuron *45*, 279-291.

[131] Honkura, N., Matsuzaki, M., Noguchi, J., Ellis-Davies, G.C., and Kasai, H. (2008). The subspine organization of actin fibers regulates the structure and plasticity of dendritic spines. Neuron *57*, 719-729.

[132] Hruska, M., Henderson, N., Le Marchand, S.J., Jafri, H., and Dalva, M.B. (2018). Synaptic nanomodules underlie the organization and plasticity of spine synapses. Nat Neurosci *21*, 671-682.

[133] Huganir, R.L., and Nicoll, R.A. (2013). AMPARs and synaptic plasticity: the last 25 years. Neuron *80*, 704-717.

[134] Jackman, S.L., Beneduce, B.M., Drew, I.R., and Regehr, W.G. (2014). Achieving high-frequency optical control of synaptic transmission. J Neurosci *34*, 7704-7714.

[135] Jackman, S.L., and Regehr, W.G. (2017). The Mechanisms and Functions of Synaptic Facilitation. Neuron *94*, 447-464.

[136] Jahr, C.E., and Stevens, C.F. (1993). Calcium permeability of the N-methyl-D-aspartate receptor channel in hippocampal neurons in culture. Proc Natl Acad Sci U S A *90*, 11573-11577.

[137] Janovjak, H., Szobota, S., Wyart, C., Trauner, D., and Isacoff, E.Y. (2010). A light-gated, potassium-selective glutamate receptor for the optical inhibition of neuronal firing. Nat Neurosci *13*, 1027-1032.

[138] Ji, N., Magee, J.C., and Betzig, E. (2008). High-speed, low-photodamage nonlinear imaging using passive pulse splitters. Nat Methods *5*, 197-202.

[139] Jing, M., Li, Y., Zeng, J., Huang, P., Skirzewski, M., Kljakic, O., Peng, W., Qian, T., Tan, K., Zou, J., *et al.* (2020). An optimized acetylcholine sensor for monitoring in vivo cholinergic activity. Nat Methods *17*, 1139-1146.

[140] Kaila, K., Price, T.J., Payne, J.A., Puskarjov, M., and Voipio, J. (2014). Cation-chloride cotransporters in neuronal development, plasticity and disease. Nat Rev Neurosci *15*, 637-654.

[141] Kampa, B.M., Letzkus, J.J., and Stuart, G.J. (2007). Dendritic mechanisms controlling spike-timing-dependent synaptic plasticity. Trends Neurosci *30*, 456-463.

[142] Kazemipour, A., Novak, O., Flickinger, D., Marvin, J.S., Abdelfattah, A.S., King, J., Borden, P.M., Kim, J.J., Al-Abdullatif, S.H., Deal, P.E., *et al.* (2019). Kilohertz frame-rate two-photon tomography. Nat Methods *16*, 778-786.

[143] Kennedy, M.J., Hughes, R.M., Peteya, L.A., Schwartz, J.W., Ehlers, M.D., and Tucker, C.L. (2010). Rapid blue-light-mediated induction of protein interactions in living cells. Nat Methods *7*, 973-975.

[144] Kerchner, G.A., and Nicoll, R.A. (2008). Silent synapses and the emergence of a postsynaptic mechanism for LTP. Nat Rev Neurosci *9*, 813-825.

[145] Kerlin, A., Boaz, M., Flickinger, D., MacLennan, B.J., Dean, M.B., Davis, C., Spruston, N., and Svoboda, K. (2019). Functional clustering of dendritic activity during decision-making. Elife *8*.

[146] Kim, J., Zhao, T., Petralia, R.S., Yu, Y., Peng, H., Myers, E., and Magee, J.C. (2011). mGRASP enables mapping mammalian synaptic connectivity with light microscopy. Nat Methods *9*, 96-102.

[147] Kim, J.M., Hwa, J., Garriga, P., Reeves, P.J., RajBhandary, U.L., and Khorana, H.G. (2005). Light-driven activation of beta 2-adrenergic receptor signaling by a chimeric rhodopsin containing the beta 2-adrenergic receptor cytoplasmic loops. Biochemistry *44*, 2284-2292.

[148] Kim, Y., Hsu, C.L., Cembrowski, M.S., Mensh, B.D., and Spruston, N. (2015). Dendritic sodium spikes are required for long-term potentiation at distal synapses on hippocampal pyramidal neurons. Elife *4*.

[149] Kleindienst, T., Winnubst, J., Roth-Alpermann, C., Bonhoeffer, T., and Lohmann, C. (2011). Activity-dependent clustering of functional synaptic inputs on developing hippocampal dendrites. Neuron *72*, 1012-1024.

[150] Kleinlogel, S., Terpitz, U., Legrum, B., Gokbuget, D., Boyden, E.S., Bamann, C., Wood, P.G., and Bamberg, E. (2011). A gene-fusion strategy for stoichiometric and co-localized expression of light-gated membrane proteins. Nat Methods *8*, 1083-1088.

[151] Knott, G.W., Holtmaat, A., Wilbrecht, L., Welker, E., and Svoboda, K. (2006). Spine growth precedes synapse formation in the adult neocortex in vivo. Nat Neurosci *9*, 1117-1124.

[152] Kovalchuk, Y., Eilers, J., Lisman, J., and Konnerth, A. (2000). NMDA receptor-mediated subthreshold Ca(2+) signals in spines of hippocampal neurons. J Neurosci *20*, 1791-1799.

[153] Koyanagi, M., Kawano, E., Kinugawa, Y., Oishi, T., Shichida, Y., Tamotsu, S., and Terakita, A. (2004). Bistable UV pigment in the lamprey pineal. Proc Natl Acad Sci U S A *101*, 6687-6691.

[154] Koyanagi, M., Takada, E., Nagata, T., Tsukamoto, H., and Terakita, A. (2013). Homologs of vertebrate Opn3 potentially serve as a light sensor in nonphotoreceptive tissue. Proc Natl Acad Sci U S A *110*, 4998-5003.

[155] Koyanagi, M., and Terakita, A. (2014). Diversity of animal opsin-based pigments and their optogenetic potential. Biochim Biophys Acta *1837*, 710-716.

[156] Kramar, E.A., Lin, B., Rex, C.S., Gall, C.M., and Lynch, G. (2006). Integrin-driven actin polymerization consolidates long-term potentiation. Proc Natl Acad Sci U S A *103*, 5579-5584.

[157] Kress, A., Wang, X., Ranchon, H., Savatier, J., Rigneault, H., Ferrand, P., and Brasselet, S. (2013). Mapping the local organization of cell membranes using excitation-polarization-resolved confocal fluorescence microscopy. Biophys J *105*, 127-136.

[158] Kristensen, A.S., Jenkins, M.A., Banke, T.G., Schousboe, A., Makino, Y., Johnson, R.C., Huganir, R., and Traynelis, S.F. (2011). Mechanism of Ca2+/calmodulin-dependent kinase II regulation of AMPA receptor gating. Nat Neurosci *14*, 727-735.

[159] Kwon, H.B., and Sabatini, B.L. (2011). Glutamate induces de novo growth of functional spines in developing cortex. Nature *474*, 100-104.

[160] Lai, C.S., Franke, T.F., and Gan, W.B. (2012). Opposite effects of fear conditioning and extinction on dendritic spine remodelling. Nature *483*, 87-91.

[161] Lambert, J.T., Hill, T.C., Park, D.K., Culp, J.H., and Zito, K. (2017). Protracted and asynchronous accumulation of PSD95-family MAGUKs during maturation of nascent dendritic spines. Dev Neurobiol *77*, 1161-1174.

[162] Lang, C., Barco, A., Zablow, L., Kandel, E.R., Siegelbaum, S.A., and Zakharenko, S.S. (2004). Transient expansion of synaptically connected dendritic spines upon induction of hippocampal long-term potentiation. Proc Natl Acad Sci U S A *101*, 16665-16670.

[163] Larkum, M.E., Nevian, T., Sandler, M., Polsky, A., and Schiller, J. (2009). Synaptic integration in tuft dendrites of layer 5 pyramidal neurons: a new unifying principle. Science *325*, 756-760.

[164] Lazar, J., Bondar, A., Timr, S., and Firestein, S.J. (2011). Two-photon polarization microscopy reveals protein structure and function. Nat Methods *8*, 684-690.

[165] Lee, H.K., Barbarosie, M., Kameyama, K., Bear, M.F., and Huganir, R.L. (2000). Regulation of distinct AMPA receptor phosphorylation sites during bidirectional synaptic plasticity. Nature *405*, 955-959.

[166] Lee, K.F., Soares, C., Thivierge, J.P., and Beique, J.C. (2016). Correlated Synaptic Inputs Drive Dendritic Calcium Amplification and Cooperative Plasticity during Clustered Synapse Development. Neuron *89*, 784-799.

[167] Lee, S., Park, H., Kyung, T., Kim, N.Y., Kim, S., Kim, J., and Heo, W.D. (2014). Reversible protein inactivation by optogenetic trapping in cells. Nat Methods *11*, 633-636.

[168] Lee, S.J., Escobedo-Lozoya, Y., Szatmari, E.M., and Yasuda, R. (2009). Activation of CaMKII in single dendritic spines during long-term potentiation. Nature *458*, 299-304.

[169] Lendvai, B., Stern, E.A., Chen, B., and Svoboda, K. (2000). Experience-dependent plasticity of dendritic spines in the developing rat barrel cortex in vivo. Nature *404*, 876-881.

[170] Li, N., Chen, S., Guo, Z.V., Chen, H., Huo, Y., Inagaki, H.K., Chen, G., Davis, C., Hansel, D., Guo, C.*, et al.* (2019). Spatiotemporal constraints on optogenetic inactivation in cortical circuits. Elife *8*.

[171] Li, X., Gutierrez, D.V., Hanson, M.G., Han, J., Mark, M.D., Chiel, H., Hegemann, P., Landmesser, L.T., and Herlitze, S. (2005). Fast noninvasive activation and inhibition of neural and network activity by vertebrate rhodopsin and green algae channelrhodopsin. Proc Natl Acad Sci U S A *102*, 17816-17821.

[172] Lin, J.Y., Sann, S.B., Zhou, K., Nabavi, S., Proulx, C.D., Malinow, R., Jin, Y., and Tsien, R.Y. (2013). Optogenetic inhibition of synaptic release with chromophore-assisted light inactivation (CALI). Neuron *79*, 241-253.

[173] Lisman, J., Yasuda, R., and Raghavachari, S. (2012). Mechanisms of CaMKII action in long-term potentiation. Nat Rev Neurosci *13*, 169-182.

[174] Lisman, J.E., Raghavachari, S., and Tsien, R.W. (2007). The sequence of events that underlie quantal transmission at central glutamatergic synapses. Nat Rev Neurosci *8*, 597-609.

[175] Liu, Q., Sinnen, B.L., Boxer, E.E., Schneider, M.W., Grybko, M.J., Buchta, W.C., Gibson, E.S., Wysoczynski, C.L., Ford, C.P., Gottschalk, A.*, et al.* (2019). A Photoactivatable Botulinum Neurotoxin for Inducible Control of Neurotransmission. Neuron *101*, 863-875 e866.

[176] Liu, X., Ramirez, S., Pang, P.T., Puryear, C.B., Govindarajan, A., Deisseroth, K., and Tonegawa, S. (2012). Optogenetic stimulation of a hippocampal engram activates fear memory recall. Nature *484*, 381-385.

[177] Losonczy, A., and Magee, J.C. (2006). Integrative properties of radial oblique dendrites in hippocampal CA1 pyramidal neurons. Neuron *50*, 291-307.

[178] Losonczy, A., Makara, J.K., and Magee, J.C. (2008). Compartmentalized dendritic plasticity and input feature storage in neurons. Nature *452*, 436-441.

[179] Lu, R., Sun, W., Liang, Y., Kerlin, A., Bierfeld, J., Seelig, J.D., Wilson, D.E., Scholl, B., Mohar, B., Tanimoto, M.*, et al.* (2017). Video-rate volumetric functional imaging of the brain at synaptic resolution. Nat Neurosci *20*, 620-628.

[180] Luscher, C., and Malenka, R.C. (2012). NMDA receptor-dependent long-term potentiation and long-term depression (LTP/LTD). Cold Spring Harb Perspect Biol *4*.

[181] Luscher, C., Xia, H., Beattie, E.C., Carroll, R.C., von Zastrow, M., Malenka, R.C., and Nicoll, R.A. (1999). Role of AMPA receptor cycling in synaptic transmission and plasticity. Neuron *24*, 649-658.

[182] MacGillavry, H.D., Song, Y., Raghavachari, S., and Blanpied, T.A. (2013). Nanoscale scaffolding domains within the postsynaptic density concentrate synaptic AMPA receptors. Neuron *78*, 615-622.

[183] Magee, J.C., and Grienberger, C. (2020). Synaptic Plasticity Forms and Functions. Annu Rev Neurosci *43*, 95-117.

[184] Mago, A., Weber, J.P., Ujfalussy, B.B., and Makara, J.K. (2020). Synaptic Plasticity Depends on the Fine-Scale Input Pattern in Thin Dendrites of CA1 Pyramidal Neurons. J Neurosci *40*, 2593-2605.

[185] Mahn, M., Gibor, L., Patil, P., Cohen-Kashi Malina, K., Oring, S., Printz, Y., Levy, R., Lampl, I., and Yizhar, O. (2018). High-efficiency optogenetic silencing with soma-targeted anion-conducting channelrhodopsins. Nat Commun *9*, 4125.

[186] Mahn, M., Prigge, M., Ron, S., Levy, R., and Yizhar, O. (2016). Biophysical constraints of optogenetic inhibition at presynaptic terminals. Nat Neurosci *19*, 554-556.

[187] Mahn, M., Saraf-Sinik, I., Patil, P., Pulin, M., Bitton, E., Karalis, N., Bruentgens, F., Palgi, S., Gat, A., Dine, J.*, et al.* (2021). Efficient optogenetic silencing of neurotransmitter release with a mosquito rhodopsin. Neuron *109*, 1621-1635 e1628.

[188] Mainen, Z.F., Malinow, R., and Svoboda, K. (1999). Synaptic calcium transients in single spines indicate that NMDA receptors are not saturated. Nature *399*, 151-155.

[189] Majewska, A.K., Newton, J.R., and Sur, M. (2006). Remodeling of synaptic structure in sensory cortical areas in vivo. J Neurosci *26*, 3021-3029.

[190] Major, G., Larkum, M.E., and Schiller, J. (2013). Active properties of neocortical pyramidal neuron dendrites. Annu Rev Neurosci *36*, 1-24.

[191] Makino, H., and Malinow, R. (2009). AMPA receptor incorporation into synapses during LTP: the role of lateral movement and exocytosis. Neuron *64*, 381-390.

[192] Malenka, R.C., and Bear, M.F. (2004). LTP and LTD: an embarrassment of riches. Neuron *44*, 5-21.

[193] Maletic-Savatic, M., Malinow, R., and Svoboda, K. (1999). Rapid dendritic morphogenesis in CA1 hippocampal dendrites induced by synaptic activity. Science *283*, 1923-1927.

[194] Malinow, R., and Tsien, R.W. (1990). Presynaptic enhancement shown by whole-cell recordings of long-term potentiation in hippocampal slices. Nature *346*, 177-180.

[195] Martinetti, L.E., Bonekamp, K.E., Autio, D.M., Kim, H.H., and Crandall, S.R. (2021). Short-Term Facilitation of Long-Range Corticocortical Synapses Revealed by Selective Optical Stimulation. Cereb Cortex.

[196] Marvin, J.S., Borghuis, B.G., Tian, L., Cichon, J., Harnett, M.T., Akerboom, J., Gordus, A., Renninger, S.L., Chen, T.W., Bargmann, C.I.*, et al.* (2013). An optimized fluorescent probe for visualizing glutamate neurotransmission. Nat Methods *10*, 162-170.

[197] Marvin, J.S., Scholl, B., Wilson, D.E., Podgorski, K., Kazemipour, A., Muller, J.A., Schoch, S., Quiroz, F.J.U., Rebola, N., Bao, H.*, et al.* (2018). Stability, affinity, and chromatic variants of the glutamate sensor iGluSnFR. Nat Methods *15*, 936-939.

[198] Marvin, J.S., Shimoda, Y., Magloire, V., Leite, M., Kawashima, T., Jensen, T.P., Kolb, I., Knott, E.L., Novak, O., Podgorski, K.*, et al.* (2019). A genetically encoded fluorescent sensor for in vivo imaging of GABA. Nat Methods *16*, 763-770.

[199] Masseck, O.A., Spoida, K., Dalkara, D., Maejima, T., Rubelowski, J.M., Wallhorn, L., Deneris, E.S., and Herlitze, S. (2014). Vertebrate cone opsins enable sustained and highly sensitive rapid control of Gi/o signaling in anxiety circuitry. Neuron *81*, 1263-1273.

[200] Matsuzaki, M., Ellis-Davies, G.C., Nemoto, T., Miyashita, Y., Iino, M., and Kasai, H. (2001). Dendritic spine geometry is critical for AMPA receptor expression in hippocampal CA1 pyramidal neurons. Nat Neurosci *4*, 1086-1092.

[201] Matsuzaki, M., Honkura, N., Ellis-Davies, G.C., and Kasai, H. (2004). Structural basis of long-term potentiation in single dendritic spines. Nature *429*, 761-766.

[202] Mattis, J., Tye, K.M., Ferenczi, E.A., Ramakrishnan, C., O'Shea, D.J., Prakash, R., Gunaydin, L.A., Hyun, M., Fenno, L.E., Gradinaru, V.*, et al.* (2011). Principles for applying optogenetic tools derived from direct comparative analysis of microbial opsins. Nat Methods *9*, 159-172.

[203] Meyer, D., Bonhoeffer, T., and Scheuss, V. (2014). Balance and stability of synaptic structures during synaptic plasticity. Neuron *82*, 430-443.

[204] Morishita, W., Marie, H., and Malenka, R.C. (2005). Distinct triggering and expression mechanisms underlie LTD of AMPA and NMDA synaptic responses. Nat Neurosci *8*, 1043-1050.

[205] Mulkey, R.M., Endo, S., Shenolikar, S., and Malenka, R.C. (1994). Involvement of a calcineurin/inhibitor-1 phosphatase cascade in hippocampal long-term depression. Nature *369*, 486-488.

[206] Mulkey, R.M., Herron, C.E., and Malenka, R.C. (1993). An essential role for protein phosphatases in hippocampal long-term depression. Science *261*, 1051-1055.

[207] Mulkey, R.M., and Malenka, R.C. (1992). Mechanisms underlying induction of homosynaptic long-term depression in area CA1 of the hippocampus. Neuron *9*, 967-975.

[208] Murakoshi, H., Wang, H., and Yasuda, R. (2011). Local, persistent activation of Rho GTPases during plasticity of single dendritic spines. Nature *472*, 100-104.

[209] Nagel, G., Ollig, D., Fuhrmann, M., Kateriya, S., Musti, A.M., Bamberg, E., and Hegemann, P. (2002). Channelrhodopsin-1: a light-gated proton channel in green algae. Science *296*, 2395-2398.

[210] Nagel, G., Szellas, T., Huhn, W., Kateriya, S., Adeishvili, N., Berthold, P., Ollig, D., Hegemann, P., and Bamberg, E. (2003). Channelrhodopsin-2, a directly light-gated cation-selective membrane channel. Proc Natl Acad Sci U S A *100*, 13940-13945.

[211] Nagerl, U.V., Eberhorn, N., Cambridge, S.B., and Bonhoeffer, T. (2004). Bidirectional activity-dependent morphological plasticity in hippocampal neurons. Neuron *44*, 759-767.

[212] Nagerl, U.V., Kostinger, G., Anderson, J.C., Martin, K.A., and Bonhoeffer, T. (2007). Protracted synaptogenesis after activity-dependent spinogenesis in hippocampal neurons. J Neurosci *27*, 8149-8156.

[213] Nair, D., Hosy, E., Petersen, J.D., Constals, A., Giannone, G., Choquet, D., and Sibarita, J.B. (2013). Super-resolution imaging reveals that AMPA receptors inside synapses are dynamically organized in nanodomains regulated by PSD95. J Neurosci *33*, 13204-13224.

[214] Nevian, T., Larkum, M.E., Polsky, A., and Schiller, J. (2007). Properties of basal dendrites of layer 5 pyramidal neurons: a direct patch-clamp recording study. Nat Neurosci *10*, 206-214.

[215] Nevian, T., and Sakmann, B. (2006). Spine Ca2+ signaling in spike-timing-dependent plasticity. J Neurosci *26*, 11001-11013.

[216] Ngo-Anh, T.J., Bloodgood, B.L., Lin, M., Sabatini, B.L., Maylie, J., and Adelman, J.P. (2005). SK channels and NMDA receptors form a Ca2+-mediated feedback loop in dendritic spines. Nat Neurosci *8*, 642-649.

[217] Niculescu, D., Michaelsen-Preusse, K., Guner, U., van Dorland, R., Wierenga, C.J., and Lohmann, C. (2018). A BDNF-Mediated Push-Pull Plasticity Mechanism for Synaptic Clustering. Cell Rep *24*, 2063-2074.

[218] Nimchinsky, E.A., Yasuda, R., Oertner, T.G., and Svoboda, K. (2004). The number of glutamate receptors opened by synaptic stimulation in single hippocampal spines. J Neurosci *24*, 2054-2064.

[219] Nishiyama, J., and Yasuda, R. (2015). Biochemical Computation for Spine Structural Plasticity. Neuron *87*, 63-75.

[220] Noam, Y., Zha, Q., Phan, L., Wu, R.L., Chetkovich, D.M., Wadman, W.J., and Baram, T.Z. (2010). Trafficking and surface expression of hyperpolarization-activated cyclic nucleotide-gated channels in hippocampal neurons. J Biol Chem *285*, 14724-14736.

[221] Noguchi, J., Matsuzaki, M., Ellis-Davies, G.C., and Kasai, H. (2005). Spine-neck geometry determines NMDA receptor-dependent Ca2+ signaling in dendrites. Neuron *46*, 609-622.

[222] Nusser, Z., Lujan, R., Laube, G., Roberts, J.D., Molnar, E., and Somogyi, P. (1998). Cell type and pathway dependence of synaptic AMPA receptor number and variability in the hippocampus. Neuron *21*, 545-559.

[223] Oertner, T.G., Sabatini, B.L., Nimchinsky, E.A., and Svoboda, K. (2002). Facilitation at single synapses probed with optical quantal analysis. Nat Neurosci *5*, 657-664.

[224] Oh, E., Maejima, T., Liu, C., Deneris, E., and Herlitze, S. (2010). Substitution of 5-HT1A receptor signaling by a light-activated G protein-coupled receptor. J Biol Chem *285*, 30825-30836.

[225] Oh, W.C., Hill, T.C., and Zito, K. (2013). Synapse-specific and size-dependent mechanisms of spine structural plasticity accompanying synaptic weakening. Proc Natl Acad Sci U S A *110*, E305-312.

[226] Oh, W.C., Parajuli, L.K., and Zito, K. (2015). Heterosynaptic structural plasticity on local dendritic segments of hippocampal CA1 neurons. Cell Rep *10*, 162-169.

[227] Okamoto, K., Nagai, T., Miyawaki, A., and Hayashi, Y. (2004). Rapid and persistent modulation of actin dynamics regulates postsynaptic reorganization underlying bidirectional plasticity. Nat Neurosci *7*, 1104-1112.

[228] Opazo, P., Labrecque, S., Tigaret, C.M., Frouin, A., Wiseman, P.W., De Koninck, P., and Choquet, D. (2010). CaMKII triggers the diffusional trapping of surface AMPARs through phosphorylation of stargazin. Neuron *67*, 239-252.

[229] Ostroff, L.E., Fiala, J.C., Allwardt, B., and Harris, K.M. (2002). Polyribosomes redistribute from dendritic shafts into spines with enlarged synapses during LTP in developing rat hippocampal slices. Neuron *35*, 535-545.

[230] Packer, A.M., Roska, B., and Hausser, M. (2013). Targeting neurons and photons for optogenetics. Nat Neurosci *16*, 805-815.

[231] Padamsey, Z., McGuinness, L., Bardo, S.J., Reinhart, M., Tong, R., Hedegaard, A., Hart, M.L., and Emptage, N.J. (2017a). Activity-Dependent Exocytosis of Lysosomes Regulates the Structural Plasticity of Dendritic Spines. Neuron *93*, 132-146.

[232] Padamsey, Z., Tong, R., and Emptage, N. (2017b). Glutamate is required for depression but not potentiation of long-term presynaptic function. Elife *6*.

[233] Palmer, L.M., Schulz, J.M., Murphy, S.C., Ledergerber, D., Murayama, M., and Larkum, M.E. (2012). The cellular basis of GABA(B)-mediated interhemispheric inhibition. Science *335*, 989-993.

[234] Patriarchi, T., Cho, J.R., Merten, K., Howe, M.W., Marley, A., Xiong, W.H., Folk, R.W., Broussard, G.J., Liang, R., Jang, M.J.*, et al.* (2018). Ultrafast neuronal imaging of dopamine dynamics with designed genetically encoded sensors. Science *360*.

[235] Penn, A.C., Zhang, C.L., Georges, F., Royer, L., Breillat, C., Hosy, E., Petersen, J.D., Humeau, Y., and Choquet, D. (2017). Hippocampal LTP and contextual learning require surface diffusion of AMPA receptors. Nature *549*, 384-388.

[236] Perez-Alvarez, A., Fearey, B.C., O'Toole, R.J., Yang, W., Arganda-Carreras, I., Lamothe-Molina, P.J., Moeyaert, B., Mohr, M.A., Panzera, L.C., Schulze, C.*, et al.* (2020a). Freeze-frame imaging of synaptic activity using SynTagMA. Nat Commun *11*, 2464.

[237] Perez-Alvarez, A., Yin, S., Schulze, C., Hammer, J.A., Wagner, W., and Oertner, T.G. (2020b). Endoplasmic reticulum visits highly active spines and prevents runaway potentiation of synapses. Nat Commun *11*, 5083.

[238] Perez-Garci, E., Gassmann, M., Bettler, B., and Larkum, M.E. (2006). The GABAB1b isoform mediates long-lasting inhibition of dendritic Ca2+ spikes in layer 5 somatosensory pyramidal neurons. Neuron *50*, 603-616.

[239] Perez-Garci, E., Larkum, M.E., and Nevian, T. (2013). Inhibition of dendritic Ca2+ spikes by GABAB receptors in cortical pyramidal neurons is mediated by a direct Gi/o-beta-subunit interaction with Cav1 channels. J Physiol *591*, 1599-1612.

[240] Petreanu, L., Huber, D., Sobczyk, A., and Svoboda, K. (2007). Channelrhodopsin-2-assisted circuit mapping of long-range callosal projections. Nat Neurosci *10*, 663-668.

[241] Petreanu, L., Mao, T., Sternson, S.M., and Svoboda, K. (2009). The subcellular organization of neocortical excitatory connections. Nature *457*, 1142-1145.

[242] Portera-Cailliau, C., Pan, D.T., and Yuste, R. (2003). Activity-regulated dynamic behavior of early dendritic protrusions: evidence for different types of dendritic filopodia. J Neurosci *23*, 7129-7142.

[243] Prakash, M., Murphy, J., St Laurent, R., Friedman, N., Crespo, E.L., Bjorefeldt, A., Pal, A., Bhagat, Y., Kauer, J.A., Shaner, N.C.*, et al.* (2022). Selective control of synaptically-connected circuit elements by all-optical synapses. Commun Biol *5*, 33.

[244] Pugh, J.R., and Jahr, C.E. (2011). Axonal GABAA receptors increase cerebellar granule cell excitability and synaptic activity. J Neurosci *31*, 565-574.

[245] Raimondo, J.V., Kay, L., Ellender, T.J., and Akerman, C.J. (2012). Optogenetic silencing strategies differ in their effects on inhibitory synaptic transmission. Nat Neurosci *15*, 1102-1104.

[246] Ravotto, L., Duffet, L., Zhou, X., Weber, B., and Patriarchi, T. (2020). A Bright and Colorful Future for G-Protein Coupled Receptor Sensors. Front Cell Neurosci *14*, 67.

[247] Roberts, T.F., Tschida, K.A., Klein, M.E., and Mooney, R. (2010). Rapid spine stabilization and synaptic enhancement at the onset of behavioural learning. Nature *463*, 948-952.

[248] Rochefort, N.L., and Konnerth, A. (2012). Dendritic spines: from structure to in vivo function. EMBO Rep *13*, 699-708.

[249] Rodgers, J., Bano-Otalora, B., Belle, M.D.C., Paul, S., Hughes, R., Wright, P., McDowell, R., Milosavljevic, N., Orlowska-Feuer, P., Martial, F.P.*, et al.* (2021). Using a bistable animal opsin for switchable and scalable optogenetic inhibition of neurons. EMBO Rep *22*, e51866.

[250] Roorda, R.D., Hohl, T.M., Toledo-Crow, R., and Miesenbock, G. (2004). Video-rate nonlinear microscopy of neuronal membrane dynamics with genetically encoded probes. J Neurophysiol *92*, 609-621.

[251] Roth, B.L. (2016). DREADDs for Neuroscientists. Neuron *89*, 683-694.

[252] Sabatini, B.L., Oertner, T.G., and Svoboda, K. (2002). The life cycle of Ca(2+) ions in dendritic spines. Neuron *33*, 439-452.

[253] Sabatini, B.L., and Regehr, W.G. (1996). Timing of neurotransmission at fast synapses in the mammalian brain. Nature *384*, 170-172.

[254] Sabatini, B.L., and Svoboda, K. (2000). Analysis of calcium channels in single spines using optical fluctuation analysis. Nature *408*, 589-593.

[255] Sabatini, B.L., and Tian, L. (2020). Imaging Neurotransmitter and Neuromodulator Dynamics In Vivo with Genetically Encoded Indicators. Neuron *108*, 17-32.

[256] Sahel, J.A., Boulanger-Scemama, E., Pagot, C., Arleo, A., Galluppi, F., Martel, J.N., Esposti, S.D., Delaux, A., de Saint Aubert, J.B., de Montleau, C.*, et al.* (2021). Partial recovery of visual function in a blind patient after optogenetic therapy. Nat Med *27*, 1223-1229.

[257] Sakaba, T., and Neher, E. (2003). Direct modulation of synaptic vesicle priming by GABA(B) receptor activation at a glutamatergic synapse. Nature *424*, 775-778.

[258] Sandoz, G., Lopez-Gonzalez, I., Stamboulian, S., Weiss, N., Arnoult, C., and De Waard, M. (2004). Repositioning of charged I-II loop amino acid residues within the electric field by beta subunit as a novel working hypothesis for the control of fast P/Q calcium channel inactivation. Eur J Neurosci *19*, 1759-1772.

[259] Sassone-Corsi, P. (2012). The cyclic AMP pathway. Cold Spring Harb Perspect Biol *4*.

[260] Scanziani, M., and Hausser, M. (2009). Electrophysiology in the age of light. Nature *461*, 930-939.

[261] Scheib, U., Broser, M., Constantin, O.M., Yang, S., Gao, S., Mukherjee, S., Stehfest, K., Nagel, G., Gee, C.E., and Hegemann, P. (2018). Rhodopsin-cyclases for photocontrol of cGMP/cAMP and 2.3 A structure of the adenylyl cyclase domain. Nat Commun *9*, 2046.

[262] Scheuss, V., Yasuda, R., Sobczyk, A., and Svoboda, K. (2006). Nonlinear [Ca2+] signaling in dendrites and spines caused by activity-dependent depression of Ca2+ extrusion. J Neurosci *26*, 8183-8194.

[263] Schiller, J., Major, G., Koester, H.J., and Schiller, Y. (2000). NMDA spikes in basal dendrites of cortical pyramidal neurons. Nature *404*, 285-289.

[264] Schneggenburger, R., and Neher, E. (2000). Intracellular calcium dependence of transmitter release rates at a fast central synapse. Nature *406*, 889-893.

[265] Schneggenburger, R., Zhou, Z., Konnerth, A., and Neher, E. (1993). Fractional contribution of calcium to the cation current through glutamate receptor channels. Neuron *11*, 133-143.

[266] Scholl, B., Thomas, C.I., Ryan, M.A., Kamasawa, N., and Fitzpatrick, D. (2021). Cortical response selectivity derives from strength in numbers of synapses. Nature *590*, 111-114.

[267] Scimemi, A., and Diamond, J.S. (2012). The number and organization of Ca2+ channels in the active zone shapes neurotransmitter release from Schaffer collateral synapses. J Neurosci *32*, 18157-18176.

[268] Sheffield, M.E.J., Adoff, M.D., and Dombeck, D.A. (2017). Increased Prevalence of Calcium Transients across the Dendritic Arbor during Place Field Formation. Neuron *96*, 490-504 e495.

[269] Shi, S.H., Hayashi, Y., Petralia, R.S., Zaman, S.H., Wenthold, R.J., Svoboda, K., and Malinow, R. (1999). Rapid spine delivery and redistribution of AMPA receptors after synaptic NMDA receptor activation. Science *284*, 1811-1816.

[270] Shichida, Y., and Matsuyama, T. (2009). Evolution of opsins and phototransduction. Philos Trans R Soc Lond B Biol Sci *364*, 2881-2895.

[271] Skeberdis, V.A., Chevaleyre, V., Lau, C.G., Goldberg, J.H., Pettit, D.L., Suadicani, S.O., Lin, Y., Bennett, M.V., Yuste, R., Castillo, P.E.*, et al.* (2006). Protein kinase A regulates calcium permeability of NMDA receptors. Nat Neurosci *9*, 501-510.

[272] Sobczyk, A., Scheuss, V., and Svoboda, K. (2005). NMDA receptor subunit-dependent [Ca2+] signaling in individual hippocampal dendritic spines. J Neurosci *25*, 6037-6046.

[273] Sobczyk, A., and Svoboda, K. (2007). Activity-dependent plasticity of the NMDA-receptor fractional Ca2+ current. Neuron *53*, 17-24.

[274] Stachniak, Tevye J., Ghosh, A., and Sternson, Scott M. (2014). Chemogenetic Synaptic Silencing of Neural Circuits Localizes a Hypothalamus→Midbrain Pathway for Feeding Behavior. Neuron *82*, 797-808.

[275] Stierl, M., Stumpf, P., Udwari, D., Gueta, R., Hagedorn, R., Losi, A., Gartner, W., Petereit, L., Efetova, M., Schwarzel, M.*, et al.* (2011). Light modulation of cellular cAMP by a small bacterial photoactivated adenylyl cyclase, bPAC, of the soil bacterium Beggiatoa. J Biol Chem *286*, 1181-1188.

[276] Sudhof, T.C. (2013). Neurotransmitter release: the last millisecond in the life of a synaptic vesicle. Neuron *80*, 675-690.

[277] Sun, F., Zeng, J., Jing, M., Zhou, J., Feng, J., Owen, S.F., Luo, Y., Li, F., Wang, H., Yamaguchi, T.*, et al.* (2018). A Genetically Encoded Fluorescent Sensor Enables Rapid and Specific Detection of Dopamine in Flies, Fish, and Mice. Cell *174*, 481-496 e419.

[278] Svoboda, K., Tank, D.W., and Denk, W. (1996). Direct measurement of coupling between dendritic spines and shafts. Science *272*, 716-719.

[279] Svoboda, K., and Yasuda, R. (2006). Principles of two-photon excitation microscopy and its applications to neuroscience. Neuron *50*, 823-839.

[280] Szabadics, J., Varga, C., Molnar, G., Olah, S., Barzo, P., and Tamas, G. (2006). Excitatory effect of GABAergic axo-axonic cells in cortical microcircuits. Science *311*, 233-235.

[281] Takahashi, N., Ebner, C., Sigl-Glockner, J., Moberg, S., Nierwetberg, S., and Larkum, M.E. (2020). Active dendritic currents gate descending cortical outputs in perception. Nat Neurosci.

[282] Takahashi, N., Kitamura, K., Matsuo, N., Mayford, M., Kano, M., Matsuki, N., and Ikegaya, Y. (2012). Locally synchronized synaptic inputs. Science *335*, 353-356.

[283] Takahashi, N., Oertner, T.G., Hegemann, P., and Larkum, M.E. (2016). Active cortical dendrites modulate perception. Science *354*, 1587-1590.

[284] Tanaka, J., Horiike, Y., Matsuzaki, M., Miyazaki, T., Ellis-Davies, G.C., and Kasai, H. (2008). Protein synthesis and neurotrophin-dependent structural plasticity of single dendritic spines. Science *319*, 1683-1687.

[285] Tang, A.H., Chen, H., Li, T.P., Metzbower, S.R., MacGillavry, H.D., and Blanpied, T.A. (2016). A trans-synaptic nanocolumn aligns neurotransmitter release to receptors. Nature *536*, 210-214.

[286] Tichy, A.M., Gerrard, E.J., Sexton, P.M., and Janovjak, H. (2019). Light-activated chimeric GPCRs: limitations and opportunities. Curr Opin Struct Biol *57*, 196-203.

[287] Tomita, S., Stein, V., Stocker, T.J., Nicoll, R.A., and Bredt, D.S. (2005). Bidirectional synaptic plasticity regulated by phosphorylation of stargazin-like TARPs. Neuron *45*, 269-277.

[288] Tong, R., Chater, T.E., Emptage, N.J., and Goda, Y. (2021). Heterosynaptic cross-talk of pre- and postsynaptic strengths along segments of dendrites. Cell Rep *34*, 108693.

[289] Toni, N., Buchs, P.A., Nikonenko, I., Bron, C.R., and Muller, D. (1999). LTP promotes formation of multiple spine synapses between a single axon terminal and a dendrite. Nature *402*, 421-425.

[290] Tonnesen, J., Katona, G., Rozsa, B., and Nagerl, U.V. (2014). Spine neck plasticity regulates compartmentalization of synapses. Nat Neurosci *17*, 678-685.

[291] Trachtenberg, J.T., Chen, B.E., Knott, G.W., Feng, G., Sanes, J.R., Welker, E., and Svoboda, K. (2002). Long-term in vivo imaging of experience-dependent synaptic plasticity in adult cortex. Nature *420*, 788-794.

[292] Tsukamoto, H., and Terakita, A. (2010). Diversity and functional properties of bistable pigments. Photochem Photobiol Sci *9*, 1435-1443.

[293] Turecek, R., and Trussell, L.O. (2001). Presynaptic glycine receptors enhance transmitter release at a mammalian central synapse. Nature *411*, 587-590.

[294] Van Harreveld, A., and Fifkova, E. (1975). Swelling of dendritic spines in the fascia dentata after stimulation of the perforant fibers as a mechanism of post-tetanic potentiation. Exp Neurol *49*, 736-749.

[295] Vierock, J., Rodriguez-Rozada, S., Dieter, A., Pieper, F., Sims, R., Tenedini, F., Bergs, A.C.F., Bendifallah, I., Zhou, F., Zeitzschel, N.*, et al.* (2021). BiPOLES is an optogenetic tool developed for bidirectional dual-color control of neurons. Nat Commun *12*, 4527.

[296] Villa, K.L., Berry, K.P., Subramanian, J., Cha, J.W., Oh, W.C., Kwon, H.B., Kubota, Y., So, P.T., and Nedivi, E. (2016). Inhibitory Synapses Are Repeatedly Assembled and Removed at Persistent Sites In Vivo. Neuron *89*, 756-769.

[297] Wan, J., Peng, W., Li, X., Qian, T., Song, K., Zeng, J., Deng, F., Hao, S., Feng, J., Zhang, P.*, et al.* (2021). A genetically encoded sensor for measuring serotonin dynamics. Nat Neurosci *24*, 746-752.

[298] Wang, H., Jing, M., and Li, Y. (2018). Lighting up the brain: genetically encoded fluorescent sensors for imaging neurotransmitters and neuromodulators. Curr Opin Neurobiol *50*, 171-178.

[299] Wang, X.B., Bozdagi, O., Nikitczuk, J.S., Zhai, Z.W., Zhou, Q., and Huntley, G.W. (2008). Extracellular proteolysis by matrix metalloproteinase-9 drives dendritic spine enlargement and long-term potentiation coordinately. Proc Natl Acad Sci U S A *105*, 19520-19525.

[300] Wang, Y., Toledo-Rodriguez, M., Gupta, A., Wu, C., Silberberg, G., Luo, J., and Markram, H. (2004). Anatomical, physiological and molecular properties of Martinotti cells in the somatosensory cortex of the juvenile rat. J Physiol *561*, 65-90.

[301] Ward, B., McGuinness, L., Akerman, C.J., Fine, A., Bliss, T.V., and Emptage, N.J. (2006). State-dependent mechanisms of LTP expression revealed by optical quantal analysis. Neuron *52*, 649-661.

[302] Watanabe, K., Al-Bassam, S., Miyazaki, Y., Wandless, T.J., Webster, P., and Arnold, D.B. (2012). Networks of polarized actin filaments in the axon initial segment provide a mechanism for sorting axonal and dendritic proteins. Cell Rep *2*, 1546-1553.

[303] Weber, J.P., Andrasfalvy, B.K., Polito, M., Mago, A., Ujfalussy, B.B., and Makara, J.K. (2016). Location-dependent synaptic plasticity rules by dendritic spine cooperativity. Nat Commun *7*, 11380.

[304] Wiegert, J.S., Mahn, M., Prigge, M., Printz, Y., and Yizhar, O. (2017). Silencing Neurons: Tools, Applications, and Experimental Constraints. Neuron *95*, 504-529.

[305] Wiegert, J.S., and Oertner, T.G. (2013). Long-term depression triggers the selective elimination of weakly integrated synapses. Proc Natl Acad Sci U S A *110*, E4510-4519.

[306] Wiegert, J.S., and Oertner, T.G. (2016). How (not) to silence long-range projections with light. Nat Neurosci *19*, 527-528.

[307] Wiegert, J.S., Pulin, M., Gee, C.E., and Oertner, T.G. (2018). The fate of hippocampal synapses depends on the sequence of plasticity-inducing events. Elife *7*.

[308] Wietek, J., Wiegert, J.S., Adeishvili, N., Schneider, F., Watanabe, H., Tsunoda, S.P., Vogt, A., Elstner, M., Oertner, T.G., and Hegemann, P. (2014). Conversion of channelrhodopsin into a light-gated chloride channel. Science *344*, 409-412.

[309] Wilson, D.E., Whitney, D.E., Scholl, B., and Fitzpatrick, D. (2016). Orientation selectivity and the functional clustering of synaptic inputs in primary visual cortex. Nat Neurosci *19*, 1003-1009.

[310] Won, J., Pankratov, Y., Jang, M.W., Kim, S., Ju, Y.H., Lee, S., Lee, S.E., Kim, A., Park, S., Lee, C.J.*, et al.* (2021). Opto-vTrap, an optogenetic trap for reversible inhibition of vesicular release, synaptic transmission, and behavior. Neuron.

[311] Wu, D., Bacaj, T., Morishita, W., Goswami, D., Arendt, K.L., Xu, W., Chen, L., Malenka, R.C., and Sudhof, T.C. (2017). Postsynaptic synaptotagmins mediate AMPA receptor exocytosis during LTP. Nature *544*, 316-321.

[312] Wu, L.G., and Saggau, P. (1995). GABAB receptor-mediated presynaptic inhibition in guinea-pig hippocampus is caused by reduction of presynaptic Ca2+ influx. J Physiol *485 (Pt 3)*, 649-657.

[313] Wu, L.G., and Saggau, P. (1997). Presynaptic inhibition of elicited neurotransmitter release. Trends Neurosci *20*, 204-212.

[314] Xu, T., Yu, X., Perlik, A.J., Tobin, W.F., Zweig, J.A., Tennant, K., Jones, T., and Zuo, Y. (2009). Rapid formation and selective stabilization of synapses for enduring motor memories. Nature *462*, 915-919.

[315] Yang, G., Pan, F., and Gan, W.B. (2009). Stably maintained dendritic spines are associated with lifelong memories. Nature *462*, 920-924.

[316] Yang, S., Constantin, O.M., Sachidanandan, D., Hofmann, H., Kunz, T.C., Kozjak-Pavlovic, V., Oertner, T.G., Nagel, G., Kittel, R.J., Gee, C.E.*, et al.* (2021). PACmn for improved optogenetic control of intracellular cAMP. BMC Biol *19*, 227.

[317] Yang, Y., Wang, X.B., Frerking, M., and Zhou, Q. (2008). Spine expansion and stabilization associated with long-term potentiation. J Neurosci *28*, 5740-5751.

[318] Yasuda, M., Johnson-Venkatesh, E.M., Zhang, H., Parent, J.M., Sutton, M.A., and Umemori, H. (2011). Multiple forms of activity-dependent competition refine hippocampal circuits in vivo. Neuron *70*, 1128-1142.

[319] Yasuda, M., Nagappan-Chettiar, S., Johnson-Venkatesh, E.M., and Umemori, H. (2021). An activity-dependent determinant of synapse elimination in the mammalian brain. Neuron *109*, 1333-1349 e1336.

[320] Yasuda, R. (2017). Biophysics of Biochemical Signaling in Dendritic Spines: Implications in Synaptic Plasticity. Biophys J *113*, 2152-2159.

[321] Yasuda, R., Sabatini, B.L., and Svoboda, K. (2003). Plasticity of calcium channels in dendritic spines. Nat Neurosci *6*, 948-955.

[322] Yizhar, O., Fenno, L., Zhang, F., Hegemann, P., and Diesseroth, K. (2011a). Microbial opsins: a family of single-component tools for optical control of neural activity. Cold Spring Harb Protoc *2011*, top102.

[323] Yizhar, O., Fenno, L.E., Davidson, T.J., Mogri, M., and Deisseroth, K. (2011b). Optogenetics in neural systems. Neuron *71*, 9-34.

[324] Yuste, R. (2015). The discovery of dendritic spines by Cajal. Front Neuroanat *9*, 18.

[325] Yuste, R., and Denk, W. (1995). Dendritic spines as basic functional units of neuronal integration. Nature *375*, 682-684.

[326] Yuste, R., Majewska, A., Cash, S.S., and Denk, W. (1999). Mechanisms of calcium influx into hippocampal spines: heterogeneity among spines, coincidence detection by NMDA receptors, and optical quantal analysis. J Neurosci *19*, 1976-1987.

[327] Zamponi, G.W., and Currie, K.P. (2013). Regulation of Ca(V)2 calcium channels by G protein coupled receptors. Biochim Biophys Acta *1828*, 1629-1643.

[328] Zhang, F., Vierock, J., Yizhar, O., Fenno, L.E., Tsunoda, S., Kianianmomeni, A., Prigge, M., Berndt, A., Cushman, J., Polle, J.*, et al.* (2011). The microbial opsin family of optogenetic tools. Cell *147*, 1446-1457.

[329] Zhang, F., Wang, L.P., Brauner, M., Liewald, J.F., Kay, K., Watzke, N., Wood, P.G., Bamberg, E., Nagel, G., Gottschalk, A.*, et al.* (2007). Multimodal fast optical interrogation of neural circuitry. Nature *446*, 633-639.

[330] Zhang, Y.P., and Oertner, T.G. (2007). Optical induction of synaptic plasticity using a light-sensitive channel. Nat Methods *4*, 139-141.

[331] Zhao, S., Ting, J.T., Atallah, H.E., Qiu, L., Tan, J., Gloss, B., Augustine, G.J., Deisseroth, K., Luo, M., Graybiel, A.M.*, et al.* (2011). Cell type-specific channelrhodopsin-2 transgenic mice for optogenetic dissection of neural circuitry function. Nat Methods *8*, 745-752.

[332] Zhou, Q., Homma, K.J., and Poo, M.M. (2004). Shrinkage of dendritic spines associated with long-term depression of hippocampal synapses. Neuron *44*, 749-757.

[333] Zhu, H., and Roth, B.L. (2014). Silencing synapses with DREADDs. Neuron *82*, 723-725.

[334] Zucker, R.S. (1999). Calcium- and activity-dependent synaptic plasticity. Curr Opin Neurobiol *9*, 305-313.

[335] Zuo, Y., Lin, A., Chang, P., and Gan, W.B. (2005). Development of long-term dendritic spine stability in diverse regions of cerebral cortex. Neuron *46*, 181-189.

[336] Zurawski, Z., Yim, Y.Y., Alford, S., and Hamm, H.E. (2019). The expanding roles and mechanisms of G protein-mediated presynaptic inhibition. J Biol Chem *294*, 1661-1670.

7 Reprints of publications

Publication I

Wiegert J. S., **Pulin M.**, Gee C. E., Oertner T. G. (2018). The fate of hippocampal synapses depends on the sequence of plasticity-inducing events. *eLife* 2018;7:e39151

Publication II

Mahn M.*, Saraf-Sinik I.*, Pritish P.*, **Pulin M.***, Bitton E., Karalis N., Bruentgens F., Palgi S., Gat A., Dine J., Wietek J., Davidi I., Levy R., Litvin A., Zhou F., Sauter K., Soba P., Schmitz D., Lüthi A., Rost R. B., Wiegert J. S., Yizhar O. (2021). Efficient optogenetic silencing of neurotransmitter release with a mosquito rhodopsin. *Neuron* 109(10):1621-1635.e8

*These authors have equally contributed to this work

Publication III

Pulin M., Stockhausen K. E., Masseck O. A., Kubitschke M., Busse B., Wiegert, J. S., Oertner T. G. (2022). Orthogonally-polarized excitation for improved two-photon and second-harmonic-generation microscopy, applied to neurotransmitter imaging with GPCR-based sensors. *Biomedical Optics Express* 13(2) 777-790

The fate of hippocampal synapses depends on the sequence of plasticity-inducing events

J Simon Wiegert[1,2], Mauro Pulin[1,2], Christine Elizabeth Gee[1], Thomas G Oertner[1]*

[1]Institute for Synaptic Physiology, Center for Molecular Neurobiology Hamburg, University Medical Center Hamburg-Eppendorf, Hamburg, Germany; [2]Research Group Synaptic Wiring and Information Processing, Center for Molecular Neurobiology Hamburg, University Medical Center Hamburg-Eppendorf, Hamburg, Germany

Abstract Synapses change their strength in response to specific activity patterns. This functional plasticity is assumed to be the brain's primary mechanism for information storage. We used optogenetic stimulation of rat hippocampal slice cultures to induce long-term potentiation (LTP), long-term depression (LTD), or both forms of plasticity in sequence. Two-photon imaging of spine calcium signals allowed us to identify stimulated synapses and to follow their fate for the next 7 days. We found that plasticity-inducing protocols affected the synapse's chance for survival: LTP increased synaptic stability, LTD destabilized synapses, and the effect of the last stimulation protocol was dominant over earlier stimulations. Interestingly, most potentiated synapses were resistant to depression-inducing protocols delivered 24 hr later. Our findings suggest that activity-dependent changes in the transmission strength of individual synapses are transient, but have long-lasting consequences for synaptic lifetime.

DOI: https://doi.org/10.7554/eLife.39151.001

*For correspondence:
thomas.oertner@zmnh.uni-hamburg.de

Introduction

Graded changes in synaptic strength, driven by specific activity patterns, are a candidate mechanism for information storage in the brain (*Chaudhuri and Fiete, 2016*). When entire pathways are potentiated by high frequency stimulation, the increase in synaptic coupling can indeed be recorded for several days (*Bliss and Lomo, 1973*). Increases in the size of synapses, the number of postsynaptic transmitter receptors and release of transmitter, have been shown to underlie increases in synaptic strength. A prevailing theory is that graded changes in synaptic strength persist as a memory trace of former activity. At the level of individual synapses, however, dramatic fluctuations in spine volume over time scales of hours to days cast doubt on whether information can be stored for long periods in the analog strength of synapses (*Holtmaat and Caroni, 2016*; *Berry and Nedivi, 2017*). An alternative hypothesis is that over longer time periods, information is stored not in the strength but in the number of connections, which, at the level of individual synapses, would manifest as a change in synaptic lifetime. Supporting evidence comes from the findings that long term depression (LTD) decreases synaptic lifetime (*Nägerl et al., 2004*; *Bastrikova et al., 2008*; *Wiegert and Oertner, 2013*) and that spine structure becomes stabilized and growth persists up to 3 days after induction of long term potentiation (LTP) (*De Roo et al., 2008*; *Hill and Zito, 2013*).

An important consideration is that new information, manifest as changing patterns of activity, constantly arrives at synapses. For example, LTP can be reversed by low-frequency stimulation (LFS), but such depotentiation may only occur 1–2 hr after LTP induction (*Fujii et al., 1991*; *O'Dell and Kandel, 1994*; *Abraham and Huggett, 1997*; *Zhou et al., 2004*). How a once potentiated synapse

responds to LFS one day later is therefore difficult to predict. Our goals were to monitor the fate of individual spine synapses after induction of LTP and to explore how sequential plasticity-inducing events affect synaptic lifetime. Using organotypic hippocampal slice cultures and optical stimulation of channelrhodopsin-expressing CA3 pyramidal neurons, we found that Schaffer collateral synapses were potentiated by 5 Hz stimulation if complex spike bursts were induced in the postsynaptic CA1 neuron (*Thomas et al., 1998*). We based our assessment of synaptic strength changes on the amplitude and probability of spine calcium transients (EPSCaTs). During successful synaptic transmission, Ca^{2+} ions enter the spine through voltage-gated calcium cannels and NMDA receptors which both have a steep dependence on membrane depolarization. Thus, EPSCaTs depend on AMPA receptor activity (*Holbro et al., 2010*) and can be used to detect changes in synaptic strength (*Emptage et al., 2003*). Compared to glutamate uncaging experiments, which only report changes in postsynaptic strength (potency), optogenetic interrogation is also sensitive to presynaptic changes (release probability), providing a more complete picture of synaptic transmission. We then followed the fate of stimulated spine synapses and their neighbors over 7 days.

As suggested by previous studies, LTD and LTP differentially affected synaptic lifetime. However, sequentially inducing LTD and LTP did not return spines to their basal state, but resulted in reduced elimination rates similar to synapses which only underwent LTP. Once LTP was induced, it became almost impossible to induce subsequent LTD. In the few experiments were LTD could be induced 24 hr after LTP, synaptic lifetime was similar to that of spines that only underwent LTD. Thus, multiple weight adjustments are not summed in a linear fashion, but the most recent plasticity event determines the lifetime of a Schaffer collateral synapse.

Results

Optical theta frequency stimulation induced LTP at Schaffer collateral synapses

CA3 neurons expressing the light-sensitive channel ChR2(E123T/T159C) (*Berndt et al., 2011*) together with the presynaptic vesicle marker synaptophysin-tdimer2 were stimulated with short pulses of blue light (2 ms long, 40 ms interval, λ = 470 nm). Paired pulses were used to reduce the number of trials necessary to detect responding spines and to be consistent with our previous study (*Wiegert and Oertner, 2013*). On CA1 pyramidal cells expressing GCaMP6s and mCerulean, active spines were identified by imaging stimulation-induced excitatory postsynaptic calcium transients (EPSCaTs). After an active spine was identified we switched to line scanning mode, defining a scan curve that intersected the responding spine and a small number of neighboring spines at high speed (500 Hz, *Figure 1A*). Calcium transients were restricted to the responding spine and were not detected in the dendrite. To provide an additional read-out of synaptic strength on the population level, a neighboring CA1 cell ('reporter neuron') was patch-clamped to record excitatory postsynaptic synaptic currents (EPSCs) before, during, and after plasticity induction. Light stimulation evoked EPSCs with a magnitude of 1330 ± 220 pA, consistent with our previous study (*Wiegert and Oertner, 2013*). To induce LTP, we stimulated CA3 pyramidal cells with 150 light pulses at 5 Hz, a theta-frequency stimulation (TFS) paradigm, which potentiates CA3-CA1 but not CA3-CA3 synapses in an NMDAR-dependent fashion (*Moody et al., 1998*; *Thomas et al., 1998*). TFS-induced LTP requires transient (30 s) stimulation of enough CA3 cells to drive postsynaptic CA1 cells to fire complex spike bursts (CSBs, *Figure 1—figure supplement 1*) (*Thomas et al., 1998*). To facilitate LTP induction, ACSF with reduced divalent ion concentration (2 mM $CaCl_2$, 1 mM $MgCl_2$) was used to increase excitability. We adjusted the stimulation light intensity to recruit more and more CA3 neurons until the synaptic drive was just below the action potential threshold in the CA1 reporter neuron. During optogenetic theta-frequency stimulation (oTFS), the reporter neuron responses changed from mostly subthreshold EPSPs with occasional single action potentials to CSBs (*Figure 1C*, *Figure 1—figure supplement 1*) (*Losonczy and Magee, 2006*). CSBs in the reporter neuron were time-locked with large calcium transients in the stretch of dendrite adjacent to the postsynaptic spine (*Figure 1B*, middle column), suggesting that synchronized CSBs were occurring in neighboring neurons. EPSCaTs were strongly potentiated 30 min after oTFS, generating calcium transients that frequently spread into the dendrite (*Figure 1B*, *Figure 2B*). Likewise, the amplitude of EPSCs in the reporter neuron increased after oTFS, indicating successful induction of LTP (*Figure 1B*, *Figure 2A*). Both
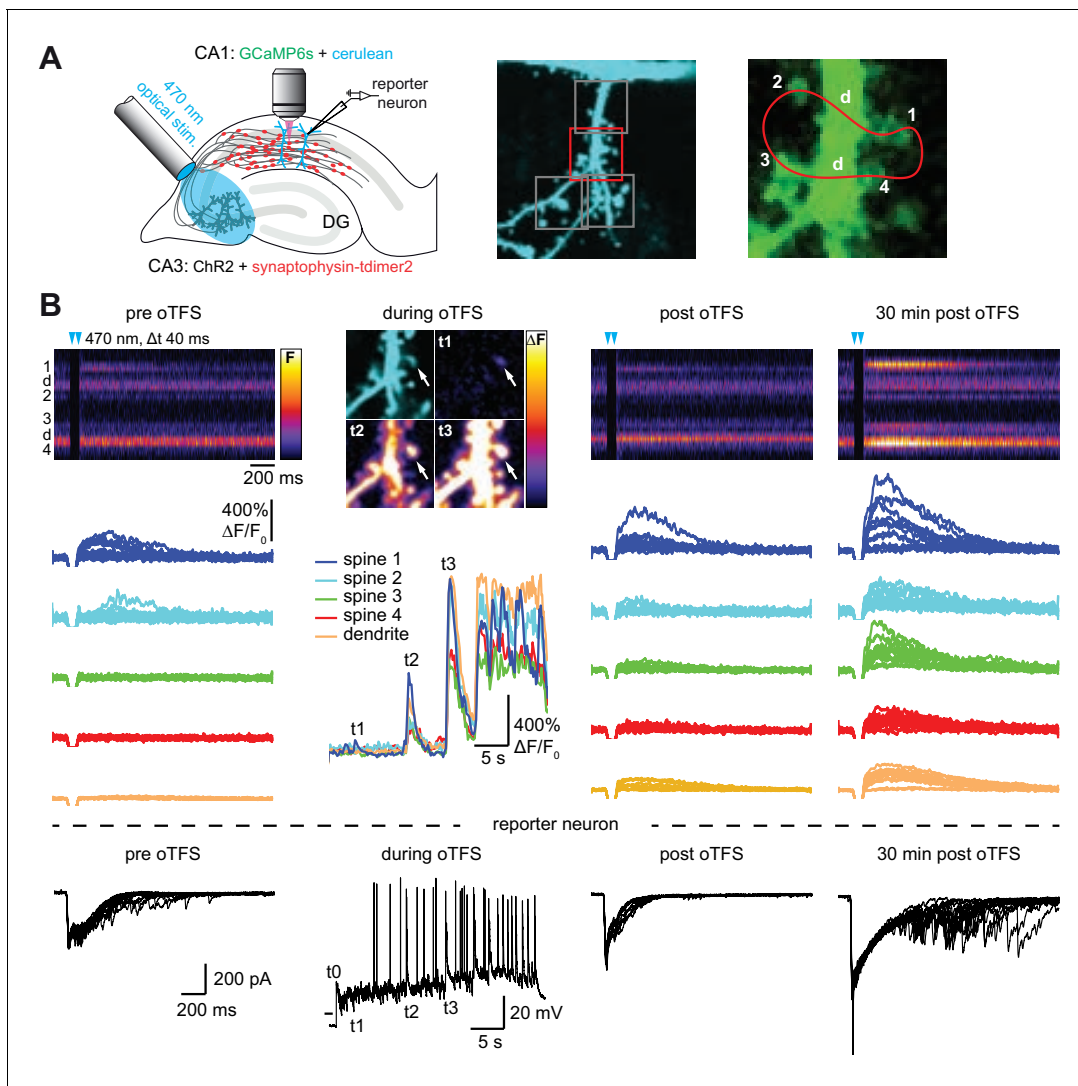
Figure 1. with two supplements: Channelrhodopsin-driven theta-frequency stimulation induces LTP. (**A**) Left: A fiber-coupled LED (λ = 470 nm) was used to locally stimulate ChR2-expressing CA3 neurons. Spines on GCaMP6s/mCerulean-expressing CA1 pyramidal cells were imaged with two-photon microscopy. For parallel electrical recordings, a second CA1 neuron was patch-clamped (reporter neuron). Middle: oblique dendrite branching off the apical trunk filled with mCerulean. Detection of active spines was done with GCaMP6s during presynaptic optogenetic stimulation. Stimulation-induced fluorescence changes (ΔF) of GCaMP6s were analyzed in fast frame scans (squares) of oblique dendrites until a responsive spine was detected (red square). Right: Magnified view of GCaMP6s fluorescence in the dendritic section harboring an activated spine. The laser was scanned in a user-defined trajectory across multiple spines and the parental dendrite during Ca^{2+} imaging (red curve). (**B**) Fluorescence signal across time from arbitrary line scan on dendrite shown in A during ChR2-stimulation before ('pre oTFS'), immediately ('post oTFS') and 30 min ('30 min post oTFS') after optical theta-frequency stimulation (oTFS). Temporally matched traces from multiple trials and electrophysiological recording from a reporter neuron are shown below. During oTFS the Ca^{2+} response was recorded in frame scan mode ('during oTFS'). The GCaMP6s-signal (ΔF) is shown for three selected time points during oTFS. GCaMP6s-traces from the same spines and dendrite imaged in line scans are shown below together with the corresponding electrophysiological recording in voltage clamp mode from the reporter neuron.

DOI: https://doi.org/10.7554/eLife.39151.002

The following figure supplements are available for figure 1:

Figure supplement 1. Examples of optogenetic TFS experiments.
DOI: https://doi.org/10.7554/eLife.39151.003

Figure supplement 2. Analysis of imaging and electrophysiology data.
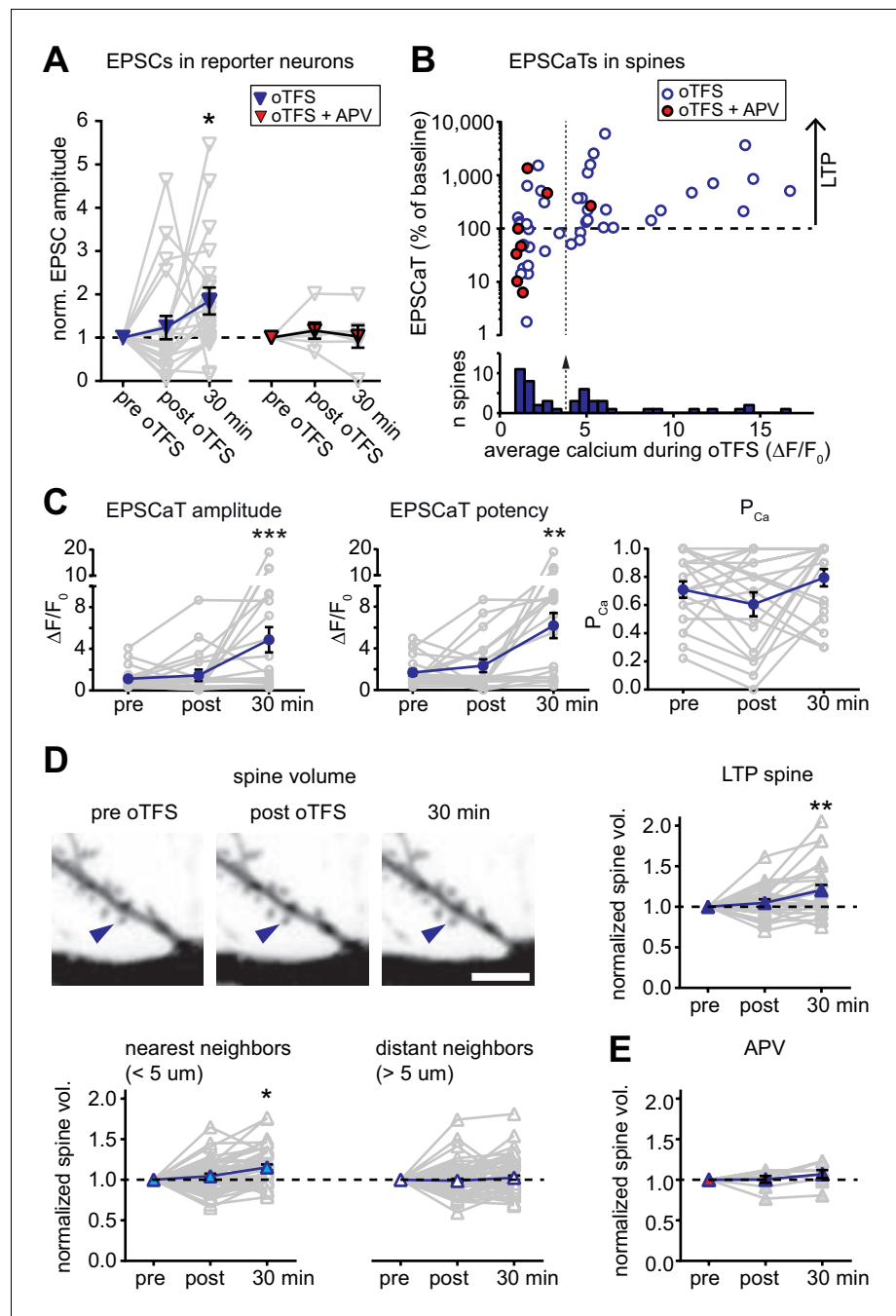DOI: https://doi.org/10.7554/eLife.39151.004

Figure 2. with two supplements: Characterization of oTFS-induced LTP. (**A**) Changes in excitatory postsynaptic current (EPSC) amplitude in reporter neurons immediately after and 30 min after oTFS in the absence (left) or presence (right) of the NMDA receptor antagonist APV during oTFS. EPSCs were significantly increased after 30 min (p=0.012, n = 20 slice cultures). The increase was blocked by APV (p=0.69, n = 6 slice cultures). (**B**) Relative change of average excitatory Ca^{2+} transients (EPCaTs) in individual spines 30 min after the oTFS protocol plotted against the average spine Ca^{2+} during oTFS. In experiments indicated by filled red circles, APV was present during oTFS. (**C**) EPSCaT amplitude (p=0.0008, n = 20 slice cultures) and EPSCaT potency (successes only, p=0.0025) but not EPSCaT probability (P_{Ca}, p>0.05) were increased 30 min after oTFS in experiments where complex spike bursts (CSBs) were induced during oTFS. (**D**) Maximum intensity projections of mCerulean fluorescence in dendritic segment harboring a responding spine that was successfully potentiated (blue arrowhead). Volume of oTFS spines (p=0.002, n = 26 spines) and nearest (p=0.0001, n = 45 spines) but not distant neighbors (p=0.83, n = 58 spines) was increased 30 min after oTFS in experiments where CSBs were induced during oTFS. (**E**) Spine volume was not increased when NMDA receptors were blocked with APV during oTFS (p>0.05, n = 7 spines).

Figure 2 continued on next page

Figure 2 continued

The following source data and figure supplements are available for figure 2:

Source data 1. Theta-frequency stimulation experiments.
Figure supplement 1. Analysis of oTFS experiments where no dendritic calcium spikes were observed during the induction protocol.
Figure supplement 2. Analysis of control experiments where no oTFS was applied to responding spines.

CSBs and LTP induction were blocked in the presence of the NMDA receptor antagonist APV (*Figure 2A and B*). Thus, oTFS induced plasticity via NMDAR activation as previously demonstrated (*Thomas et al., 1998*). In some experiments, CSBs and large dendritic calcium transients did not occur during oTFS, likely due to insufficient numbers of virus-transfected CA3 pyramidal neurons. When no large dendritic calcium transients were triggered during oTFS, spine calcium signals were not consistently potentiated 30 min after oTFS (*Figure 2B*, *Figure 2—figure supplement 1A and B*). To estimate changes in EPSCaT and EPSC amplitude, 10–20 successive traces before and after stimulation were analyzed and averaged (*Figure 1—figure supplement 2*). EPSCs, integrating the activity of many synapses, showed considerably lower trial-to-trial variability (no failures) compared to EPSCaTs.

Taking into consideration only those experiments in which CSBs and dendritic calcium transients were evoked during oTFS, we observed that neither the amplitude nor the potency (amplitude of successes) of EPSCaTs changed immediately after oTFS. Thirty minutes later, however, both were significantly increased (*Figure 2C*), whereas spines that did not experience oTFS showed no change in EPSCaTs over time (*Figure 2—figure supplement 2*). The slowly developing potentiation was also reflected in the EPSCs recorded in the reporter neuron (*Figure 2A*), consistent with previous reports (*Moody et al., 1998*; *Thomas et al., 1998*). LTP had no significant effect on the probability of EPSCaT occurrence (P_{Ca}, *Figure 2C*), suggesting that the potentiation was mainly due to postsynaptic changes. Interestingly, while EPSCaT potency was not affected in experiments where no CSBs were elicited during oTFS, P_{Ca} was significantly reduced (*Figure 2—figure supplement 1C*). Thus, in experiments where the synaptic drive was not strong enough to trigger postsynaptic spikes, presynaptic activity in the theta frequency range appeared to elicit a weak form of presynaptic depression. No such reduction in P_{Ca} was seen when no oTFS was applied (*Figure 2—figure supplement 2*).

Optogenetic TFS-induced synaptic potentiation was accompanied by slow changes in spine structure (mCerulean, *Figure 2D*). The head volume of spines that experienced CSBs was unchanged immediately after oTFS, but increased by 21 ± 6% during the next 30 min. The nearest neighboring spines also showed a small but significant increase in volume (15 ± 3%), whereas no consistent change was detected at more distant spines (2 ± 3%). When no oTFS was applied, the volume of responding spines (5 ± 4%) and neighbors (−4 ± 3%) remained stable (*Figure 2—figure supplement 2*). In oTFS experiments that failed to elicit CSBs or when NMDA receptors were blocked during oTFS, stimulated spines did not exhibit significant volume changes (*Figure 2E*; *Figure 2—figure supplement 1D*), suggesting similar requirements for the successful induction of functional and structural plasticity. As our functional assessment was limited to the few spines that were synaptically connected to ChR2-expressing CA3 neurons, we could not test whether neighboring enlarged spines were also functionally potentiated.

Synaptic properties 24 hr after LTP

We next asked whether synaptic potentiation was maintained during the 24 hr following oTFS. Consistent with our first data set, spine head volume and EPSCaT potency were significantly increased 30 min after oTFS (*Figure 3A and B*). Twenty-four hours after LTP induction, however, both measures had returned to baseline. We detected no significant change in EPSCaT probability either 30 min or 24 hr after oTFS (*Figure 3C*). Thus, beyond the acute effects on the day of potentiation, we did not observe permanent changes in synaptic strength after oTFS-induced LTP.
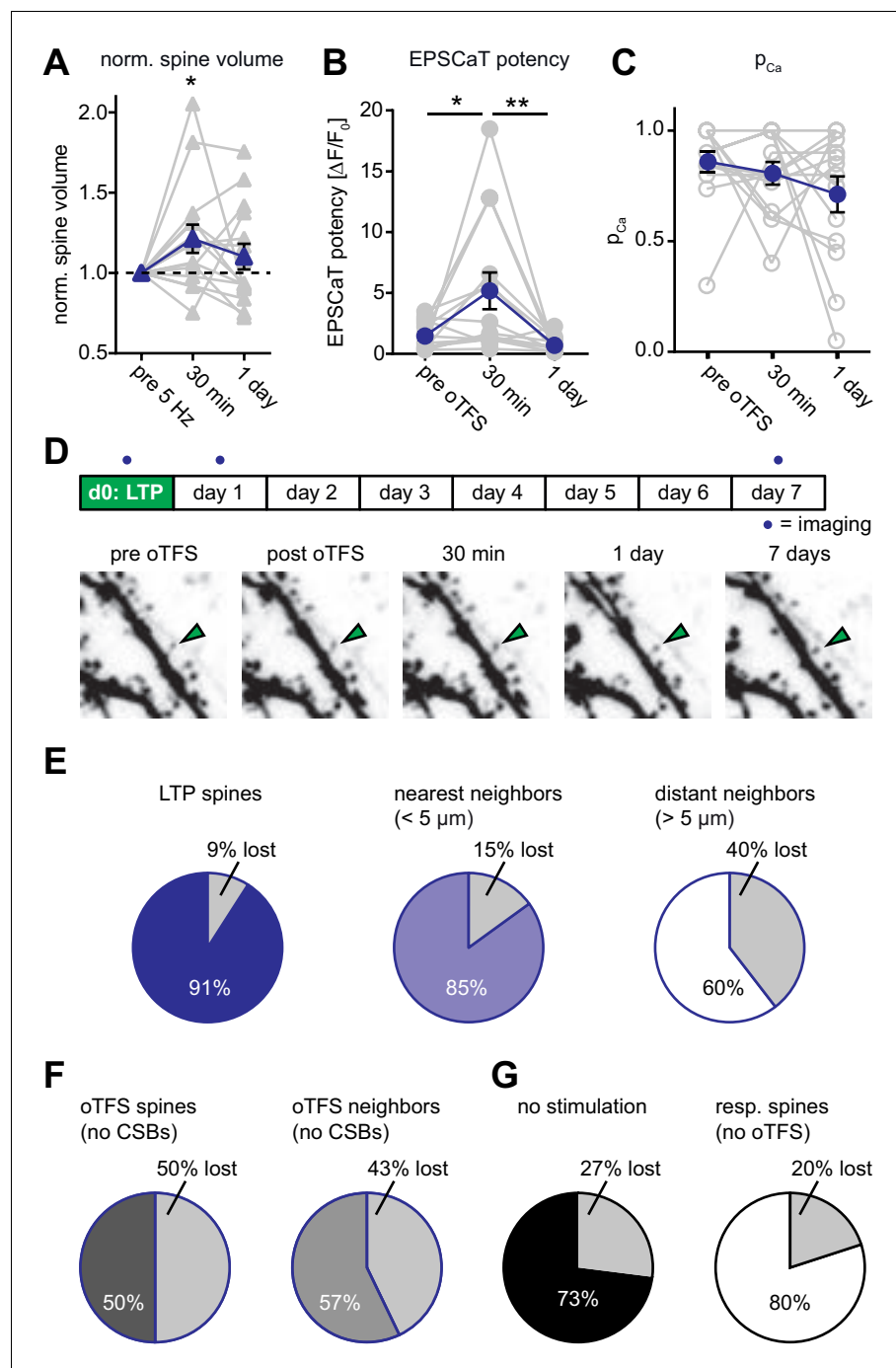
Figure 3. Long-term outcome of oTFS-induced LTP. (**A**) Analysis of volume changes of oTFS spines 30 min and 24 hr after oTFS. The volume increase 30 min after oTFS (p=0.03, n = 15 slice cultures) was not maintained 24 hr later (p=0.42). (**B**) Analysis of EPSCaT potency before, 30 min and 24 hr after oTFS. The increased potency 30 min after oTFS (p=0.015, n = 14 slice cultures) has significantly decreased again 24 hr later (p=0.005) and was similar to the condition before oTFS (p=0.55). (**C**) EPSCaT probability (P_{Ca}) did not change 30 min and 24 hr after oTFS (p=0.32, n = 14 slice cultures). For details on the statistical tests, please refer to the Materials and Methods section. (**D**) Long-term survival analysis after LTP. Spines were imaged at d0, d1 and d7. Maximum intensity projections of mCerulean fluorescence in dendritic segment harboring a responding spine that was successfully potentiated (green arrowhead). (**E**) Spine survival 7 days after successful LTP induction on day 0. Surviving fractions are shown for responding spines, nearest and distant neighbors. (**F**) Spine survival 7 days after oTFS in experiments where no complex spike bursts were induced. Directly stimulated spines and their neighbors were analyzed separately. (**G**)

Figure 3 continued on next page

Figure 3 continued

Spine survival over 7 days under baseline conditions without any optical stimulation (black) and in spines responsive to optical test pulses (resp. spines, white) which were not exposed to plasticity-inducing protocols.

DOI: https://doi.org/10.7554/eLife.39151.009

The following source data is available for figure 3:

Source data 1. Theta-frequency stimulation: Spine volume changes.

DOI: https://doi.org/10.7554/eLife.39151.010

Effect of long-term potentiation on synaptic lifetime

Next, we determined whether oTFS-induced LTP affected synaptic lifetime. Previous work showed that potentiated spines are not characterized by permanently enlarged heads, but are less likely to be eliminated during the next 3 days (*De Roo et al., 2008*). We therefore assessed the stability of potentiated spines and their neighbors during the following week. Under control conditions without external stimulation, 27% of all spines disappeared between days 1 and 7. This turnover rate is in agreement with previous measurements in hippocampal slice cultures (*Wiegert and Oertner, 2013*) and mouse hippocampus in vivo (*Attardo et al., 2015*). LTP induced by oTFS appeared to increase synaptic lifetime. In a dataset of 14 spines, 11 spines experienced CSBs and were potentiated. During the following 7 days, only one of these 11 potentiated spines disappeared (*Figure 3D and E*). The stability of spines next to the potentiated spine was also affected, mirroring the transient head volume increase on day 0 (*Figures 2D* and *3A*). Compared to controls, nearest-neighbor spines disappeared less often between days 1 and 7 whereas more distant spines (>5 μm) were eliminated more often (*Figure 3E*). These findings are consistent with the concept of biochemical signaling molecules activated inside stimulated spines during oTFS and diffusing into neighboring, non-stimulated spines (*Nishiyama and Yasuda, 2015*), affecting acutely their size and on longer timer scales, their survival. As a control, we also analyzed oTFS experiments in which no CSBs were elicited in CA1 neurons. In these experiments, stimulated spines as well as their neighbors had reduced survival rates (*Figure 3F*). This destabilizing effect was contingent on 5 Hz presynaptic activation, as spines that were not stimulated at all or only stimulated by test pulses (responsive spines) had higher survival rates (*Figure 3G*).

Effects of sequential plasticity-inducing protocols on synaptic lifetime

As we established previously (*Wiegert and Oertner, 2013*), optogenetic low frequency stimulation (oLFS, 900 APs at 1 Hz) induced long-term depression (LTD) at Schaffer collateral synapses, frequently abolishing EPSCaTs in the stimulated spine altogether (*Figure 4A*). In agreement with our previous results, 45% of spines that received oLFS disappeared between days 1 and 7. We speculated that if we induced LTP 24 hr after LTD, the doomed spines could perhaps be stabilized (*Figure 4B*). LTD on day 0 was considered successful when the average spine Ca^{2+} response dropped to less than 90% of the baseline response 30 min after oLFS, which was the case in 70% (28/40) of the experiments (*Figure 4—figure supplement 1*). Twenty-four hours later, we recorded a new baseline, since EPSCaT amplitudes frequently changed from one day to the other. We then applied oTFS to the spines that were depressed on the previous day. LTP induction was considered successful when the average spine Ca^{2+} response increased to more than 110% of the day one baseline response after oTFS, which was the case in 64% (18/28) of all experiments on day 1 (*Figure 4C*). We also considered spines that did not experience CSBs to assess whether the oTFS protocol itself would affect synapse lifetime independently of successful LTP induction. Thus, we compared two groups: synapses that underwent LTD followed by LTP (45% of all tested synapses) and synapses that also experienced LTD and oTFS, but did not show any potentiation in response to oTFS (25% of all tested synapses). Synapses that did not display LTD after oLFS on day 0 (30% of all tested synapses) were not considered further. When LTP was induced after LTD, only 12% of spines disappeared between days 1 and 7, indicating stabilization of doomed synapses. Of the spines that received oTFS after LTD but did not get potentiated, 43% disappeared between days 1 and 7, similar to the 45% disappearance rate seen after oLFS only. These results confirmed that successful LTP induction was necessary to rescue synapses from elimination. Without LTP, the oTFS stimulation protocol by itself had no measurable effect on the survival of previously depressed synapses.
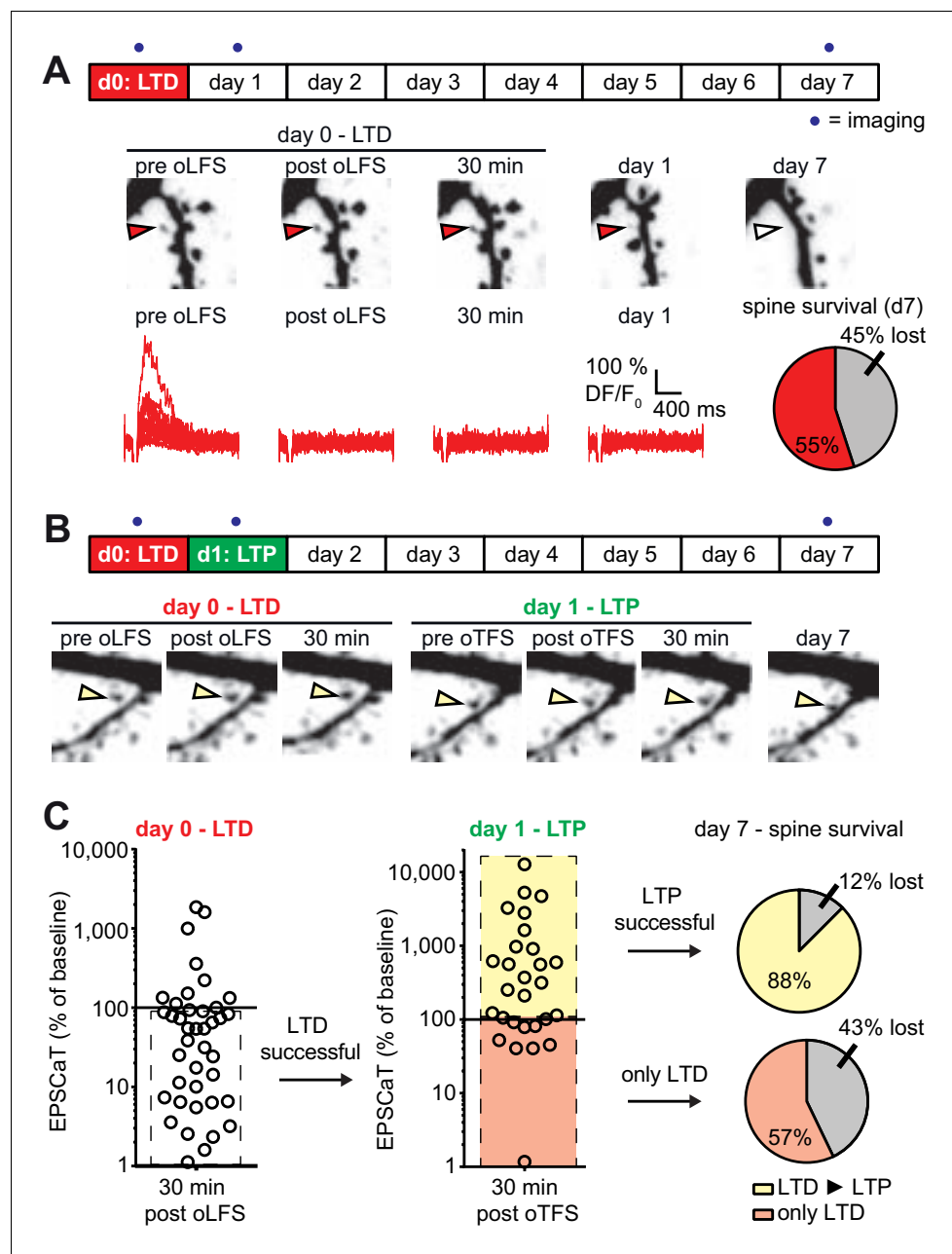
Figure 4. with one supplement: LTD-induced spine elimination is reversed by LTP or sustained synaptic transmission. (**A**) Long-term survival analysis after LTD. Spines were imaged at d0, d1 and d7. Below: Maximum intensity projections of mCerulean fluorescence in dendritic segment harboring a responding spine that was successfully depressed (red arrowhead). Open arrowhead on day seven indicates position of eliminated spine. Corresponding EPSCaT traces from indicated time points are shown in red. Pie chart shows quantification of spine survival after 7 days. (**B**) LTP 24 hr after LTD. Below: Dendritic segment harboring a responding spine that was successfully depressed on day 0 and potentiated on day 1 (yellow arrowhead). (**C**) Assessment of synaptic weight changes induced by oLFS on day 0 and oTFS on day 1. Dashed box in left graph indicates all experiments where LTD was successfully induced on day 0. Only these spines were considered in the LTP experiment on day 1 (middle). Yellow shaded box indicates all experiments where LTP was successfully induced on day 1 (after LTD on day 0; LTD ▶ LTP). Red shaded box indicates experiments where oTFS did not lead to LTP (only LTD). Pie charts show quantification of spine survival after 7 days for these two conditions.

DOI: https://doi.org/10.7554/eLife.39151.011

The following source data and figure supplement are available for figure 4:

Source data 1. Low-frequency stimulation followed by theta-freuqency stimulation.

Figure 4 continued on next page

We next tested whether the LTP-induced stabilization of spines would persist even if LTD was subsequently induced (*Figure 5A*). LTP on day 0 was induced in 72% (18/25) of spines after oTFS (*Figure 5B*, *Figure 5—figure supplement 1*), similar to the set of oTFS experiments 1 day after oLFS (64%, p=0.85) and the first set of oTFS experiments (*Figure 2B*, 62%, 26/42, p=0.41). Again, we considered only spines where LTP was successfully induced. When oLFS was applied 24 hr later, we observed that LTD was induced in only 33% (6/18) of previously potentiated synapses on the next day (*Figure 5B*), a much lower success rate than the 70% when oLFS was applied with no prior plasticity. Since we were concerned that the 1 Hz induction protocol could have become supra-threshold 24 hr after LTP, we counted the number of spikes generated in the reporter neuron during oLFS. The median number of APs in reporter neurons during the 900 pulses of the oLFS protocol was 1.5 in naive cultures (n = 32) and 5.0 one day after LTP (n = 13, p=0.4, Mann-Whitney), corresponding to a postsynaptic spike probability below 1% in both cases. Thus, strong postsynaptic spiking during the oLFS protocol is not a likely explanation for the difficulty to depress previously potentiated synapses. We also considered the possibility that some synapses were already in a depressed state and could therefore not be depressed further. However, the initial EPSCaT amplitude (before oLFS) was not a predictor of successful LTD induction (*Figure 5—figure supplement 1C*). These results point to a synapse-specific memory of past potentiation events that cannot be detected as increased spine volume, increased release probability or increased EPSCaT potency (see *Figure 3*).

In the few experiments where LTD was successfully induced 24 hr after LTP, 50% of spines disappeared by day 7 (*Figure 5B*). In the more typical case where oLFS failed to induce LTD, only 8% of spines disappeared by day 7. One explanation for the different survival rates could be that the absolute strength of the synapse before the oLFS protocol determined whether it survived, irrespective of the sign of plasticity on day 1 (i.e. the synapse has a memory of its strength and not of its plastic change). However, the strength of the synapse on day 0 or on day one did not predict its survival (*Figure 5—figure supplement 1D and E*), leaving successful induction of depression as the only risk factor we could identify. In summary, the stabilizing effect of LTP on spines can be overwritten by subsequent LTD (*Figure 5C*), but this sequence of plasticity events is not very likely to happen.

Discussion

In vitro studies of synaptic plasticity are most relevant if stimulation protocols resemble in vivo activity patterns. Theta burst stimulation (TBS, 100 Hz bursts repeated at 5 Hz) is a commonly used experimental protocol to induce LTP in vitro (*Abraham and Huggett, 1997*), but individual CA3 pyramidal cells do not spike at 100 Hz in vivo (*Mizuseki and Buzsáki, 2013*). During exploratory behavior, CA3 pyramidal cells fire single action potentials which are synchronized across the population by the activity of local interneurons. Here we show that LTP and spine-specific stabilization can be induced at 5 Hz, the typical carrier frequency of rodent hippocampus, if a sufficient number of inputs are activated synchronously (*Moody et al., 1998*; *Thomas et al., 1998*). We consider theta-frequency stimulation (TFS) the physiological equivalent of spike-timing-dependent potentiation (STDP) protocols, replacing the artificial current injection into the postsynaptic neuron by highly synchronized excitatory synaptic input. Synchronized synaptic input can trigger dendritic calcium spikes, local regenerative events caused by the opening of voltage-dependent channels (NMDARs and VDCCs). These events can be electrophysiogically identified as complex spike bursts, consisting of several fast sodium spikes on top of a broader depolarization mediated by dendritic calcium currents (*Magee and Johnston, 1997*; *Golding et al., 2002*; *Losonczy and Magee, 2006*; *Grienberger et al., 2014*). In our experiments, the occurrence of dendritic calcium spikes during the induction protocol was highly predictive of successful LTP induction at individual synapses (*Figure 2B*). Recent studies in head-fixed mice running on a treadmill suggest that theta-frequency-modulated synaptic input to CA1 pyramidal cells triggers dendritic calcium spikes which are required
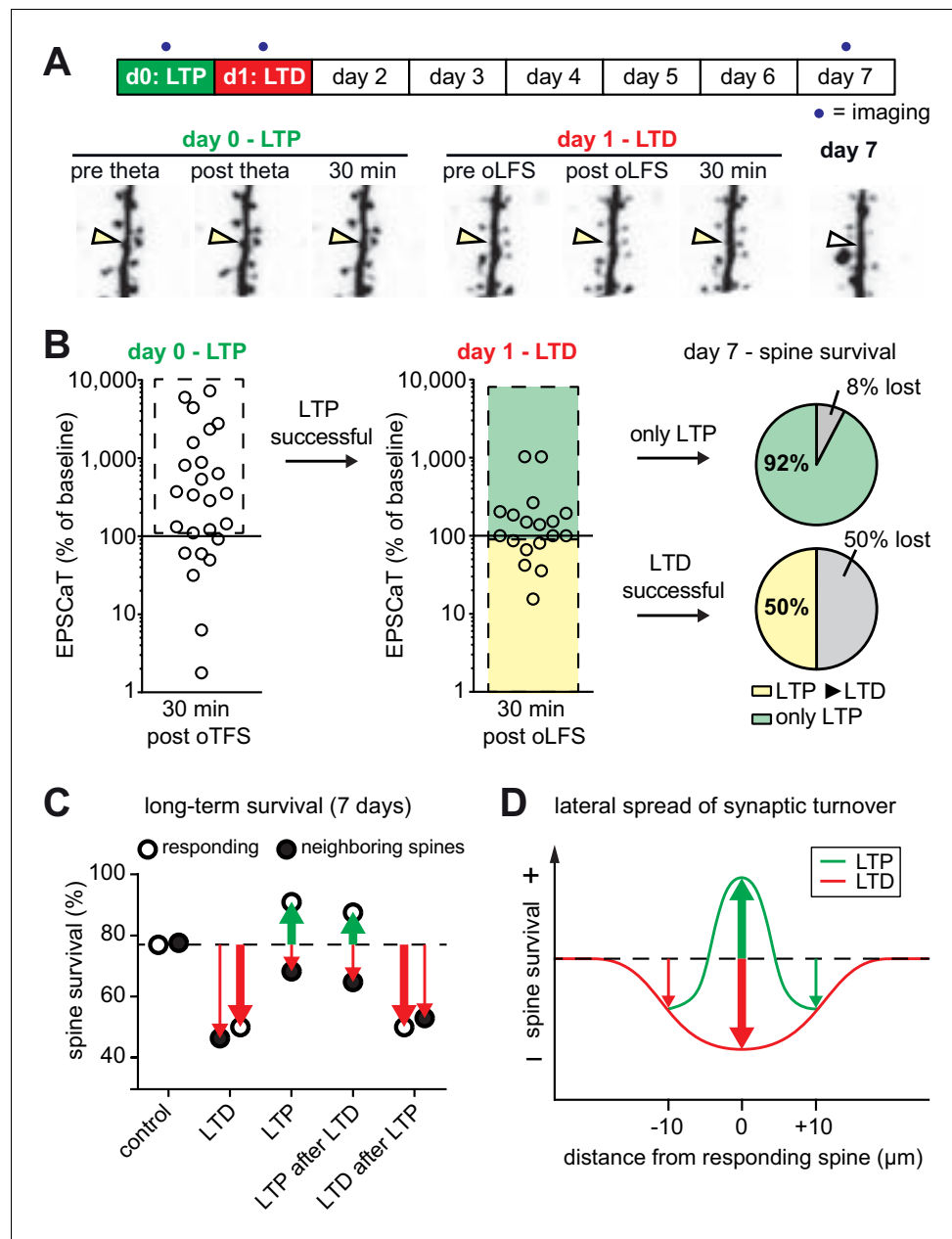
Figure 5. with one supplement: The most recent plasticity event fully accounts for synaptic tenacity. (**A**) Long-term survival analysis of experiments where LTD was induced 24 hr after LTP. Maximum intensity projections of mCerulean fluorescence in dendritic segment harboring a responding spine that was successfully potentiated on day 0 and depressed on day 1 (yellow arrowhead). (**B**) Assessment of synaptic weight changes induced by oTFS on day 0 and oLFS on day 1. Dashed box in left graph indicates all experiments where LTP was successfully induced on day 0. Only these spines were considered in the LTD experiment on day 1 (middle). Yellow shaded box indicates all experiments where LTD was successfully induced on day 1 (after LTP on day 0, LTP ▶ LTD). Note the low probability of depression after potentiation. Green shaded box encompasses experiments where oLFS did not lead to LTD or even led to LTP (only LTP). Pie charts show quantification of spine survival after 7 days for these two conditions. (**C**) Comparison of spine survival 7 days after various plasticity paradigms. Stimulated spines are shown as open circles; non-stimulated neighbors within 10 μm are shown as filled circles. Values for 'control' and 'LTD' are from *Wiegert and Oertner, 2013*. (**D**) LTP stabilizes the spine carrying the potentiated synapse, but reduces the average lifetime of more distant (>5 μm) spines on the same dendrite.
DOI: https://doi.org/10.7554/eLife.39151.014

The following source data and figure supplement are available for figure 5:

Figure 5 continued on next page

for synaptic potentiation and place cell formation (*Bittner et al., 2015*; *Sheffield et al., 2017*). Thus, dendritic calcium spikes during complex spike bursts, evoked by synchronized input from entorhinal cortex and CA3 pyramidal cells, are part of the physiological mechanism for the selective potentiation of active Schaffer collateral synapses during behavior (*Hasselmo et al., 2002*).

Spine calcium imaging allowed us to detect synaptic plasticity at single synapses without electrodes. Newly inserted AMPA receptors lead to stronger depolarization of the spine head during the EPSP, more efficient unblocking of NMDA receptors and EPSCaT potentiation. It is important to note, however, that EPSCaT amplitudes are not linearly related to somatic EPSCs. The ratio between AMPA and NMDA receptors is not constant between spines, and peak calcium concentrations depend on spine head volume and spine neck resistance (*Grunditz et al., 2008*). High EPSCaT amplitudes can even lead to SK channel activation and dampening of the EPSP (*Bloodgood and Sabatini, 2007*). These confounds, which make EPSCaT amplitude comparisons between spines difficult, are less of a problem when the same spine is compared before and after plasticity induction to differentiate between LTP and LTD.

Counting the number of EPSCaTs in a set of stimulated trials can be used as a proxy for presynaptic release probability, as postsynaptic failures (successful glutamate release without postsynaptic calcium influx) are thought to be rare at Schaffer collateral synapses (*Nimchinsky et al., 2004*). In contrast to LTD, where the reduction in average EPSCaT amplitude was mainly due to decreased release probability (*Wiegert and Oertner, 2013*), oTFS-induced LTP strongly enhanced EPSCaT potency, but did not seem to affect release probability. This confirms that postsynaptic mechanisms such as AMPA receptor insertion account for this form of potentiation (*Shi et al., 1999*; *Lu et al., 2001*; *Matsuzaki et al., 2004*). Analyzing spine volume changes supported the notion of pre- vs postsynaptic plasticity mechanisms: While LTD induction did not affect spine volume (*Wiegert and Oertner, 2013*), LTP triggered significant growth of the postsynaptic compartment (*Figure 2D*). Going beyond the first hours after plasticity induction, we asked how these different forms of plasticity would influence the tenacity of synapses that actively contributed to postsynaptic spiking in comparison to inactive synapses on the same dendrite.

Twenty-four hours after induction of LTP, synapses were back to their baseline state with respect to the amplitude and probability of spine calcium transients as well as the volume of the spine head. Yet, a long-lasting, synapse-specific memory of the potentiation event was maintained, since these once-potentiated spines were more likely to persist during the following week compared to other spines on the same dendritic branch, or non-stimulated controls. Similarly, the effects of LTD may outlast the actual depression: CA1 spines did not show any lasting reduction in volume, but their life expectancy was significantly reduced after LTD (*Wiegert and Oertner, 2013*). A similar sequence of transient LTD followed by delayed spine elimination was found at the parallel fiber synapse on Purkinje cells in the cerebellum (*Aziz et al., 2014*). These findings support the theoretical concept that information could be robustly stored in the topology of the network rather than in the analog strength of individual synapses. The mechanism linking LTP to synaptic stabilization, and LTD to destabilization, is likely to involve several processes. Synaptic tenacity is known to be affected by trans-synaptic proteins such as Neuroligin-1 and SynCAM-1 (*Zeidan and Ziv, 2012*; *Körber and Stein, 2016*), PSD-95 (*De Roo et al., 2008*; *Cane et al., 2014*), ubiquitin protein ligase E3A (*Kim et al., 2016*), ensheathment of the synapse by astrocyte processes (*Bernardinelli et al., 2014*) and many other local factors. It may be a combination of local physical changes and distributed network effects, such as the recurrent reactivation of a specific circuit (*Wei and Koulakov, 2014*; *Novitskaya et al., 2016*), which makes once potentiated synapses robust against depression (*Figure 5B*) and pruning (*Figure 3E*). New tools for chronic activity modulation may allow dissecting use-dependent synapse stabilization in future experiments (*Lopez et al., 2016*; *Beck et al., 2018*). The link between LTP and long-term structural stability we show on the single-synapse level could explain why learning-induced spines in motor cortex are more stable than their pre-existing

neighbors and persist for months after training (*Xu et al., 2009*; *Yang et al., 2009*). LTP-induced tenacity might be a general principle to connect different time scales of cortical circuit plasticity.

Failure to evoke postsynaptic CSBs upon oTFS led to presynaptic depression in our experiments, which was followed by increased spine elimination (*Figure 3F*). This effect has been shown to be mediated by autocrine glutamate signaling at the presynaptic terminal and may not involve postsynaptic signaling (*Padamsey et al., 2017*). If, on the other hand, the postsynaptic neuron is driven to spike, retrograde signaling via NO (nitric oxide) leads to an increase in release probability, which explains why we did not see presynaptic depression in synapses that experienced CSBs (*Figure 2C*). Thus, the classical Hebbian rule of rewarding only synapses that causally contribute to postsynaptic AP firing also seems to apply to long-term stability. However, our results suggest that changes are not perfectly confined to the directly driven synapse: Optogenetic TFS not only affected strength, volume and long-term stability of the stimulated spines, but also increased volume and stability of its immediate neighbors (*Figure 2D*, *Figure 3E*). This is consistent with short-range diffusion of 'potentiating factors' such as activated RhoA and Cdc42 out of the directly stimulated spine (*Murakoshi et al., 2011*; *Yasuda, 2017*). In contrast, more distant spines on the same dendrite (5–10 µm) showed no increase in volume and a decrease in lifetime (*Figure 2D*, *Figure 3E*), confirming an earlier 3 day study (*De Roo et al., 2008*). Since we increased the optogenetic drive to CA3 during oTFS, we could not map the position of all spines that were active during plasticity induction. Therefore, we were not able to study the spatial extent of spine destabilization, for example by selecting a 'control' branch that received no input during oTFS. Nevertheless, our 7 day follow-up points to a center-surround function that stabilizes the immediate neighbors (<5 µm) of potentiated synapses, although they were most likely not active during the induction protocol (*Figure 5D*). As we have previously shown, LTD-induced destabilization has an even larger (>10 µm) lateral spread (*Wiegert and Oertner, 2013*). Apparently, the local environment is as important for the long-term survival of a synaptic connection as its own activity history. This could put a limit to the uniformity of synaptic inputs in dendritic sections, as it might be impossible to prune a synapse next to a strongly potentiated spine.

By inducing two rounds of plasticity, we demonstrated that synaptic pruning is not a random process, but determined by the last plasticity-inducing activity pattern. In the organotypic culture system, the latency between LTD induction and spine loss was several days. This period could be considerably shorter in vivo, given the highly rhythmic activity of the hippocampal circuit and in consequence, intense synaptic competition. Our approach allows imposing any kind of spike pattern to a select group of synapses over several days. It complements in vivo studies of structural plasticity, which provide information about spine turnover, but not about the activity patterns in pre- and postsynaptic neurons (*Attardo et al., 2015*). Once the conditions for synaptic maintenance are understood, the protracted process of circuit refinement by constant removal of irrelevant synapses could be simulated. Networks with self-organized connectivity might generate activity patterns that are different from the randomly connected networks underlying current large-scale simulations (*Markram et al., 2015*). Together with realistic simulations of synaptic network dynamics and long-term investigations of synapse remodeling in vivo, long-term analysis of the structure-function relationship of individual synapses may help understanding how the brain stores and retrieves memories.

Materials and methods

Key resources table

Reagent type (species) or resource	Designation	Source or reference	Identifiers	Additional information
Strain, strain background (Rattus norvegicus, male)	Wistar	Charles River	Crl:WI	bred in the animal facility, UKE Hamburg

Continued on next page

Continued

Reagent type (species) or resource	Designation	Source or reference	Identifiers	Additional information
Strain, strain background (R. norvegicus, male)	Wistar	Janvier	RjHAN:WI	bred in the animal facility, UKE Hamburg
Genetic reagent (Clamydomonas reinhardtii)	ChR2(ET/TC)	doi: 10.1073/pnas.1017210108		channelrhodopsin
Genetic reagent (Aequorea victoria)	GCaMP6s	doi: 10.1038/nature12354		calcium indicator
Genetic reagent (A. victoria)	mCerulean	doi: 10.1038/nbt945		fluorescent protein
Transfected construct (R. norvegicus)	ChR2(ET/TC)−2A-synaptophysin-tdimer2	doi: 10.1073/pnas.1315926110		transfection of CA3 neurons
Recombinant DNA reagent	rAAV2/7	Vector Facility UKE Hamburg		viral vector
Chemical compound, drug	APV	Tocris Bioscience	CAS Number 79055-68-8	NMDA receptor blocker
Software, algorithm	ScanImage3.8	DOI: 10.1186/1475-925X-2–13		modified for arbitrary line scans

Slice culture preparation and transfection

Hippocampal slice cultures from male Wistar rats were prepared at postnatal day 4–5 as described (*Gee et al., 2017*). Animal procedures were in accordance with the guidelines of local authorities and Directive 2010/63/EU. At DIV 3, we pressure-injected rAAV2/7 encoding ChR2(ET/TC)−2A-synaptophysin-tdimer2 into CA3. At DIV 18, single-cell electroporation was used to transfect CA1 pyramidal neurons in rAAV-infected slices with GCaMP6s and mCerulean (ratio 1:1) as described (*Wiegert et al., 2017*).

Electrophysiology

Experiments were performed between DIV 21 and 25. Whole-cell recordings from CA1 pyramidal cells were made at 25°C with a Multiclamp 700B amplifier (Molecular Devices). Patch pipettes with a tip resistance of 3–4 MΩ were filled with (in mM) 135 K-gluconate, 4 MgCl$_2$, 4 Na$_2$-ATP, 0.4 Na-GTP, 10 Na$_2$-phosphocreatine, three ascorbate, and 10 HEPES (pH 7.2). LTD experiments were conducted in ACSF containing (in mM) 135 NaCl, 2.5 KCl, 4 CaCl$_2$, 4 MgCl$_2$, 10 Na-HEPES, 12.5 D-glucose, 1.25 NaH$_2$PO$_4$, 0.03 D-Serine (pH 7.4, sterile filtered). During LTP induction, ACSF with lower divalent ion concentration (2 CaCl$_2$, 1 MgCl$_2$) was used to increase excitability. Access resistance was monitored continuously and recordings with a drift of >20% were discarded.

Two-Photon microscopy

The custom-built two-photon imaging setup was based on an Olympus BX51WI microscope equipped with a LUMPLFLN 60 × 1.0 NA objective, controlled by the open-source software package ScanImage (*Pologruto et al., 2003*) which was modified to allow user-defined arbitrary line scans at 500 Hz. Two Ti:Sapphire lasers (MaiTai DeepSee, Spectra-Physics) controlled by electro-optic modulators (350–80, Conoptics) were used to excite cerulean (810 nm) and GCaMP6s (980 nm). To activate ChR2(ET/TC)-expressing cells outside the field of view of the objective, we used a fiber-coupled LED (200 µm fiber, NA 0.37, Mightex Systems) to deliver light pulses to CA3. During the blue light pulses, sub-stage PMTs (H7422P-40SEL, Hamamatsu) were protected by a shutter (NS45B, Uniblitz).

Measuring excitatory postsynaptic calcium transients (EPSCaTs)

Frame scans (10 × 10 µm) of oblique dendrites were acquired to detect spines responding to opto-genetic stimulation of CA3 neurons. Two brief (2 ms) light pulses with an inter-pulse interval of 40 ms were applied to increase release probability and thus the chance of detecting responding spines. In each trial, 14 frames (64 × 64 pixel) were acquired at 7.8 Hz. At least five trials were recorded from each dendritic segment. The relative change in GCaMP6s fluorescence ($\Delta F/F_0$) was calculated on-line. If the spine signal exceeded two times the standard deviation (SD) of its resting fluores-cence, this spine was considered as 'potentially responding'. To measure Ca^{2+} transients with better signal-to-noise ratio, line scans were acquired across potentially responding spine heads and their parent dendrites (500 Hz, 20 trials/spine). To measure the amplitude of Ca^{2+} transients and to distin-guish successful synaptic transmission events (EPSCaTs) from failures, we used a template-based fit-ting algorithm. The characteristic fluorescence time constant was extracted for every spine by fitting a double exponential function (τ_{rise}, τ_{decay}) to the average GCaMP6s signal. To estimate the Ca^{2+} transient amplitude for every trial, we fit the spine-specific template to every response, amplitude being the only free parameter. Response amplitude was defined as the value of the fit function at its maximum. A trace was classified as 'success' when its amplitude exceeded two standard deviations (2σ) of baseline noise.

Long-term imaging of spine morphology

The use of HEPES-buffered sterile-filtered ACSF allowed us to optically stimulate and image slice cultures under near-sterile conditions, using no perfusion system. The custom recording chamber (1 mm quartz glass bottom) and 60 × water immersion objective were sterilized with 70% ethanol and filled with 1.5 ml sterile ACSF. A small patch of membrane (5 × 6 mm) supporting the hippocampal culture was cut out of the cell culture insert (Millipore PICM0RG50), placed in the recording chamber and weighted down with a u-shaped gold wire. During imaging, the temperature of the slice culture was maintained at 25°C via a permanently heated oil-immersion condenser (NA = 1.4, Olympus). After each imaging session, the membrane patch was placed on a fresh sterile membrane insert and returned to the incubator. In the first imaging session, a spine displaying stimulation-induced EPS-CaTs was centered and a three-dimensional image stack (XY: 10 × 10 µm, Z: 5–15 µm) of the mCeru-lean signal was acquired. Additional image stacks were acquired at low magnification to ensure identity of the dendritic segment. For post-hoc analysis of spine turnover, the three-dimensional image stacks were aligned based on a rigid-body algorithm (ImageJ). All spines identified in the three-dimensional image stack acquired before the plasticity induction protocol were analyzed in the subsequent stacks, with the following exception: Spines that appeared shifted from their original position on the dendrite by more than 1 µm in any direction between two consecutive imaging ses-sions were not included in the analysis, as it was not clear whether the original spine was replaced by a new one. If the imaged neuron showed any sign of compromised health at day 7 (bright GCaMP6 fluorescence at rest, dendritic swelling or beading), the experiment was excluded from the analysis. Maximum intensity projections are shown for illustrative purposes only and were not used for analysis. To estimate spine volume, we integrated the fluorescence intensity of the spine head (mCerulean) taken from a single optical section through the center of the spine. For each spine the point-spread-function (PSF) of the microscope was immersed in the apical trunk of the dendrite to obtain the maximum intensity. In case of different depth of spine and calibration measurement, we corrected for laser attenuation in the tissue. The volume of the PSF was determined with PSFj (*Theer et al., 2014*) using 170 nm fluorescent beads (Invitrogen). Knowing the volume of the PSF and the brightness of a given cell's cytoplasm allowed us to convert spine intensity into absolute spine volume (*Svoboda et al., 1996*).

Statistics

All statistical analysis was performed using GraphPad Prism 6.0. Data were tested for Gaussian distri-bution by D'Agostino and Pearson omnibus normality test. Normally distributed data were tested for significant differences with a two-tailed t-test (*Figure 3A*) or one-way repeated-measures analysis of variance (ANOVA) followed by Sidak's multiple comparisons test (*Figure 3B,C*). Data with non-normal distribution data were tested with the following nonparametric tests: Two-tailed Wilcoxon matched-pairs signed rank test (*Figures 2A,D* and *3A*), Friedman test followed by Dunn's multiple

comparison test (*Figure 2C*; *Figure 2—figure supplementary 1A-C*). Investigators were not blinded to the group allocation during the experiments. Data analysis was automated as much as possible to preclude investigator biases. All experiments were done with interleaved controls; pharmacological treatments were mixed with untreated cultures.

Acknowledgements

Additional information

Author contributions

J Simon Wiegert, Conceptualization, Data curation, Software, Formal analysis, Supervision, Investigation, Methodology, Writing—original draft, Writing—review and editing; Mauro Pulin, Data curation, Formal analysis, Investigation; Christine Elizabeth Gee, Supervision, Writing—review and editing; Thomas G Oertner, Conceptualization, Supervision, Funding acquisition, Methodology, Writing—original draft, Project administration, Writing—review and editing

Author ORCIDs

J Simon Wiegert https://orcid.org/0000-0003-0893-9349
Mauro Pulin https://orcid.org/0000-0001-6255-0276
Christine Elizabeth Gee https://orcid.org/0000-0003-0345-3665
Thomas G Oertner https://orcid.org/0000-0002-2312-7528

Ethics

Animal experimentation: Animal procedures were in accordance with the guidelines of local authorities and Directive 2010/63/EU.

Decision letter and Author response

Decision letter https://doi.org/10.7554/eLife.39151.019
Author response https://doi.org/10.7554/eLife.39151.020

Additional files

Supplementary files
• Transparent reporting form
DOI: https://doi.org/10.7554/eLife.39151.017

Data availability
All data generated or analysed during this study are included in the manuscript and supporting files. Source data files have been provided for Figures 2, 3, 4 and 5.

References

Abraham WC, Huggett A. 1997. Induction and reversal of long-term potentiation by repeated high-frequency stimulation in rat hippocampal slices. *Hippocampus* **7**:137–145. DOI: https://doi.org/10.1002/(SICI)1098-1063(1997)7:2<137::AID-HIPO3>3.0.CO;2-K, PMID: 9136046

Attardo A, Fitzgerald JE, Schnitzer MJ. 2015. Impermanence of dendritic spines in live adult CA1 hippocampus. *Nature* **523**:592–596. DOI: https://doi.org/10.1038/nature14467, PMID: 26098371

Aziz W, Wang W, Kesaf S, Mohamed AA, Fukazawa Y, Shigemoto R. 2014. Distinct kinetics of synaptic structural plasticity, memory formation, and memory decay in massed and spaced learning. *PNAS* **111**:E194–E202. DOI: https://doi.org/10.1073/pnas.1303317110, PMID: 24367076

Bastrikova N, Gardner GA, Reece JM, Jeromin A, Dudek SM. 2008. Synapse elimination accompanies functional plasticity in hippocampal neurons. *PNAS* **105**:3123–3127. DOI: https://doi.org/10.1073/pnas.0800027105, PMID: 18287055

Beck S, Yu-Strzelczyk J, Pauls D, Constantin OM, Gee CE, Ehmann N, Kittel RJ, Nagel G, Gao S. 2018. Synthetic Light-Activated ion channels for optogenetic activation and inhibition. *Frontiers in Neuroscience* **12**:643. DOI: https://doi.org/10.3389/fnins.2018.00643

Bernardinelli Y, Randall J, Janett E, Nikonenko I, König S, Jones EV, Flores CE, Murai KK, Bochet CG, Holtmaat A, Muller D. 2014. Activity-dependent structural plasticity of perisynaptic astrocytic domains promotes excitatory synapse stability. *Current Biology* **24**:1679–1688. DOI: https://doi.org/10.1016/j.cub.2014.06.025, PMID: 25042585

Berndt A, Schoenenberger P, Mattis J, Tye KM, Deisseroth K, Hegemann P, Oertner TG. 2011. High-efficiency channelrhodopsins for fast neuronal stimulation at low light levels. *PNAS* **108**:7595–7600. DOI: https://doi.org/10.1073/pnas.1017210108, PMID: 21504945

Berry KP, Nedivi E. 2017. Spine dynamics: are they all the same? *Neuron* **96**:43–55. DOI: https://doi.org/10.1016/j.neuron.2017.08.008, PMID: 28957675

Bittner KC, Grienberger C, Vaidya SP, Milstein AD, Macklin JJ, Suh J, Tonegawa S, Magee JC. 2015. Conjunctive input processing drives feature selectivity in hippocampal CA1 neurons. *Nature Neuroscience* **18**:1133–1142. DOI: https://doi.org/10.1038/nn.4062, PMID: 26167906

Bliss TV, Lomo T. 1973. Long-lasting potentiation of synaptic transmission in the dentate area of the anaesthetized rabbit following stimulation of the perforant path. *The Journal of Physiology* **232**:331–356. DOI: https://doi.org/10.1113/jphysiol.1973.sp010273, PMID: 4727084

Bloodgood BL, Sabatini BL. 2007. Nonlinear regulation of unitary synaptic signals by CaV(2.3) voltage-sensitive calcium channels located in dendritic spines. *Neuron* **53**:249–260. DOI: https://doi.org/10.1016/j.neuron.2006.12.017, PMID: 17224406

Cane M, Maco B, Knott G, Holtmaat A. 2014. The relationship between PSD-95 clustering and spine stability in vivo. *Journal of Neuroscience* **34**:2075–2086. DOI: https://doi.org/10.1523/JNEUROSCI.3353-13.2014, PMID: 24501349

Chaudhuri R, Fiete I. 2016. Computational principles of memory. *Nature Neuroscience* **19**:394–403. DOI: https://doi.org/10.1038/nn.4237, PMID: 26906506

De Roo M, Klauser P, Mendez P, Poglia L, Muller D. 2008. Activity-dependent PSD formation and stabilization of newly formed spines in hippocampal slice cultures. *Cerebral Cortex* **18**:151–161. DOI: https://doi.org/10.1093/cercor/bhm041, PMID: 17517683

Emptage NJ, Reid CA, Fine A, Bliss TV. 2003. Optical quantal analysis reveals a presynaptic component of LTP at hippocampal Schaffer-associational synapses. *Neuron* **38**:797–804. DOI: https://doi.org/10.1016/S0896-6273(03)00325-8, PMID: 12797963

Fujii S, Saito K, Miyakawa H, Ito K-ichi, Kato H. 1991. Reversal of long-term potentiation (depotentiation) induced by tetanus stimulation of the input to CA1 neurons of guinea pig hippocampal slices. *Brain Research* **555**:112–122. DOI: https://doi.org/10.1016/0006-8993(91)90867-U

Gee CE, Ohmert I, Wiegert JS, Oertner TG. 2017. Preparation of slice cultures from rodent Hippocampus. *Cold Spring Harbor Protocols* **2017**:pdb.prot094888. DOI: https://doi.org/10.1101/pdb.prot094888

Golding NL, Staff NP, Spruston N. 2002. Dendritic spikes as a mechanism for cooperative long-term potentiation. *Nature* **418**:326–331. DOI: https://doi.org/10.1038/nature00854, PMID: 12124625

Grienberger C, Chen X, Konnerth A. 2014. NMDA receptor-dependent multidendrite ca(2+) spikes required for hippocampal burst firing in vivo. *Neuron* **81**:1274–1281. DOI: https://doi.org/10.1016/j.neuron.2014.01.014, PMID: 24560703

Grunditz A, Holbro N, Tian L, Zuo Y, Oertner TG. 2008. Spine neck plasticity controls postsynaptic calcium signals through electrical compartmentalization. *Journal of Neuroscience* **28**:13457–13466. DOI: https://doi.org/10.1523/JNEUROSCI.2702-08.2008, PMID: 19074019

Hasselmo ME, Bodelón C, Wyble BP. 2002. A proposed function for hippocampal theta rhythm: separate phases of encoding and retrieval enhance reversal of prior learning. *Neural Computation* **14**:793–817. DOI: https://doi.org/10.1162/089976602317318965, PMID: 11936962

Hill TC, Zito K. 2013. LTP-induced long-term stabilization of individual nascent dendritic spines. *Journal of Neuroscience* **33**:678–686. DOI: https://doi.org/10.1523/JNEUROSCI.1404-12.2013, PMID: 23303946

Holbro N, Grunditz A, Wiegert JS, Oertner TG. 2010. AMPA receptors gate spine ca(2+) transients and spike-timing-dependent potentiation. *PNAS* **107**:15975–15980. DOI: https://doi.org/10.1073/pnas.1004562107, PMID: 20798031

Holtmaat A, Caroni P. 2016. Functional and structural underpinnings of neuronal assembly formation in learning. *Nature Neuroscience* **19**:1553–1562. DOI: https://doi.org/10.1038/nn.4418, PMID: 27749830

Kim H, Kunz PA, Mooney R, Philpot BD, Smith SL. 2016. Maternal loss of Ube3a impairs Experience-Driven dendritic spine maintenance in the developing visual cortex. *Journal of Neuroscience* **36**:4888–4894. DOI: https://doi.org/10.1523/JNEUROSCI.4204-15.2016, PMID: 27122043

Körber N, Stein V. 2016. In vivo imaging demonstrates dendritic spine stabilization by SynCAM 1. *Scientific Reports* **6**:24241. DOI: https://doi.org/10.1038/srep24241, PMID: 27053173

Lopez AJ, Kramar E, Matheos DP, White AO, Kwapis J, Vogel-Ciernia A, Sakata K, Espinoza M, Wood MA. 2016. Promoter-Specific effects of DREADD modulation on hippocampal synaptic plasticity and memory formation. *Journal of Neuroscience* **36**:3588–3599. DOI: https://doi.org/10.1523/JNEUROSCI.3682-15.2016

Losonczy A, Magee JC. 2006. Integrative properties of radial radial oblique dendrites in hippocampal CA1 pyramidal neurons. *Neuron* **50**:291–307. DOI: https://doi.org/10.1016/j.neuron.2006.03.016, PMID: 16630839

Lu W, Man H, Ju W, Trimble WS, MacDonald JF, Wang YT. 2001. Activation of synaptic NMDA receptors induces membrane insertion of new AMPA receptors and LTP in cultured hippocampal neurons. *Neuron* **29**:243–254. DOI: https://doi.org/10.1016/S0896-6273(01)00194-5, PMID: 11182095

Magee JC, Johnston D. 1997. A synaptically controlled, associative signal for Hebbian plasticity in hippocampal neurons. *Science* **275**:209–213. DOI: https://doi.org/10.1126/science.275.5297.209, PMID: 8985013

Markram H, Muller E, Ramaswamy S, Reimann MW, Abdellah M, Sanchez CA, Ailamaki A, Alonso-Nanclares L, Antille N, Arsever S, Kahou GA, Berger TK, Bilgili A, Buncic N, Chalimourda A, Chindemi G, Courcol JD, Delalondre F, Delattre V, Druckmann S, et al. 2015. Reconstruction and Simulation of Neocortical Microcircuitry. *Cell* **163**:456–492. DOI: https://doi.org/10.1016/j.cell.2015.09.029, PMID: 26451489

Matsuzaki M, Honkura N, Ellis-Davies GC, Kasai H. 2004. Structural basis of long-term potentiation in single dendritic spines. *Nature* **429**:761–766. DOI: https://doi.org/10.1038/nature02617, PMID: 15190253

Mizuseki K, Buzsáki G. 2013. Preconfigured, skewed distribution of firing rates in the hippocampus and entorhinal cortex. *Cell Reports* **4**:1010–1021. DOI: https://doi.org/10.1016/j.celrep.2013.07.039, PMID: 23994479

Moody TD, Thomas MJ, Makhinson M, O'Dell TJ. 1998. 5-Hz stimulation of CA3 pyramidal cell axons induces a beta-adrenergic modulated potentiation at synapses on CA1, but not CA3, pyramidal cells. *Brain Research* **794**:75–79. DOI: https://doi.org/10.1016/S0006-8993(98)00217-0, PMID: 9630529

Murakoshi H, Wang H, Yasuda R. 2011. Local, persistent activation of Rho GTPases during plasticity of single dendritic spines. *Nature* **472**:100–104. DOI: https://doi.org/10.1038/nature09823, PMID: 21423166

Nägerl UV, Eberhorn N, Cambridge SB, Bonhoeffer T. 2004. Bidirectional activity-dependent morphological plasticity in hippocampal neurons. *Neuron* **44**:759–767. DOI: https://doi.org/10.1016/j.neuron.2004.11.016, PMID: 15572108

Nimchinsky EA, Yasuda R, Oertner TG, Svoboda K. 2004. The number of glutamate receptors opened by synaptic stimulation in single hippocampal spines. *Journal of Neuroscience* **24**:2054–2064. DOI: https://doi.org/10.1523/JNEUROSCI.5066-03.2004, PMID: 14985448

Nishiyama J, Yasuda R. 2015. Biochemical Computation for Spine Structural Plasticity. *Neuron* **87**:63–75. DOI: https://doi.org/10.1016/j.neuron.2015.05.043, PMID: 26139370

Novitskaya Y, Sara SJ, Logothetis NK, Eschenko O. 2016. Ripple-triggered stimulation of the locus coeruleus during post-learning sleep disrupts ripple/spindle coupling and impairs memory consolidation. *Learning & Memory* **23**:238–248. DOI: https://doi.org/10.1101/lm.040923.115, PMID: 27084931

O'Dell TJ, Kandel ER. 1994. Low-frequency stimulation erases LTP through an NMDA receptor-mediated activation of protein phosphatases. *Learning & Memory* **1**:129–139. DOI: https://doi.org/10.1101/lm.1.2.129, PMID: 10467591

Padamsey Z, Tong R, Emptage N. 2017. Glutamate is required for depression but not potentiation of long-term presynaptic function. *eLife* **6**:e29688. DOI: https://doi.org/10.7554/eLife.29688, PMID: 29140248

Pologruto TA, Sabatini BL, Svoboda K. 2003. ScanImage: flexible software for operating laser scanning microscopes. *BioMedical Engineering OnLine* **2**:13. DOI: https://doi.org/10.1186/1475-925X-2-13, PMID: 12801419

Sheffield MEJ, Adoff MD, Dombeck DA. 2017. Increased Prevalence of Calcium Transients across the Dendritic Arbor during Place Field Formation. *Neuron* **96**:490–504. DOI: https://doi.org/10.1016/j.neuron.2017.09.029, PMID: 29024668

Shi SH, Hayashi Y, Petralia RS, Zaman SH, Wenthold RJ, Svoboda K, Malinow R. 1999. Rapid spine delivery and redistribution of AMPA receptors after synaptic NMDA receptor activation. *Science* **284**:1811–1816. DOI: https://doi.org/10.1126/science.284.5421.1811, PMID: 10364548

Svoboda K, Tank DW, Denk W. 1996. Direct measurement of coupling between dendritic spines and shafts. *Science* **272**:716–719. DOI: https://doi.org/10.1126/science.272.5262.716, PMID: 8614831

Theer P, Mongis C, Knop M. 2014. PSFj: know your fluorescence microscope. *Nature Methods* **11**:981–982. DOI: https://doi.org/10.1038/nmeth.3102, PMID: 25264772

Thomas MJ, Watabe AM, Moody TD, Makhinson M, O'Dell TJ. 1998. Postsynaptic complex spike bursting enables the induction of LTP by theta frequency synaptic stimulation. *The Journal of Neuroscience* **18**:7118–7126. DOI: https://doi.org/10.1523/JNEUROSCI.18-18-07118.1998, PMID: 9736635

Wei Y, Koulakov AA. 2014. Long-Term memory stabilized by Noise-Induced rehearsal. *Journal of Neuroscience* **34**:15804–15815. DOI: https://doi.org/10.1523/JNEUROSCI.3929-12.2014

Wiegert JS, Gee CE, Oertner TG. 2017. Single-Cell electroporation of neurons. *Cold Spring Harbor Protocols* **2017**:pdb.prot094904. DOI: https://doi.org/10.1101/pdb.prot094904

Wiegert JS, Oertner TG. 2013. Long-term depression triggers the selective elimination of weakly integrated synapses. *PNAS* **110**:E4510–E4519. DOI: https://doi.org/10.1073/pnas.1315926110, PMID: 24191047

Xu T, Yu X, Perlik AJ, Tobin WF, Zweig JA, Tennant K, Jones T, Zuo Y. 2009. Rapid formation and selective stabilization of synapses for enduring motor memories. *Nature* **462**:915–919. DOI: https://doi.org/10.1038/nature08389, PMID: 19946267

Yang G, Pan F, Gan WB. 2009. Stably maintained dendritic spines are associated with lifelong memories. *Nature* **462**:920–924. DOI: https://doi.org/10.1038/nature08577, PMID: 19946265

Yasuda R. 2017. Biophysics of Biochemical Signaling in Dendritic Spines: Implications in Synaptic Plasticity. *Biophysical Journal* **113**:2152–2159. DOI: https://doi.org/10.1016/j.bpj.2017.07.029, PMID: 28866426

Zeidan A, Ziv NE. 2012. Neuroligin-1 loss is associated with reduced tenacity of excitatory synapses. *PLoS ONE* **7**:e42314. DOI: https://doi.org/10.1371/journal.pone.0042314, PMID: 22860111

Zhou Q, Homma KJ, Poo MM. 2004. Shrinkage of dendritic spines associated with long-term depression of hippocampal synapses. *Neuron* **44**:749–757. DOI: https://doi.org/10.1016/j.neuron.2004.11.011, PMID: 15572107

Figures and figure supplements

The fate of hippocampal synapses depends on the sequence of plasticity-inducing events
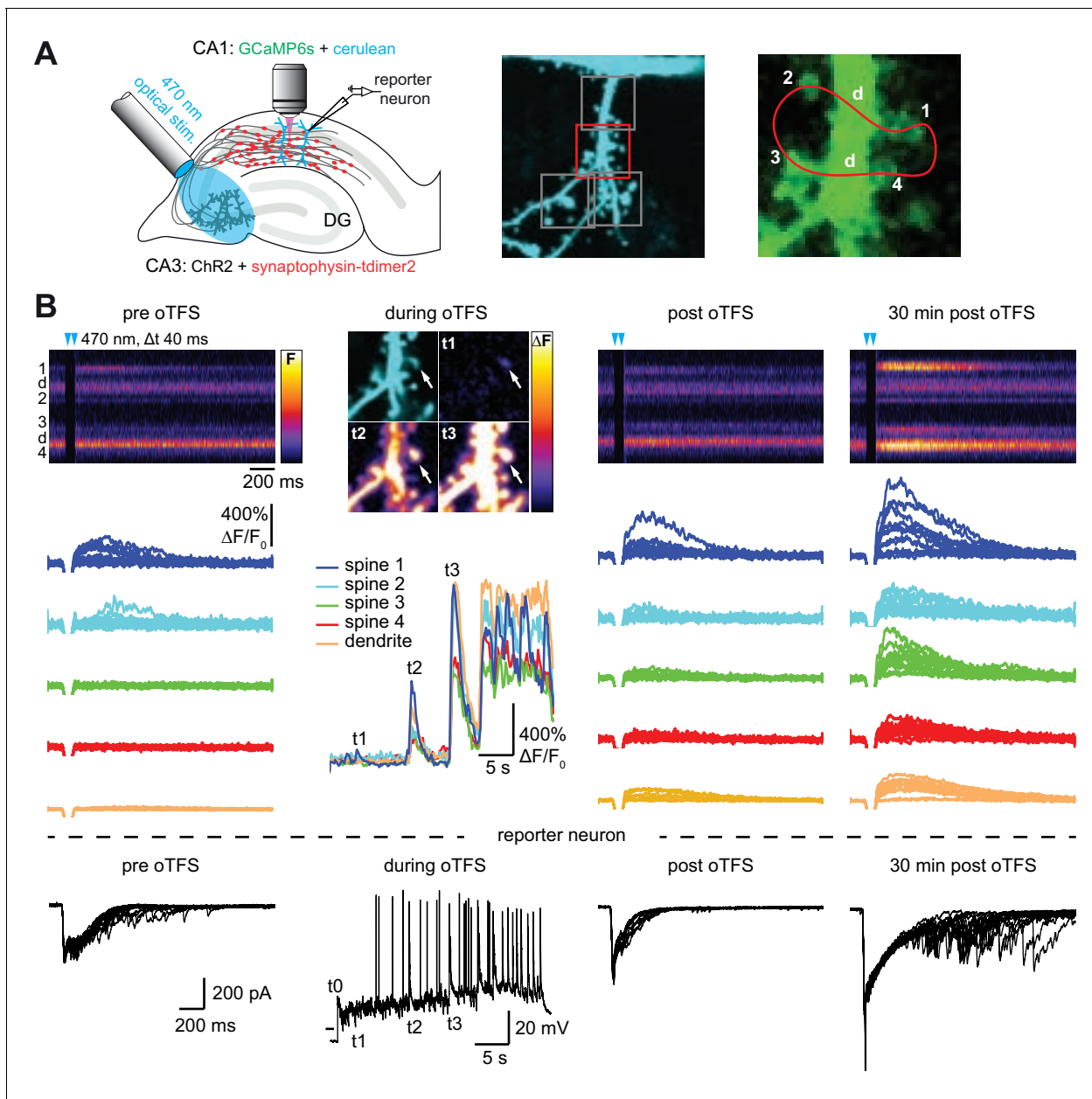
J Simon Wiegert *et al*

Figure 1. with two supplements: Channelrhodopsin-driven theta-frequency stimulation induces LTP. (**A**) Left: A fiber-coupled LED (λ = 470 nm) was used to locally stimulate ChR2-expressing CA3 neurons. Spines on GCaMP6s/mCerulean-expressing CA1 pyramidal cells were imaged with two-photon microscopy. For parallel electrical recordings, a second CA1 neuron was patch-clamped (reporter neuron). Middle: oblique dendrite branching off the apical trunk filled with mCerulean. Detection of active spines was done with GCaMP6s during presynaptic optogenetic stimulation. Stimulation-induced fluorescence changes (ΔF) of GCaMP6s were analyzed in fast frame scans (squares) of oblique dendrites until a responsive spine was detected (red square). Right: Magnified view of GCaMP6s fluorescence in the dendritic section harboring an activated spine. The laser was scanned in a user-defined trajectory across multiple spines and the parental dendrite during Ca^{2+} imaging (red curve). (**B**) Fluorescence signal across time from arbitrary line scan on dendrite shown in A during ChR2-stimulation before ('pre oTFS'), immediately ('post oTFS') and 30 min ('30 min post oTFS') after optical theta-frequency stimulation (oTFS). Temporally matched traces from multiple trials and electrophysiological recording from a reporter neuron are shown below. During oTFS the Ca^{2+} response was recorded in frame scan mode ('during oTFS'). The GCaMP6s-signal (ΔF) is shown for three selected time points during oTFS. GCaMP6s-traces from the same spines and dendrite imaged in line scans are shown below together with the corresponding electrophysiological recording in voltage clamp mode from the reporter neuron.
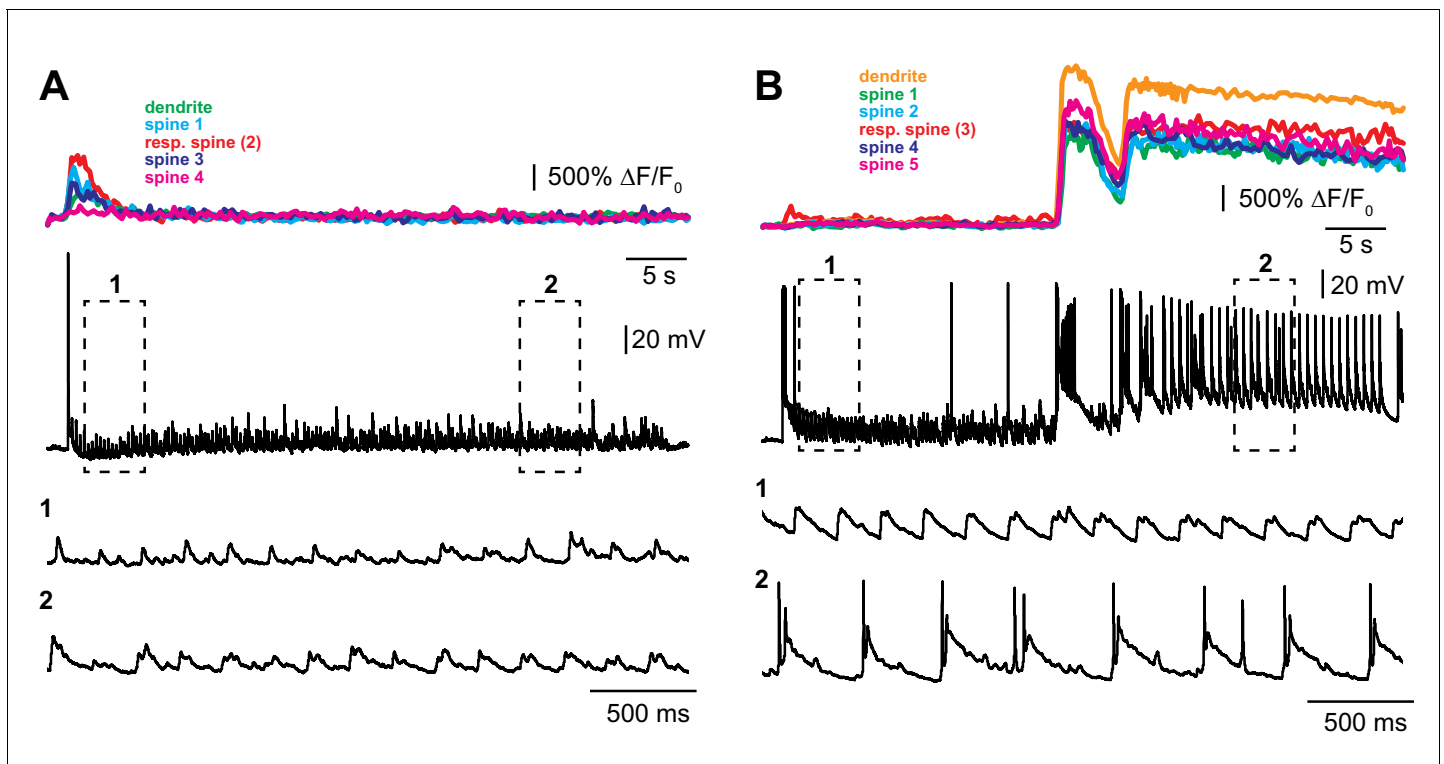
Figure 1—figure supplement 1. Examples of optogenetic TFS experiments. (**A**) Experiment where no dendritic calcium spikes were observed in the GCaMP6s-expressing CA1 pyramidal cell (colored traces, top) and no complex spike bursts (CSBs) were triggered in the neighboring 'reporter' neuron (black traces). (**B**) Experiment with dendritic calcium spikes and synchronous CSBs in the reporter neuron.
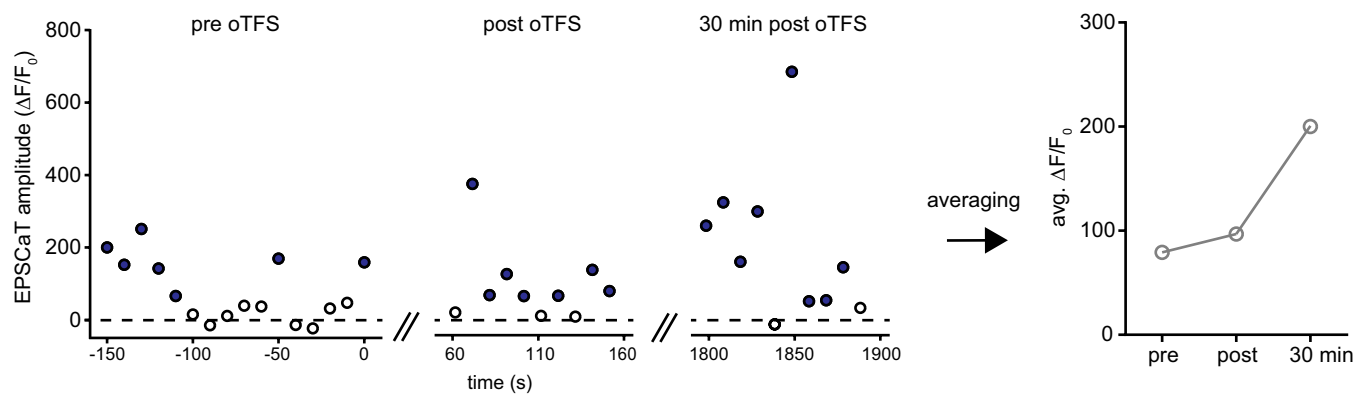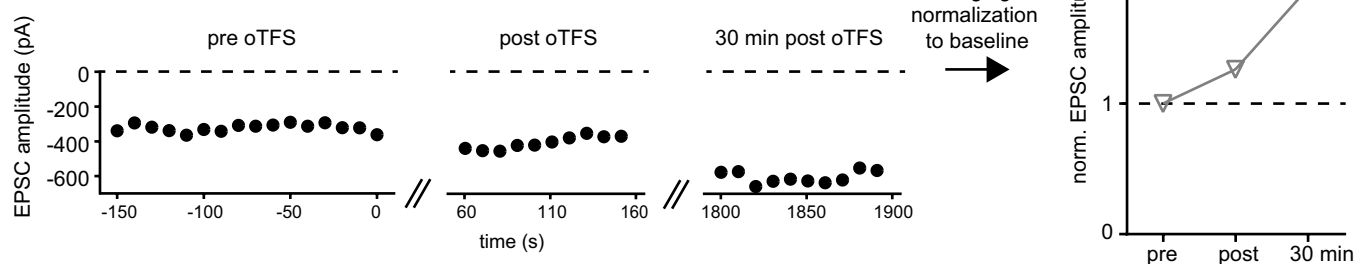
Figure 1—figure supplement 2. Analysis of imaging and electrophysiology data. (**A**) EPSCaT amplitude of spine one is plotted for all trials shown in *Figure 1B*. Open circles show failures, filled circles show successes. Baseline responses ('pre oTFS') and responses immediately ('post oTFS') and 30 min after oTFS ('30 min post oTFS') are averaged and plotted below. (**B**) EPSC amplitude is plotted for the recording from the reporter neuron shown in *Figure 1B*. Average responses plotted below were normalized to the baseline ('pre oTFS').

DOI: https://doi.org/10.7554/eLife.39151.004

Figure 2. with two supplements: Characterization of oTFS-induced LTP. (**A**) Changes in excitatory postsynaptic current (EPSC) amplitude in reporter neurons immediately after and 30 min after oTFS in the absence (left) or presence (right) of the NMDA receptor antagonist APV during oTFS. EPSCs were significantly increased after 30 min (p=0.012, n = 20 slice cultures). The increase was blocked by APV (p=0.69, n = 6 slice cultures). (**B**) Relative change of average excitatory Ca^{2+} transients (EPCaTs) in individual spines 30 min after the oTFS protocol plotted against the average spine Ca^{2+} during oTFS. In experiments indicated by filled red circles, APV was present during oTFS. (**C**) EPSCaT amplitude (p=0.0008, n = 20 slice cultures) and EPSCaT potency (successes only, p=0.0025) but not EPSCaT probability (P_{Ca}, p>0.05) were increased 30 min after oTFS in experiments where complex spike bursts (CSBs) were induced during oTFS. (**D**) Maximum intensity projections of mCerulean fluorescence in dendritic segment harboring a responding spine that was successfully potentiated (blue arrowhead). Volume of oTFS spines (p=0.002, n = 26 spines) and nearest (p=0.0001, n = 45 spines) but not distant neighbors (p=0.83, n = 58 spines)

Figure 2 continued on next page

Figure 2 continued

was increased 30 min after oTFS in experiments where CSBs were induced during oTFS. (E) Spine volume was not increased when NMDA receptors were blocked with APV during oTFS ($p > 0.05$, n = 7 spines).
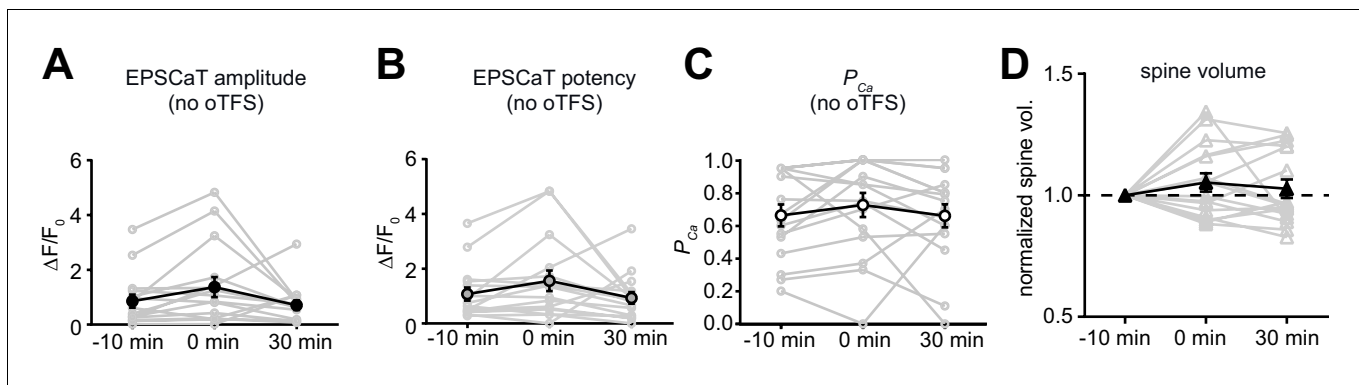
Figure 2—figure supplement 1. Analysis of oTFS experiments where no dendritic calcium spikes were observed during the induction protocol. (A) The null hypothesis, no change in average EPSCaT amplitude after oTFS, could not be rejected ($p > 0.05$, $n = 17$). (B) The null hypothesis, no change in EPSCaT potency after oTFS, could not be rejected ($p > 0.05$, $n = 17$). (C) The probability of EPSCaTs was significantly reduced after oTFS ($p = 0.0098$, $n = 17$). (A) – (C): nonparametric Friedman test followed by Dunn's multiple comparison test. (D) The null hypothesis, no change in spine head volume after oTFS, could not be rejected ($p > 0.05$, $n = 11$, Wilcoxon matched-pairs signed rank test).
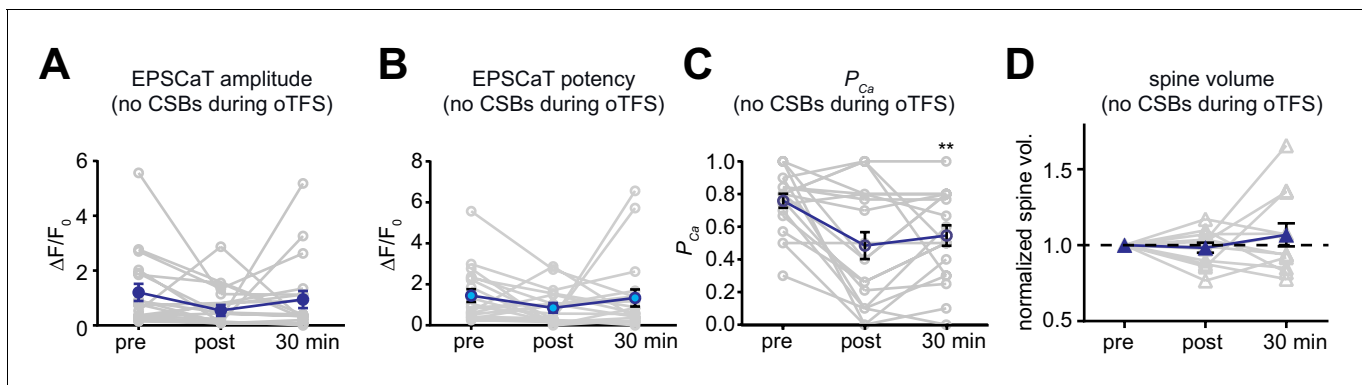
DOI: https://doi.org/10.7554/eLife.39151.006

Figure 2—figure supplement 2. Analysis of control experiments where no oTFS was applied to responding spines. (A) The null hypothesis, no change in average EPSCaT amplitude over time, could not be rejected (p>0.05, n = 16). (B) The null hypothesis, no change in EPSCaT potency over time, could not be rejected (p>0.05, n = 16). (C) The null hypothesis, no change in EPSCaT probability (P_{Ca}) over time, could not be rejected (p>0.05, n = 16). (A) – (C): nonparametric Friedman test followed by Dunn's multiple comparison test. (D) The null hypothesis, no change in spine head volume after oTFS, could not be rejected (p>0.05, n = 16, RM one-way ANOVA).
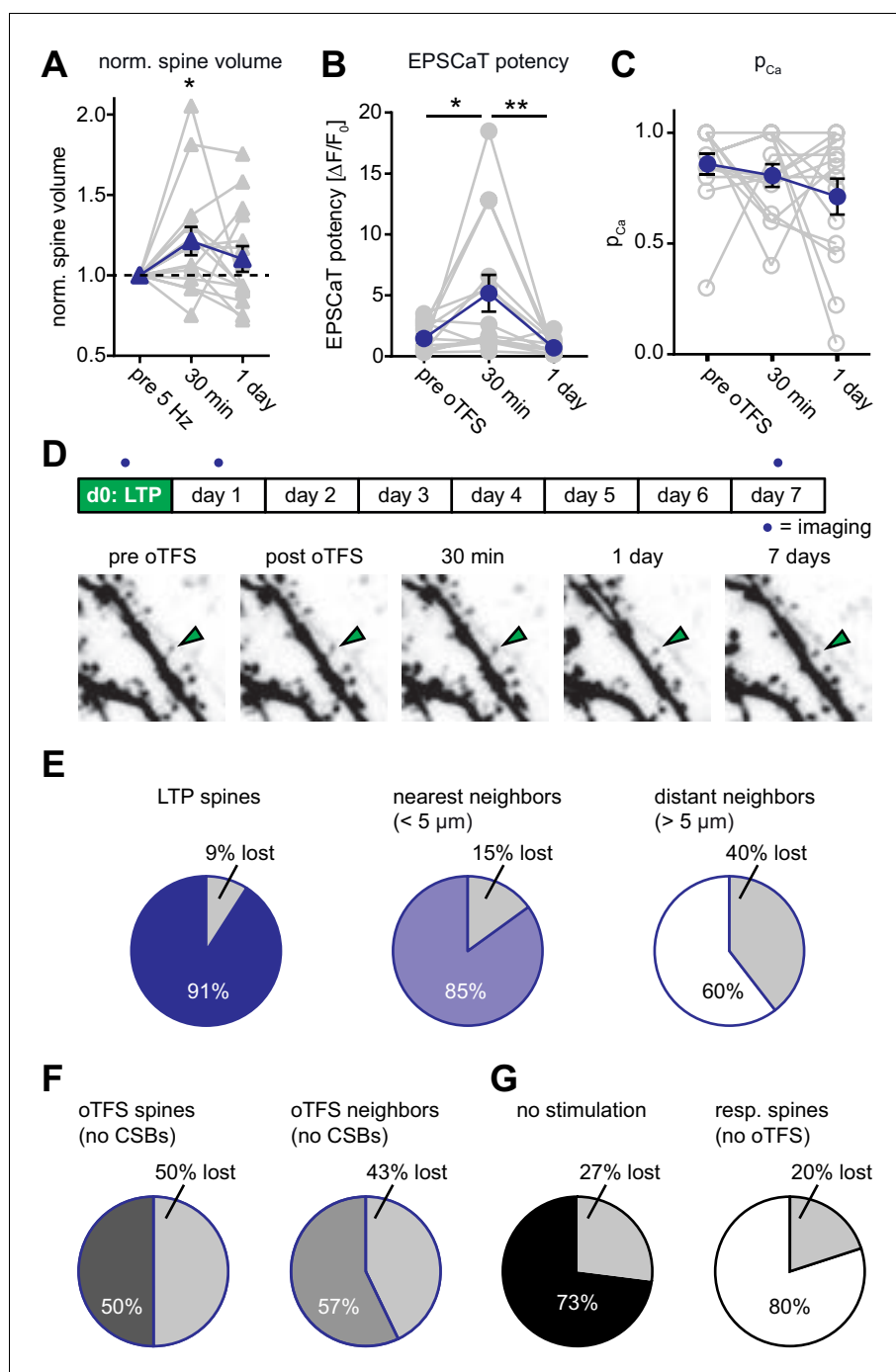
Figure 3. Long-term outcome of oTFS-induced LTP. (**A**) Analysis of volume changes of oTFS spines 30 min and 24 hr after oTFS. The volume increase 30 min after oTFS (p=0.03, n = 15 slice cultures) was not maintained 24 hr later (p=0.42). (**B**) Analysis of EPSCaT potency before, 30 min and 24 hr after oTFS. The increased potency 30 min after oTFS (p=0.015, n = 14 slice cultures) has significantly decreased again 24 hr later (p=0.005) and was similar to the condition before oTFS (p=0.55). (**C**) EPSCaT probability (P_{Ca}) did not change 30 min and 24 hr after oTFS (p=0.32, n = 14 slice cultures). For details on the statistical tests, please refer to the Materials and Methods section. (**D**) Long-term survival analysis after LTP. Spines were imaged at d0, d1 and d7. Maximum intensity projections of mCerulean fluorescence in dendritic segment harboring a responding spine that was successfully potentiated (green arrowhead). (**E**) Spine survival 7 days after successful LTP induction on day 0. Surviving fractions are shown for responding spines, nearest and distant neighbors. (**F**) Spine survival 7 days after oTFS in experiments where no complex spike bursts were induced. Directly stimulated spines and their neighbors were analyzed separately. (**G**)

Figure 3 continued on next page

Figure 3 continued

Spine survival over 7 days under baseline conditions without any optical stimulation (black) and in spines responsive to optical test pulses (resp. spines, white) which were not exposed to plasticity-inducing protocols.
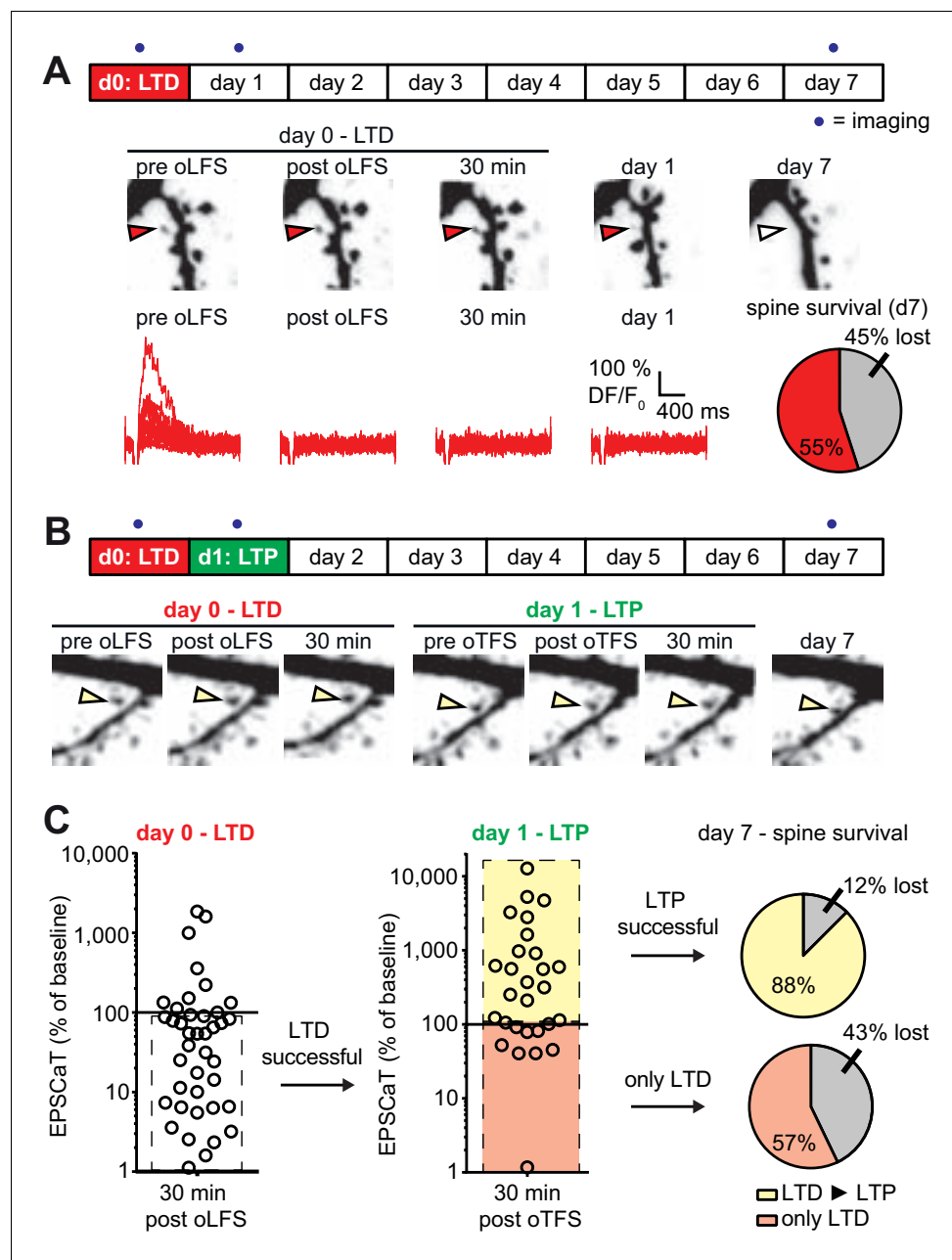
Figure 4. with one supplement: LTD-induced spine elimination is reversed by LTP or sustained synaptic transmission. (**A**) Long-term survival analysis after LTD. Spines were imaged at d0, d1 and d7. Below: Maximum intensity projections of mCerulean fluorescence in dendritic segment harboring a responding spine that was successfully depressed (red arrowhead). Open arrowhead on day seven indicates position of eliminated spine. Corresponding EPSCaT traces from indicated time points are shown in red. Pie chart shows quantification of spine survival after 7 days. (**B**) LTP 24 hr after LTD. Below: Dendritic segment harboring a responding spine that was successfully depressed on day 0 and potentiated on day 1 (yellow arrowhead). (**C**) Assessment of synaptic weight changes induced by oLFS on day 0 and oTFS on day 1. Dashed box in left graph indicates all experiments where LTD was successfully induced on day 0. Only these spines were considered in the LTP experiment on day 1 (middle). Yellow shaded box indicates all experiments where LTP was successfully induced on day 1 (after LTD on day 0; LTD ▶ LTP). Red shaded box indicates experiments where oTFS did not lead to LTP (only LTD). Pie charts show quantification of spine survival after 7 days for these two conditions.
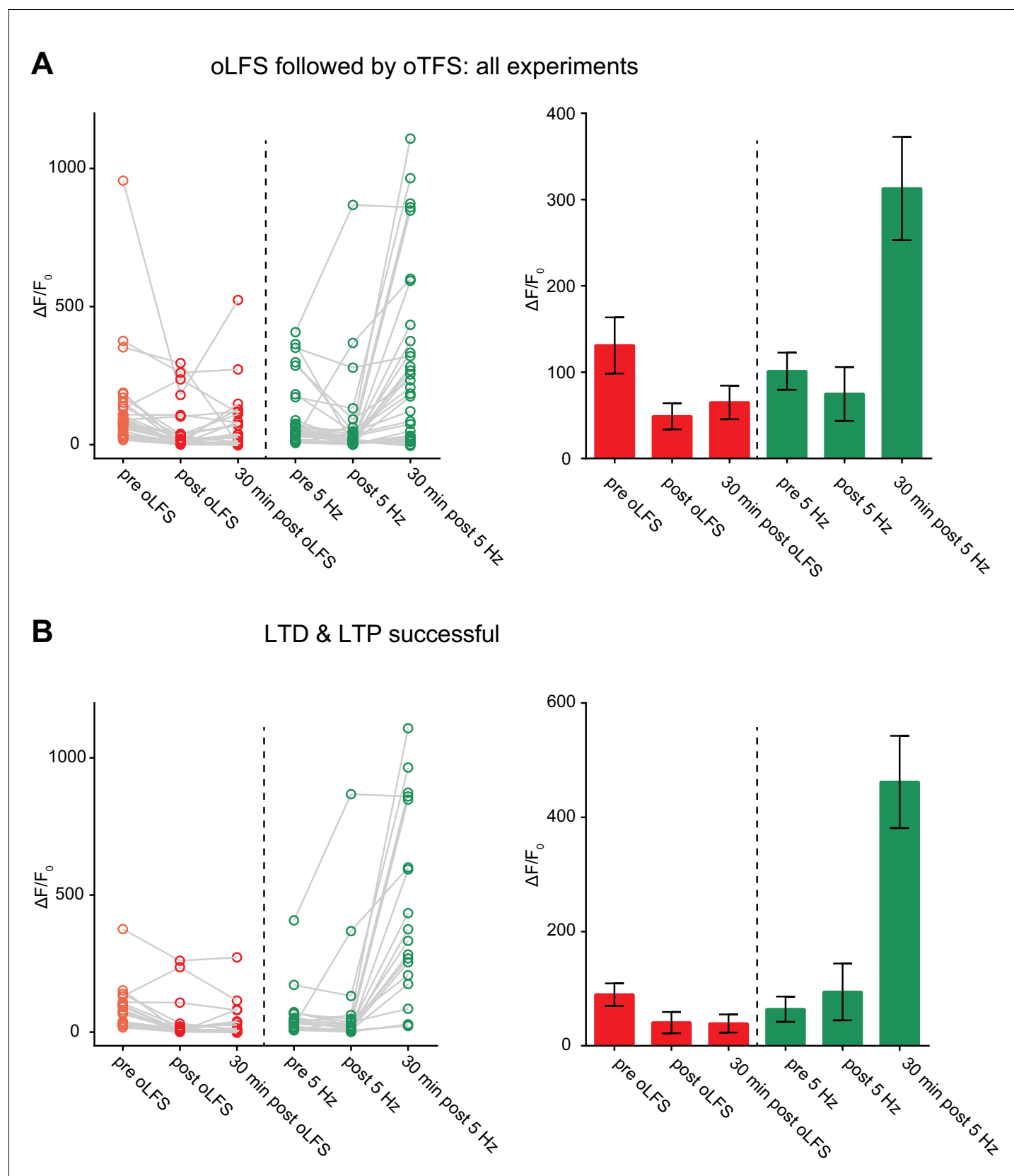DOI: https://doi.org/10.7554/eLife.39151.011

A   oLFS followed by oTFS: all experiments

B   LTD & LTP successful

Figure 4—figure supplement 1. LTD followed by LTP. (**A**) Outcome of all experiments where optogenetic low-frequency stimulation (oLFS) on day 0 was followed by optogenetic theta-frequency stimulation (oTFS) on day 1 (n = 30). (**B**) Outcome of selected experiments (subset of A, n = 18) where oLFS induced LTD (on day 0) and oTFS induced LTP of spine calcium signals (on day 1). Survival rate of this group (88%) is shown in *Figure 4c*.
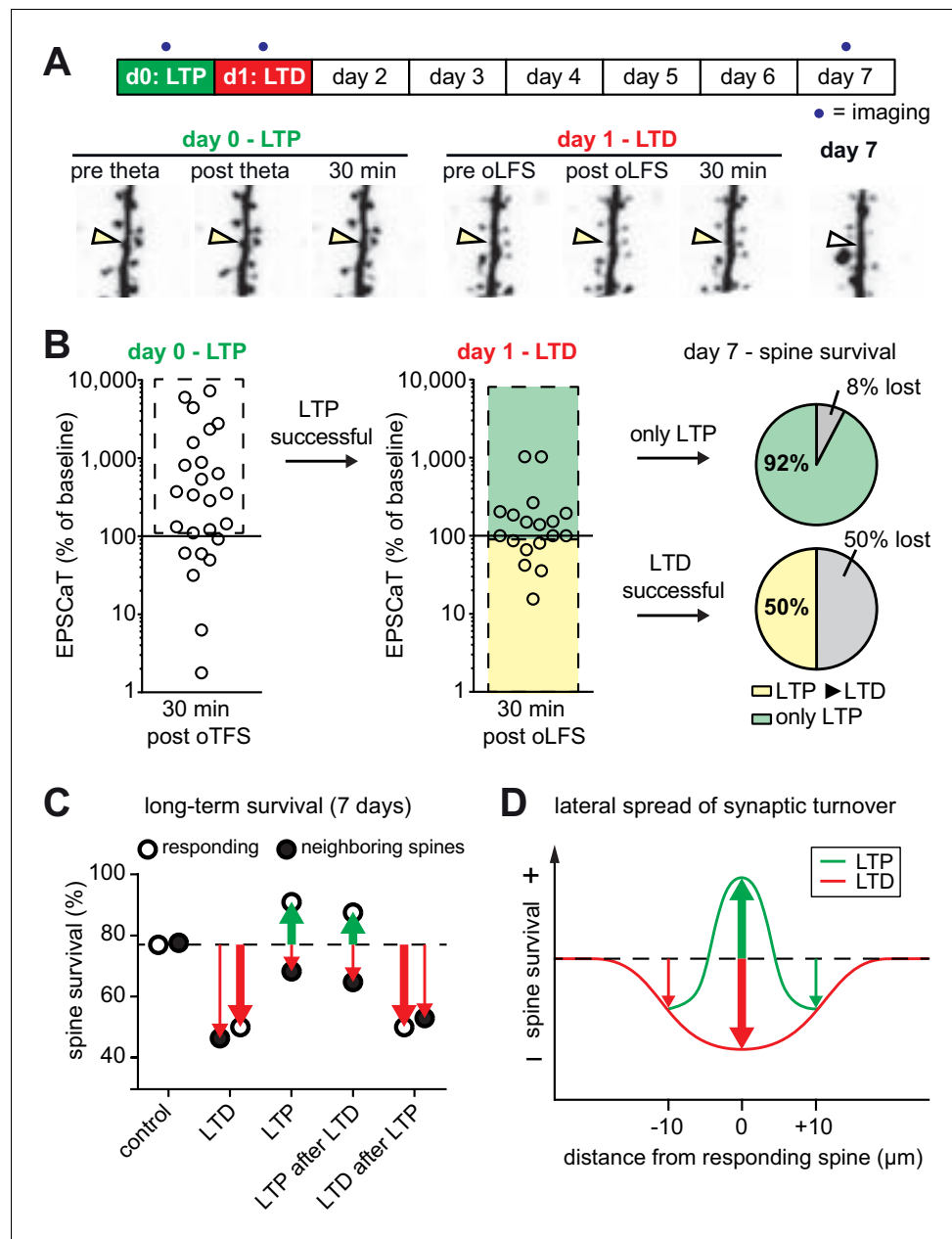
Figure 5. with one supplement: The most recent plasticity event fully accounts for synaptic tenacity. (**A**) Long-term survival analysis of experiments where LTD was induced 24 hr after LTP. Maximum intensity projections of mCerulean fluorescence in dendritic segment harboring a responding spine that was successfully potentiated on day 0 and depressed on day 1 (yellow arrowhead). (**B**) Assessment of synaptic weight changes induced by oTFS on day 0 and oLFS on day 1. Dashed box in left graph indicates all experiments where LTP was successfully induced on day 0. Only these spines were considered in the LTD experiment on day 1 (middle). Yellow shaded box indicates all experiments where LTD was successfully induced on day 1 (after LTP on day 0, LTP ▶ LTD). Note the low probability of depression after potentiation. Green shaded box encompasses experiments where oLFS did not lead to LTD or even led to LTP (only LTP). Pie charts show quantification of spine survival after 7 days for these two conditions. (**C**) Comparison of spine survival 7 days after various plasticity paradigms. Stimulated spines are shown as open circles; non-stimulated neighbors within 10 μm are shown as filled circles. Values for 'control' and 'LTD' are from *Wiegert and Oertner, 2013*. (**D**) LTP stabilizes the spine carrying the potentiated synapse, but reduces the average lifetime of more distant (>5 μm) spines on the same dendrite.
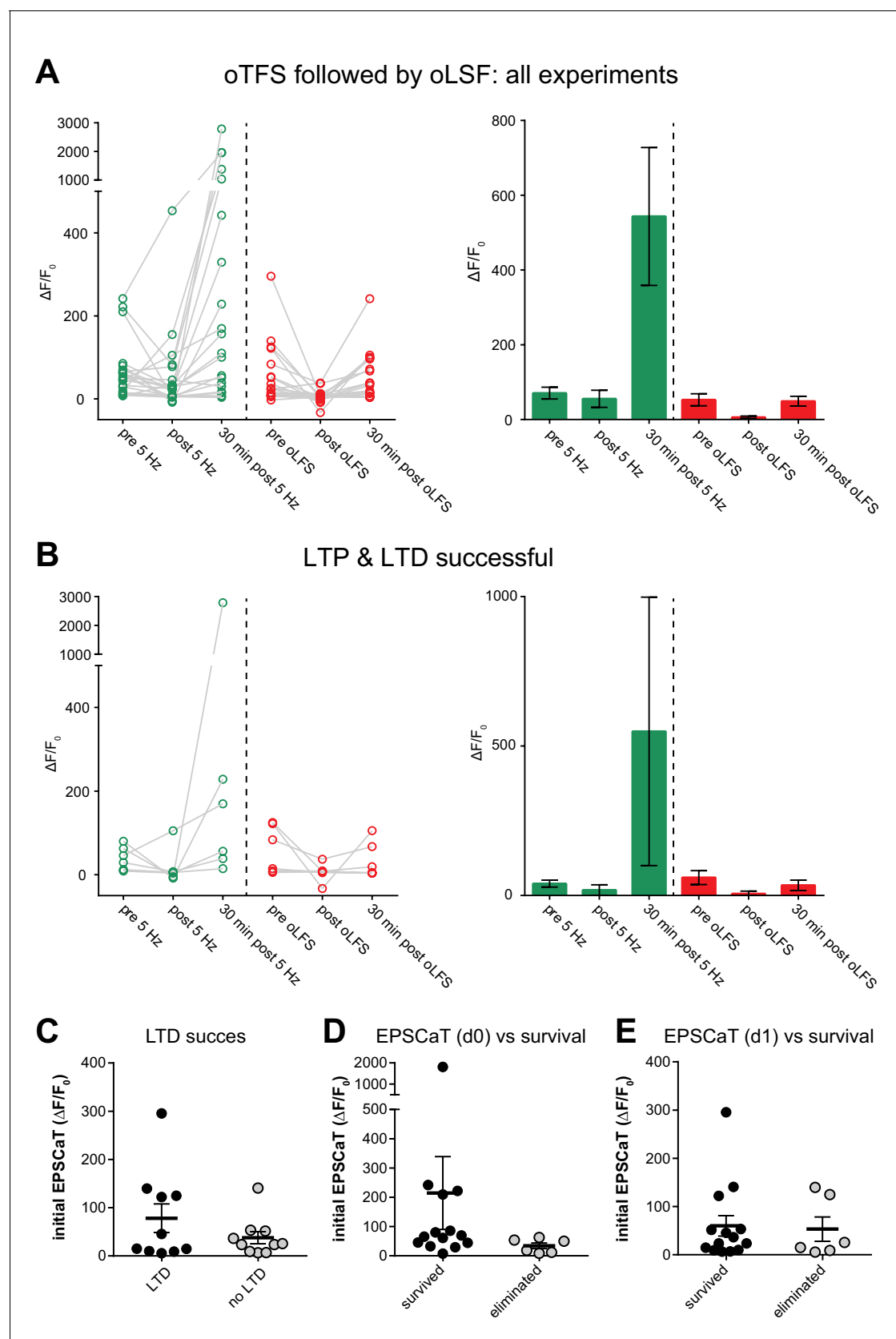
DOI: https://doi.org/10.7554/eLife.39151.014

Figure 5—figure supplement 1. LTP followed by LTD. (**A**) Outcome of all experiments where oTFS on day 0 was followed by oLFS on day 1 (n = 20). (**B**) Outcome of selected experiments where oTFS induced LTP (on day 0) and oLFS induced LTD of spine calcium signals (on day 1, n = 6). Survival rate

Figure 5—figure supplement 1 continued on next page

of this group (50%) is shown in ***Figure 5b***. (C) Initial EPSCaT amplitude on day one did not predict success of LTD induction (p>0.05, n = 20). (D) Initial EPSCaT amplitude on day 0 (before oTFS) did not predict 7 day survival (p>0.05, n = 20). (E) EPSCaT amplitude on day1 (before oLFS) did not predict 7 day survival (p>0.05, n = 20).

Efficient optogenetic silencing of neurotransmitter release with a mosquito rhodopsin

Highlights

- eOPN3 is a mosquito-derived rhodopsin that inhibits neurotransmission in neurons

- Activation of eOPN3 activates the $G_{i/o}$ pathway and reduces Ca^{2+} channel activity

- eOPN3 can suppress neurotransmission in a variety of cell types *in vitro* and *in vivo*

- Activation of eOPN3 in nigrostriatal dopamine axons modulates locomotor behavior

Authors

Mathias Mahn, Inbar Saraf-Sinik, Pritish Patil, ..., Benjamin R. Rost, J. Simon Wiegert, Ofer Yizhar

Correspondence

ofer.yizhar@weizmann.ac.il

In brief

This study describes the engineering, validation, and application of a novel optogenetic tool, eOPN3, based on a mosquito homolog of encephalopsin. Illumination of eOPN3-expressing synaptic terminals leads to robust and stable suppression of synaptic transmission through activation of inhibitory G protein signaling.

CellPress

Neuron

NeuroResource

Efficient optogenetic silencing of neurotransmitter release with a mosquito rhodopsin

Mathias Mahn,[1,2,11] Inbar Saraf-Sinik,[1,11] Pritish Patil,[1,11] Mauro Pulin,[3,11] Eyal Bitton,[1] Nikolaos Karalis,[2]
Felicitas Bruentgens,[5] Shaked Palgi,[1] Asaf Gat,[1] Julien Dine,[1] Jonas Wietek,[1] Ido Davidi,[1] Rivka Levy,[1] Anna Litvin,[1]
Fangmin Zhou,[3] Kathrin Sauter,[3] Peter Soba,[3,4] Dietmar Schmitz,[5,6,7,8,9,10] Andreas Lüthi,[2] Benjamin R. Rost,[6]
J. Simon Wiegert,[3] and Ofer Yizhar[1,12,*]

[1]Department of Neurobiology, Weizmann Institute of Science, Rehovot 76100, Israel
[2]Friedrich Miescher Institute for Biomedical Research, Basel, 4058, Switzerland
[3]Center for Molecular Neurobiology Hamburg, Hamburg 20251, Germany
[4]LIMES Institute, University of Bonn, Bonn 53115, Germany
[5]Charité-Universitätsmedizin Berlin, Berlin 10117, Germany
[6]German Center for Neurodegenerative Diseases (DZNE), Berlin 10117, Germany
[7]Bernstein Center for Computational Neuroscience, Berlin 10115, Germany
[8]Cluster of Excellence NeuroCure, Berlin 10117, Germany
[9]Einstein Center for Neurosciences Berlin, Berlin 10117, Germany
[10]Max-Delbrück Center for Molecular Medicine, Berlin 13125, Germany
[11]These authors contributed equally
[12]Lead contact
*Correspondence: ofer.yizhar@weizmann.ac.il
https://doi.org/10.1016/j.neuron.2021.03.013
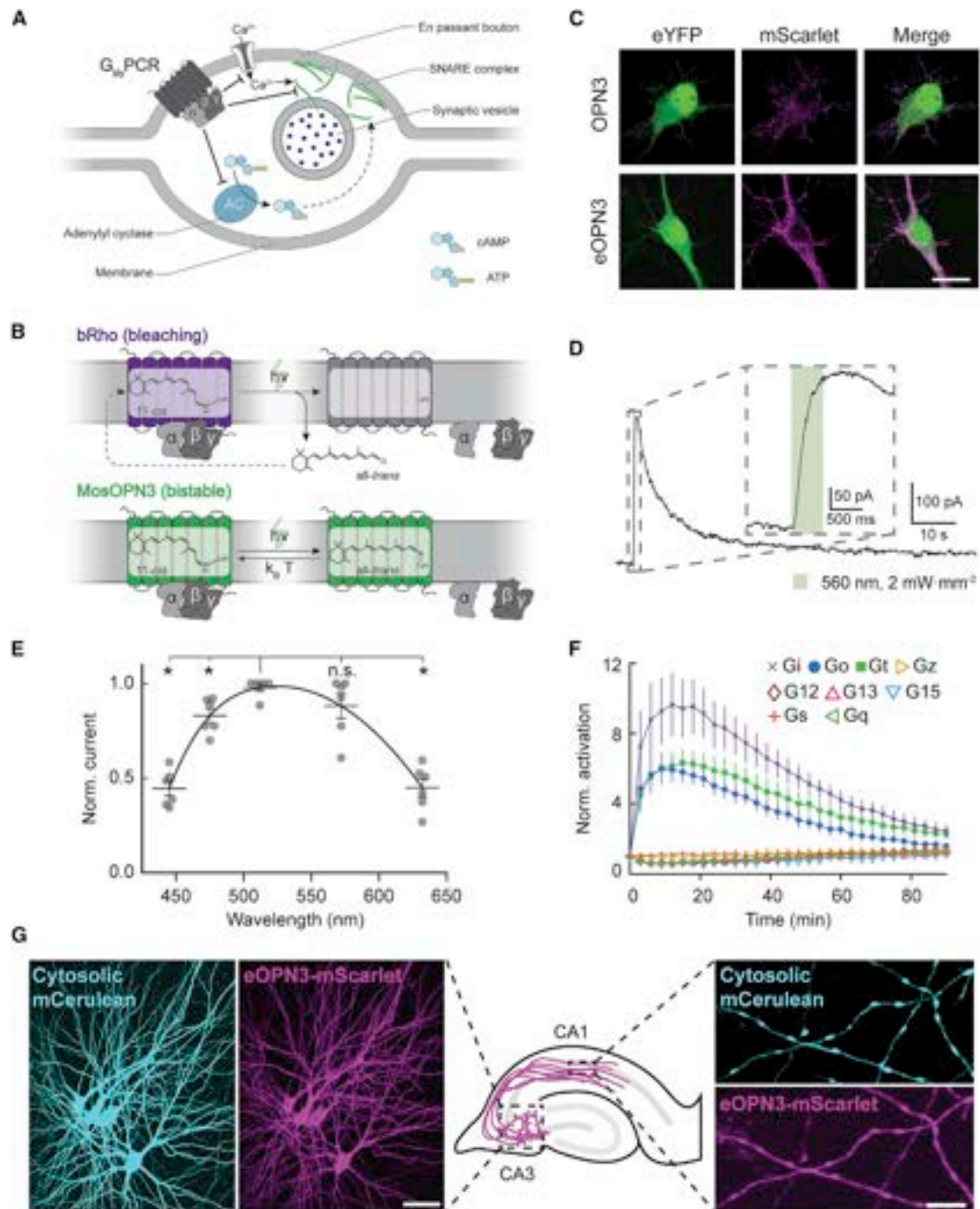
SUMMARY

Information is carried between brain regions through neurotransmitter release from axonal presynaptic terminals. Understanding the functional roles of defined neuronal projection pathways requires temporally precise manipulation of their activity. However, existing inhibitory optogenetic tools have low efficacy and off-target effects when applied to presynaptic terminals, while chemogenetic tools are difficult to control in space and time. Here, we show that a targeting-enhanced mosquito homolog of the vertebrate encephalopsin (eOPN3) can effectively suppress synaptic transmission through the $G_{i/o}$ signaling pathway. Brief illumination of presynaptic terminals expressing eOPN3 triggers a lasting suppression of synaptic output that recovers spontaneously within minutes *in vitro* and *in vivo*. In freely moving mice, eOPN3-mediated suppression of dopaminergic nigrostriatal afferents induces a reversible ipsiversive rotational bias. We conclude that eOPN3 can be used to selectively suppress neurotransmitter release at presynaptic terminals with high spatiotemporal precision, opening new avenues for functional interrogation of long-range neuronal circuits *in vivo*.

INTRODUCTION

Neurons form local and long-range synaptic connections, through which they interact with neighboring neurons and with distant neuronal circuits, respectively. Long-range neuronal communication is crucial for synchronized activity across the brain and for the transmission of information between brain regions with distinct information processing capabilities. For example, dopaminergic neurons in the substantia nigra project to the dorsal striatum via the nigrostriatal pathway and play a critical role in movement control as part of the basal ganglia circuitry (Alcaro et al., 2007). Manipulating the activity of such long-range projection pathways allows a detailed evaluation of their functional contribution to cognitive and behavioral processes. However, while optogenetics allows robust and temporally pre-

cise excitation of long-range projecting axons (Yizhar et al., 2011), silencing such long-range connections with existing optogenetic tools has proven difficult (Wiegert et al., 2017a). We have previously shown that the light-driven chloride pump halorhodopsin (eNpHR3.0) only partially suppresses neurotransmitter release. The proton-pumping archaerhodopsin (eArch3.0) triggers off-target effects, including an increase in intracellular pH and elevated spontaneous neurotransmission (Mahn et al., 2016), potentially leading to off-target behavioral consequences (Lafferty and Britt, 2020). While halorhodopsin-mediated inhibition has no effect on intra-synaptic pH (Mahn et al., 2016), it does temporarily shift the chloride reversal potential and can lead to GABA-mediated excitation (Raimondo et al., 2012). Furthermore, both halorhodopsin and archaerhodopsin require continuous delivery of high light power to sustain their ion

Figure 1. G$_{i/o}$-coupled rhodopsins for light-mediated presynaptic inhibition

(A) Schematic diagram depicting the mechanism through which G$_{i/o}$ signaling reduces the synaptic vesicle release probability. An activated GPCR leads to inhibition of voltage-gated Ca^{2+} channels as well as reduced cAMP levels, both leading directly (solid arrow) and indirectly (dashed arrow) to a reduction of Ca^{2+}-dependent vesicle release.

(B) Schematic diagram of distinct retinal binding mechanisms in bleaching (top) and bistable (bottom) rhodopsins. Bleaching rhodopsins release all-*trans*-retinal following photon absorption ($h \cdot \nu$) and need to bind a new 11-*cis*-retinal before being able to enter the next photocycle. Bistable rhodopsins sustain their covalent bond with retinal independent of its configuration, removing the influence of 11-*cis*-retinal tissue availability. In bistable rhodopsins, all-*trans*-retinal switches back to 11-*cis*-retinal either by absorbing another photon or spontaneously in the dark with a probability depending on the kinetic energy of the molecule ($k_B \cdot T$). k_B = Boltzmann constant; T = thermodynamic temperature; h = Planck constant; ν = photon frequency.

pumping activity (Zhang et al., 2007). Alternative approaches, such as optogenetic induction of synaptic plasticity (Creed et al., 2015; Klavir et al., 2017; Nabavi et al., 2014), or inhibition by disruption of the release machinery (InSynC [Lin et al., 2013]; photo-uncaging of botulinum toxin-B [Liu et al., 2019]), can effectively decrease synaptic transmission but are not as temporally precise as direct optogenetic manipulations.

Chemogenetic tools (Armbruster et al., 2007; Magnus et al., 2011) can effectively suppress presynaptic terminal function upon delivery of the cognate ligands of these engineered receptors (Basu et al., 2016; Stachniak et al., 2014). However, these approaches depend on infusion of the ligand to the location of the targeted presynaptic terminals, and their temporal specificity is fundamentally limited by the binding affinity to and clearance of the ligand. The designer receptor activated by designer drug (DREADD) hM4Di inhibits synaptic transmission (Stachniak et al., 2014) through a mechanism used by native inhibitory GPCRs, presumably through suppression of Ca^{2+} channel activity (Herlitze et al., 1996) and inhibition of the vesicle release machinery downstream of Ca^{2+} influx (Gerachshenko et al., 2005; Zhu and Roth, 2014; Zurawski et al., 2019a). We reasoned that a light-activated $G_{i/o}$-coupled rhodopsin could potentially trigger the same type of synaptic suppression (Figure 1A). However, while many known vertebrate rhodopsins couple to the $G_{i/o}$ pathway, these proteins are difficult to utilize as optogenetic tools since they undergo photobleaching after G protein dissociation as part of their natural phototransduction cycle (Bailes et al., 2012) (Figure 1B). Previous studies have revealed that bistable type-II rhodopsins are abundant across vertebrates and invertebrates (Tsukamoto and Terakita, 2010). These photoreceptors form a stable association with both the cis- and trans-configuration of the retinal chromophore (similar to the microbial type-I rhodopsin family including channelrhodopsin) and are therefore often referred to as bistable photopigments (Koyanagi et al., 2004; Terakita, 2005). Importantly, bistable type-II rhodopsins show reduced photobleaching (Bailes et al., 2012) (Figure 1B). We reasoned that members of the bistable type-II rhodopsin family that couple to $G_{i/o}$ signaling would be suitable candidates for light-mediated silencing of neurotransmitter release from presynaptic terminals.

Here, we tested several bistable rhodopsin variants for use as optogenetic tools, specifically addressing their expression in mammalian neurons and their capacity for $G_{i/o}$ pathway activation and light-driven inhibition of presynaptic release. While many of these invertebrate opsins failed to express in mammalian neurons, we were able to optimize the expression of a mosquito-

derived homolog of the mammalian encephalopsin/panopsin protein (OPN3). The mosquito OPN3 is a bistable photopigment that, upon activation, allows efficient and specific recruitment of the $G_{i/o}$ signaling cascade (Koyanagi et al., 2013). Using a targeting-enhanced OPN3 (eOPN3) protein, we were able to suppress synaptic release in rodent hippocampal, cortical, thalamic, and mesencephalic neurons. In behaving mice, eOPN3 triggered robust pathway-specific behavioral effects. These findings suggest that eOPN3, and potentially other members of the bistable rhodopsin family, can be utilized as optogenetic tools for potent G protein-mediated modulation of the activity of presynaptic terminals with high spatiotemporal precision.

RESULTS

Expression of naturally occurring and engineered $G_{i/o}$-coupled bistable rhodopsins in mammalian neurons

We reasoned that the efficient suppression of presynaptic function by the DREADD hM4Di (Figure 1A; Stachniak et al., 2014) arises from the stable binding of the engineered ligands of these receptors (Sternson and Roth, 2014) and the subsequent, stable $G_{i/o}$-mediated signal transduction. We therefore hypothesized that rhodopsins coupling to the $G_{i/o}$ pathway could serve as potent presynaptic silencing tools provided that persistent activation of such a tool can be achieved with light. While vertebrate visual rhodopsins, which dissociate from their retinal chromophore upon illumination (Figure 1B, bRho), can in principle be used for presynaptic silencing (Li et al., 2005), it remains unclear whether these rhodopsins can provide sufficiently robust activation of the $G_{i/o}$ pathway at presynaptic terminals to support potent and sustained effects. Recent work has identified several new members of the encephalopsin subfamily of ciliary opsins, which couple to the $G_{i/o}$ pathway. Encephalopsins exist in a wide range of organisms, including the pufferfish teleost multi-tissue opsin 3a (PufTMT3a) and the mosquito opsin 3 (OPN3). These rhodopsins are intrinsically bistable, as they retain the covalent bond between the retinal chromophore and the protein moiety (Figure 1B) and display prolonged signal transduction following activation (Koyanagi et al., 2013). We tested several photoreceptors of this family for expression in mammalian neurons.

Generation and characterization of a targeting-enhanced OPN3

We previously showed that addition of an ER export signal (ER) along with a Golgi trafficking signal (ts) to the light-gated chloride

---

(C) Representative confocal images of neurons co-transfected with expression vectors for eYFP and OPN3 or eOPN3. Images show fluorescence in the eYFP channel (left), the mScarlet channel (middle) and the merged images (right). See Figure S2 for all tested rhodopsin variants and quantifications. Scale bar, 15 μm.

(D) Sample whole-cell voltage-clamp recording of a cultured hippocampal neuron co-expressing eOPN3 and GIRK2-1, held at −70 mV. Inset shows an expanded view of the GIRK current onset during the light pulse.

(E) Action spectrum of endogenous GIRK-mediated currents in neurons expressing eOPN3, normalized to peak activation per cell (n = 6, p = $3.45 \cdot 10^{-4}$ Friedman rank sum test followed by pairwise comparisons using Conover's test). Peak excitation occurred at 512 nm (p < $4.24 \cdot 10^{-3}$ Holm corrected pairwise comparisons to all other wavelengths except 572 nm).

(F) Light-dependent G protein activation by eOPN3, assayed as in Figure S3. eOPN3 specifically and strongly activated inhibitory G proteins (G_i, G_o, G_t) in a light-dependent manner (n = 5). See Figure S3 for complete assay and statistics.

(G) Two-photon maximum-intensity projections of CA3 neurons co-expressing the cytosolic fluorophore mCerulean (cyan) and eOPN3-mScarlet (magenta). Shown are the somatodendritic compartment of neurons electroporated with the two plasmids (left; scale bar, 50 μm) and their axons projecting into stratum radiatum of CA1 (right; scale bar, 5 μm). Plots depict individual data points and average ± SEM.

channel GtACR2 (eGtACR2) (Mahn et al., 2018) leads to an increase in axonal membrane localization. Applying this modification to OPN3, yielding the enhanced OPN3-ts-mScarlet-ER (eOPN3), led to an increased overall expression and enhanced membrane targeting in cultured hippocampal neurons (Figures 1C and S2A). Green light pulses delivered to neurons co-expressing eOPN3 and G protein-coupled inwardly rectifying potassium (GIRK2-1) channels triggered robust GIRK-mediated currents (Figures 1D and S2B). Activation of GIRK currents was maximal at 512 nm (Figure 1E), consistent with previous characterization of light absorption by OPN3 protein (Koyanagi et al., 2013).

We confirmed that eOPN3 retained its capacity to specifically activate the $G_{i/o}$ pathway using the GsX assay. Light-activation of GsX-expressing HEK cells yielded selective and strong activation of G_i-, G_o-, and G_t-mediated signal transduction, but not of other G proteins (Figures 1F, S2C, and S3B). To rule out undesired consequences of heterologous rhodopsin overexpression, such as impaired cell health or light-independent effects on the physiological activity of expressing neurons, we examined the intrinsic excitability of cultured hippocampal neurons expressing eOPN3-mScarlet. Whole-cell patch-clamp recordings revealed no significant difference in intrinsic properties between neurons expressing eOPN3-mScarlet and neighboring, non-expressing neurons from the same neuronal culture (Figure S4). We therefore conclude that expression of eOPN3 is well tolerated in mammalian neurons and does not result in significant light-independent physiological changes in neuronal excitability.

Next, we tested eOPN3 in pyramidal neurons of organotypic hippocampal slice cultures, a preparation that preserves the anatomical and functional connectivity between neurons in the CA3 and CA1 regions. Light delivery directly to the somatodendritic region of cells co-expressing eOPN3-mScarlet with cytoplasmic mCerulean (Figure 1G) triggered long-lasting photocurrents reversing at -105.1 ± 0.9 mV (Figure S5A), close to the calculated K$^+$ reversal potential of -102.5 mV, indicating activation of endogenous GIRK channels. This eOPN3-dependent K$^+$-conductance led to a lower input resistance (Figure S5B), a decrease in electrically evoked action potential firing (Figure S5C), a slight hyperpolarization of the resting membrane potential (Figure S5D), and an increased rheobase (Figure S5E).

Activation of eOPN3 leads to suppression of neurotransmitter release

Our findings demonstrated that eOPN3 reliably couples to the $G_{i/o}$-signaling pathway and evokes GIRK-mediated currents. Axons and boutons of mCerulean-expressing CA3 pyramidal neurons in the *stratum radiatum* in CA1 of hippocampal slice cultures (Figure 1G) showed expression of eOPN3-mScarlet, indicating that the rhodopsin is present at presynaptic terminals as well. We therefore used the autaptic neuron preparation (Bekkers and Stevens, 1991) to ask whether activation of eOPN3 triggers changes in neurotransmission via G-protein activation, similar to the DREADD hM4Di (Figure S6). Light delivery to eOPN3-expressing autaptic neurons resulted in a robust and long-lasting decrease of excitatory postsynaptic currents (EPSCs; Figure 2A) and led to an increase in the paired-pulse ra-

tio (Figure 2B), consistent with a decrease in release probability (Dobrunz et al., 1997). Light-triggered suppression of release was also found in autaptic hippocampal interneurons and was similarly accompanied by an increase in the paired-pulse ratio of the inhibitory postsynaptic currents (Figure 2C). To determine the light sensitivity of eOPN3, we varied the light exposure between 0.2 μW·s·mm^{-2} and 20 mW·s·mm^{-2} (Figure 2D). The half-maximal effect size was reached at 2.90 mW·s·mm^{-2}, meaning that 1 s continuous illumination at 2.9 mW·mm^{-2} was sufficient to reach half maximal inhibition of synaptic vesicle release. The onset of eOPN3-mediated suppression of release was rapid, with a time constant (t_{on}) of 0.24 s, and saturated after 1 s (Figure 2E). Furthermore, activation of eOPN3 significantly decreased the frequency of AP-independent miniature EPSCs (Figure 2F), but not their amplitude (Figure 2G). Together, these results are consistent with a presynaptic action of this photoreceptor on neurotransmission.

The effect of eOPN3 activation on synaptic transmission was similar to the effect of the GABA$_B$ agonist baclofen, a potent modulator of neurotransmitter release (Figures 3A and 3B; Rost et al., 2011; Scanziani et al., 1992), indicating that they both act through the $G_{i/o}$ signaling pathway. Accordingly, pre-incubating the neurons with the $G\alpha_{i/o}$ subunit blocker pertussis toxin (PTX) blocked both the eOPN3- and the baclofen-mediated effects (Figures 3A and 3B), indicating that eOPN3 acts through the PTX-sensitive $G_{i/o}$ protein signaling cascade. To examine whether the effects on synaptic transmission are dependent on GIRK channel activation, we applied SCH23390, which blocks GIRK channel currents (Kuzhikandathil and Oxford, 2002). Bath application of SCH23390 abolished the outward currents evoked by green light at the somatic compartment (Figure 3C) but had no detectable impact on the light-activated suppression of synaptic release in the same neurons (Figure 3D). These results suggest that the synaptic effects of eOPN3 are not mediated by blocking the propagation of APs, but rather by direct G protein-mediated effects at the presynaptic compartment (Wu and Saggau, 1994; Zurawski et al., 2019b).

We next tested whether presynaptically expressed eOPN3 can be used to inhibit synaptic transmission in organotypic slices, where axon terminals can be locally illuminated independently of the neuronal soma (Figure 4A). In whole-cell recordings from pairs of CA3 and CA1 neurons, local illumination of the axonal terminals in CA1 induced a potent, long-lasting, and reversible reduction of the evoked EPSC amplitude (Figures 4B–4E and S7). Light application in CA1 neither induced AP failure nor GIRK-mediated hyperpolarization in the recorded presynaptic neurons (Figure S7), suggesting that activation of eOPN3 in the axonal compartment does not reduce somatic excitability. In accordance with a reduction in evoked release and thus a direct effect of eOPN3 on neurotransmitter release, we found that both the coefficient of variation (CV, Figure 4F) and the paired-pulse ratio (PPR, Figure 4G) increased following illumination in nearly all recorded pairs. The time until 50% EPSC recovery was 6.58 $\pm$ 1.78 min (Figures S7C–S7F). Synaptic transmission in non-expressing CA3-CA1 control pairs was unaffected by light stimulation (Figures 4E–4G). We therefore conclude that eOPN3 robustly activates the $G_{i/o}$ pathway in neurons, leading to efficient
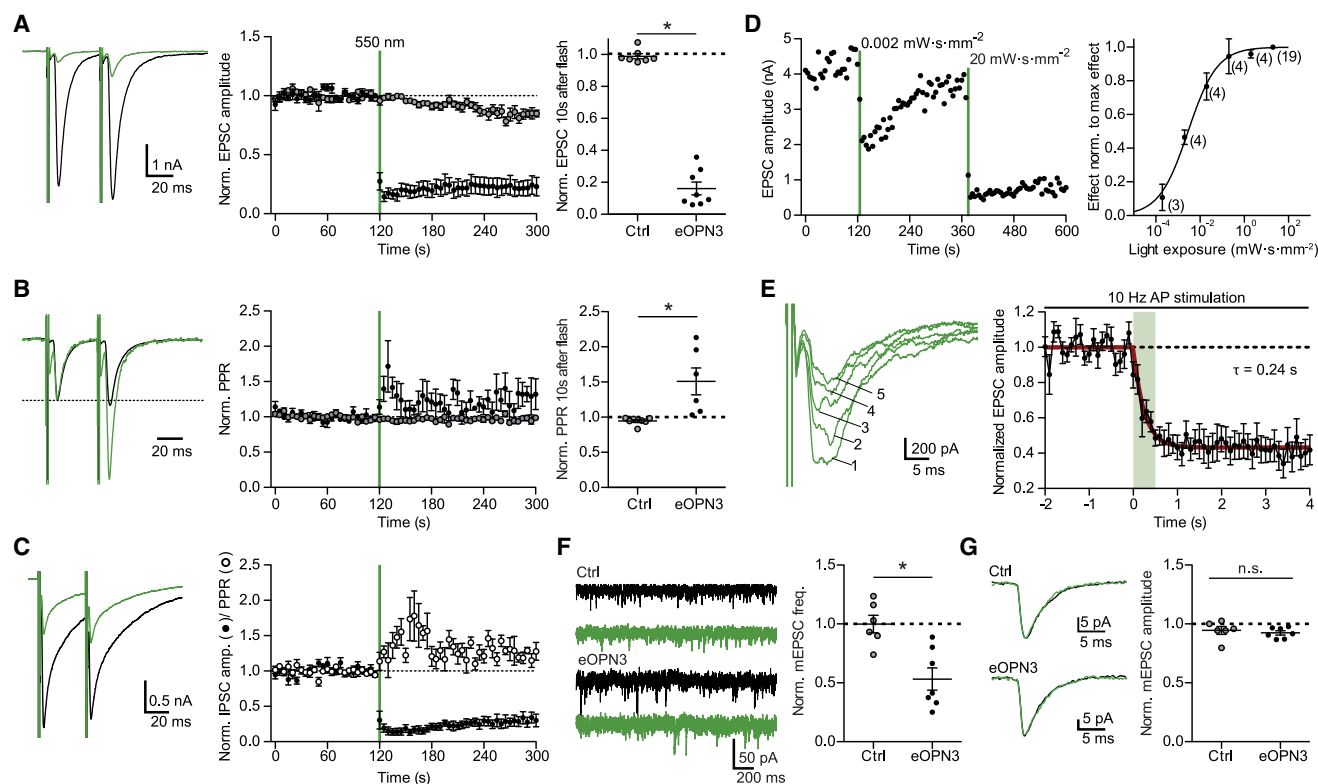
Figure 2. Light-induced inhibition of neurotransmitter release in autaptic hippocampal neurons expressing eOPN3

(A) Typical autaptic EPSCs evoked by a pair of 1 ms depolarizing current injections (40 ms inter-stimulus interval, injected currents clipped for presentation) before (black) and after (green) illumination with 550 nm light (40 mW·mm^{-2}, unless otherwise indicated). Traces are averages of 6 sweeps. A 500 ms light pulse caused sustained suppression of EPSCs in eOPN3-expressing neurons. EPSCs decreased to 16 ± 4% of baseline (n = 8), while EPSCs in control neurons were not affected by illumination (open circles, n = 7, p = $3 \cdot 10^{-4}$ two-tailed Mann-Whitney test).

(B) Traces from (A) scaled to the amplitude of the first EPSC (dashed line). Illumination increased the paired-pulse ratio (EPSC$_2$/EPSC$_1$) in the eOPN3-positive neurons (n = 6) compared to controls (p = $1.2 \cdot 10^{-3}$ unpaired, two-tailed Student's t test).

(C) Amplitudes and PPR of evoked autaptic IPSCs in GABAergic neurons, compared to the pre-light baseline (IPSCs: n = 7; PPR: n = 5).

(D) Quantification of light exposure required for half maximal synaptic inhibition. Normalized effect size was fit as a sigmoidal dose-response curve (n is reported next to the measurement points, EC$_{50}$ = 2.895 μW·s·mm^{-2}).

(E) Time-course of the eOPN3 activation on EPSC amplitudes evoked by APs triggered at 10 Hz. Traces show five consecutive EPSCs of the train following the onset of a single 500 ms light pulse. EPSCs decreased with a time constant t$_{on}$ of 240 ms (n = 6).

(F) Representative traces of mEPSCs (left) and quantification (right). eOPN3 activation decreased mEPSC frequency to 53 ± 9% compared to baseline (n = 7), significantly different from controls (n = 6, p = $3 \cdot 10^{-3}$, two-tailed Mann-Whitney test).

(G) Quantal EPSC amplitude in eOPN3-expressing and control neurons after illumination (p = 0.3 unpaired, two-tailed Student's t test). Plots show individual data points and average (black) ± SEM.

---

suppression of presynaptic vesicle release that recovers spontaneously within minutes.

To predict the effects of eOPN3-mediated inhibition *in vivo*, we virally transduced CA3 pyramidal cells in organotypic hippocampal slice cultures, emulating the most commonly used method for gene transfer *in vivo* (Figures 4H–4M). To avoid both recurrent polysynaptic activity of the CA3 network and contribution of somatic eOPN3 activation, CA3 axons were dissected from their somata at the boundary of CA3 to CA1 (Figure 4H). The PSC amplitude evoked by electrical stimulation of isolated Schaffer collateral axons was attenuated by 56 ± 5% following a single 500 ms light pulse to the terminal field in the CA1 (Figures 4I–4L) and recovered to baseline levels with a time constant of 4.57 min (95% CI: 4.19 to 4.97; R^2: 0.90; Figure 4M). As before,

the CV of synaptic responses increased in the 5 min following light stimulation, and eventually returned to baseline values. The lower efficacy of PSC amplitude reduction recorded in this experimental setup (Figure 4K) compared with the efficacy observed in paired recordings (81 ± 4%, Figure 4E) is likely due to the contribution of non-expressing axons to the PSCs evoked by field stimulation.

GPCRs may act at presynaptic terminals as canonical or noncanonical modulators of synaptic transmission (Zurawski et al., 2019a). It has been reported that canonical GPCR-mediated presynaptic inhibition decreases neurotransmission by altering the probability of vesicle release and changing the short-term plasticity profile of modulated synapses (Chalifoux and Carter, 2011), leading in some cases to suppression of initial release
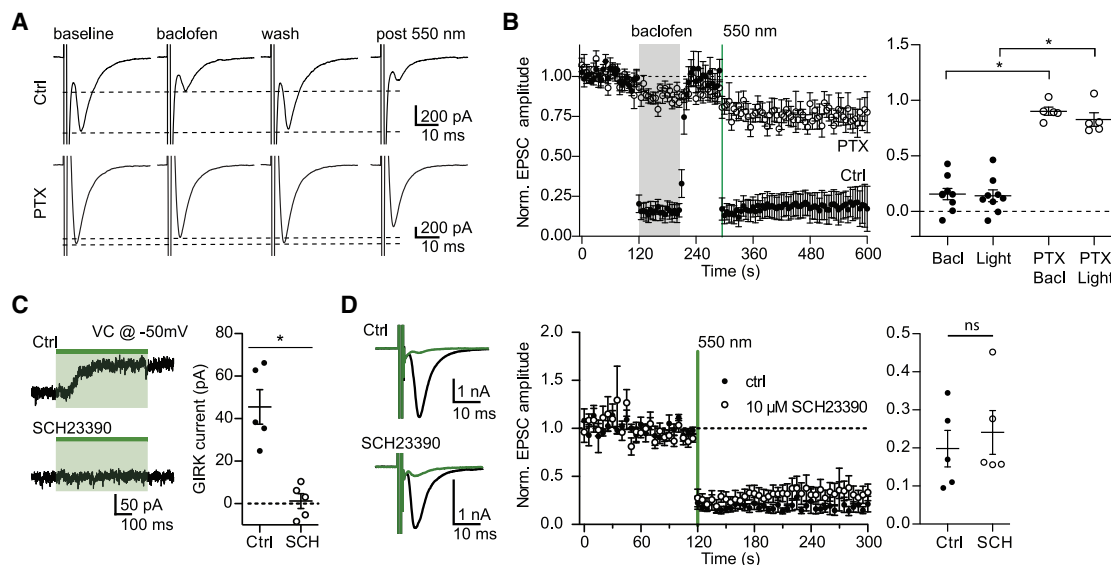
Figure 3. The effect of eOPN3 on neurotransmitter release is sensitive to pharmacological inhibition of $G_{i/o}$-protein signaling but is not affected by a GIRK channel blocker

(A) Action potential-evoked EPSCs in control neurons (upper row) were suppressed both by the $GABA_BR$ agonist baclofen (30 μM) and by subsequent activation of eOPN3 with 550 nm light (500 ms, 40 $mW \cdot mm^{-2}$). In pertussis toxin (PTX)-treated neurons (20–26 h pre-treatment, 0.5 $\mu g \cdot mL^{-1}$, bottom row), both baclofen and eOPN3 largely failed to suppress release.

(B) Averaged time-course of EPSCs recorded in neurons treated with PTX (open circles; n = 5) and neurons not treated with PTX (filled circles; n = 9; p = $3 \cdot 10^{-4}$ Kruskal-Wallis test followed by Dunn's multiple comparison tests: p < 0.05 for Bacl versus PTX Bacl, Light versus PTX Bacl and Light versus PTX Light).

(C) Illumination of eOPN3-expressing neurons evokes robust outward currents (45.5 ± 8.1 pA, n = 5), which are abolished in the presence of the GIRK channel blocker SCH23390 (10 μM, 1.2 ± 3.5 pA; n = 5; p = $1 \cdot 10^{-3}$ unpaired, two-tailed Student's t test).

(D) The extent and time-course of EPSC suppression by eOPN3 activation is not affected by the GIRK channel blocker SCH23390 (filled circles: ctrl recordings, n = 5; open circles: SCH23390, n = 5; p = 0.59 unpaired, two-tailed Student's t test). Plots show individual data points and average ± SEM.

but facilitation of subsequent responses. To better characterize the efficacy of eOPN3-mediated synaptic inhibition during higher firing rates, we applied trains of 10 stimulations at 25 Hz (Figures 4N–4P). Postsynaptic responses in the dark showed facilitation for the initial pulses while displaying depression toward the end of the train. In accordance with our previous single-pulse field stimulation results, light activation of eOPN3 inhibited the first pulse by an almost identical amount (single pulse stimulation: 44 ± 5% versus train stimulation: 47 ± 5% of initial strength). Consistent with our paired recording data, eOPN3 increased the PPR of the initial two pulses (PSC 2 / PSC 1) and maintained facilitation throughout the train. Nonetheless, light activation of eOPN3 robustly suppressed the entire sequence of PSCs in the stimulus train, albeit to a slightly lower degree for all the consecutive pulses relative to the initial one (suppression of the 10th pulse was 43 ± 2% of the initial strength).

Integration of eOPN3-based manipulation with two-photon Ca^{2+} imaging

To assess whether eOPN3 can be combined with two-photon imaging, we tested eOPN3 activation by two-photon absorption. In CA3 pyramidal cells of organotypic hippocampal cultures expressing eOPN3 and GIRK2-1, we compared green light-evoked GIRK channel currents to fast spiral scanning on the soma or slow raster scanning across the somatodendritic compartment with a femtosecond-pulsed infrared laser at wavelengths

ranging from 800 to 1070 nm and at intensities ranging from 10 to 100 mW (Figures 5A–5C). Spiral scans did not evoke any detectable photocurrents (Figure 5B). Only slow raster scans at wavelengths above 980 nm and intensities above 30 mW resulted in very small photocurrents of less than 10 pA on average (Figure 5C). In contrast, green-light activation of eOPN3 in the same cells evoked more than 20-fold larger photocurrents (Figure 5B). Thus, eOPN3 can be combined with two-photon imaging of blue-shifted sensors with minimal cross-activation.

Based on this characterization, we used two-photon imaging to determine whether eOPN3 alters Ca^{2+} influx through presynaptic voltage-gated Ca^{2+} channels, as shown for different neuromodulators (Wu and Saggau, 1994; Ikeda, 1996; Herlitze et al., 1996; Chalifoux and Carter, 2011; Burke et al., 2018). G_i-coupled GPCRs can suppress neurotransmitter release via $G_{\beta\gamma}$-mediated inhibition of voltage-gated Ca^{2+} channels (Herlitze et al., 1996; Kajikawa et al., 2001), possibly by delaying the time of first opening or by shifting the voltage-dependency of channel activation (Bean, 1989). We therefore tested whether eOPN3 activation in presynaptic terminals reduces AP-evoked Ca^{2+} influx. We evoked single APs in CA3 cells co-expressing eOPN3 and jGCaMP7f (Dana et al., 2019) while imaging the corresponding presynaptic Ca^{2+} transients in CA3 cell axonal boutons in CA1 stratum radiatum (Figures 5D and 5E). The GIRK channel blocker SCH23390 was added to exclude potentially confounding GIRK channel-mediated hyperpolarization effects. Green light pulses
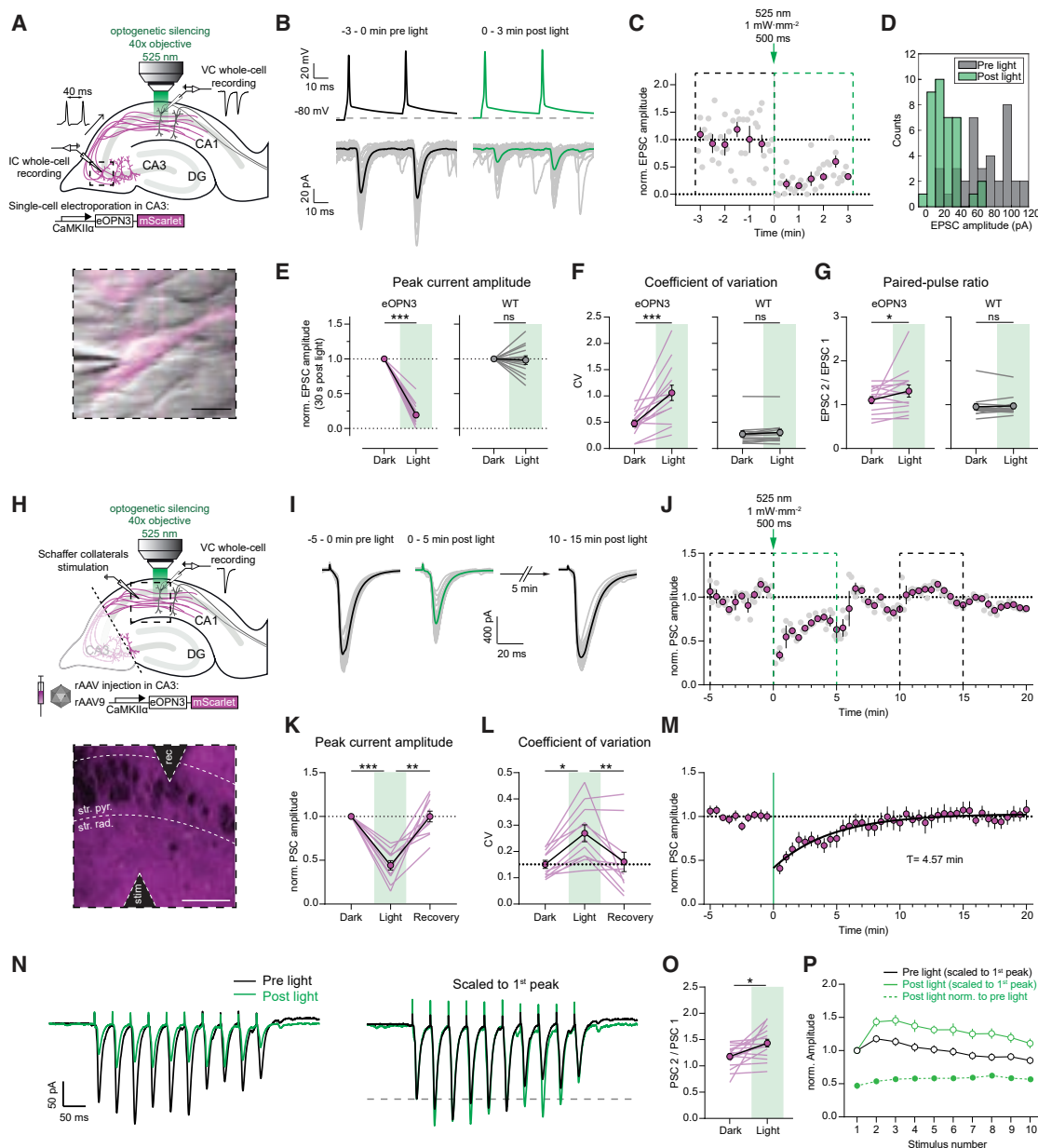
Figure 4. eOPN3 activation induces long-lasting, reversible inhibition of synaptic transmission at Schaffer collateral synapses

(A) Schematic diagram of experimental setup for whole-cell paired-recordings in organotypic hippocampal slices (see STAR Methods for details). Inset: IR-scanning gradient contrast image overlaid with the fluorescence image of patch-clamped, eOPN3 expressing CA3 neuron. Scale bar, 20 μm.

(B) Top: representative voltage traces of electrically induced APs from an eOPN3 expressing CA3 neuron, before and after light delivery to the CA1 region (dashed line shows the resting membrane potential at the beginning of the experiment. Note that APs were still reliably evoked after light stimulation). Bottom: corresponding current traces from a postsynaptic CA1 neuron in response to the paired-pulse stimulation, before and after light delivery (gray: single trials, black and green: averaged trials).

(C) Time course of the normalized EPSCs peak amplitudes from the example shown in (B) (gray circles: single trials, magenta: means of 30 s time bins ± SEM).

(D) Histogram count of peak current amplitudes of the example shown in (B).

(E) Normalized EPSC amplitudes in the eOPN3 group (left) and wild-type (WT) control group (right) (eOPN3: 0.19 ± 0.04, n = 14 pairs from 14 slices, p = 1·10^{-4}, Wilcoxon test; WT: 0.98 ± 0.06, n = 13 pairs from 13 slices, p = 0.5, Wilcoxon test).

(F) Coefficient of variation of EPSCs in the dark and after light application for the eOPN3 (left) and control group (right) (eOPN3 dark: 0.48 ± 0.06, eOPN3 light: 1.06 ± 0.15, n = 14 pairs from 14 slices, p = 4·10^{-4}, paired t test; WT dark: 0.27 ± 0.06, WT light: 0.31 ± 0.06, n = 13 pairs from 13 slices, p = 0.11, Wilcoxon test).

(G) Paired-pulse ratio change in the dark compared to after light application for the eOPN3 (left) and control group (right) (eOPN3 dark: 1.11 ± 0.08, eOPN3 light: 1.32 ± 0.14, n = 14 pairs from 14 slices, p = 0.02, Wilcoxon test; WT dark: 0.95 ± 0.07, WT light: 0.97 ± 0.06, n = 13 pairs from 13 slices, p = 0.59, Wilcoxon test). Circles in (E–G): mean ± SEM.

(legend continued on next page)

locally applied to the CA1 region before each trial significantly reduced presynaptic Ca^{2+} influx in a GIRK-independent manner (Figures 5F–5G), indicating that eOPN3 acts directly at voltage-dependent Ca^{2+} channels at presynaptic terminals similar to native G_i-coupled receptors.

In vivo characterization of eOPN3-mediated terminal inhibition

Next, we examined the efficacy and kinetics of eOPN3-mediated presynaptic silencing using *in vivo* electrophysiology. We chose to modulate the visual thalamocortical pathway, since the visual responses of V1 neurons depend on input from the lateral geniculate nucleus of the thalamus (LGN), which constitutes the main feed-forward projection from the retina to V1 (Niell and Stryker, 2008; Froudarakis et al., 2019). Using multi-shank silicon probes, we recorded bilaterally from V1 in mice expressing eOPN3 in the LGN (Figure 6A). Visual stimulation (4 s compound visual stimulus every 30 s) led to reliable evoked responses in V1 (Figures 6C and 6D left). A subset of units showed an increase in their average firing rates during visual stimulus presentation (Figure 6D). After 10 trials of visual stimulus presentation, we activated eOPN3 in LGN terminals unilaterally by 30 s continuous illumination (2 mW at the fiber tip) directed at V1. eOPN3 activation resulted in a reduced impact of visual stimulation on evoked network activity in V1 (Figures 6C and 6D), with responsive units reducing their response amplitude (Figure 6E). In units that showed a strong suppression of visually evoked responses (more than 50% during eOPN3 activation; 14 of 54 units), the average response amplitude recovered with a time constant of 5.17 min (95% CI: 1.12 to 7.20 min; R^2: 0.82; Figure 6F). By contrast, units recorded simultaneously at the contralateral (non-illuminated) side did not show a change in their visual stimulus presentation response after eOPN3 activation on the ipsilateral hemisphere (Figure 6F), demonstrating the spatial specificity of the manipulation.

To examine the efficacy and kinetics of eOPN3-mediated presynaptic silencing *in vivo* on the behavioral level, we used eOPN3 to inhibit dopaminergic (DA) input to the dorsomedial striatum (DMS) of mice during free locomotion. Previous work has demonstrated the important role of nigrostriatal DA projections in the control of animal locomotion (Alcaro et al., 2007; Kravitz et al., 2010; Grealish et al., 2010; Tecuapetla et al.,

2014; Barter et al., 2015; Borgkvist et al., 2015; da Silva et al., 2018). Briefly, striatal D1-expressing medium spiny neurons (D1-MSNs) facilitate motion upon selective, bilateral activation and induce a contralateral rotation upon unilateral stimulation. Conversely, D2-expressing MSNs (D2-MSNs) decrease motion and, upon unilateral stimulation, induce ipsilateral rotation. While D1 and D2 neurons drive motion in opposite directions, their common substantia nigra pars compacta (SNc) dopaminergic input stimulate D1-MSNs while inhibiting D2-MSNs. Overall, these studies suggest that unilateral inhibition of SNc DA projections would introduce an ipsiversive bias in free locomotion (Figure 7A). We thus expressed an eOPN3- or an eYFP-expressing control vector unilaterally in SNc DA neurons and implanted an optical fiber above the ipsilateral DMS to allow illumination of nigrostriatal DA projections (Figure 7B). Activation of eOPN3 in DA terminals (500 ms light pulses at 0.1 Hz, 540 nm, 10 mW at the fiber tip) triggered an ipsiversive bias in locomotion (Figures 7C and 7D). The rotational preference was not observed during the baseline period, became evident within the first minute following light onset, and recovered within <10 min of the last light pulse (Figure 7E), in line with the recovery kinetics of eOPN3 observed in our experiments *in vitro* and *in vivo* (Figures 4M, 6F, and S7C–S7F). Control eYFP-expressing mice did not show such side bias or light-induced equivalent dynamics (Figures 7C–7E). Apart from their strong side preference, eOPN3 mice did not differ from control mice in distance traveled (p = 0.54, Kruskal-Wallis test), center entries (p = 0.99, Kruskal-Wallis test), or time in center (p = 0.69, Kruskal-Wallis test). The magnitude of the observed behavioral effect of eOPN3 activation, quantified as the rotation index (Figure 7D, *insets*; see STAR Methods), was positively correlated with expression levels across individual mice (p = $6.1 \cdot 10^{-3}$, R^2 = 0.81) during the light activation period, but not before light delivery or after its termination (Figure 7F). No significant correlation was found with the average velocity before, during, or after eOPN3 activation (Figure 7F). Finally, one week after the initial test, we repeated the test using the same parameters. We found a high correlation in the light evoked rotational bias between the first and second trial in each mouse (Pearson's correlation coefficient: 0.8147; p = 0.0256). Taken together, our results demonstrate that eOPN3 can be used for synaptic terminal inhibition in behaving animals, with high

---

(H) Schematic diagram of experimental setup for field stimulation (see STAR Methods for details). Inset: two-photon single-plane image of the CA1 region with the stimulating and recording electrodes. eOPN3-expressing axons (magenta) surround CA1 pyramidal neurons (dark shadows). Scale bar, 50 μm.

(I) Representative voltage traces (PSCs) before, immediately and 10 min after light (gray: single trials, black and green: average trials).

(J) Time course of the normalized PSC peak amplitudes from the example shown in (I). Dashed boxes indicate the time periods shown in (I) (gray circles: single trials, magenta: 30 s time bins ± SEM).

(K) Quantification of eOPN3 effect on PSC peak amplitudes ("Dark": 5 min period before light; "Light": maximal eOPN3 effect during first 30 s post light, 0.44 ± 0.05, p < $1 \cdot 10^{-4}$; "Recovery": 10–15 min period after light, 0.99 ± 0.06, p = $1.9 \cdot 10^{-3}$; n = 11 slices, Friedman test with Dunn's multiple comparison test).

(L) Quantification of the effect of eOPN3 activation on the coefficient of variation. "Light" refers to the 5 min post light application matching the duration of the two other conditions ("Dark": 0.15 ± 0.02; "Light": 0.27 ± 0.03, p = 0.02; "Recovery": 0.16 ± 0.04, p = $8.5 \cdot 10^{-3}$, n = 11 slices, Friedman test with Dunn's multiple comparison test).

(M) Summary of all field stimulation experiments. Mono-exponential fit is shown in black.

(N) Left: representative voltage traces in response to a 10-pulse stimulus train (25 Hz). Traces are averages of 5 sweeps each. Right: same traces as on the left, each scaled to its 1st PSC peak amplitude.

(O) Quantification of the PPR (PSC 2 / PSC 1 of the train), showing increased facilitation (Dark: 1.18 ± 0.05, Light: 1.43 ± 0.07, p = 0.01, n = 16 slices, Paired t test).

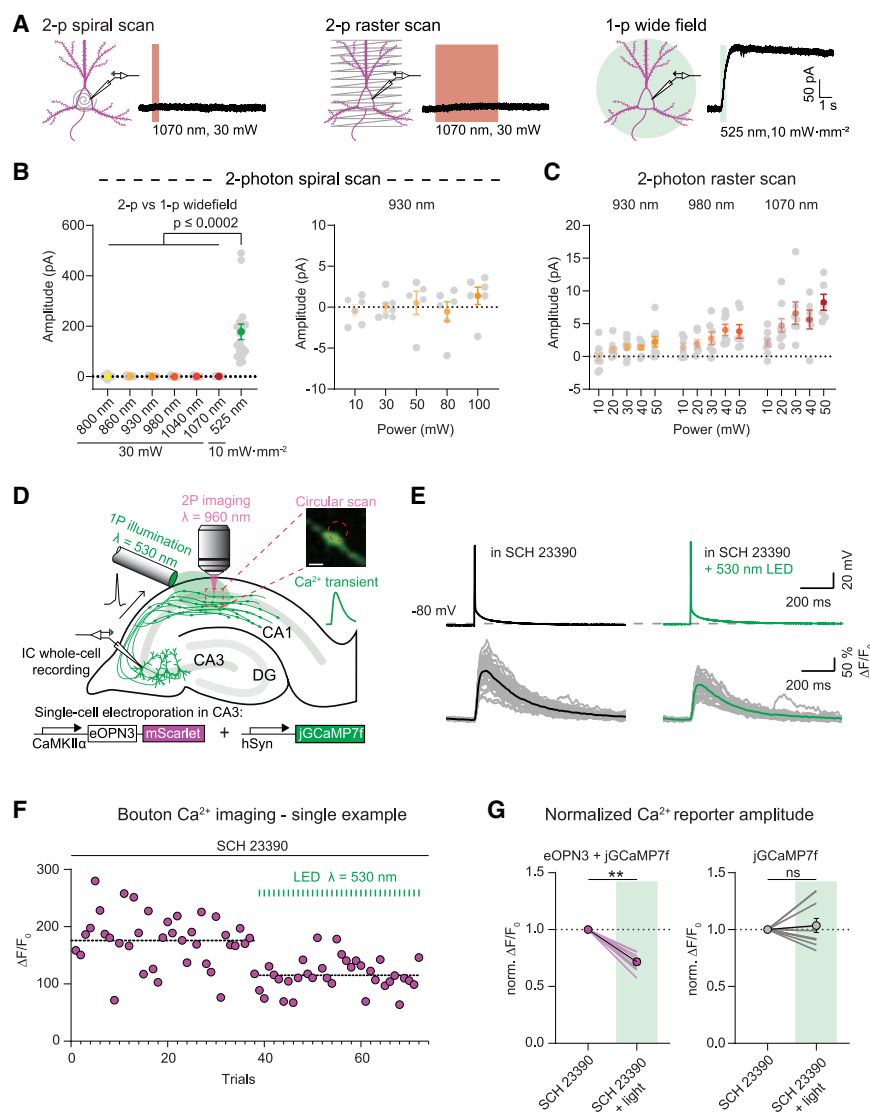(P) Summary of all train stimulation experiments.

Circles in (K–P): mean ± SEM.

Figure 5. eOPN3 two-photon activation properties and modulation of presynaptic voltage-gated Ca^{2+} channels

(A) Two-photon (left, middle) versus single-photon (right) activation of eOPN3 in CA3 pyramidal neurons in organotypic hippocampal slice cultures expressing eOPN3-mScarlet and GIRK2-1. Somatic 500 Hz spiral scans (2 ms/spiral, 250 cycles, 500 ms total duration) or raster scans (FOV = 106*106 μm, 512x512 pixels, 1.8 ms/line, 5 frames, 4.6 s total duration) at 1.09 Hz over the somatodendritic compartment were used for two-photon activation characterization. Example voltage-clamp traces show photocurrents obtained by the different stimulation modalities in the same cell.

(B) Quantification of the photocurrents elicited by two-photon versus single-photon illumination. Left: GIRK-mediated currents in eOPN3 expressing neurons stimulated with two-photon spiral scanning at wavelengths from 800 nm to 1070 nm at 30 mW, or with full-field 525 nm light (Kruskal-Wallis test, Dunn's multiple comparisons test). Right: Increasing laser intensity during spiral scans at 930 nm did not result in significant photocurrent.

(C) Slower and longer raster scanning over a larger field of view resulted in minimal outward currents and was wavelength and laser-intensity dependent (Linear regression indicated positive slopes. Bonferroni-Holm corrected p values: wavelength: p = 6.1·10^{-4}; laser power: 930 nm: p = 0.01; 980 nm: p = 7.2·10^{-3}; 1070 nm: p = 1.2·10^{-3}).

(D) Schematic diagram of presynaptic Ca^{2+} imaging experiments (see STAR Methods for details). Inset shows a single-plane jGCaMP7f image of an en passant bouton and the circular imaging-laser scanning path (red dashed circle, scale bar, 1 μm). A fiber-coupled LED was used to locally activate eOPN3 in CA1 the presence of the GIRK channel blocker SCH 23390.

(E) Top: representative voltage traces of electrically evoked APs in a transfected CA3 pyramidal neuron in the dark and after a green light pulse (dashed line shows the resting membrane potential at the beginning of the experiment). Bottom:

corresponding Ca^{2+} responses from a presynaptic bouton. Single trials are shown in gray; black and green traces represent the averaged responses before and after light, respectively.

(F) Peak jGCaMP7f transients in the dark and after green light pulses in a single experiment, indicating a light-dependent decrease in presynaptic Ca^{2+} influx. Dashed lines show the average for the two conditions.

(G) Quantification of normalized eOPN3-jGCaMP7f transients (left) (SCH 23390 + light = 0.72 ± 0.026, p = 2·10^{-3}, Wilcoxon-test, n = 10 slices) and jGCaMP7f alone (right) (SCH 23390 + light = 1.04 ± 0.06, p = 0.89, paired t test, n = 10 slices). Plots show individual data points (lines), and average (circles) ± SEM.

light-sensitivity, precisely timed onset, and behaviorally relevant recovery time.

DISCUSSION

Optogenetic silencing is a powerful tool for functionally dissecting neuronal circuits and understanding the contribution of defined neuronal populations to behavioral processes. However, silencing of long-range axonal projections has posed a formidable challenge. Our results demonstrate that a mosquito homolog of encephalopsin (OPN3) can selectively recruit G$_{i/o}$ signaling in mammalian neurons. Optimization of this rhodopsin (yielding

eOPN3) led to enhanced membrane targeting and improved expression in long-range axons. Activation of eOPN3 in four different neuronal preparations (autaptic hippocampal neurons, organotypic hippocampal slices, thalamocortical afferents, and nigrostriatal DA fibers) led to effects that are consistent with robust suppression of neurotransmitter release. In autaptic neurons, eOPN3 activation led to an inhibitory effect that was similar in its magnitude to the effect of activating endogenous GABA$_B$ receptors and was blocked by pertussis toxin, consistent with G$_{i/o}$-mediated inhibition. One potential caveat to the use of G$_{i/o}$-mediated inhibition for the manipulation of neuronal and synaptic activity is that the biochemical signaling pathways and
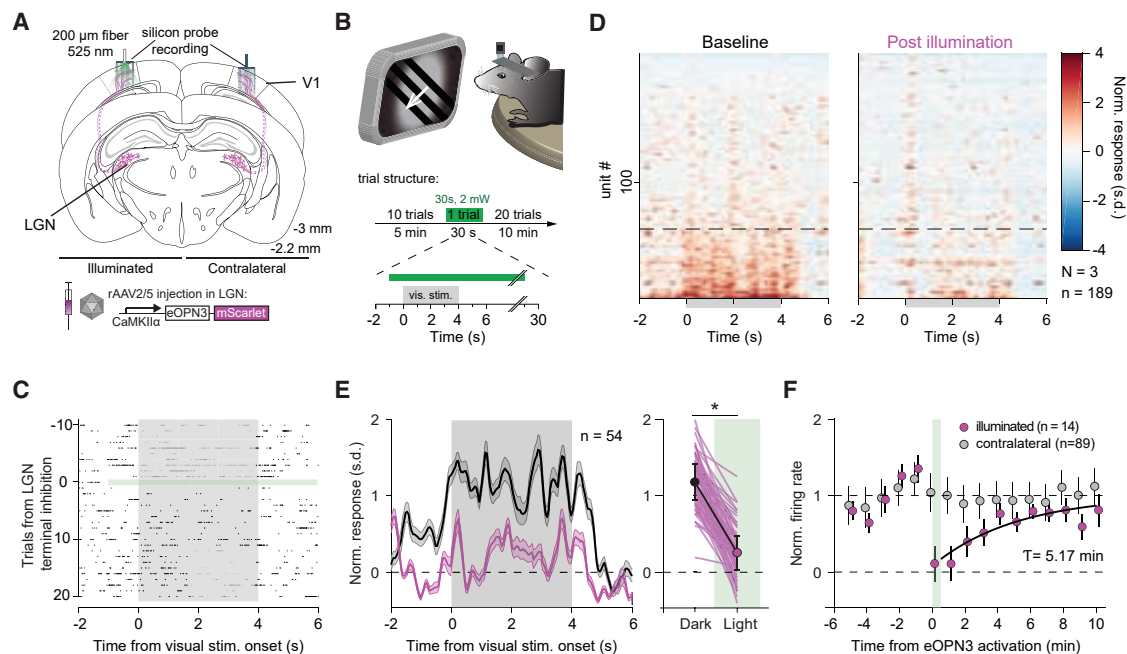
Figure 6. eOPN3 mediated suppression of thalamocortical inputs in awake head-fixed mice

(A) Schematic diagram of the investigated circuit. Lateral geniculate nucleus (LGN) neurons were bilaterally transduced with eOPN3. Acute silicon probe recordings were performed bilaterally in primary visual cortex (V1) before and after unilateral illumination of LGN terminals in V1.

(B) During recordings, head-fixed mice were presented with a compound drifting grating stimulus (4 s duration) every 30 s for 21 trials (top). Ten baseline trials were followed by a single trial paired with 30 s of light delivery (525 nm at ~2 mW from a 200 μm, 0.5 NA optical fiber) to V1, and 20 post-light trials.

(C) Raster plot of a representative V1 unit with reduced firing rate induced by eOPN3 activation.

(D) Heat plot of the population response to visual stimulus presentation of all recorded units (189 units from 3 mice) on the hemisphere of eOPN3 activation before (left) and after (right) eOPN3 activation. Units were sorted by their response magnitude to visual stimulus presentation during baseline condition. Units below the dashed line (n = 54) show a positive average response during the 4 s visual stimulus presentation.

(E) Left: Average peristimulus time histogram of the visual stimulus responsive units (below dashed line in D). Each unit's activity was normalized to the average firing rate in the 15 s prior to stimulus presentation during the two trials before eOPN3 activation. Right: Quantification of the average response during 4 s visual stimulus presentation in the two trials before (Dark) and first two trials after eOPN3 activation onset (Light). Dark: 1.17 ± 0.23, Light: 0.25 ± 0.22, $p < 1 \cdot 10^{-3}$, Wilcoxon test, n = 54 units. Plot shows individual units (lines), and population average (circles) ± SEM.
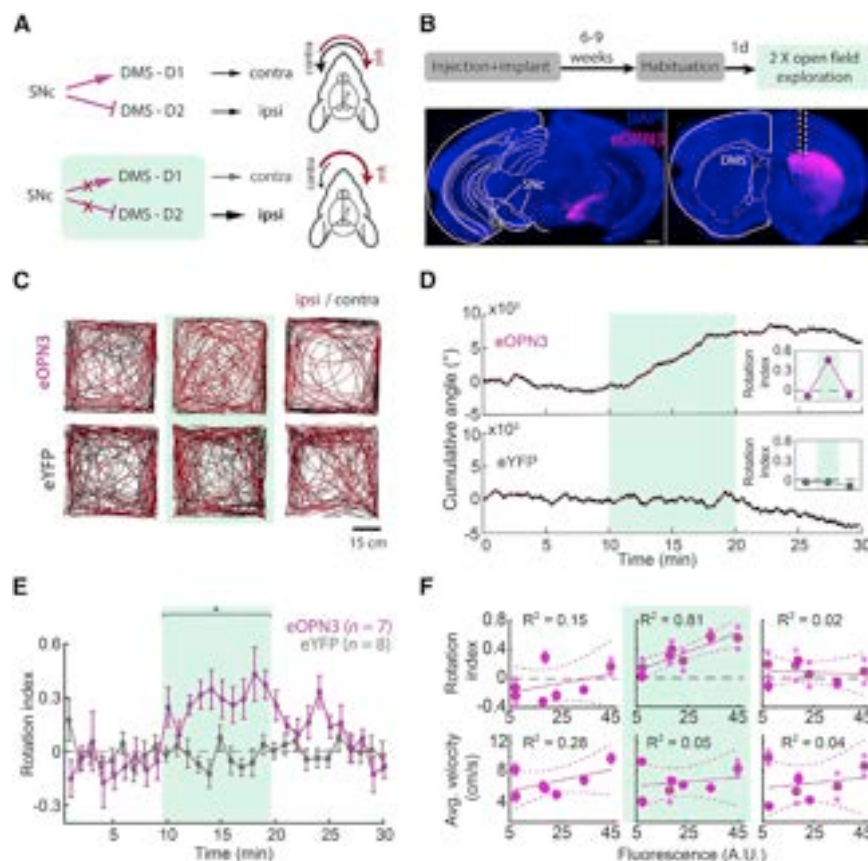
(F) Kinetics of the recovery of visual stimulus response amplitude for units that showed a reduction >50% in their visual stimulus response (magenta), fitted with a mono-exponential function (black line). Units recorded simultaneously from the contralateral hemisphere (gray) did not change their response following ipsilateral eOPN3 activation. During the baseline and post light period, the plot shows the averages of two consecutive trials (circles) ± SEM.

the effector proteins might differ among cell types and subcellular compartments. Furthermore, $G_{i/o}$-mediated inhibition is known to be activity-dependent to some extent (Brenowitz et al., 1998), and its efficacy might be dependent on the initial firing patterns and short-term synaptic plasticity features of the targeted neurons. We therefore recommend that eOPN3 effects are rigorously characterized using electrophysiology before this tool is applied in a behavioral setting.

Although we detected eOPN3-mediated GIRK currents, the effect of eOPN3 activation on the intrinsic excitability of expressing neurons was relatively weak. This suggests that activation of eOPN3 in the somatodendritic compartment induces a less efficient inhibition of neuronal spiking compared to other K+ channel-mediated optogenetic silencing approaches (Bernal Sierra et al., 2018; Beck et al., 2018). In contrast, silencing of synaptic transmission with eOPN3 was highly efficient and independent of GIRK channel activity, suggesting that eOPN3-mediated synaptic inhibition occurs through direct activity on the highly conserved presynaptic release apparatus and on Ca2+ channel

function (Dittman and Regehr, 1996; Kajikawa et al., 2001; Sakaba and Neher, 2003; Zurawski et al., 2019b). This is consistent with our observation of GIRK-channel-independent suppression of spike-evoked Ca2+ transients after eOPN3 activation. Thus, if locally activated at synaptic terminals, eOPN3 is a robust and broadly applicable optogenetic tool for inhibition of synaptic neurotransmission, similar to the DREADD receptor hM4Di, which has been successfully used for presynaptic silencing in a variety of neuronal cell types and systems (Stachniak et al., 2014; Evans et al., 2018; Malvaez et al., 2019).

The effects of GPCRs on presynaptic neurotransmitter release have been partially attributed to G-protein modulation of presynaptic Ca2+ influx (Herlitze et al., 1996). Meanwhile, non-canonical presynaptic GPCR modulators have been shown to decrease the vesicle release probability without a concomitant change in short term plasticity, through Ca2+-dependent and independent mechanisms (Hamid et al., 2014; Burke et al., 2018). Our paired-pulse facilitation results suggest that eOPN3 acts as a canonical presynaptic GPCR modulator, suppressing the initial synaptic

Figure 7. eOPN3-mediated suppression of dopaminergic projections from the substantia nigra to the dorsomedial striatum leads to ipsiversive bias during free locomotion

(A) Schematic diagram of the experimental setup and hypothesis. Unilateral expression of eOPN3 in SNc dopaminergic neurons and light-mediated suppression of their striatal projections would induce an ipsiversive side bias during free locomotion.

(B) Top: experimental timeline. Bottom: Representative images of neurons expressing eOPN3-mScarlet in the SNc (left) and their striatal projections (right) in DAPI-stained brain sections. Scale bars, 500 μm.

(C) Locomotion trajectories of representative eOPN3 (top) and eYFP (bottom) mice, over successive 10-min periods: (left to right) before, during and after light delivery (540 nm, 500 ms pulses at 0.1 Hz, 10 mW from the fiber tip), together covering continuous 30 min sessions. Red and black color code trajectory segments where the mice showed ipsilateral or contralateral angle gain, respectively.

(D) Representative cumulative angle traces of individual eOPN3-expressing (top) and eYFP-expressing (bottom) mice, over 30 min of free locomotion in an open field arena. Red and black colors depict ipsilateral or contralateral segments, respectively. Green shaded region marks the light delivery period.

(E) The rotation index (mean ± SEM), calculated as the difference between cumulative ipsilateral and contralateral rotations, divided by their sum, over 1-min bins for eOPN3-expressing mice (magenta, n = 7) and eYFP controls (gray, n = 8). Green shaded region marks the light delivery period, where eOPN3 demonstrate significant ipsiversive bias (p = $1.3 \cdot 10^{-3}$ Kruskal-Wallis test followed by Bonferroni-Holm corrected pairwise comparisons using Wilcoxon rank sum tests. Baseline: ctrl versus eOPN3 p = 1; light: ctrl versus eOPN3 p = $1.9 \cdot 10^{-3}$; post light: ctrl versus eOPN3 p = 0.09).

(F) Top: rotation index, calculated for individual mice before (left), during (middle), and after (right) light-induced activation of eOPN3, plotted against eOPN3 expression levels measured at the DMS projections (symbols). Solid and dashed lines are linear regression fit with 95% confidence intervals, respectively. Bottom: average velocity of individual mice, plotted against expression levels in the same manner shown above. R^2 values are indicated separately for each plot.

response more strongly than it does the consecutive pulses (Figures 4N–4P). This could be due to presynaptic Ca^{2+} accumulation (Jackman and Regehr, 2017) and a depolarization-triggered relief of the G-protein interaction with voltage-gated Ca^{2+} channels (Currie, 2010). Thus, eOPN3 activation biases short-term synaptic plasticity toward short-term facilitation.

We have previously shown that current approaches utilizing ion pumps for vesicle release inhibition are not suitable for suppressing presynaptic release for extended time periods (Mahn et al., 2016; Wiegert et al., 2017a; Lafferty and Britt, 2020). Although bistable rhodopsins such as eOPN3 cannot replace ion-pumping type-I rhodopsins in the sub-second range, eOPN3 can be used for experiments that require modulation in the range of minutes to hours. For even longer inhibition periods, tools such as the photoactivatable botulinum neurotoxin are likely also suitable (Liu et al., 2019). Silencing synaptic transmission using hM4Di with local agonist infusion at the terminal field (Stachniak et al., 2014) should in principle allow for similar efficiency compared to eOPN3. However, eOPN3 has the advantage of more precise temporal control and reduced problems with agonist microinfusion such as potential off-site effects due

to leakage to the cerebrospinal fluid. The time course of recovery after eOPN3 activation that we observed in vitro (Figures 4M and S7C–S7F) and in vivo (Figures 6F and 7E) is consistent across the four preparations and three cell types used. However, we would like to emphasize that the exact time constants will depend on cell type and expression level and should ideally be determined experimentally in every preparation.

Our in vitro experiments showed that eOPN3 is highly light sensitive (Figure 2D), likely due to its recovery kinetics. By relaxing the limitations imposed by tissue heating in vivo, eOPN3 allows for optical access to large brain volumes, a major constraint of type-I rhodopsins such as NpHR and Arch (Stujenske et al., 2015; Owen et al., 2019). In our single-photon excitation experiments, we used light exposures above 0.5 mW·s·mm^{-2}, leading to complete eOPN3 activation. This approach was aimed at achieving the maximal effect, making the effect of light exposures comparable as long as they are beyond saturation while not leading to tissue heating. However, for experiments where subsets of postsynaptic targets need to be specifically inhibited, light exposure should be minimized to prevent inadvertent eOPN3 activation in neighboring areas. Furthermore, the high

light sensitivity of eOPN3 necessitates working in light shielded conditions when using *in vitro* preparations or transparent organisms. For behavioral experiments, we used single light pulses spaced at 0.1 Hz. The exact irradiance and duty cycle in such experiments should be calibrated based on the volume of the targeted terminal field and the distance from other projections and somata that should remain unaffected.

We also show that eOPN3 has a small two-photon absorption cross section at the typical wavelength ranges used for two-photon Ca^{2+} indicator imaging (Figure 5B). Even continuous raster scanning on the soma and proximal dendrites of neurons expressing eOPN3 and GIRK2-1 only led to a mild somatic hyperpolarization, indicating that eOPN3 is not effectively activated. A potential use case would be to image the activity of a local network before and during inhibition of a given afferent via eOPN3 activation. Here, one potential concern is that the slow recovery kinetics of eOPN3 might lead to an accumulation of $G_{i/o}$ signaling over time, even with the low two-photon absorption properties of eOPN3. This certainly warrants careful controls, but we do not expect this to represent a major constraint in classical raster scanning two-photon imaging. Typical experiments in which network activity is continuously imaged typically involve a larger field of view (1×1 mm versus 106×106 μm used here). This effectively reduces the irradiance per illuminated presynaptic terminal. Second, whatever activation of eOPN3 molecules does take place, it will be limited to the imaging plane, meaning that out-of-focus eOPN3 molecules will not be affected. In contrast, combination of eOPN3-mediated inhibition with scanless two-photon approaches, such as temporal focusing or holographic imaging, might lead to an increased crosstalk. Although we did not observe such an effect in our experiments, one should also take into account that eOPN3 can potentially be activated by the emission light of the imaged indicator. In both types of experiments, the imaging parameters should be optimized to minimize such cross-activation.

To the best of our knowledge, this study along with the adjoining manuscript from the Bruchas and Gereau labs using the lamprey parapinopsin (PPO; Copits et al., 2021) are the first to describe an optogenetic application of bistable nonvisual rhodopsins for efficient light-gated silencing of synaptic transmission. The unique spectral features of eOPN3 and PPO, particularly in their two-photon cross sections, will potentially allow them to be utilized in concert for dual-channel optogenetic control of intracellular signaling. These two rhodopsins are part of a widespread family of non-visual rhodopsins, some of which have been shown to similarly couple to $G_{i/o}$ signaling when expressed heterologously (Koyanagi and Terakita, 2014). Thus, additional members of this rhodopsin family could potentially serve as effective tools for controlling the activity of presynaptic terminals and might be further engineered for spectral tuning or G-protein coupling specificity. Further work is needed to examine the functional properties of these little-explored photoreceptors and adapt them for optogenetic applications. Nevertheless, eOPN3-mediated silencing of transmitter release constitutes a much-needed experimental approach for light-triggered suppression of neuronal communication in the target area of long-range projections, and we expect its application will facilitate research in a variety of neurobiological studies.

STAR★METHODS

Detailed methods are provided in the online version of this paper and include the following:

- KEY RESOURCES TABLE
- RESOURCE AVAILABILITY
  ○ Lead contact
  ○ Materials availability
  ○ Data and code availability
- EXPERIMENTAL MODEL AND SUBJECT DETAILS
  ○ Animals
  ○ Cell lines
  ○ Primary cell cultures
- METHOD DETAILS
  ○ Molecular cloning of bistable rhodopsin constructs
  ○ Production of recombinant AAV vectors
  ○ Primary hippocampal neuron culture
  ○ Confocal imaging and quantification
  ○ Histology, imaging, and quantification
  ○ Cell culture and live-cell cAMP assay
  ○ Slice culture preparation and transgene delivery
  ○ Electrophysiology in cultured neurons
  ○ Slice culture electrophysiology and two-photon microscopy
  ○ *In vivo* electrophysiological recordings
  ○ *In vivo* optogenetic silencing of the nigrostriatal pathway
- QUANTIFICATION AND STATISTICAL ANALYSIS

Neuron
NeuroResource

SUPPORTING CITATIONS

The following references appear in the supplemental information: Edgar et al. (2004); Lesage et al. (1994).

REFERENCES

Alcaro, A., Huber, R., and Panksepp, J. (2007). Behavioral functions of the mesolimbic dopaminergic system: an affective neuroethological perspective. Brain Res. Brain Res. Rev. *56*, 283–321.

Armbruster, B.N., Li, X., Pausch, M.H., Herlitze, S., and Roth, B.L. (2007). Evolving the lock to fit the key to create a family of G protein-coupled receptors potently activated by an inert ligand. Proc. Natl. Acad. Sci. USA *104*, 5163–5168.

Bailes, H.J., Zhuang, L.-Y., and Lucas, R.J. (2012). Reproducible and sustained regulation of Gαs signalling using a metazoan opsin as an optogenetic tool. PLoS ONE *7*, e30774.

Ballister, E.R., Rodgers, J., Martial, F., and Lucas, R.J. (2018). A live cell assay of GPCR coupling allows identification of optogenetic tools for controlling Go and Gi signaling. BMC Biol. *16*, 10.

Barter, J.W., Li, S., Lu, D., Bartholomew, R.A., Rossi, M.A., Shoemaker, C.T., Salas-Meza, D., Gaidis, E., and Yin, H.H. (2015). Beyond reward prediction errors: the role of dopamine in movement kinematics. Front. Integr. Nuerosci. *9*, 39.

Basu, J., Zaremba, J.D., Cheung, S.K., Hitti, F.L., Zemelman, B.V., Losonczy, A., and Siegelbaum, S.A. (2016). Gating of hippocampal activity, plasticity, and memory by entorhinal cortex long-range inhibition. Science *351*, aaa5694.

Bean, B.P. (1989). Neurotransmitter inhibition of neuronal calcium currents by changes in channel voltage dependence. Nature *340*, 153–156.

Beck, S., Yu-Strzelczyk, J., Pauls, D., Constantin, O.M., Gee, C.E., Ehmann, N., Kittel, R.J., Nagel, G., and Gao, S. (2018). Synthetic Light-Activated ion channels for optogenetic activation and inhibition. Front. Neurosci. *12*, 643.

Bekkers, J.M., and Stevens, C.F. (1991). Excitatory and inhibitory autaptic currents in isolated hippocampal neurons maintained in cell culture. Proc. Natl. Acad. Sci. USA *88*, 7834–7838.

Bernal Sierra, Y.A., Rost, B.R., Pofahl, M., Fernandes, A.M., Kopton, R.A., Moser, S., Holtkamp, D., Masala, N., Beed, P., Tukker, J.J., et al. (2018). Potassium channel-based optogenetic silencing. Nat. Commun. *9*, 4611.

Bindels, D.S., Haarbosch, L., van Weeren, L., Postma, M., Wiese, K.E., Mastop, M., Aumonier, S., Gotthard, G., Royant, A., Hink, M.A., and Gadella, T.W.J., Jr. (2017). mScarlet: a bright monomeric red fluorescent protein for cellular imaging. Nat. Methods *14*, 53–56.

Borgkvist, A., Avegno, E.M., Wong, M.Y., Kheirbek, M.A., Sonders, M.S., Hen, R., and Sulzer, D. (2015). Loss of Striatonigral GABAergic Presynaptic Inhibition Enables Motor Sensitization in Parkinsonian Mice. Neuron *87*, 976–988.

Brenowitz, S., David, J., and Trussell, L. (1998). Enhancement of synaptic efficacy by presynaptic GABA(B) receptors. Neuron *20*, 135–141.

Burke, K.J., Jr., Keeshen, C.M., and Bender, K.J. (2018). Two Forms of Synaptic Depression Produced by Differential Neuromodulation of Presynaptic Calcium Channels. Neuron *99*, 969–984.e7.

Chalifoux, J.R., and Carter, A.G. (2011). GABAB receptor modulation of voltage-sensitive calcium channels in spines and dendrites. J. Neurosci. *31*, 4221–4232.

Copits, B.A., Gowrishankar, R., O'Neill, P.R., Li, J.-N., Girven, K.S., Yoo, J.J., Meshik, X., Parker, K.E., Spangler, S.M., Elerding, A.J., et al. (2021). A photoswitchable GPCR-based opsin for presynaptic inhibition. Neuron *109*. Published online May 11, 2021. https://doi.org/10.1016/j.neuron.2021.04.026.

Creed, M., Pascoli, V.J., and Lüscher, C. (2015). Addiction therapy. Refining deep brain stimulation to emulate optogenetic treatment of synaptic pathology. Science *347*, 659–664.

Currie, K.P.M. (2010). G protein modulation of CaV2 voltage-gated calcium channels. Channels (Austin) *4*, 497–509.

da Silva, J.A., Tecuapetla, F., Paixão, V., and Costa, R.M. (2018). Dopamine neuron activity before action initiation gates and invigorates future movements. Nature *554*, 244–248.

Dana, H., Sun, Y., Mohar, B., Hulse, B.K., Kerlin, A.M., Hasseman, J.P., Tsegaye, G., Tsang, A., Wong, A., Patel, R., et al. (2019). High-performance calcium sensors for imaging activity in neuronal populations and microcompartments. Nat. Methods *16*, 649–657.

Dittman, J.S., and Regehr, W.G. (1996). Contributions of calcium-dependent and calcium-independent mechanisms to presynaptic inhibition at a cerebellar synapse. J. Neurosci. *16*, 1623–1633.

Dobrunz, L.E., Huang, E.P., and Stevens, C.F. (1997). Very short-term plasticity in hippocampal synapses. Proc. Natl. Acad. Sci. USA *94*, 14843–14847.

Edgar, R.C. (2004). MUSCLE: multiple sequence alignment with high accuracy and high throughput. Nucleic Acids Res. *32*, 1792–1797.

Evans, D.A., Stempel, A.V., Vale, R., Ruehle, S., Lefler, Y., and Branco, T. (2018). A synaptic threshold mechanism for computing escape decisions. Nature *558*, 590–594.

Froudarakis, E., Fahey, P.G., Reimer, J., Smirnakis, S.M., Tehovnik, E.J., and Tolias, A.S. (2019). The Visual Cortex in Context. Annu Rev Vis Sci *5*, 317–339.

Gee, C.E., Ohmert, I., Wiegert, J.S., and Oertner, T.G. (2017). Preparation of Slice Cultures from Rodent Hippocampus. Cold Spring Harb. Protoc. *2017*, https://doi.org/10.1101/pdb.prot094888.

Gerachshenko, T., Blackmer, T., Yoon, E.-J., Bartleson, C., Hamm, H.E., and Alford, S. (2005). Gbetagamma acts at the C terminus of SNAP-25 to mediate presynaptic inhibition. Nat. Neurosci. *8*, 597–605.

Graham, F.L., and van der Eb, A.J. (1973). A new technique for the assay of infectivity of human adenovirus 5 DNA. Virology *52*, 456–467.

Grealish, S., Mattsson, B., Draxler, P., and Björklund, A. (2010). Characterisation of behavioural and neurodegenerative changes induced by intranigral 6-hydroxydopamine lesions in a mouse model of Parkinson's disease. Eur. J. Neurosci. *31*, 2266–2278.

Grimm, D., Kay, M.A., and Kleinschmidt, J.A. (2003). Helper virus-free, optically controllable, and two-plasmid-based production of adeno-associated virus vectors of serotypes 1 to 6. Mol. Ther. *7*, 839–850.

Hamid, E., Church, E., Wells, C.A., Zurawski, Z., Hamm, H.E., and Alford, S. (2014). Modulation of neurotransmission by GPCRs is dependent upon the microarchitecture of the primed vesicle complex. J. Neurosci. *34*, 260–274.

Herlitze, S., Garcia, D.E., Mackie, K., Hille, B., Scheuer, T., and Catterall, W.A. (1996). Modulation of Ca2+ channels by G-protein beta gamma subunits. Nature *380*, 258–262.

Ikeda, S.R. (1996). Voltage-dependent modulation of N-type calcium channels by G-protein beta gamma subunits. Nature *380*, 255–258.

Jackman, S.L., and Regehr, W.G. (2017). The mechanisms and functions of synaptic facilitation. Neuron *94*, 447–464.

Kajikawa, Y., Saitoh, N., and Takahashi, T. (2001). GTP-binding protein β γ subunits mediate presynaptic calcium current inhibition by GABA(B) receptor. Proc. Natl. Acad. Sci. USA *98*, 8054–8058.

Klavir, O., Prigge, M., Sarel, A., Paz, R., and Yizhar, O. (2017). Manipulating fear associations via optogenetic modulation of amygdala inputs to prefrontal cortex. Nat. Neurosci. 20, 836–844.

Koyanagi, M., and Terakita, A. (2014). Diversity of animal opsin-based pigments and their optogenetic potential. Biochim. Biophys. Acta 1837, 710–716.

Koyanagi, M., Kawano, E., Kinugawa, Y., Oishi, T., Shichida, Y., Tamotsu, S., and Terakita, A. (2004). Bistable UV pigment in the lamprey pineal. Proc. Natl. Acad. Sci. USA 101, 6687–6691.

Koyanagi, M., Takada, E., Nagata, T., Tsukamoto, H., and Terakita, A. (2013). Homologs of vertebrate Opn3 potentially serve as a light sensor in nonphotoreceptive tissue. Proc Natl Acad Sci U S A 110, 4998–5003.

Kravitz, A.V., Freeze, B.S., Parker, P.R., Kay, K., Thwin, M.T., Deisseroth, K., and Kreitzer, A.C. (2010). Regulation of parkinsonian motor behaviours by optogenetic control of basal ganglia circuitry. Nature 466, 622–626.

Kuzhikandathil, E.V., and Oxford, G.S. (2002). Classic D1 dopamine receptor antagonist R-(+)-7-chloro-8-hydroxy-3-methyl-1-phenyl-2,3,4,5-tetrahydro-1H-3-benzazepine hydrochloride (SCH23390) directly inhibits G protein-coupled inwardly rectifying potassium channels. Mol Pharmacol 62, 119–126.

Lafferty, C.K., and Britt, J.P. (2020). Off-Target Influences of Arch-Mediated Axon Terminal Inhibition on Network Activity and Behavior. Front. Neural Circuits 14, 10.

Lesage, F., Duprat, F., Fink, M., Guillemare, E., Coppola, T., Lazdunski, M., and Hugnot, J.P. (1994). Cloning provides evidence for a family of inward rectifier and G-protein coupled K+ channels in the brain. FEBS Lett. 353, 37–42.

Li, X., Gutierrez, D.V., Hanson, M.G., Han, J., Mark, M.D., Chiel, H., Hegemann, P., Landmesser, L.T., and Herlitze, S. (2005). Fast noninvasive activation and inhibition of neural and network activity by vertebrate rhodopsin and green algae channelrhodopsin. Proc. Natl. Acad. Sci. USA 102, 17816–17821.

Lin, J.Y., Sann, S.B., Zhou, K., Nabavi, S., Proulx, C.D., Malinow, R., Jin, Y., and Tsien, R.Y. (2013). Optogenetic inhibition of synaptic release with chromophore-assisted light inactivation (CALI). Neuron 79, 241–253, https://doi.org/10.1016/j.neuron.2013.05.022.

Liu, Q., Sinnen, B.L., Boxer, E.E., Schneider, M.W., Grybko, M.J., Buchta, W.C., Gibson, E.S., Wysoczynski, C.L., Ford, C.P., Gottschalk, A., et al. (2019). A Photoactivatable Botulinum Neurotoxin for Inducible Control of Neurotransmission. Neuron 101, 863–875.

Magnus, C.J., Lee, P.H., Atasoy, D., Su, H.H., Looger, L.L., and Sternson, S.M. (2011). Chemical and genetic engineering of selective ion channel-ligand interactions. Science 333, 1292–1296.

Mahn, M., Prigge, M., Ron, S., Levy, R., and Yizhar, O. (2016). Biophysical constraints of optogenetic inhibition at presynaptic terminals. Nat Neurosci 19, 554–556.

Mahn, M., Gibor, L., Patil, P., Cohen-Kashi Malina, K., Oring, S., Printz, Y., Levy, R., Lampl, I., and Yizhar, O. (2018). High-efficiency optogenetic silencing with soma-targeted anion-conducting channelrhodopsins. Nat Commun 9, 4125.

Malvaez, M., Shieh, C., Murphy, M.D., Greenfield, V.Y., and Wassum, K.M. (2019). Distinct cortical-amygdala projections drive reward value encoding and retrieval. Nat Neurosci 22, 762–769.

Mathis, A., Mamidanna, P., Cury, K.M., Abe, T., Murthy, V.N., Mathis, M.W., and Bethge, M. (2018). DeepLabCut: markerless pose estimation of user-defined body parts with deep learning. Nat. Neurosci. 21, 1281–1289.

Nabavi, S., Fox, R., Proulx, C.D., Lin, J.Y., Tsien, R.U., and Malinow, R. (2014). Engineering a memory with LTD and LTP. Nature 511, 348–352.

Niell, C.M., and Stryker, M.P. (2008). Highly selective receptive fields in mouse visual cortex. J. Neurosci. 28, 7520–7536.

Owen, S.F., Liu, M.H., and Kreitzer, A.C. (2019). Thermal constraints on in vivo optogenetic manipulations. Nat. Neurosci. 22, 1061–1065.

Pachitariu, M., Steinmetz, N., Kadir, S., Carandini, M., and Harris, K.D. (2016). Kilosort: realtime spike-sorting for extracellular electrophysiology with hundreds of channels. bioRxiv. Published online June 30, 2016. https://doi.org/10.1101/061481.

Pologruto, T.A., Sabatini, B.L., and Svoboda, K. (2003). ScanImage: Flexible software for operating laser scanning microscopes. BioMed Eng Online 2, https://doi.org/10.1186/1475-925X-2-13.

Raimondo, J.V., Kay, L., Ellender, T.J., and Akerman, C.J. (2012). Optogenetic silencing strategies differ in their effects on inhibitory synaptic transmission. Nat Neurosci 15, 1102–1104.

Rizzo, M.A., Springer, G.H., Granada, B., and Piston, D.W. (2004). An improved cyan fluorescent protein variant useful for FRET. Nat. Biotechnol. 22, 445–449.

Rost, B.R., Breustedt, J., Schoenherr, A., Grosse, G., Ahnert-Hilger, G., and Schmitz, D. (2010). Autaptic cultures of single hippocampal granule cells of mice and rats. Eur J Neurosci 32, 939–947.

Rost, B.R., Nicholson, P., Ahnert-Hilger, G., Rummel, A., Rosenmund, C., Breustedt, J., and Schmitz, D. (2011). Activation of metabotropic GABA receptors increases the energy barrier for vesicle fusion. J. Cell Sci. 124, 3066–3073.

Rost, B.R., Schneider, F., Grauel, M.K., Wizny, C., Bentz, C., Blessing, A., Rosenmund, T., Jentsch, T.J., Schmitz, D., Hegemann, P., and Rosenmund, C. (2015). Optogenetic acidification of synaptic vesicles and lysosomes. Nat Neurosci 18, 1845–1852.

Sakaba, T., and Neher, E. (2003). Direct modulation of synaptic vesicle priming by GABA(B) receptor activation at a glutamatergic synapse. Nature 424, 775–778.

Scanziani, M., Capogna, M., Gähwiler, B.H., and Thompson, S.M. (1992). Presynaptic inhibition of miniature excitatory synaptic currents by baclofen and adenosine in the hippocampus. Neuron 9, 919–927.

Schindelin, J., Arganda-Carreras, I., Frise, E., Kaynig, V., Longair, M., Pietzsch, T., Preibisch, S., Rueden, C., Saalfeld, S., and Schmid, B. (2012). Fiji: an open-source platform for biological-image analysis. Nat Methods 9, 676–682.

Stachniak, T.J., Ghosh, A., and Sternson, S.M. (2014). Chemogenetic synaptic silencing of neural circuits localizes a hypothalamus→midbrain pathway for feeding behavior. Neuron 82, 797–808.

Sternson, S.M., and Roth, B.L. (2014). Chemogenetic tools to interrogate brain functions. Annu. Rev. Neurosci. 37, 387–407.

Stujenske, J.M., Spellman, T., and Gordon, J.A. (2015). Modeling the Spatiotemporal Dynamics of Light and Heat Propagation for In Vivo Optogenetics. Cell Rep. 12, 525–534.

Suter, B.A., O'Connor, T., Iyer, V., Petreanu, L.T., Hooks, B.M., Kiritani, T., Svoboda, K., and Shepherd, G.M. (2010). Ephus: multipurpose data acquisition software for neuroscience experiments. Front. Neural Circuits 4, 100.

Tecuapetla, F., Matias, S., Dugue, G.P., Mainen, Z.F., and Costa, R.M. (2014). Balanced activity in basal ganglia projection pathways is critical for contraversive movements. Nat. Commun. 5, 4315.

Terakita, A. (2005). The opsins. Genome Biol. 6, 213.

Tsukamoto, H., and Terakita, A. (2010). Diversity and functional properties of bistable pigments. Photochem Photobiol Sci 9, 1435–1443.

Wiegert, J.S., Mahn, M., Prigge, M., Printz, Y., and Yizhar, O. (2017a). Silencing Neurons: Tools, Applications, and Experimental Constraints. Neuron 95, 504–529.

Wiegert, J.S., Gee, C.E., and Oertner, T.G. (2017b). Single-Cell Electroporation of Neurons. Cold Spring Harb Protoc 2017, https://doi.org/10.1101/pdb.prot094904.

Wiegert, J.S., Gee, C.E., and Oertner, T.G. (2017c). Viral Vector-Based Transduction of Slice Cultures. Cold Spring Harb Protoc 2017, https://doi.org/10.1101/pdb.prot094896.

Wimmer, V.C., Nevian, T., and Kuner, T. (2004). Targeted in vivo expression of proteins in the calyx of Held. Pflugers Arch. 449, 319–333, https://doi.org/10.1007/s00424-004-1327-9.

Wu, L.G., and Saggau, P. (1994). Adenosine inhibits evoked synaptic transmission primarily by reducing presynaptic calcium influx in area CA1 of hippocampus. Neuron 12, 1139–1148.

Yang, L., Lee, K., Villagracia, J., and Masmanidis, S.C. (2020). Open source silicon microprobes for high throughput neural recording. J Neural Eng *17*, 016036.

Yizhar, O., Fenno, L.E., Davidson, T.J., Mogri, M., and Deisseroth, K. (2011). Optogenetics in neural systems. Neuron *71*, 9–34.

Zhang, F., Wang, L.P., Brauner, M., Liewald, J.F., Kay, K., Watzke, N., Wood, P.G., Bamberg, E., Nagel, G., Gottschalk, A., and Deisseroth, K. (2007). Multimodal fast optical interrogation of neural circuitry. Nature *446*, 633–639.

Zhu, H., and Roth, B.L. (2014). Silencing synapses with DREADDs. Neuron *82*, 723–725.

Zurawski, Z., Thompson Gray, A.D., Brady, L.J., Page, B., Church, E., Harris, N.A., Dohn, M.R., Yim, Y.Y., Hyde, K., Mortlock, D.P., et al. (2019a). Disabling the Gβγ-SNARE interaction disrupts GPCR-mediated presynaptic inhibition, leading to physiological and behavioral phenotypes. Science *12*, eaat8595.

Zurawski, Z., Yim, Y.Y., Alford, S., and Hamm, H.E. (2019b). The expanding roles and mechanisms of G protein-mediated presynaptic inhibition. J Biol Chem *294*, 1661–1670.

STAR★METHODS

KEY RESOURCES TABLE

REAGENT or RESOURCE	SOURCE	IDENTIFIER
Bacterial and virus strains		
rAAV2/1&2.CamKIIα(0.4).OPN3-mScarlet	This paper	N/A
rAAV2/1&2.CamKIIα.eYFP.WPRE	This paper	N/A
rAAV2/1&2.CamKIIα(0.4).eOPN3-mScarlet	This paper	www.addgene.org/125712/
rAAV2/1&2.hSyn.SIO-eOPN3-mScarlet	This paper	www.addgene.org/125713/
Chemicals, peptides, and recombinant proteins		
(R)-baclofen	Tocris	Cat#0796
Clozapine-N-Oxide	Enzo Life Science	Cat#-BML-NS105
CPPene	Tocris	Cat#1265
Gabazine	Tocris	Cat#1262
NBQX	Tocris	Cat#1044
Pertussis toxin	Sigma-Aldrich	Cat#516560
Picrotoxin	Tocris	Cat#1128
SCH23390	Tocris	Cat#0925
Critical commercial assays		
GloSensor cAMP Assay	Promega	Cat#E1171
Experimental models: Cell lines		
HEK293T	Sigma-Aldrich	Cat#12022001 RRID:CVCL_0063
Experimental models: Organisms/strains		
Mouse: C57BL/6JRccHsd	Envigo	Cat#043
Mouse: C57BL/6NHsd	Envigo	Cat#044
Mouse: DAT-IRES-Cre	The Jackson Laboratory	Strain #006660
Rattus norvegicus: Sprague-Dawley	Envigo	Cat#002
Rattus norvegicus: Wistar	Charles River, bred in the animal facility, UKE Hamburg	Cat#003
Recombinant DNA		
pAAV-CaMKIIa(0.4)-OPN3-mScarlet	This Paper	N/A
pAAV-CaMKIIa(0.4)-PufTMT3a-mScarlet	This Paper	N/A
pAAV-CaMKIIa(0.4)-OPN3-M4-mScarlet	This Paper	N/A
pAAV-CaMKIIa(0.4)-PufTMT3a-M4-mScarlet	This Paper	N/A
pAAV-CamKIIα-eYFP	Karl Deisseroth	RRID:Addgene_105622; www.addgene.org/105622
pcDNA3.1-GIRK2-1	Eitan Reuveny	GenBank: NM_001025584.2
pcDNA3.1-mCerulean	Dave Piston; Rizzo et al.,2004	RRID:Addgene_15214; www.addgene.org/15214/
pAAV-CaMKIIa(0.4)-eOPN3-mScarlet	This Paper	RRID:Addgene_125712; www.addgene.org/125712/
pAAV-hSyn-SIO-eOPN3-mScarlet	This Paper	RRID:Addgene_125713; www.addgene.org/125713/
Software and algorithms		
Fiji	Schindelin et al., 2012	RRID:SCR_002285; http://imagej.net/Fiji
MATLAB 2018b	Mathworks	RRID:SCR_001622; www.mathworks.com
Prism 8.2.1	Graphpad	RRID:SCR_002798; https://www.graphpad.com
RStudio Desktop	RStudio	RRID:SCR_000432; https://www.rstudio.com
Ephus	Suter et al., 2010	https://doi.org/10.3389/fncir.2010.00100
WaveSurfer	Janelia	https://wavesurfer.janelia.org

(Continued on next page)

Continued

REAGENT or RESOURCE	SOURCE	IDENTIFIER
ScanImage	Vidrio Technologies	RRID:SCR_014307; v2017b http://www.scanimage.org/
EthoVision XT 11.5	Noldus	RRID:SCR_000441; https://www.noldus.com/ethovision-xt
DeepLabCut	Mathis et al., 2018	www.mackenziemathislab.org/deeplabcut

RESOURCE AVAILABILITY

Lead contact
Further information and requests for resources and reagents should be directed to and will be fulfilled by the lead contact, Ofer Yizhar (ofer.yizhar@weizmann.ac.il).

Materials availability
Plasmids and viral vectors for expression of eOPN3 are available from Addgene (https://www.addgene.org/Ofer_Yizhar/).

Data and code availability
The datasets and the code that support the findings of this study are available from the lead contact upon reasonable request.

EXPERIMENTAL MODEL AND SUBJECT DETAILS

Animals
Animal experiments were carried out according to the guidelines stated in directive 2010/63/EU of the European Parliament on the protection of animals used for scientific purposes. Animal experiments at the Weizmann Institute were approved by the Weizmann Institute Institutional Animal Care and Use Committee (IACUC); experiments in Berlin were approved by local authorities in Berlin and the animal welfare committee of the Charité – Universitätsmedizin Berlin, Germany. Experiments in Hamburg were done in accordance with the guidelines of local authorities and Directive 2010/63/EU. Experiments in Basel were done in accordance with institutional guidelines at the Friedrich Miescher Institute for Biomedical Research and were approved by the Veterinary Department of the Canton of Basel-Stadt. For *in vivo* electrophysiological recordings male mice (C57BL/6JRccHsd; Envigo, Cat#043) at 8-9 weeks old were used. Mean weight at the day of surgery was 23.8 g. Experimental mice were individually housed. All mice were assigned to the same experimental group. For *in vivo* behavioral experiments male and female mice (DAT-IRES-Cre; The Jackson Laboratory, Strain #006660) were used. Mice were housed in single gender groups, 2-4 littermates/cage. Littermates from single cages underwent surgery on the same day and were assigned to the eOPN3 or control group such that cages always included mixed groups. The control group included 8 mice (3 males and 5 females). Age at day of surgery was 9-14 weeks (mean = 12 weeks). Mean weight at the day of surgery was 19.6 g for females and 24.6 g for males. The eOPN3 group included 7 mice (3 males and 4 females). Age at day of surgery was 9-14 weeks (mean = 11.9 weeks). Mean weight at the day of surgery was 19.2 g for females and 24.75 g for males. The room temperature was set at 22°C (±2°C) and room humidity was set at 55% (±10%). Mice were kept in a 12-h light/dark cycle with access to food and water *ad libitum*. Mice were checked daily by animal caretakers.

Cell lines
HEK293T cells (RRID:CVCL_0063) were incubated at 37°C (5% CO2) in DMEM containing 4500 mg/L glucose, L-glutamine, (Sigma) with penicillin (100 U/mL), streptomycin (100 mg/mL), and 10% FBS. The cell line is authenticated by the European collection of authenticated cell cultures. Sex of these cells is female, and the cell line is derived from fetal human tissue.

Primary cell cultures
Primary cultured hippocampal neurons were prepared from post-natal day 0 Sprague-Dawley rat pups (Envigo, Cat#002) of either sex.

Autaptic cultures of primary hippocampal neurons on glia cell micro-islands were prepared from newborn mice (C57BL/6NHsd; Envigo, Cat#044) of either sex.

Organotypic hippocampal slices were prepared from post-natal day 5-7 Wistar rats (Charles River Cat#003 bred in the animal facility, UKE Hamburg) of either sex.

METHOD DETAILS

Molecular cloning of bistable rhodopsin constructs

The genes encoding mScarlet (Bindels et al., 2017), OPN3, PufTMT3a, OPN3-M4 and PufTMT3a-M4 were synthesized using the Twist gene synthesis service (Twist Bioscience, USA). The Rho1D4 sequence (TETSQVAPA) was added at the C terminus of all rhodopsins. All genes were subcloned into pAAV vectors under the CamKIIa promoter and in-frame with mScarlet at the C terminus. The eOPN3 plasmid was generated by adding the Kir2.1 membrane trafficking signal (KSRITSEGEYIPLDQIDINV) between the OPN3 and the mScarlet coding sequences and the Kir2.1 ER export signal (FCYENEV) following the C terminus of mScarlet. eOPN3 constructs and viruses are available from Addgene: https://www.addgene.org/Ofer_Yizhar/

Production of recombinant AAV vectors

HEK293T cells were seeded at 25%–35% confluence. The cells were transfected 24 h later with plasmids encoding AAV rep, cap of AAV1 and AAV2 and a vector plasmid for the rAAV cassette expressing the relevant DNA using the PEI method (Grimm et al., 2003). Cells and medium were harvested 72 h after transfection, pelleted by centrifugation (300 g), resuspended in lysis solution ([mM]: 150 NaCl, 50 Tris-HCl; pH 8.5 with NaOH) and lysed by three freeze-thaw cycles. The crude lysate was treated with 250 U benzonase (Sigma) per 1 mL of lysate at 37°C for 1.5 h to degrade genomic and unpackaged AAV DNA before centrifugation at 3,000 g for 15 min to pellet cell debris. The virus particles in the supernatant (crude virus) were purified using heparin-agarose columns, eluted with soluble heparin, washed with phosphate buffered saline (PBS) and concentrated by Amicon columns. Viral suspension was aliquoted and stored at –80°C. Viral titers were measured using real-time PCR. In experiments that compared between different constructs, viral titers were matched by dilution to the lowest concentration. AAV vectors used for neuronal culture transduction were added 4 days after cell seeding. Recordings were carried out between 4-20 days after viral transduction. The following viral vectors were used in this study:

AAV2/1&2.CamKIIa(0.4).OPN3-mScarlet, AAV2/1&2.CamKIIa(0.4).eOPN3-mScarlet, AAV2/5.CamKIIa(0.4).eOPN3-mScarlet, AAV2/9.CamKIIa(0.4).eOPN3-mScarlet AAV2/1&2.CamKIIa.eYFP.WPRE, AAV2/1&2.hSyn.SIO-eOPN3-mScarletAAV2/1&2.EF1a.DIO.eYFP.WPRE.

Primary hippocampal neuron culture

Primary cultured hippocampal neurons were prepared from male and female P0 Sprague-Dawley rat pups (Envigo). CA1 and CA3 were isolated, digested with 0.4 mg ml^{-1} papain (Worthington), and plated into a 24-well plate at a density of 65,000 cells per well, onto glass coverslips pre-coated with 1:30 Matrigel (Corning). Cultured neurons were maintained in a 5% CO_2 humidified incubator in Neurobasal-A medium (Invitrogen) containing 1.25% fetal bovine serum (FBS, Biological Industries), 4% B-27 supplement (GIBCO), and 2 mM Glutamax (GIBCO). To inhibit glial overgrowth, 200 μM fluorodeoxyuridine (Sigma) was added after 4 days of *in vitro* culture (DIV).

Neurons were transfected using the Ca^{2+} phosphate method (Graham and van der Eb, 1973). Briefly, the medium of primary hippocampal neurons cultured in a 24 well plate was collected and replaced with 400 μl serum-free modified eagle medium (MEM, Thermo Fisher Scientific). 30 μl transfection mix (2 μg plasmid DNA and 250 μM $CaCl_2$ in HBS at pH 7.05) were added per well. After 1 h incubation the cells were washed 2 times with MEM and the medium was changed back to the collected original medium. Cultured neurons were used between 14 – 17 DIV for experiments. The following plasmids were used in this study: pAAV-CamKIIa(0.4)-OPN3-mScarlet, pAAV-CamKIIa(0.4)-eOPN3-mScarlet, pAAV-CamKIIa(0.4)-PufTMT3a-mScarlet, pAAV-CamKIIa(0.4)-OPN3-M4-mScarlet, pAAV-CamKIIa-(0.4)PufTMT3a-M4-mScarlet, pAAV-CamKIIa(0.4)-eYFP. The pcDNA3.1-GIRK2-1 plasmid was a gift from Eitan Reuveny.

Autaptic cultures of primary hippocampal neurons on glia cell micro-islands were prepared from newborn mice (C57BL/6NHsd; Envigo, Cat#044) of either sex as previously described (Rost et al., 2010). Briefly, 300 μm diameter spots of growth permissive substrate consisting of 0.7 mg ml^{-1} collagen and 0.1 mg ml^{-1} poly-D-lysine was applied with a custom-made stamp on coverslips coated with a thin film of agarose. Astrocytes were seeded onto the glass coverslips and were allowed to proliferate in Dulbecco's modified eagle medium (DMEM) supplemented with 10% fetal calf serum and 0.2% penicillin/streptomycin (Invitrogen) for one more week to form glia micro-islands. After changing the medium to Neurobasal-A supplemented with 2% B27 and 0.2% penicillin/streptomycin, hippocampal neurons prepared from P0 mice were added at a density of 370 cells cm^{-2}. Neurons were infected with AAVs at DIV 1–3 and recorded between DIV 14 and DIV 21.

Confocal imaging and quantification

Primary cultured hippocampal neurons were transfected at 5 DIV with plasmids encoding a rhodopsin protein (mScarlet, OPN3, PufTMT3a, OPN3-M4, PufTMT3a-M4, eOPN3) along with pAAV-CamKIIa-eYFP. Four days after transfection, cells were fixed and permeabilized, washed 4 times with PBS and stained for 3 min with DAPI (5 mg/mL solution diluted 1:30,000 prior to staining). Coverslips were then mounted using PVA-DABCO (Sigma) and allowed to dry. Images of mScarlet and EYFP fluorescence were acquired using a Zeiss LSM 700 confocal microscope with a 20X magnification objective. Fluorescence was quantified using ImageJ (Schindelin et al., 2012) by marking a region containing the somatic cytoplasm using the EYFP fluorescence and then measuring the average pixel intensity in the red imaging channel.

Histology, imaging, and quantification

Mice were deeply anesthetized using pentobarbital (130 mg per kg, intraperitoneally) and then transcardially perfused with ice-cold PBS (pH 7.4, 10 ml) followed by 4% paraformaldehyde (PFA, 10 ml) solution. Heads were removed and post-fixed overnight at 4 °C in 4% PFA. Then, brains were extracted and transferred to 30% sucrose solution for at least 24 h. Coronal sections (40 μm) were acquired using a microtome (Leica Microsystems) and stained with a nucleic acid dye (4,6-diamidino-2-phenylindole (DAPI), 1:10,000). Slices were then mounted on gelatin-coated slides, dehydrated, and embedded in DABCO mounting medium (Sigma). Slices were imaged using a VS120 microscope (Olympus), at 10x magnification with two channels: 1) DAPI, to identify brain structures, the corresponding anterior-posterior coordinates and sites of lesions created by the optic fiber. 2) Either Cy3 (mScarlet - eOPN3 mice) or FITC (eYFP - control mice), to measure expression levels in cells and projections. The resulting images were then analyzed using ImageJ to measure the fluorescence of DAPI and additional fluorophores within specific target regions. For each slice, a rectangle outlining the target site was defined and copied to the contralateral (non-expressing) hemisphere. Mean fluorescence values were measured separately for each channel and compared between hemispheres, demonstrating differences in fluorophore expression but not in DAPI staining. Imaging acquisition parameters and the ensuing analysis pipeline were kept constant across mice to allow comparison between the eOPN3 and the control groups.

Cell culture and live-cell cAMP assay

Optical activation and G protein coupling of mosOPN3-mScarlett and chimeric GPCR constructs was tested in HEK293T cells using a live cell assay (Ballister et al., 2018). Briefly, GPCR constructs were subcloned into pcDNA3.1 (ThermoFisher). HEK293T cells were incubated at 37°C (5% CO_2) in DMEM containing 4500 mg/L glucose, L-glutamine (Sigma Aldrich) with penicillin (100 U/mL), streptomycin (100 mg/mL), and 10% FBS. For transfection, cells were seeded into solid white 96-well plates (Greiner) coated with poly-L-Lysine (Sigma Aldrich) and transfected with Lipofectamine 2000 (ThermoFisher) together with individual G protein chimera (GsX) and Glo22F (Promega). Cells were incubated for 24 h at 37°C, 5% CO2 and, subsequently, in L-15 media (without phenol-red, with L-glutamine, 1% FBS, penicillin, streptomycin (100 mg/mL)) and 9-*cis* retinal (10 mM) and beetle luciferin (2 mM in 10 mM HEPES pH 6.9) for 1 h at RT. Cells were kept in the dark throughout the entire time. Baseline luminescence was measured 3 times and opto-GPCR activation was then induced by illuminating cells for 1 s with an LED plate (530 nm, 5.5 μW·mm^{-2}, Phlox Corp.) Changes in cAMP levels were measured over time using GloSensor luminescence. For the assay quantification each technical repeat was normalized to its pre-light baseline.

Slice culture preparation and transgene delivery

Organotypic hippocampal slices were prepared from Wistar rats at postnatal day 5-7 as described (Gee et al., 2017). Briefly, dissected hippocampi were cut into 400 μm slices with a tissue chopper and placed on a porous membrane (Millicell CM, Millipore). Cultures were maintained at 37°C, 5% CO2 in a medium containing 80% MEM (Sigma M7278), 20% heat-inactivated horse serum (Sigma H1138) supplemented with 1 mM L-glutamine, 0.00125% ascorbic acid, 0.01 mg/mL insulin, 1.44 mM $CaCl_2$, 2 mM $MgSO_4$ and 13 mM D-glucose. No antibiotics were added to the culture medium.

For transgene delivery in organotypic slices, individual CA3 pyramidal cells were transfected by single-cell electroporation between DIV 15-20 as previously described (Wiegert et al., 2017b). The plasmids pAAV-CKIIa(0.4)-eOPN3-mScarlet, pCI-hSyn-mCerulean, CAG-GIRK2-1 and pGP-AAV-hSyn-jGCaMP7f-WPRE were all diluted to 50 ng/μl in K-gluconate-based solution consisting of (in mM): 135 K-gluconate, 10 HEPES, 0.2 EGTA, 4 Na_2-ATP, 0.4 Na-GTP, 4 $MgCl_2$, 3 ascorbate, 10 Na_2- phosphocreatine, pH 7.2, 295 mOsm/kg. An Axoporator 800A (Molecular Devices) was used to deliver 25 hyperpolarizing pulses (−12 V, 0.5 ms) at 50 Hz. During electroporation slices were maintained in pre-warmed (37°C) HEPES-buffered solution in (mM): 145 NaCl, 10 HEPES, 25 D-glucose, 2.5 KCl, 1 $MgCl_2$ and 2 $CaCl_2$ (pH 7.4, sterile filtered).

For targeted viral vector-based transduction of organotypic hippocampal slice cultures (Wiegert et al., 2017c), adeno-associated viral particles encoding AAV2/9.CamKIIa(0.4).eOPN3-mScarlet were pressure injected (20 PSI/2.5 bar, 50 ms duration) using a Picospritzer III (Parker) under visual control (oblique illumination) into CA3 *stratum pyramidale* between DIV 2-5. Slice cultures were then maintained in the incubator for 2-3 weeks allowing for virus payload expression.

Electrophysiology in cultured neurons

Whole-cell patch clamp recordings in dissociated cultures were performed under visual control using differential interference contrast infrared (DIC-IR) illumination on an Olympus IX-71 microscope equipped with a monochrome scientific CMOS camera (Andor Neo). Borosilicate glass pipettes (Sutter Instrument BF100-58-10) with resistances ranging from 3–7 MΩ were pulled using a laser micropipette puller (Sutter Instrument Model P-2000). For hippocampal neuron cultures, electrophysiological recordings from neurons were obtained in Tyrode's medium ([mM] 150 NaCl, 4 KCl, 2 $MgCl_2$, 2 $CaCl_2$, 10 D-glucose, 10 HEPES; 320 mOsm; pH adjusted to 7.35 with NaOH). The recording chamber was perfused at 0.5 mL min^{-1} and maintained at 29°C or 23°C (Figure S4A). Pipettes were filled using a potassium gluconate-based intracellular solution ([mM] 135 K-gluconate, 4 KCl, 2 NaCl, 10 HEPES, 4 EGTA, 4 MgATP, 0.3 NaGTP; 280 mOsm kg^{-1}; pH adjusted to 7.3 with KOH). Whole-cell voltage clamp recordings were performed using a MultiClamp 700B amplifier, filtered at 8 kHz and digitized at 20 kHz using a Digidata 1440A digitizer (Molecular Devices). Light was delivered using a Lumencor SpecraX light engine, using band-pass filters at 445/20, 475/28, 512/25, 572/35 and 632/22 nm

(peak wavelength/bandwidth). Photon flux was calibrated to be similar for all five wavelengths at the sample plane to allow comparison of activation efficiency. Remaining photon flux differences were less than 6%.

Whole-cell recordings in autaptic neurons were performed on an Olympus IX73 microscope using a Multiclamp 700B amplifier (Molecular Devices) under control of Clampex 10 (Molecular Devices). Data was acquired at 10 kHz and filtered at 3 kHz. Extracellular solution contained (in mM): 140 NaCl, 2.4 KCl, 10 HEPES, 10 glucose, 2 CaCl$_2$, and 4 MgCl$_2$ (pH adjusted to 7.3 with NaOH, 300 mOsm). Internal solution contained the following (in mM): 136 KCl, 17.8 HEPES, 1 EGTA, 0.6 MgCl$_2$, 4 MgATP, 0.3 Na$_2$GTP, 12 Na$_2$ phosphocreatine, 50 U ml^{-1} phosphocreatine kinase (300 mOsm); pH adjusted to 7.3 with KOH. Fluorescence light from a TTL-controlled LED system (pE4000, CoolLED) was filtered using single band-pass filters (AHF F66-415), coupled into the back port of the microscope by a liquid light guide, and delivered through an Olympus UPLSAPO 20×, 0.75 NA objective. Membrane potential was set to −70 mV, and series resistance and capacitance were compensated by 70%. To obtain strong GIRK currents, cells were voltage clamp briefly to −50 mV for the light flash only, while EPSCs were recorded at −70 mV. Synaptic transmitter release was elicited by 1 ms depolarization to 0 mV, causing an unclamped AP in the axon. To estimate the onset time course of the eOPN3-mediated effect on synaptic release, trains of APs were evoked at 10 Hz. Light was applied after 200 such APs, when EPSC amplitudes reached a steady state. Baclofen and SCH23390 were applied via a rapid perfusion system (Rost et al., 2010). Pertussis toxin was applied to the cultures 24 h before the recordings, at a concentration of 0.5 μg ml^{-1}. Cells were excluded from the analysis of the paired-pulse ratio if eOPN3 activation completely abolished the first EPSC, and mEPSCs were not analyzed when noise-events detected by an inverted template occurred at > 1 Hz, as previously described (Rost et al., 2015).

Slice culture electrophysiology and two-photon microscopy

To characterize the effects of eOPN3-activation on neuronal cell parameters, targeted whole-cell recordings of transfected CA3 pyramidal neurons were performed at room temperature (21-23°C), between 1-2 weeks after electroporation or viral transduction, under visual guidance using a BX 51WI microscope (Olympus) and a Multiclamp 700B amplifier (Molecular Devices) controlled by either Ephus (Suter et al., 2010) or WaveSurfer software (https://www.janelia.org/open-science/wavesurfer), both written in MATLAB. Patch pipettes with a tip resistance of 3-4 MΩ were filled with (in mM): 135 K-gluconate, 4 MgCl$_2$, 4 Na$_2$-ATP, 0.4 Na-GTP, 10 Na$_2$-phosphocreatine, 3 ascorbate, 0.2 EGTA, and 10 HEPES (pH 7.2). Artificial cerebrospinal fluid (ACSF) consisted of (in mM): 135 NaCl, 2.5 KCl, 4 CaCl$_2$, 4 MgCl$_2$, 10 Na-HEPES, 12.5 D-glucose, 1.25 NaH$_2$PO$_4$ (pH 7.4). To block synaptic transmission, 10 μM CPPene, 10 μM NBQX, and 100 μM picrotoxin (Tocris, Bristol, UK) were added to the recording solution. Measurements were corrected for a liquid junction potential of −14 mV.

In dual patch-clamp experiments (Figure 4), we recorded from pairs of synaptically connected CA3 pyramidal cells expressing eOPN3 and non-expressing CA1 pyramidal cells. CA3 pyramidal neurons were stimulated in current clamp to elicit 2 action potentials (40 ms Inter Stimulus Interval, 0.2 Hz) by brief somatic current injection (2 - 3 ms, 3 - 4 nA) in the absence of synaptic blockers while recording EPSCs by holding the CA1 cell at −60 mV in voltage clamp mode. A brief light pulse (500 ms, 525 nm, 1 mW·mm^{-2}) through the objective (illuminated area = 0.322 mm^2) in CA1 was used to activate eOPN3 locally at axon terminals innervating the postsynaptic CA1 pyramidal cell. For extracellular stimulation, afferent Schaffer collateral axons were stimulated (0.2 ms, 20-70 μA every 10 s) with a monopolar glass electrode connected to a stimulus isolator (IS4 stimulator, Scientific Devices). For train stimulation, 10 pulses were delivered every 40 ms. Access resistance of the recorded non-transfected CA1 neuron was continuously monitored and recordings above 20 MΩ and/or with a drift > 30% were discarded. A 16-channel pE-4000 LED light engine (CoolLED, Andover, UK) was used for epifluorescence excitation and light activation of eOPN3 (500 ms, 525 nm, 1 mW mm^{-2}). Light intensity was measured in the object plane with a 1918 R power meter equipped with a calibrated 818 ST2 UV/D detector (Newport, Irvine CA) and divided by the illuminated field of the Olympus LUMPLFLN 60XW objective (0.134 mm^2) or of the Olympus LUMPLFLN 40XW objective (0.322 mm^2). All the electrophysiological synaptic measurements in organotypic hippocampal slice cultures were performed at 33 ± 1°C.

For the eOPN3 two-photon stimulation experiments (Figure 5), a custom-built two-photon imaging setup was used based on an Olympus BX51WI microscope controlled by ScanImage 2017b (Vidrio Technologies). Electrophysiological recordings were acquired using a Multiclamp 700B amplifier controlled by the WaveSurfer software written in MATLAB (https://www.janelia.org/open-science/wavesurfer). A tunable, pulsed Ti:Sapphire laser (MaiTai DeepSee, Spectra Physics) controlled by an electro-optic modulator (350-80, Conoptics) tuned to 1040 nm was used to excite the mScarlet-labeled eOPN3. Red fluorescence was detected through the objective (LUMPLFLN 60XW, 60x, 1.0 NA, Olympus) and through the oil immersion condenser (numerical aperture 1.4, Olympus) by photomultiplier tubes (H7422P-40SEL, Hamamatsu). 560 DXCR dichroic mirrors and 525/50 and 607/70 emission filters (Chroma Technology) were used to separate green and red fluorescence. Excitation light was blocked by short-pass filters (ET700SP-2P, Chroma). In addition, the forward-scattered IR laser light was collected through the condenser, spatially filtered by a Dodt contrast tube (Luigs& Neumann) attached to the trans-illumination port of the microscope and detected with a photodiode connected to a detection channel of the laser scanning microscope. This generated an IR-scanning gradient contrast image (IR-SGC) synchronized with the fluorescence images(Wimmer et al., 2004). This approach was used for targeted patch-clamp recordings avoiding prior activation of the ultrasensitive eOPN3 with epifluorescence illumination. The two-photon laser scanning pattern used for stimulation was either a spiral scan with a repetition rate of 500 Hz above the soma (2 ms/spiral, 250 cycles, 500 ms total duration) or standard raster scans at 1.09 Hz over the somatodendritic compartment (FOV = 106×106 μm, 512×512 pixels, 1.8 ms/line, 5 frames, 4.6 s total duration). The laser wavelengths used for stimulation were 800 nm, 860 nm, 930 nm, 980 nm and 1040 nm, all at 30 mW, measured at the back focal aperture of the objective. Wide field illumination at 525 nm (10 mW/mm^2) was done with a 16 channel pE-4000 LED light engine

(CoolLED, Andover, UK) for 500 ms. An additional set of experiments was performed on a second custom-modified two-photon imaging setup (DF-Scope, Sutter) based on an Olympus BX51WI microscope controlled by ScanImage 2017b (Vidrio Technologies) and equipped with an Ytterbium-doped 1070-nm pulsed fiber laser (Fidelity-2, Coherent) for far infrared stimulation. Electrophysiological recordings were performed using a Double IPA integrated patch amplifier controlled with SutterPatch software (Sutter Instrument).

The same microscope was used to acquire images of eOPN3-expressing CA3 cells co-transfected with the cyan cell-filler fluorophore mCerulean (Rizzo et al., 2004) and their projecting axons in *stratum radiatum* of CA1 (Figure 1). The 1070-nm laser was used to excite fluorescence of mScarlet-labeled eOPN3. mCerulean was excited by a pulsed Ti:Sa laser (Vision-S, Coherent) tuned to 810 nm. Laser power was controlled by electro-optic modulators (350-80, Conoptics). Red and cyan fluorescence were detected through the objective (Olympus LUMPLFLN 60XW, 1.0 NA, or Leica HC FLUOTAR L 25x/0.95 W VISIR) and through the oil immersion condenser (numerical aperture 1.4, Olympus) by GaAsP photomultiplier tubes (Hamamatsu, H11706-40). Dichroic mirrors (560 DXCR, Chroma Technology) and emission filters (ET525/70 m-2P, ET605/70 m-2P, Chroma Technology) were used to separate cyan and red fluorescence. Excitation light was blocked by short-pass filters (ET700SP-2P, Chroma Technology). All electrophysiology recordings were analyzed using custom written scripts in MATLAB except for recordings acquired with the Double IPA integrated patch amplifier, which were analyzed with the SutterPatch software.

For presynaptic Ca^{2+} imaging experiments (Figure 5), single action potentials were triggered via a patch pipette in a CA3 pyramidal neuron co-expressing eOPN3 and jGCaMP7f or jGCaMP7f alone as control while evoked Ca^{2+} influx at distal presynaptic terminals in *stratum radiatum* of CA1 was monitored by two-photon microscopy. A custom-modified version of ScanImage 3.8 (Pologruto et al., 2003) was used to allow user-defined arbitrary line scans. jGCaMP7f was excited at 960 nm. Similar to the two-photon stimulation experiments, targeted patch-clamp recordings were achieved using IR-scanning gradient contrast image (IR-SGC) synchronized with the fluorescence images. Action potentials were triggered by brief somatic current injection (2 - 3 ms, 3 - 4 nA) in the absence of synaptic blockers while monitoring fluorescent transients at single Schaffer collateral terminals in CA1 (70-80 trials on average at 0.1 Hz). User-defined circular scans at 500 Hz across the bouton were used to repeatedly sample the fluorescent changes. During each trial (3 s), laser exposure was restricted to the periods of expected Ca^{2+} response ($\sim$1.3 s) to minimize bleaching. To activate eOPN3 selectively at the terminals, we used a fiber-coupled LED (400 μm fiber, NA 0.39, M118L02, ThorLabs) to deliver 500 ms green light pulses (l = 530 nm, 83 μW at the fiber tip) 1 s prior to the onset of electrical stimulation. During the LED pulses, upper and lower PMTs were protected by TTL triggered shutters (NS45B, Uniblitz). GIRK channels were blocked by SCH 23390 (10 μM, Tocris, Bristol, UK) throughout the entire experiment to exclude hyperpolarization-mediated effects on action potential propagation and presynaptic Ca^{2+} influx.

The photon shot-noise subtracted relative change in jGCaMP7f fluorescence ($\Delta F/F_0$) was measured by using a template-based fitting algorithm. The characteristic fluorescence time constant was extracted for every bouton by fitting a double exponential function (t_{rise}, t_{decay}) to the average jGCaMP7f signal. To estimate the Ca^{2+} transient amplitude for every trial, we fitted the bouton-specific template to every response, amplitude being the only free parameter. Response amplitude was defined as the value of the fit function at its maximum.

In vivo electrophysiological recordings

8-9 weeks old male C75/Bl6 mice were pressure injected (Picospritzer III; Parker) bilaterally into LGN (AP: - 2.2 mm; ML: +/− 2.3 mm; DV: −3.1 mm) at 50 nL/min with 200 nL adeno-associated viral particles encoding eOPN3 (AAV2/5.CKIIa(0.4).eOPN3-mScarlet) diluted to 2.5 × 10^{12} viral genomes per ml using a pulled glass capillary. Following 5-6 weeks of recovery, mice underwent 3-4 head fixation habituation sessions starting with 15 min and gradually increasing to 25 min. 7-12 weeks after virus injection, craniotomies were performed bilaterally to provide access to V1 spanning from −2.3 mm to −4.7 mm in the anterior posterior direction and 2 mm at its widest part (at AP: −3.8 mm) from ± 1.3 mm to ± 3.3 mm along the medio-lateral axis. Craniotomies were covered with Kwik-Cast (WPI Inc) to protect the brain surface from mechanical impact, dehydration, and light exposure between the silicon probe recording sessions.

For the electrophysiological recordings, two 4-shank, 128 channel silicon microprobes (128DN; 4 shanks, 150 μm shank spacing, 25 μm channel spacing, 100 μm^2 electrode area, 7 mm x 65 μm x 23 μm shank dimensions) (Yang et al., 2020) (kindly provided by Dr. S. Masmanidis, UCLA) were inserted bilaterally in the V1 at a depth of approximately 1 mm, with an insertion speed of 100 μm/min. Before each recording session, silicon probe recording sites were electroplated in a PEDOT solution to an impedance of $\sim$100 kOhm. Each silicon probe was connected to an RHD2000 chip-based 128 channel amplifier board (Intan Technologies). Broadband (0.1 Hz-7.5 kHz) signals were acquired at 30 kHz. Signals were digitized at 16 bit and transmitted to an OpenEphys recording controller (OEPS).

Raw data were processed to detect spikes and extract single-unit activity. Briefly, the wide-band signals were band-pass filtered (0.6 kHz-6 kHz), spatially whitened across channels and thresholded for isolation of putative spikes. Clustering was performed using template matching implemented in Kilosort2 (Pachitariu et al., 2016) and computed cluster metrics were used to pre-select units for later manual curation using custom-written software.

For the optogenetic inhibition of LGN axons, the silicon probe inserted in one of the two craniotomies was coupled with a 200 μm 0.5 NA optic fiber (Thorlabs, FP200URT), placed between the two middle shanks and at $\sim$300 μm above the top-most channel of the

silicon probe, thus the optic fiber remained just outside the surface of the cortex during the recordings. This fiber was coupled with a 525 nm LED (PlexBright, Plexon), controlled using a Cyclops 3.6 LED driver and a custom Teensy3.2-based stimulation system, calibrated to deliver ~2 mW of light at the tip of the fiber.

Following a long baseline period, the paradigm used to investigate the effect of eOPN3 on the synaptic vesicle release *in vivo* consisted of 31 presentations of a visual stimulus every 30 s. The 10 first trials were used to establish the baseline of the visual response and the 11th trial was coupled with optogenetic stimulation, starting 1 s before the visual stimulation and lasting for a total of 30 s. Each visual stimulus presentation trial consisted of 8 repeats of a 500 ms visual drifting grating presentations in the cardinal and intercardinal directions. The stimuli were presented on a 23.5" monitor placed 20 cm centrally in front of the mouse, so that the monitor was visible to both eyes. The stimulus presentation was controlled using a custom-written Python program and utilized PsychoPy3.0. For the accurate detection of the stimulus onset to allow for alignment with electrophysiological data, a photodetector was mounted in one corner of the monitor. The mouse was gradually habituated to head-fixation over multiple sessions and was running freely on a horizontal wheel. Each mouse was recorded for 1 or 2 identical sessions on different days and data were pooled for the subsequent analyses. Recording sessions in which no units showed visual stimulus-evoked activity were excluded from the analysis.

For visual stimulus response characterization, the spike rates were calculated in 50 ms bins. Each unit's activity was normalized to the average firing rate in the 15 s prior to stimulus presentation during the baseline period. The baseline period in Figure 6D was defined as the activity during the two trials before eOPN3 activation. For clarity, the peristimulus time histograms shown in Figure 6E were low pass filtered using a Gaussian function (window: 250 ms, σ = 100 ms). The recovery time constant shown in Figure 6F was calculated by fitting the post eOPN3 activation visual stimulus response to $f(t) = 1-a \cdot exp(-t/tau)$, with the effect size (a) and recovery time constant (tau) as free parameters.

In vivo optogenetic silencing of the nigrostriatal pathway

AAV vectors encoding a Cre-dependent eOPN3-mScarlet transgene (AAV2/1&2.hSyn.SIO-eOPN3-mScarlet; 6×10^{12} viral genomes / ml) or eYFP (AAV2/1&2.EF1a.DIO.eYFP; 2×10^{13} viral genomes / ml) were unilaterally injected into the substantia nigra (AP: - 3.5 mm, ML: + or - 1.4 mm DV: - 4.25 mm; 500 nL per mouse) of DAT-Cre transgenic mice. Optical fibers (200 μm diameter, NA 0.5) were unilaterally implanted above the ipsilateral dorsomedial striatum (AP: + 0.6 mm, ML: + or – 1.5 mm DV: - 2.1 mm). Left and right implanted mice were counterbalanced among the eOPN3 and control groups. Mice were allowed to recover for 6-9 weeks to allow for viral expression. Following recovery, mice underwent a single 10-min habituation session, to habituate to handling, patch cord attachment and the open field arena. In experimental sessions, we attached individual mice to a patch cord and video recorded their free locomotion continuously in the open field under near-infrared illumination.

To measure eOPN3 induced bias in locomotion, we video recorded the free locomotion of single mice in an open field arena (50× 50×50 *cm*) continuously over 30 min. After a 10-min baseline no-light period, we delivered 500 ms light pulses (540 nm, 10 mW at the fiber tip), at 0.1 Hz for 10 min, followed by an additional 10-min no-light period. Offline video processing and mouse tracking was done using DeepLabCut (DLC; (Mathis et al., 2018)). Briefly, we trained DLC to detect 6 features on the mouse body (nose, head center, left and right ears, center of mass, tail) and 3 bottom corners of the arena. X-Y coordinates of each feature were then further processed to complete missing or noisy values (high amplitude and short duration changes in X or Y dynamics) using linear interpolation (*interp1*) of data from neighboring frames. This was followed by a low pass filtering of the signals (*malowess*, with 50 points span and of linear order). Finally, a pixel to cm conversion was done based on the video-detected arena features and its physical measurements. A linear fit to the nose, head, center and tail features defined the mouse angle with respect to the south arena wall at each frame. Following its dynamics over the session, we identified direction shifts as a direction change in angle that exceeds 20° and 1 s. To achieve a comparable measurement between right- and left- hemisphere injected mice, we measured motion in the ipsilateral direction as positive and contralateral motion as negative from the cumulative track of angle. The net angle gain was calculated as the sum of ipsilateral and contralateral angle gained over each time bin (1- or 10-min bins as indicated). For each time bin we then calculated a rotation index, based on angle gains, as follows:

$$Rotation\ index = \frac{(ipsilateral - contralateral)}{ipsilateral + contralateral}$$

For each mouse, rotation index scores were calculated for two complete sessions on different days. Individual scores were plotted for each mouse against the expression levels measured in that mouse (see section: Histology, imaging, and quantification). Results were then averaged across individual sessions, and used for all statistical comparisons, and linear regressions analysis. Mouse positions and velocities were measured by the "center of mass" feature.

QUANTIFICATION AND STATISTICAL ANALYSIS

Mean was used as center measure and standard error of the mean (SEM) as dispersion measure throughout the manuscript. The data was tested for violations of assumptions of parametric tests (Gaussian distribution of the residuals was assessed using the Kolmogorov-Smirnov test; Equality of variances was assessed using the Levene's test), and non-parametric tests were utilized where assumptions were violated. The statistical details for the specific experiments, including the statistical tests used, exact value of n, what n represents (e.g., number of animals, number of brain slices, number of cells, or number of trials), can be found in the figures, figure

legends or Results text. Significance was determined at a level of 0.05 using the statistical test as reported in the figure legend or Results. P values were corrected for multiple comparison as reported in the figure legends or Results. For fitting results, confidence intervals are reported. No statistical tests were run to predetermine sample size, but sample sizes were similar to those commonly used in the field. Blinding and randomization were performed only in the behavioral experiments (Figure 7); in other experiments, automated analysis was used whenever possible. For autaptic neuron recordings (Figure 2), cells were excluded from the analysis of the paired-pulse ratio if eOPN3 activation completely abolished the first EPSC, and mEPSCs were not analyzed when noise-events detected by an inverted template occurred at > 1 Hz, as previously described (Rost et al., 2015). For organotypic slice culture recordings the access resistance of the recorded non-transfected CA1 neuron was continuously monitored and recordings with access resistance above 20 MΩ and/or with a drift > 30% were discarded. For *in vivo* electrophysiology (Figure 6), recording sessions in which no units showed visual stimulus-evoked activity were excluded from the analysis. Statistical analysis was performed using MATLAB (Mathworks), RStudio Desktop (RStudio), and Prism (Graphpad).

Supplemental information

Efficient optogenetic silencing

of neurotransmitter release

with a mosquito rhodopsin

Mathias Mahn, Inbar Saraf-Sinik, Pritish Patil, Mauro Pulin, Eyal Bitton, Nikolaos Karalis, Felicitas Bruentgens, Shaked Palgi, Asaf Gat, Julien Dine, Jonas Wietek, Ido Davidi, Rivka Levy, Anna Litvin, Fangmin Zhou, Kathrin Sauter, Peter Soba, Dietmar Schmitz, Andreas Lüthi, Benjamin R. Rost, J. Simon Wiegert, and Ofer Yizhar
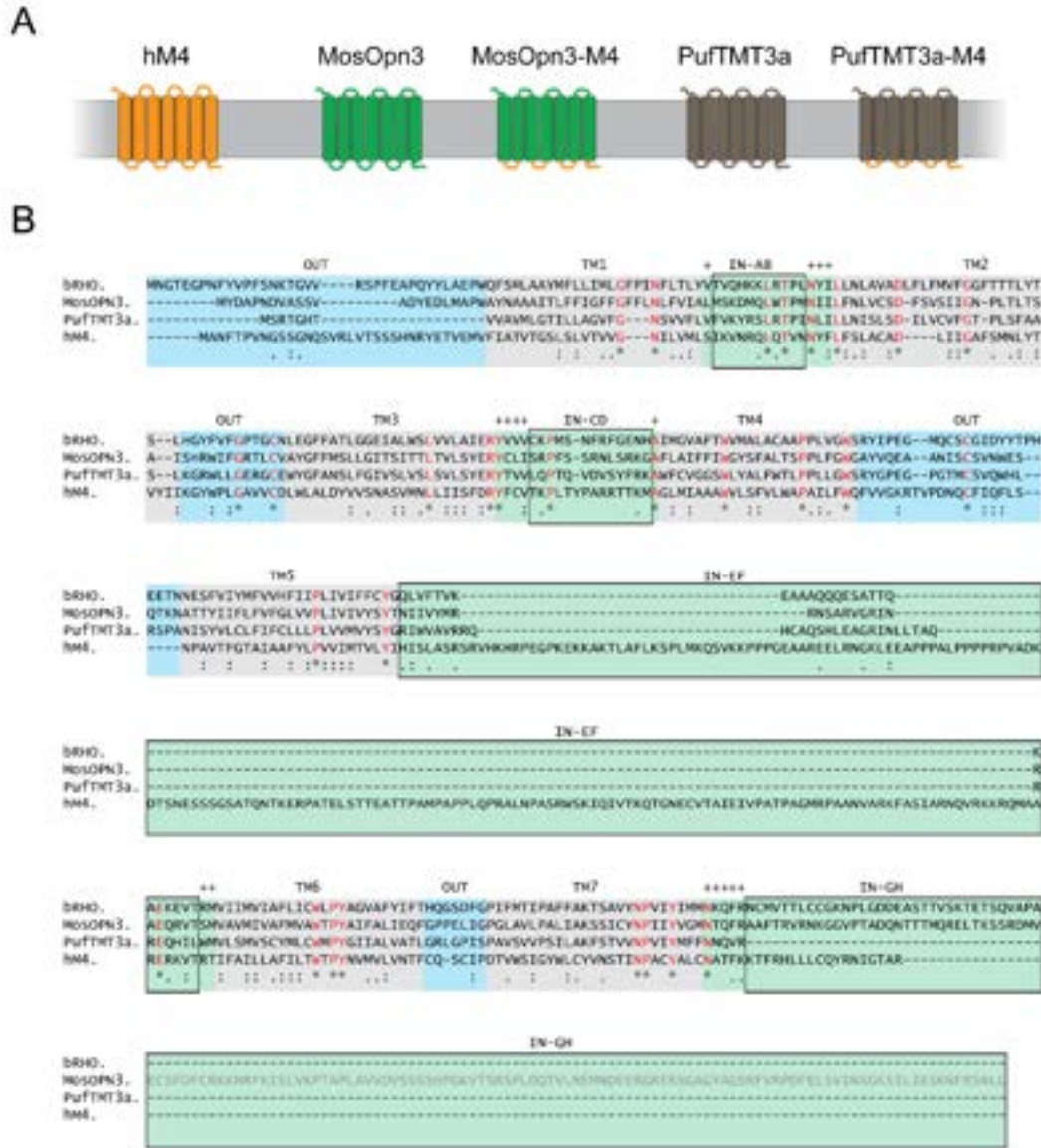
Figure S1. hM4 chimera design. Related to Figure 1. To maximally recapitulate the signaling pathway of the M4 acetylcholine receptor, as utilized by hM4Di, we also generated chimeric photoreceptors composed of bistable invertebrate rhodopsins and the intracellular domains of the M4 receptor. **(A)** Schematic diagrams of chimeric proteins comprising transmembrane and extracellular domains from the bistable mosquito OPN3 opsin (OPN3, GenBank: AB753162.1) or the teleost multiple tissue opsin 3a from pufferfish (PufTMT3a, UniParc: UPI00016E4442) and intracellular domains of the human muscarinic receptor 4 (hM4, GenBank: NM_000741). **(B)** Multiple sequence alignment (Edgar, 2004) of the amino acid sequences of visual and non-visual rhodopsins, along with hM4. Shown are sequences of the bovine rhodopsin (bRho), OPN3, PufTMT3a, and hM4. Intracellular domains are labeled with green background, extracellular domains are labeled with blue background and the transmembrane domains are in gray. "*" indicates an identical amino acid in all sequences in the alignment (red letters), ":" indicates conserved amino acid substitutions according to the COLOUR table (http://www.jalview.org/help/html/colourSchemes/clustal.html), and "." indicates semi-conserved substitutions. Intracellular regions that were replaced by the hM4 sequence to create chimeric proteins are indicated by black boxes. Non-replaced amino acids within the intracellular region are indicated by a + above the column. The 99 amino acid deletion in OPN3, introduced to improve expression in neurons, is indicated by gray amino acid letters (bottom row).
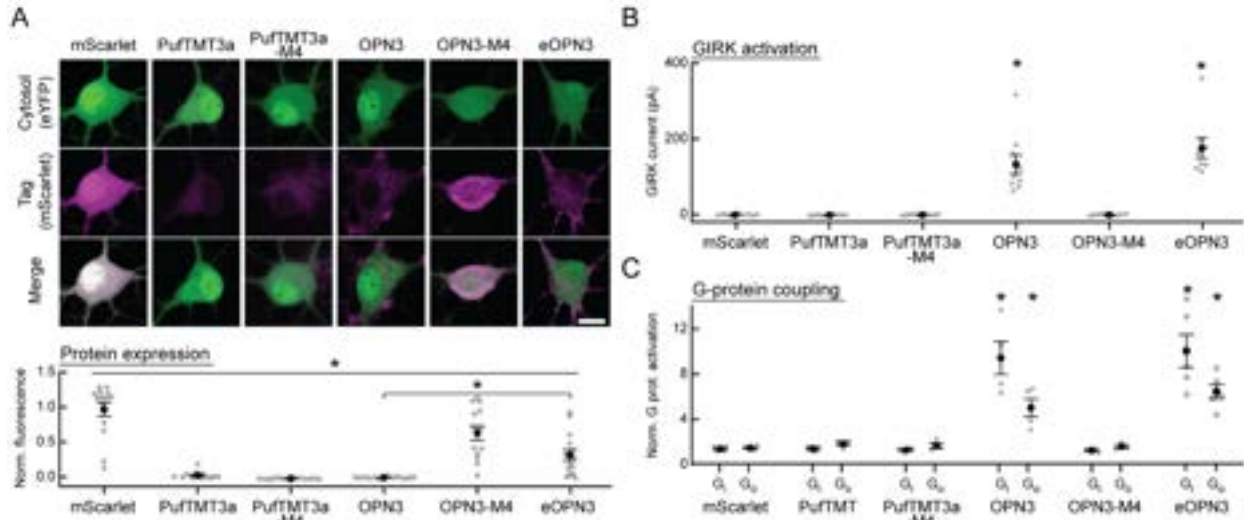
Figure S2. In vitro characterization of bistable rhodopsins and their M4 chimeras. Related to Figure 1. To evaluate the utility of the bistable rhodopsins PufTMT3a, wild-type mosquito OPN3 (referred to as OPN3 hereafter), and their M4 chimeras, we first characterized their expression and membrane targeting in neurons. We transfected primary cultured hippocampal neurons with mammalian codon-optimized versions of these rhodopsins, with C-terminal mScarlet fusions for direct visualization. **(A)** Representative confocal images of neurons co-transfected with expression vectors for eYFP and the indicated rhodopsin variant. Images show fluorescence in the eYFP channel (*top*), the mScarlet channel (*middle*) and the merged images (*bottom*). Bottom: Expression level of each of the displayed rhodopsin-mScarlet constructs, quantified as the average pixel intensity in n > 13 neurons for each construct normalized to cells expressing only mScarlet. The amount of measured fluorescence differed between all conditions (p = $1.34 \cdot 10^{-12}$ Kruskal-Wallis test followed by Bonferroni-Holm corrected pairwise comparisons using Wilcoxon rank sum tests: OPN3 vs. eOPN3 fluorescence n = 14, p = $1.3 \cdot 10^{-4}$. The expression of OPN3 was low, punctate, and mostly intracellular. The OPN3-M4 chimera, containing the intracellular loops of the M4 acetylcholine receptor, expressed at higher levels in comparison to OPN3, but showed a predominantly intracellular localization. Scale bar, 15 μm. Images in the mScarlet channel are individually scaled for visualization of low fluorescence levels. Fluorescence measurements were taken under matched imaging conditions for all variants tested. **(B)** Characterization of the ability of the rhodopsins to evoke G protein-coupled inwardly-rectifying potassium channel-mediated (GIRK) currents in cultured neurons as a readout for functional activation of the $G_{i/o}$ pathway. Co-expressing one of each of the rhodopsin variants along with a GIRK2-1 channel (Lesage, et al., 1994) allowed us to quantify and compare the magnitude of $G_{i/o}$ pathway activity through the measurement of GIRK2-1-mediated hyperpolarizing K^+-currents. GIRK currents evoked by a 500 ms pulse of 560 nm light at 2 mW·mm^{-2} in hippocampal neurons during a voltage clamp recording, held at -70 mV. Both the wild-type PufTMT3a opsin and the PufTMT3a-M4 chimera did not yield light-activated GIRK currents, in contrast to OPN3 and eOPN3 expressing neurons (p = $1.71 \cdot 10^{-6}$ Kruskal-Wallis test followed by Bonferroni-Holm corrected pairwise comparisons using Wilcoxon rank sum tests). OPN3-M4 did not evoke any detectable GIRK currents. **(C)** We determined the interactions between the rhodopsin variants and specific G proteins using a HEK cell-based GPCR screening assay that couples the opsin to a Gs-chimera (GsX assay, see fig. S3 for complete assay and statistics, (Ballister, et al., 2018)). This approach allowed us to analyze their interaction with all major G proteins (Gi, Go, Gt, Gq, Gs, Gz, G12, G13, G15). Only OPN3 and eOPN3 showed G_i and G_o activation. PufTMT3a-expressing cells only activated G_z (see also Fig. S3B). In combination, these results show that PufTMT3a cannot be used to fully recapitulate the efficient inhibition of vesicle release induced by hM4Di. Plots depict individual data points and average ± SEM.
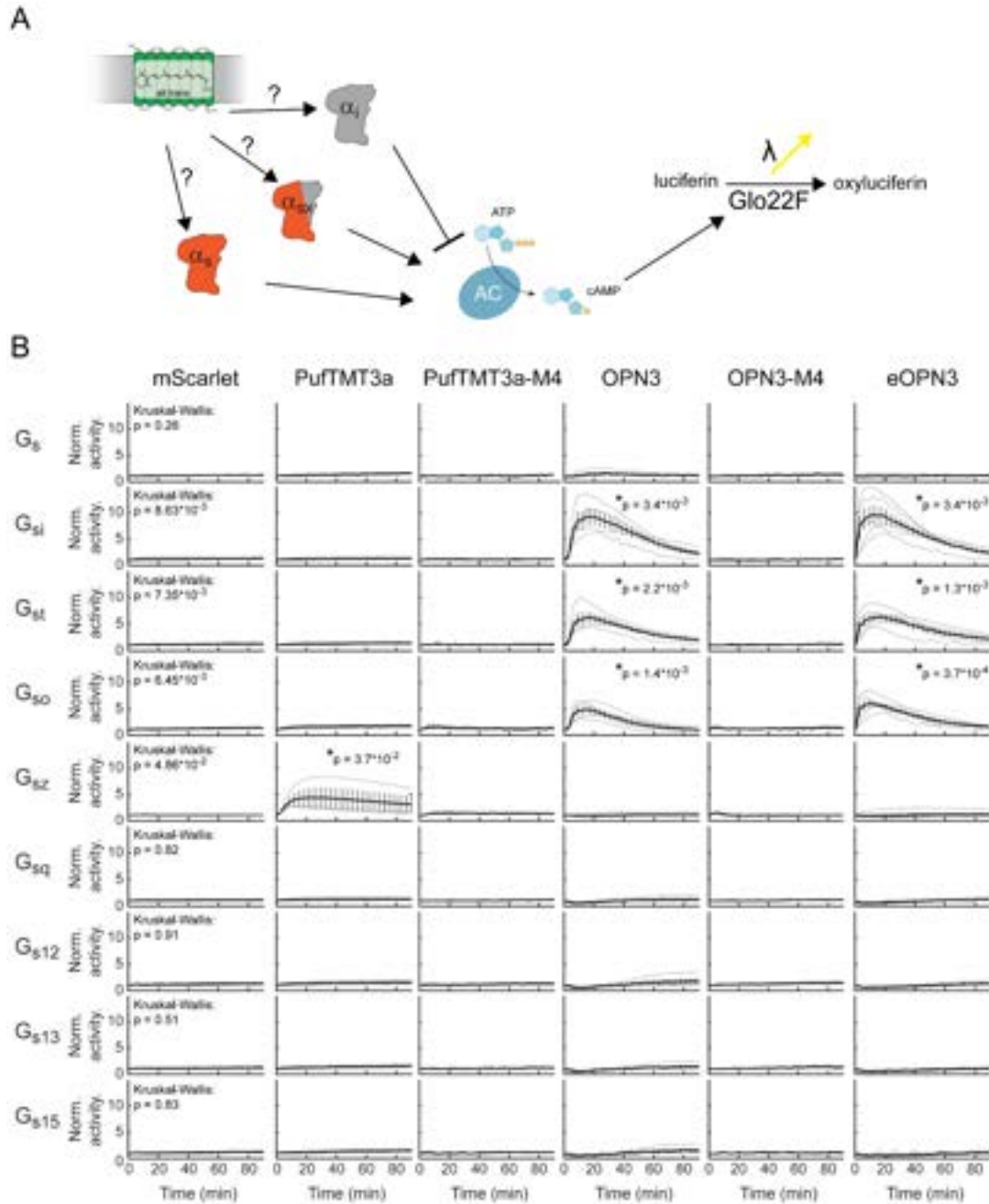
Figure S3. G protein activation assay. Related to Figure 1. Light-dependent G protein activation by several opto-GPCR constructs, assayed in HEK293T cells. **(A)** Essay scheme. HEK293T cells are transfected with chimeras of G_α proteins and the $G_{\alpha s}$ C-terminus. cAMP levels in live cells are measured through the cAMP reporter (Glo22F). This allows for measuring cAMP levels as readout of chimera activation by the co-expressed opto-GPCR. **(B)** opto-GPCRs were activated with a green LED pulse (1s, 530nm, 5.5 µW·mm^{-2}) and luminescence was measured over time. Graphs show the light-induced response, normalized to pre-activation baseline, for mScarlet (control, n = 4), PufTMT3a-mScarlet (n = 3), PufTMT3a-M4-mScarlet (n = 3), OPN3-mScarlet (n = 4), OPN3-M4-mScarlet (n = 3), and eOPN3-mScarlet (n = 5). Only OPN3-mScarlet and eOPN3-mScarlet specifically and strongly activated inhibitory G proteins (G_i, G_t, G_o) in a light-dependent manner (Kruskal-Wallis tests of the maximal measured values per G protein, followed by Bonferroni-Holm corrected pairwise comparisons using Conover–Iman tests; reported p-values describe the comparison against the mScarlet control). Single trials are depicted in gray, mean ± SEM are in black.
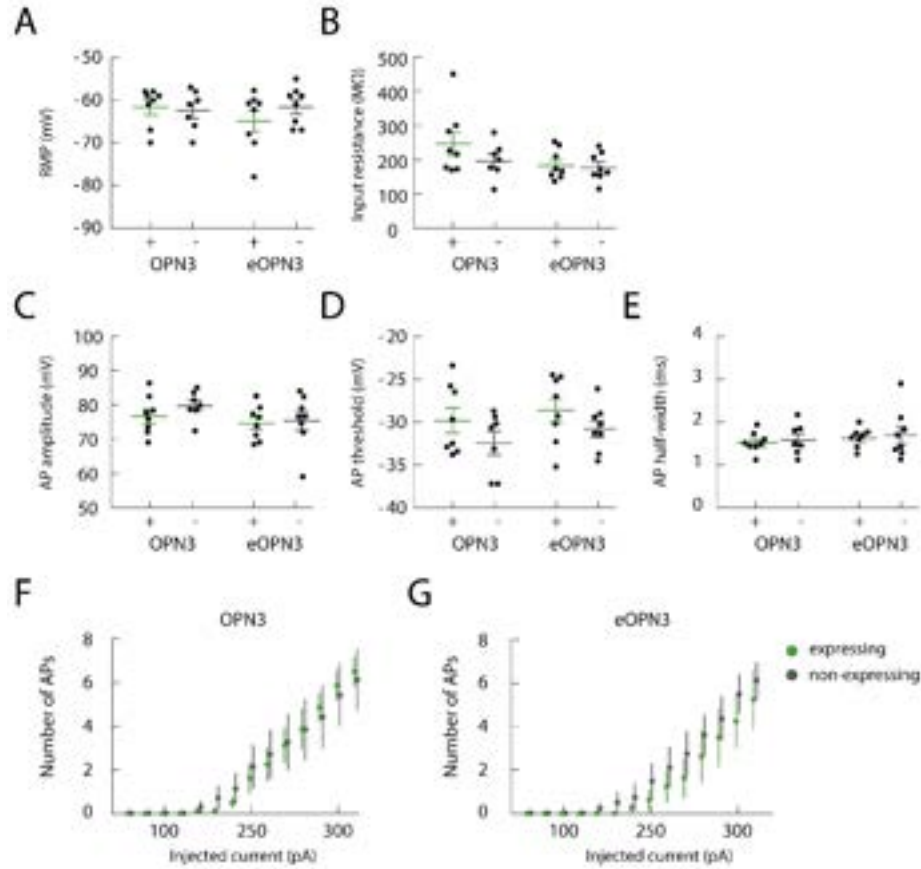
Figure S4. No change in the intrinsic excitability of cultured hippocampal neurons expressing OPN3-mScarlet or eOPN3-mScarlet in the absence of light. Related to Figure 1. The following intrinsic properties were characterized in cultured hippocampal neurons: **(A)** resting membrane potential (RMP, OPN3 vs. ctrl: p = 0.79; eOPN3 vs. ctrl: 0.27; two-tailed Mann-Whitney tests), **(B)** membrane input resistance (OPN3 vs ctrl: p = 0.35; eOPN3 vs. ctrl: 0.82; two-tailed Mann-Whitney tests), **(C)** action potential (AP) amplitude (OPN3 vs. ctrl: p = 0.19; eOPN3 vs. ctrl: 0.57; two-tailed Mann-Whitney tests), **(D)** AP threshold (OPN3 vs. ctrl: p = 0.38; eOPN3 vs. ctrl: 0.23; two-tailed Mann-Whitney tests), and **(E)** AP half-width (OPN3 vs. ctrl: p = 0.85; eOPN3 vs. ctrl: 0.94; two-tailed Mann-Whitney tests). No differences between neurons expressing OPN3-mScarlet (n = 7) or eOPN3-mScarlet (n = 8) and neighboring non-transfected control cells (n = 7 and n = 8, respectively) were detected. **(F-G)** The number of evoked APs in response to current injection were not different in neurons expressing OPN3 or eOPN3 and non-expressing controls (p = 0.91 and 0.46, respectively; two-way repeated measures ANOVA). Plots show individual data points and average ± SEM.
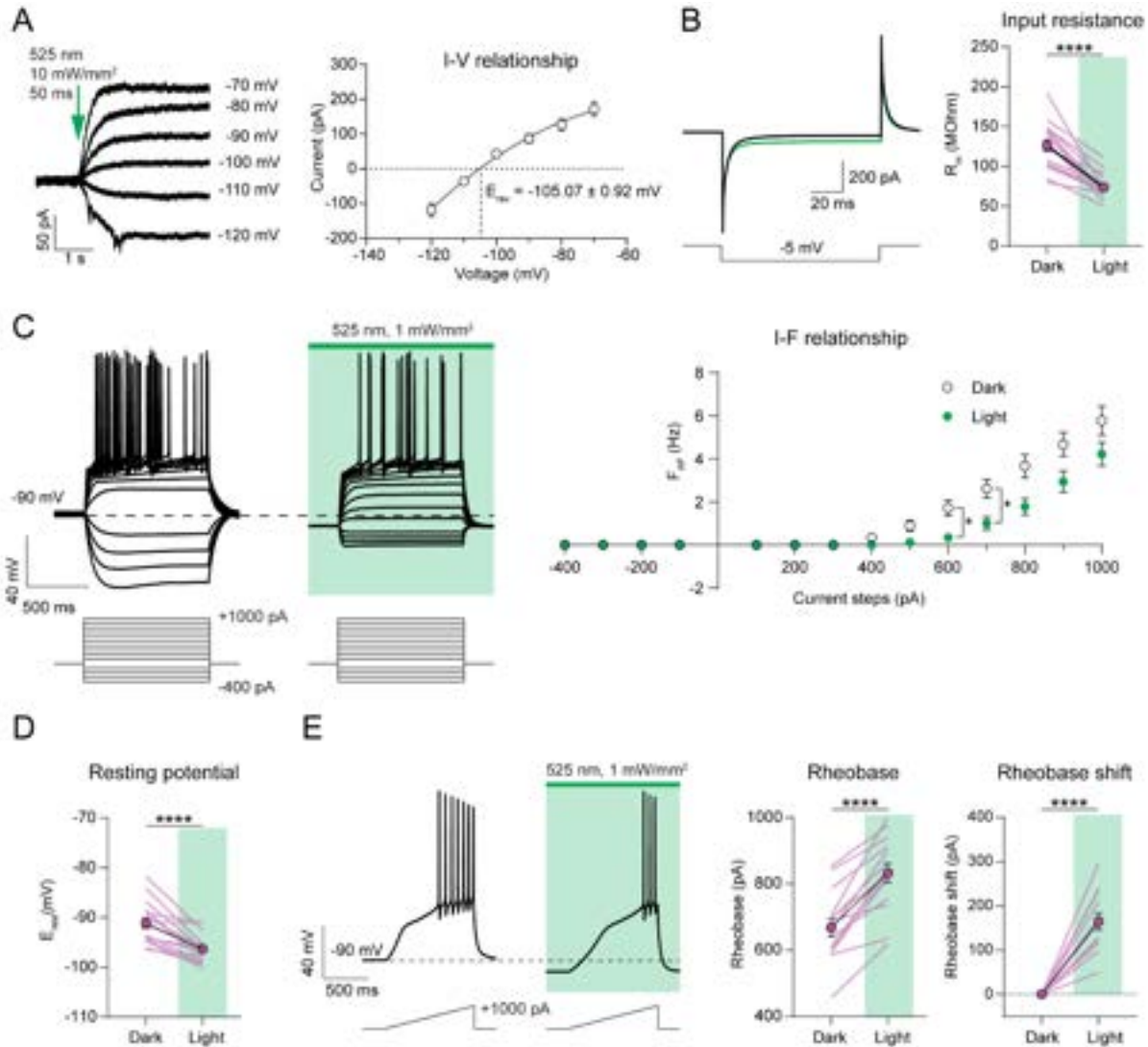
Figure S5: Passive and active membrane properties of eOPN3-expressing CA3 pyramidal neurons in organotypic hippocampal slices. Related to Figure 4. **(A)** Light-evoked (putative GIRK) currents evoked by 50-ms green-light pulses (525 nm, 10 mW·mm^{-2}) at different holding potentials, ranging from -70 to -120 mV. Values are baseline-subtracted and corrected for a liquid junction potential of -14 mV. Representative traces are shown on the *left*, quantification of the current-voltage relationship is shown on the *right* (n = 6). The photocurrent reversal potential of -105.07 ± 0.92 mV (determined with a non-linear fit) is close to the calculated K$^+$ equilibrium potential of -102.5 mV. **(B)** *Left*: Representative current traces in response to a negative voltage step (-5 mV, 100 ms) in the dark (black traces) and during continuous green light (525 nm, 1 mW·mm^{-2}). Note the drop of the stationary current resulting from a decreased input resistance due to increased GIRK channel conductance under illumination. *Right*: Quantification of input resistance. (Dark: 126 ± 6.79 MΩ, Light: 73 ± 3.46 MΩ, p < 1·10^{-4}, Wilcoxon-test, n = 18). **(C)** *Left*: representative voltage responses to somatic current injections ranging from -400 pA to +1000 pA in the dark and during illumination (525 nm, 1 mW·mm^{-2}). *Right*: I-F plot showing decreased spike frequency in response to positive current injections, likely due to G$_{i/o}$-mediated GIRK channel opening (p < 0.05, n = 18, two-way ANOVA with Sidak's multiple comparisons test). **(D)** Quantification of the resting membrane potential from the current step experiments shown in C (Dark: -91.18 ± 0.96 mV; Light: -96.34 ± 0.62 mV; p < 1·10^{-4}, paired t-test, n = 18). **(E)** *Left*: representative voltage traces in response to depolarizing current ramps to assess the eOPN3-mediated rheobase shift (0 - 1000 pA). Injected current at the time of the first spike was defined as the rheobase. Green light (525 nm, 1 mW·mm^{-2}) raised the rheobase of current-ramp-evoked APs. *Right*: quantification of the absolute rheobase (dark: 667.9 ± 26.79 pA, light: 832.7 ± 28.69 pA; p < 1·10^{-4}, paired t-test, n = 15) and the rheobase shift (light: 164.8 ± 19.30 pA, p < 1·10^{-4}, paired t-test, n = 15).
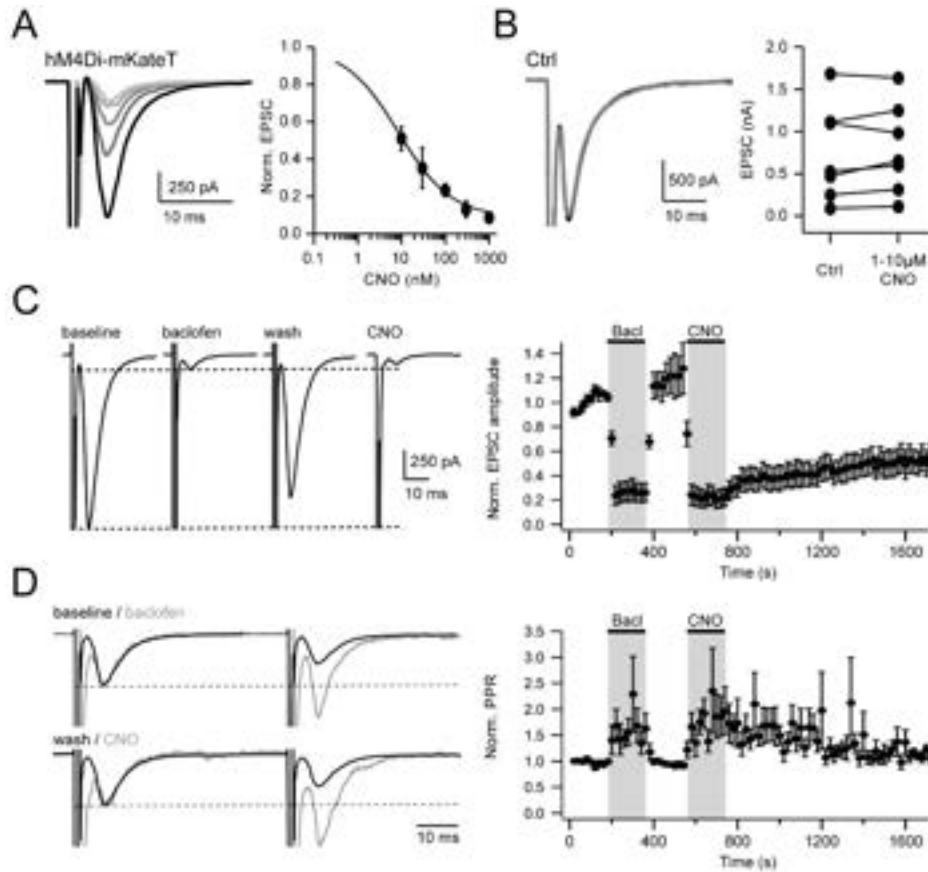
Figure S6. Presynaptic inhibition of neurotransmitter release by hM4Di expressed in autaptic cultures of hippocampal neurons. Related to Figure 2. **(A)** Application of increasing concentrations of clozapine-N-oxide (CNO; 10, 30, 100, 300, 1000 nM, from black to light gray) leads to reduction in EPSC amplitude (IC_{50} = 8.6 nM, n = 3-12). **(B)** CNO (1-10 µM) has no effect on EPSC amplitude in neurons not expressing hM4Di (ctrl 0.746 ± 0.215 nA; CNO: 0.79 ± 0.201 nA; p = 0.3, paired t-test, n = 7). **(C-D)** Comparison of presynaptic inhibition by $GABA_B$R and presynaptic inhibition by hM4Di. After 30 µM baclofen application for 180 s and washout, 100 nM CNO was added for 180 s to the same cells. Action potentials were evoked by depolarization to 0 mV for 1 ms at 0.2 Hz. Data were binned by 2. **(C)** Both types of GPCRs suppress EPSC amplitudes to a similar extent (Baclofen: to 0.267 ± 0.083 of Baseline, CNO: to 0.218 ± 0.076; p = 0.06, paired t-test, n = 6). However, washout kinetics of CNO is dramatically slower compared to baclofen. **(D)** Increased paired-pulse ratio in response to both $GABA_B$ and hM4Di receptor activation ($GABA_B$R: 1.776 ± 0.329; hM4D: 1.864 ± 0.355; p = 0.2, paired t-test, n = 6), indicating a presynaptic action. Example traces are scaled to the peak of the first EPSC under control conditions for both baclofen and CNO applications.
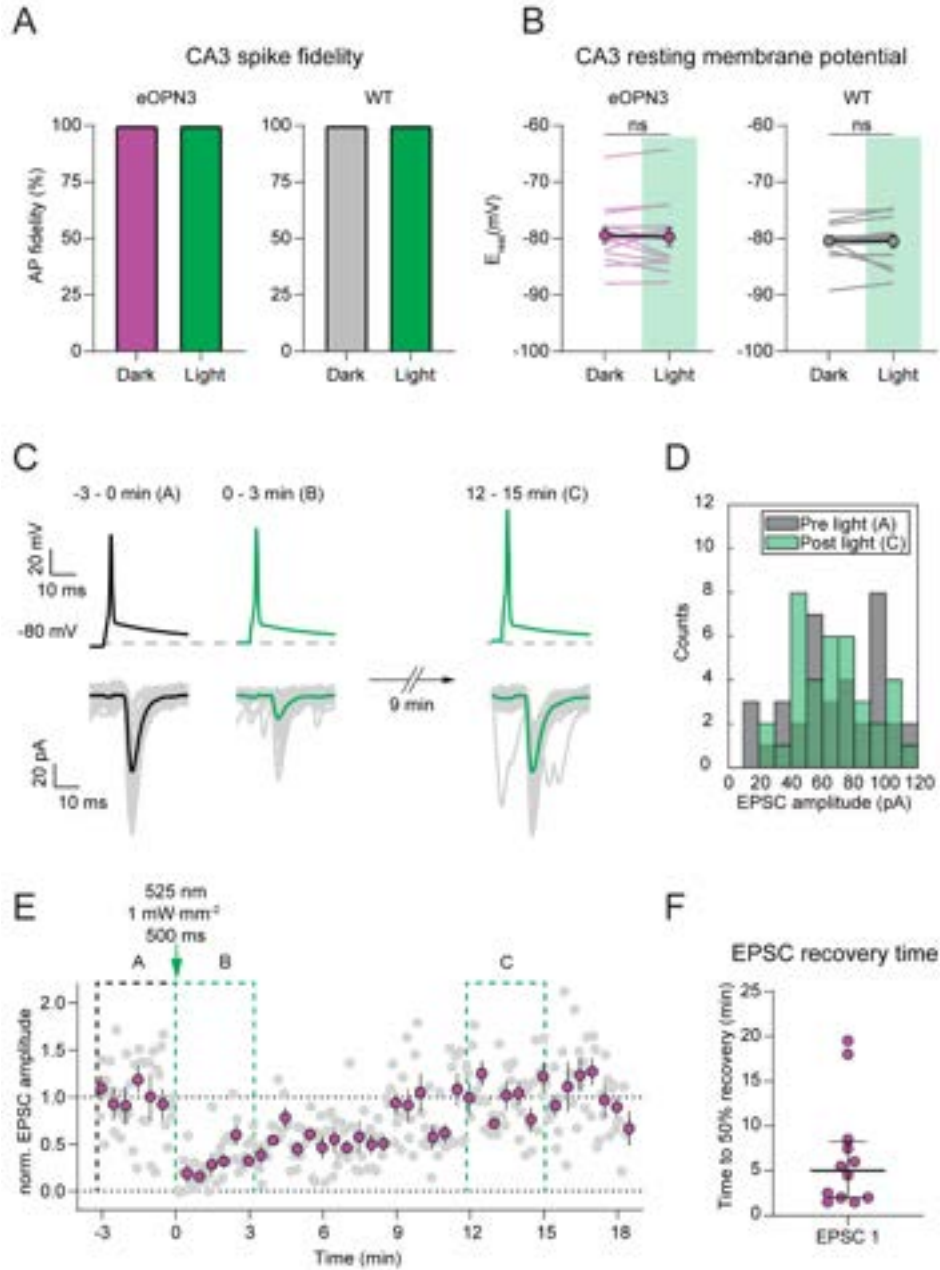
Figure S7: Excitability of CA3 neurons and EPSC recovery in paired-recording experiments. Related to Figure 4. **(A)** Comparison of action potential success rate in CA3 in the dark and in the 30 s after light stimulation in CA1 (eOPN3 dark, eOPN3 light = 100%, n = 14; WT dark, WT light = 100%, n = 13). **(B)** Quantification of the resting membrane potential of CA3 pyramidal cells used in paired recordings in the dark and in the 30 s after light stimulation in CA1 (500 ms of 525 nm light at 1 mW·mm^{-2}; eOPN3 dark: -79.41 ± 1.43, eOPN3 light: -79.71 ± 1.62, p = 0.9032, Wilcoxon test, n = 14; WT dark: -80.41 ± 0.94, WT light: -80.47 ± 1.14, p = 0.3396, Wilcoxon test, n = 13). Plots show individual data points (lines), and average (circles) ± SEM. Note absence of effects of local CA1 illumination on CA3-cell somatic properties. **(C)** Representative voltage (*top*) and current (*bottom*) traces from the example shown in E. For display purposes "pulse 2" of the paired-pulse stimulation was omitted. Note the EPSC recovery within minutes after light application. **(D)** Histogram count of peak current amplitudes of the example shown in C. **(E)** Quantification of the normalized EPSC peak amplitude shown in C (gray: individual trials, magenta: 30 s bins). **(F)** The EPSC recovery time was defined as the first 30 s-bin post light reaching at least 50% recovery of the EPSC peak amplitude compared to the average baseline EPSC peak amplitude (EPSC 1: 6.58 ± 1.78 min, mean + SEM, n = 12). Each circle represents an individual paired recording experiment.
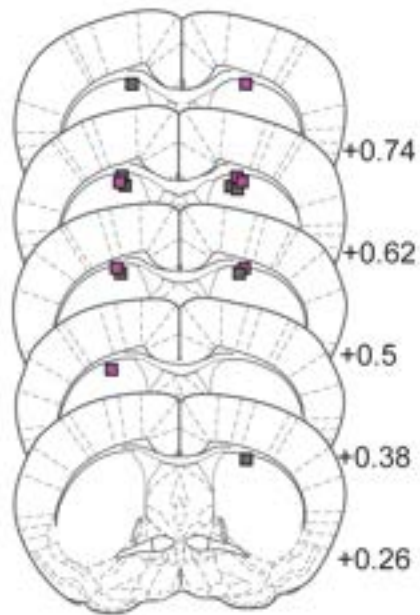
Figure S8: Histological analysis of optic fiber placements in nigrostriatal projection inhibition experiments. Related to Figure 7. Each point represents the fiber tip position of mice expressing eYFP (N = 8 mice, gray squares) or eOPN3-mScarlet (N = 7 mice, magenta squares). Numbers indicate anterior – posterior position relative to Bregma.

Orthogonally-polarized excitation for improved two-photon and second-harmonic-generation microscopy, applied to neurotransmitter imaging with GPCR-based sensors

MAURO PULIN,[1,2] **KILIAN E. STOCKHAUSEN,**[3] **OLIVIA A. MASSECK,**[4] **MARTIN KUBITSCHKE,**[4] **BJÖRN BUSSE,**[3,5] **J. SIMON WIEGERT,**[2] **AND THOMAS G. OERTNER**[1,*] ⓘ

[1]*Institute for Synaptic Physiology, ZMNH, University Medical Center Hamburg-Eppendorf, 20251 Hamburg, Germany*
[2]*Research Group Synaptic Wiring and Information Processing, ZMNH, University Medical Center Hamburg-Eppendorf, 20251 Hamburg, Germany*
[3]*Department of Osteology and Biomechanics, University Medical Center Hamburg-Eppendorf, 22529 Hamburg, Germany*
[4]*Synthetic Biology, University of Bremen, Leobener Str. 5, 28359 Bremen, Germany*
[5]*Interdisciplinary Competence Center for Interface Research (ICCIR), University Medical Center Hamburg-Eppendorf, 20251 Hamburg, Germany*
[*]*thomas.oertner@zmnh.uni-hamburg.de*

Abstract: Fluorescent proteins are excited by light that is polarized parallel to the dipole axis of the chromophore. In two-photon microscopy, polarized light is used for excitation. Here we reveal surprisingly strong polarization sensitivity in a class of genetically encoded, GPCR-based neurotransmitter sensors. In tubular structures such as dendrites, this effect led to a complete loss of membrane signal in dendrites running parallel to the polarization direction of the excitation beam. To reduce the sensitivity to dendritic orientation, we designed an optical device that generates interleaved pulse trains of orthogonal polarization. The passive device, which we inserted in the beam path of an existing two-photon microscope, removed the strong direction bias from fluorescence and second-harmonic (SHG) images. We conclude that for optical measurements of transmitter concentration with GPCR-based sensors, orthogonally polarized excitation is essential.

1. Introduction

Excitation of fluorescence depends on the orientation of the fluorophore with respect to the polarization of the excitation light. The emitted photons are also polarized, an effect known as fluorescence anisotropy. This effect can be exploited to measure the speed of rotation of fluorescent proteins in solution [1,2], for example to detect interactions during molecular signaling. Commercial two-photon microscopes use linearly polarized light for excitation. In the case of two-photon light-sheet microscopy, where fluorescence is detected orthogonally to the excitation sheet, it has been noted that better results are achieved when the direction of polarization is optimized [3]. In classical point-scanning two-photon microscopes, however, the direction of polarized excitation is ignored, as fluorescent or fluorescently-labeled molecules in biological preparations are in most cases randomly oriented.

To detect the release of neurotransmitters and neuromodulators in intact brain tissue, numerous genetically encoded sensors have been developed. A very successful strategy is to splice circularly permuted GFP (cpGFP) into G protein-coupled neurotransmitter receptors (GPCRs), which resulted in several highly specific sensors with a large dynamic range [4–8]. GPCRs have

seven transmembrane domains, and the cpGFP is inserted into the third intracellular loop, tethering both sides of the GFP barrel to transmembrane helices of the receptor. Upon ligand binding, movements of the helices are transferred to the cpGFP, changing its fluorescence. The relative change in fluorescence ($\Delta f/f_0$) depends on neurotransmitter concentration in a logistic fashion. However, depending on the length and rigidity of the linker sections, tethering cpGFP to transmembrane domains may orient the barrel parallel to the membrane.

Here we show that two-photon imaging of GPCR-based sensors is surprisingly sensitive to the orientation of the imaged dendrite relative to the polarization of the excitation beam. As a consequence, entire sections of reporter neurons can be non-fluorescent, which makes it impossible to draw conclusions about the spatial distribution of neurotransmitter release from the relative change in fluorescence. To solve this problem, we developed a passive optical device that produces two collinear output beams with orthogonal polarization ('X-Pol'). When inserted into the beam path of a two-photon microscope, the X-Pol device removes the orientation bias when imaging membrane proteins. As the polarization sensitivity of genetically encoded sensors cannot be known *a priori*, we suggest using orthogonal polarized pulse trains as a new standard for two-photon microscopy.

2.   Materials and methods

2.1.   Organotypic slice cultures

Hippocampal slice cultures from Wistar rats of either sex were prepared at postnatal day 4–6. Rats were anesthetized with 80% CO_2 20% O_2 and decapitated. Hippocampi were dissected in cold slice culture dissection medium containing (in mM): 248 sucrose, 26 $NaHCO_3$, 10 glucose, 4 KCl, 5 $MgCl_2$, 1 $CaCl_2$, 2 kynurenic acid, 0.001% phenol red (saturated with 95% O_2, 5% CO_2, pH 7.4). Tissue was cut into 400 μM thick sections on a tissue chopper (McIlwain) and cultured on membranes (Millipore PICMORG50) at 37° C in 5% CO_2. The slice culture medium contained (for 500 ml): 394 ml Minimal Essential Medium, 100 ml heat inactivated donor horse serum, 1 mM L-glutamine, 0.01 mg ml^{-1} insulin, 1.45 ml 5M NaCl, 2 mM $MgSO_4$, 1.44 mM $CaCl_2$, 0.00125% ascorbic acid, 13 mM D-glucose. Wistar rats were housed and bred at the University Medical Center Hamburg-Eppendorf. All procedures were performed in compliance with German law and according to the guidelines of Directive 2010/63/EU. Protocols were approved by the Behörde für Gesundheit und Verbraucherschutz of the City of Hamburg.

2.2.   Single cell electroporation

At DIV 13-17, CA1 neurons in rat organotypic hippocampal slice culture were transfected by single-cell electroporation [9]. Thin-walled borosilicate pipettes (~10 MΩ) were filled with plasmid DNA encoding the GFP-based sensors along with a cytoplasmic red fluorescent protein tdimer2 diluted in intracellular solution to 50 ng μl^{-1} and 10 ng μl^{-1}, respectively. Pipettes were positioned against neurons under visual control (IR-DIC) and DNA was ejected using an Axoporator 800A (Molecular Devices) with 50 hyperpolarizing pulses (−12 V, 0.5 ms) at 50 Hz. Imaging experiments were conducted 2-4 days after electroporation at room temperature (21-23°) in artificial cerebrospinal fluid (ACSF) containing (in mM) 135 NaCl, 2.5 KCl, 2 $CaCl_2$, 1 $MgCl_2$, 10 Na-HEPES, 12.5 D-glucose, 1.25 NaH_2PO_4 (pH 7.4).

2.3.   sDarken sensor

We developed an improved serotonin darkening 5-HT1A receptor-based sensor named sDarken (darkening 5-HT$_{1A}$ receptor-based sensor). The sensor design is based on dLight$_1$ [4]. Due to its high sensitivity, the native human 5-HT$_{1A}$ receptors was used as the sensing scaffold. We replaced the third intracellular loop of 5-HT$_{1A}$ with a circular mutated form of GFP (cpGFP)

from GCaMP6 [10] flanked by mutated linker sequences. Linker length is identical to dLight$_{1.2}$. sDarken is bright in the unbound form and decreases its fluorescence upon serotonin binding.

2.4. Bone sections

Femoral bone was obtained during autopsy in accordance with the local ethics regulations (PV 3486) [10]. A femoral cross section was cut from the mid-diaphysis using a diamond belt saw (EXAKT Advanced Technologies) and fixed in 3.7% formaldehyde. The sample was dehydrated in an increasing alcohol series and infiltrated with a plastic embedding medium based on glycolmethacrylate (Technovit 7200). Using an automatic grinding system (EXAKT Advanced Technologies), the sample was ground to a thickness of 100 μm. An osteon with an uninterrupted outer border was selected for the analysis.

2.5. Two-photon microscopy

The custom-built two-photon imaging setup was based on an Olympus BX51WI microscope with LUMPlan W-IR2 60× 1.0 NA objective. A galvanometric scanner (6215H, Cambridge Technology) was controlled by the open-source software package ScanImage [11]. Two pulsed Ti:Sapph lasers (MaiTai DeepSee, Spectra Physics) tuned to 930 nm and controlled by electro-optic modulators (350-80, Conoptics) were coupled at orthogonal polarization to excite GFP and tdimer2. In some experiments, we activated one or the other to generate images at orthogonal polarization (Fig. 2). For all other experiments, the polarization of a single Ti:Sapph laser was either rotated by 90° using a half-wave plate (690–1080 nm achromatic; Thorlabs) or split into orthogonally polarized pulse trains using the X-Pol device. Emitted photons were collected through the objective and oil-immersion condenser (1.4 NA, Olympus) with two pairs of photomultiplier tubes (H7422P-40, Hamamatsu) [12]. 560 DXCR dichroic mirrors and 525/50 and 607/70 emission filters (Chroma) were used to separate green and red fluorescence. Excitation light was blocked by short-pass filters (ET700SP-2P, Chroma).

2.6. X-Pol device

The prototype device used in this study is based on the 30 mm cage system (Linos, Thorlabs) and can be rotated around the optical axis. It consists of the following parts (Table 1):

Table 1. X-Pol device, parts list

ITEM	DESCRIPTION	Cat No.	QTY
1	Polarizing Beamsplitter Cube, 10 mm, N-BK7, 980 nm	Edmund Opt. #48-880	2
2	Right-Angle Prism Mirror, Protected Silver, L = 10 mm	Thorlabs MRA10-P01	2
3	Counter Support (mounting platform for optics)	Linos G061161000	2
4	Solid Cage Plate (drill and tap to accept mirror mount)	Linos G061008000	1
5	Compact Kinematic Mirror Mount	Thorlabs KMSS/M	1
6	30 mm Cage Plate, SM1-Threaded	Thorlabs CP08/M	2
7	Cage Assembly Rod, 2" long, Ø 6 mm	Thorlabs ER2	4
8	SM1 Lens Tube	Thorlabs SM1L10	2
9	Clamp for SM1 Lens Tubes	Thorlabs SM1TC	2
10	Ø12.7 mm Optical Post, M6 Tap, L = 50 mm	Thorlabs TR50/M	2
11	Ø12.7 mm Pedestal Post Holder, L = 54.7 mm	Thorlabs PH50E/M	2
12	Clamping Fork, 31.5 mm counterbored slot	Thorlabs CF125C/M	2
13	Ring-Actuated Iris Diaphragm (for alignment)	Thorlabs SM1D12D	1

2.7.   Alignment procedure

The device was inserted with a 45° tilt before the beam expander and centered on the excitation laser beam using the entrance pinhole (iris diaphragm) and an infrared scope. Axial orientation is not very critical as the device basically acts as a parallel plate. Some angular deviation of the exit beam was noted due to the limited parallelism of the beam splitting cubes (+/- 3 arcmin). This deviation was compensated by adjusting the following beam steering mirrors (periscope). The mirror prism inside the device was coarsely adjusted so that a single output spot was produced on an infrared viewer card held at a distance of about 1 m. Imaging a fluorescent structure in focusing mode, the mirror prism was fine adjusted to achieve maximum image brightness, corresponding to perfect overlap of the PSFs generated by the orthogonally polarized beams. This is best achieved when the person adjusting the mirror prism is able to see the live image on the computer screen. Lastly, we adjusted the pulse pre-compensation (MaiTai DeepSee) to account for the added GVD of 20 mm N-BK7 glass (1400 fs^2). Conveniently, rotating the device in its holders to horizontal (0°) or vertical (90°) orientation switches off its beam splitting function, resulting in output polarization (and repetition rate) that is identical to the input beam. In working position (near 45°), some power (~12%) is lost at the second, beam-combining cube. This is due to imperfect polarization of the reflected beam in the first, beam-splitting cube. For safety, the exit of this light must be blocked, either with a black metal plate or by a Si-photodiode to measure laser power. Due to this power loss in the reflected sub-beam, the ideal 50/50 splitting position is ~55° rotation, not 45°. The position can be optimized by temporarily blocking the reflected sub-beam inside the device, which should drop the output power to exactly 50%.

2.8.   Image analysis

Two-photon image stacks were de-interleaved (red/green channel) and z-projected (maximum intensity projection, MIP). Displayed images are MIPs; magenta and green levels were adjusted separately and linearly (Gamma = 1). Intensity profiles along the x-axis of a rectangular region of interest placed across the apical dendrite were generated with Fiji/ImageJ 1.53c and plotted with GraphPad Prism 8.4.3.

3.   Results

We transfected hippocampal CA1 neurons in organotypic slice culture [13] by single-cell electroporation [9] to express the following membrane-bound cpGFP-based sensors together with the red cytoplasmic label tdimer2 [14]: The GPCR-based dopamine sensor $dLight_{1.2}$[4], the norepinephrine sensor $GRAB_{NE1h}$ [7], a newly developed serotonin sensor (sDarken) based on $dLight_1$, and the glutamate sensor iGluSnFR [15]. For comparison, we also expressed GPI-anchored GFP [16] together with tdimer2 in some cells. Coupling two identical Ti:Sapph lasers tuned to 930 nm with a polarizing beam splitter cube allowed us to image the same structure using two different (orthogonal) polarization directions. For better comparison, we selected cells with vertically oriented apical dendrites for imaging.

The dopamine sensor $dLight_{1.2}$ contains a circularly permuted GFP inserted between trans-membrane domain 5 and 6 of the D1 dopamine receptor, orienting the GFP barrel parallel to the plasma membrane. For optical measurements, we added 10 µM dopamine to the extracellular solution to maximize the brightness of $dLight_{1.2}$. Fluorescence of $dLight_{1.2}$ was strongly dependent on the direction of laser polarization (Fig. 1(a)-(c)). Dendrites orthogonal to the direction of laser polarization were fluorescent while parallel ones were not. In contrast, polarization direction had no effect on the red fluorescence signal of (freely diffusible) tdimer2. When we compared $dLight_{1.2}$ fluorescence intensity in response to dopamine application, we observed a strong dopamine-dependent fluorescence increase for dendrite-normal polarization (background-subtracted $\Delta f/f_0 = 123\%$), but no signal for dendrite-parallel polarization (Fig. 1(d)).

Thus, using linear polarized excitation, it is not possible to relate the relative changes in dLight$_{1.2}$ fluorescence to dopamine concentration changes.
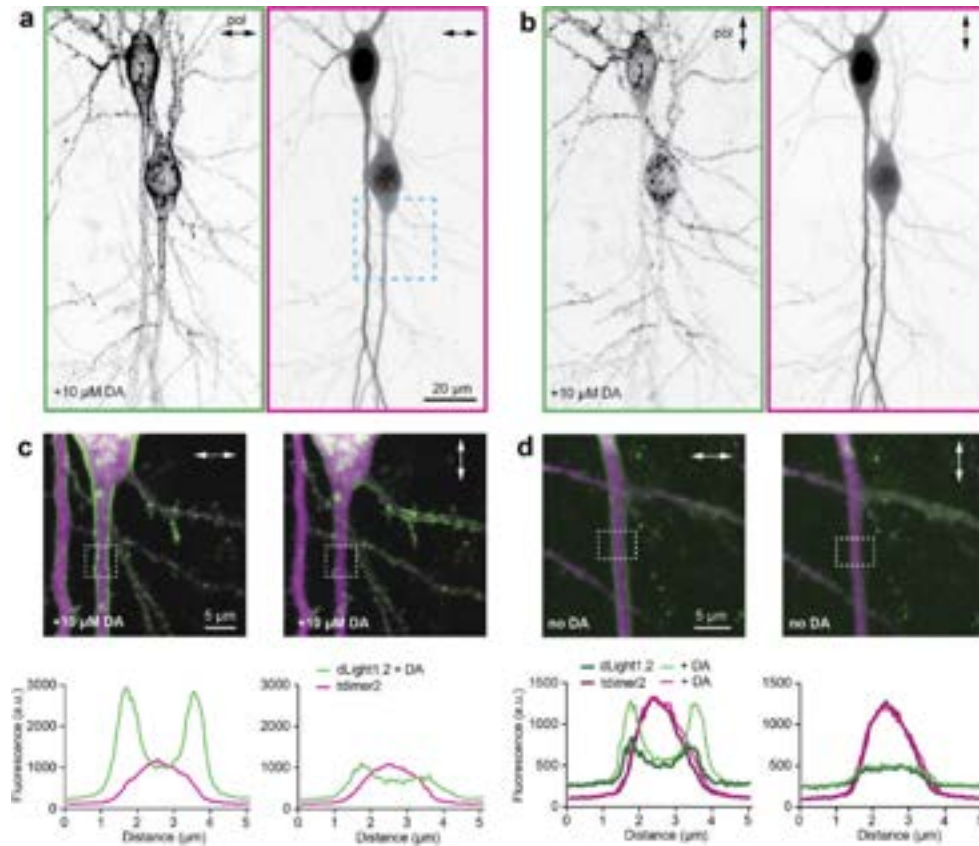

Fig. 1. Effect of laser polarization (930 nm) on the brightness of GPCR-based dopamine sensor dLight$_{1.2}$. (a) Laser polarization (arrow) orthogonal to the apical dendrites of CA1 pyramidal cells excites bright fluorescence of dLight$_{1.2}$ (left) and cytoplasmic tdimer2 (right). Images are contrast-inverted maximum intensity projections. dLight$_{1.2}$ was saturated with dopamine (10 μM). Apical dendrite (blue box) is enlarged in panel c. (b) Laser polarization (arrow) parallel to the apical dendrites excites no fluorescence of dLight$_{1.2}$ in the apical dendrites (left) while cytoplasmic fluorescence (right) is unchanged. (c) Fluorescence profiles across the vertically oriented apical dendrite (same neuron as a, b; 10 μM dopamine). Laser polarization orthogonal to dendrite excites membrane-localized green fluorescence of dLight$_{1.2}$ (left). Polarization parallel to dendrite excites little green fluorescence while red (cytoplasmic) fluorescence is unchanged (right). Note that dLight$_{1.2}$ fluorescence in horizontally oriented branches shows the opposite polarization-dependence. (d) Application of 10 μM dopamine strongly increases dLight$_{1.2}$ fluorescence when laser polarization is normal to dendrite (left). Dopamine application had no effect on fluorescence when laser polarization was parallel to the dendrite (right).

Next, we tested sDarken, a genetically encoded sensor for serotonin we recently developed. It is based on the architecture of dLight$_{1.2}$, but decreases its fluorescence in response to serotonin. Thus, we could visualize bright images of sDarken-expressing CA1 pyramidal cells in the absence of the agonist serotonin (Fig. 2(a)). Again, we observed no membrane-localized green fluorescence when the polarization of the laser was parallel to the dendritic membrane (Fig. 2(b)).

Diffuse green fluorescence in the cytoplasm likely results from sensor molecules that were not trafficked to the surface as well as immature (green fluorescent) tdimer2.
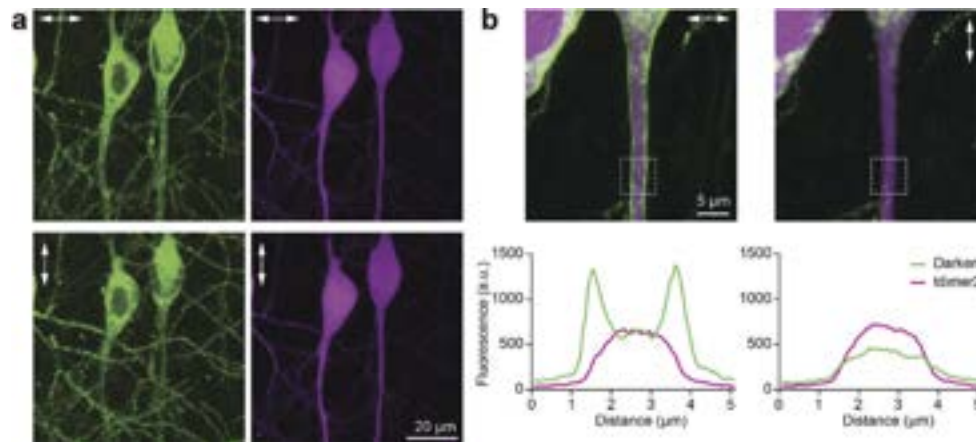

Fig. 2. Effect of laser polarization (930 nm) on the brightness of GPCR-based serotonin sensor sDarken. (a) Laser polarization normal to the apical dendrites of CA1 pyramidal cells excites bright fluorescence of sDarken (left) and cytoplasmic tdimer2 (right). Laser polarization parallel to the apical dendrites excites no fluorescence of sDarken in the apical dendrites (left) while cytoplasmic fluorescence (right) is unchanged. (b) Fluorescence profiles across the apical dendrite (same neuron as a). Polarization normal to dendrite shows membrane-localized green fluorescence of sDarken (left), polarization parallel to dendrite shows no membrane-localized fluorescence.

To change the polarization of excitation, we used two different methods: We either coupled two separate lasers tuned to the same wavelength at orthogonal polarization, activating one or the other (Fig. 2), or we rotated the polarization of a single laser by 90° using a half-wave plate (Fig. 1, Fig. 3). The results were identical, confirming that the direction of polarization determined which parts of the neuronal membrane were visible.

Interestingly, not all membrane-tethered GFP constructs are sensitive to laser polarization. The glutamate sensor iGluSnFR, which is anchored to the membrane via a single transmembrane segment, did not change its fluorescence intensity when excited at different polarization directions (Fig. 3(a)), and neither did GFP tethered to the membrane via glycosylphosphatidylinositol (GPI-GFP, Fig. 3(b)). We conclude that single-sided anchors leave sufficient degrees of freedom to randomize the angle of the fluorophore with respect to the membrane plane. $GRAB_{NE1h}$ is a GPCR-based, high affinity norepinephrine sensor with cpGFP attached to transmembrane segments on both ends, but in contrast to $dLight_{1.2}$ and sDarken, it retains a large part of the third intracellular loop as a flexible linker. When expressed in CA1 pyramidal cells, $GRAB_{NE1h}$ did show a strong fluorescence increase in response to noradrenaline application, but no polarization dependence (Fig. 3(c)).

For quantitative measurements of neurotransmitter concentrations *in vivo*, the orientation-sensitivity of some of the GPCR-based sensors is a problem. Coupling two lasers tuned to the same wavelength at orthogonal polarization is possible, but not very economical. We designed a compact device that splits the beam of a single laser into two sub-beams of equal power (50/50) but orthogonal polarization, and recombines the sub-beams collinearly (Fig. 4(a)-(c)). The device uses two polarizing beam-splitter cubes with 980 nm antireflection coating. To minimize group velocity dispersion (GVD), we used cubes made of n-BK7, rather than the denser N-SF1 (Flint) glass. For the same reason, we used silver coated prisms to direct the reflected beam through air instead of using total internal reflection in right angle prisms. The device is mounted in circular
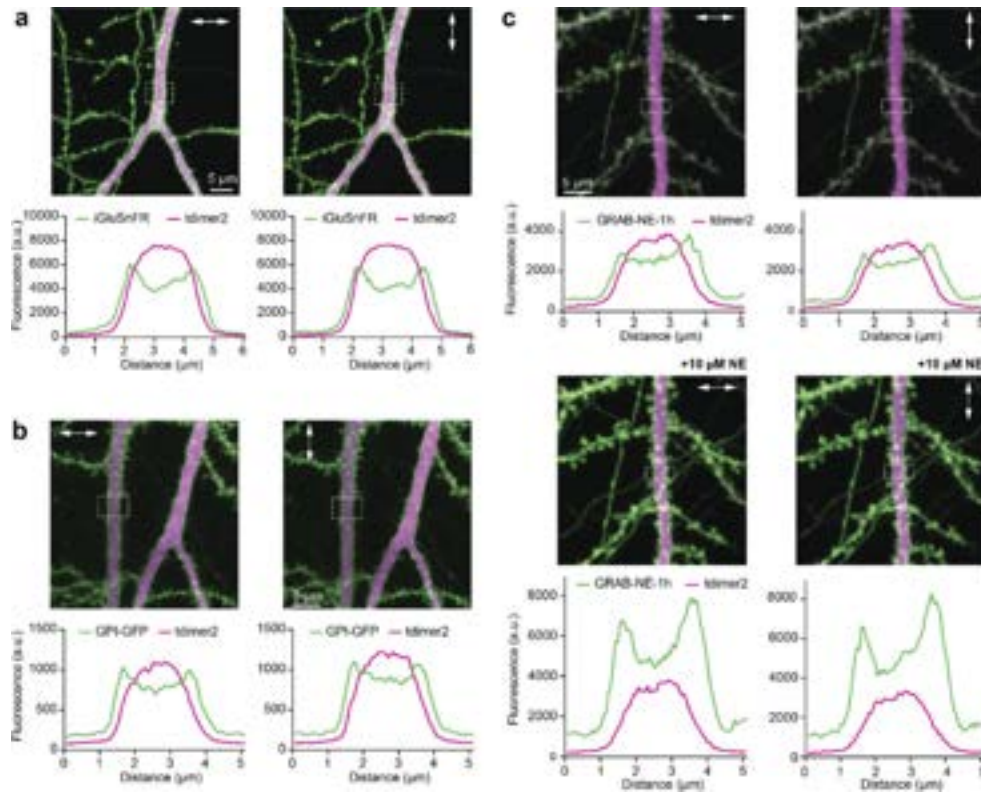
Fig. 3. Examples of membrane-anchored GFP constructs that are not polarization-sensitive. Dotted boxes mark analyzed regions. (a) The glutamate sensor iGluSnFR was not sensitive to polarization direction. (b) Membrane-anchored GFP (GPI-GFP) was not sensitive to polarization direction. (c) Norepinephrine sensor GRAB$_{NE1h}$ did not show strong polarization dependence of baseline fluorescence (without agonist). Addition of norepinephrine (NE) led to a strong increase in fluorescence independent of polarization direction.

clamps so it can be rotated around the beam to 45° (for 50/50 splitting) or used horizontally (no beam splitting). At 45° (the 'on' position), it works for horizontally and vertically polarized input beams, creating a stream of output of pulses with alternating polarization (45°, 135°). Both horizontal (0°) and vertical (90°) orientation of the device result in an unchanged output beam ('off' positions).

We inserted a beam splitting cube in a rotating mount to analyze the average power after the X-Pol device at different polarization directions (Fig. 4(d)). With the X-Pol device in the 'off' position (horizontal), the output beam was still horizontally polarized. When the device was tilted around the optical axis, it started splitting the beam into orthogonal components, reaching equal power at all polarization directions at a device tilt angle of ~55°. In this position, a power loss of ~12% occurred at the device (at 930 nm), mostly due to the mixed polarization of the reflected beam exiting the first beam splitter cube. The horizontally polarized component is not reflected at the second beam splitting cube; it crosses the cube and is lost. Therefore, slightly more power has to be directed into the reflected path to achieve a balanced output, which in our prototype was reached at 55° tilt angle. For safety reasons, lateral exit of the 'lost' beam has to be prevented. In our prototype, it is absorbed by a strip of matte black aluminum. With a side-mounted Si photodiode, it could be utilized to measure the power of the imaging beam.
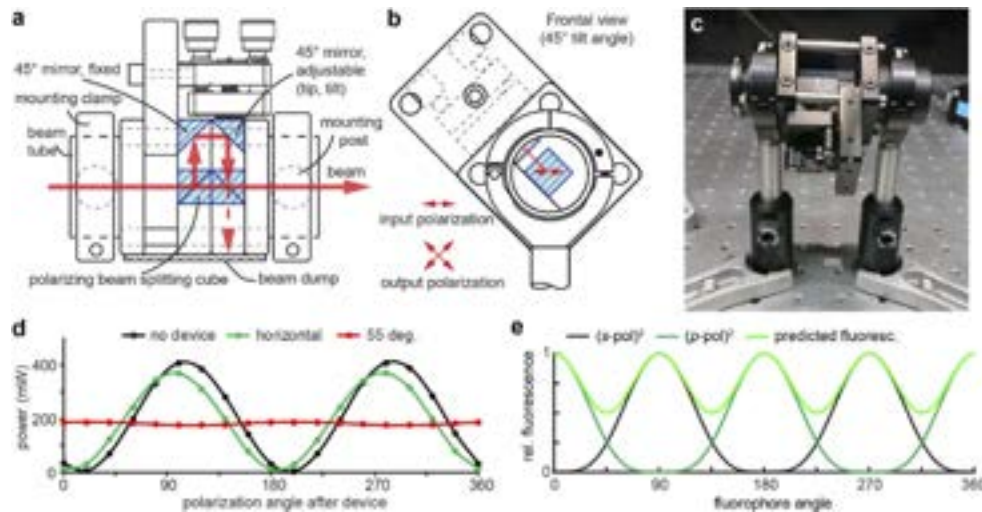
Fig. 4. X-Pol device to produce orthogonal pulse trains. (a) Schematic drawing of the beam path through the X-Pol device. One of the mirror prisms is adjustable to align the output beams. (b) In operation, the device is tilted 45° with respect to the polarization direction of the input beam. (c) Prototype mounted at 45° tilt. (d) Laser power at different polarization directions. Inserting the device leads to a small power loss due to surface reflections (green). The total output power is independent of polarization angle at a tilt angle of ~55° (red curve), due to some power loss of the reflected beam at the 2nd (recombining) cube. (e) Simulation of fluorescence-dependence on fluorophore orientation (with X-Pol device). As two-photon excitation is proportional to the square of the pulse power, and total fluorescence is the sum of emission from molecules excited by s-polarized and p-polarized pulses, respectively, we predict a residual orientation-dependence of fluorescence.

Although we achieved a flat distribution of laser power across all polarization directions, two-photon excitation of (perfectly aligned) fluorophores would still be expected to show some polarization dependence (Fig. 4(e)). Two-photon excitation depends on the pulse power squared, and molecules oriented at 45° to the two orthogonally polarized pulse trains are excited at twice the frequency, but with half the power per pulse. Note that pulses cannot interact; they have a temporal offset of ~70 ps (20 mm in air).

We tested the X-Pol device first on the bright serotonin sensor sDarken, which was completely invisible on dendrites aligned with the polarization direction of the laser, but perfectly visible on membranes orthogonal to the polarization direction (Fig. 5(a)). Inserting the device in the beam path at 55° tilt angle achieved the same results than combining two separate lasers with orthogonal polarization: Using the same average laser power, green fluorescence appeared bright along the entire membrane, independent of dendritic orientation (Fig. 5(b)). The intensity of red fluorescence (cytoplasmic tdimer2) is near identical in images 5a and 5b. The less efficient excitation when pulses with half the energy are used at twice the frequency was apparently compensated by the larger fraction of fluorophores available for excitation. Note that the green/red ratio is higher in thinner dendrites as it reflects the surface-to-volume ratio of the compartment.

We tested the X-Pol device also in label-free imaging of thin sections from human bone. Oriented collagen fibers generate a strong second harmonic signal when oriented parallel to the polarization direction of the excitation laser, revealing details of fiber organization below the diffraction limit of the microscope [17]. We used polarization sensitive second harmonic generation (P-SHG) to investigate the lamellar organization of osteons (Fig. 6(a)). In standard configuration, the two-photon microscope did not generate green emission from the sectors of
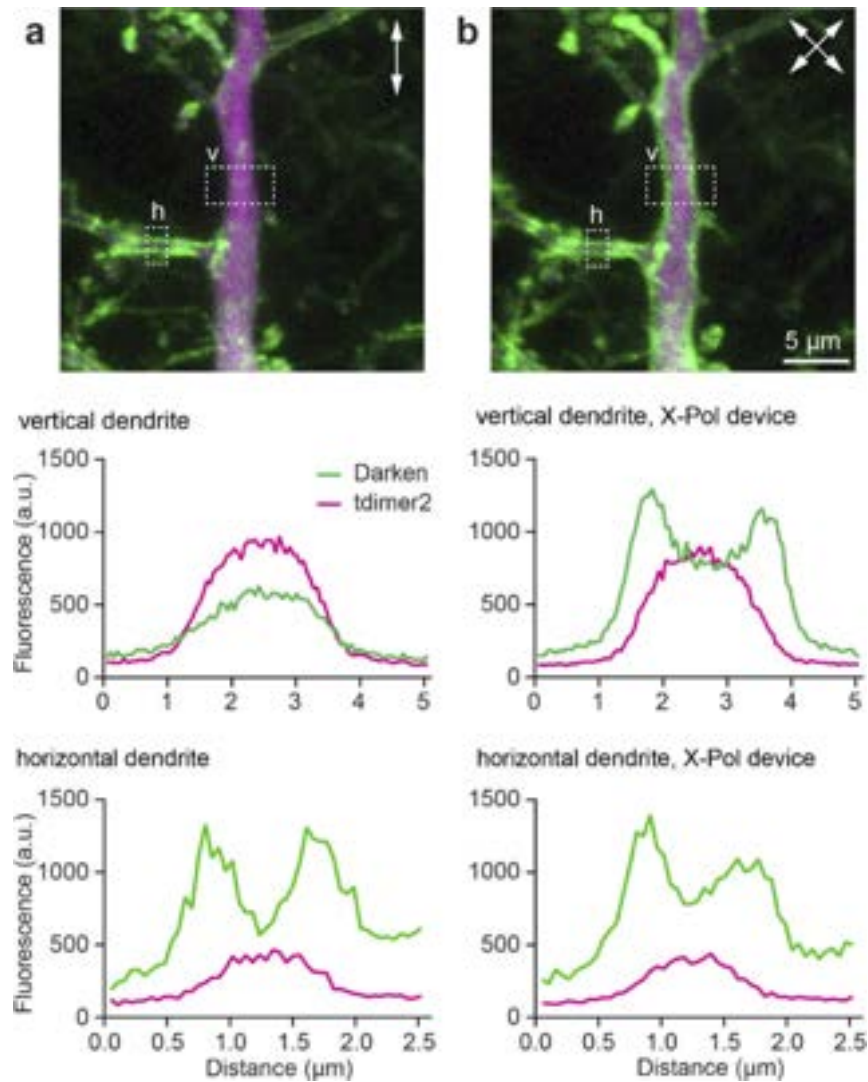
Fig. 5. CA1 pyramidal cell apical dendrite expressing the serotonin sensor sDarken (green) and cytoplasmic tdimer2 (red). (a) X-Pol device oriented horizontally (no beam spitting) rendered sDarken on the apical dendrite (vertical, v) invisible, while there was bright sDarken fluorescence on horizontal dendrites (h). (b) X-Pol device at 55° resulted in excellent visibility of sDarken on all dendrites. Note that the red (cytoplasmic) fluorescence is weaker in thinner dendrites due to their small volume.

the osteon where its lamellae were orthogonal to the polarization, resulting in two dark sectors. The tilt of the dark sectors in our images reflects a 15° tilt of the galvanometric x-mirror's axis of rotation (XY Galvo Block, Cambridge Technology), resulting in a 75° polarization angle in the images.

Inserting the X-Pol device into the beam path (Fig. 6(b)) and rotating it to 55° with respect to the laser polarization (Fig. 6(c)) resulted in evenly distributed signals from all sectors of the osteon, removing the artifact produced by linear polarization. To compensate for light loss inside the polarization device, laser power was increased by ~20% (Fig. 6(c)). We did not see dark sectors between the cardinal polarization directions generated by the X-Pol device (as we
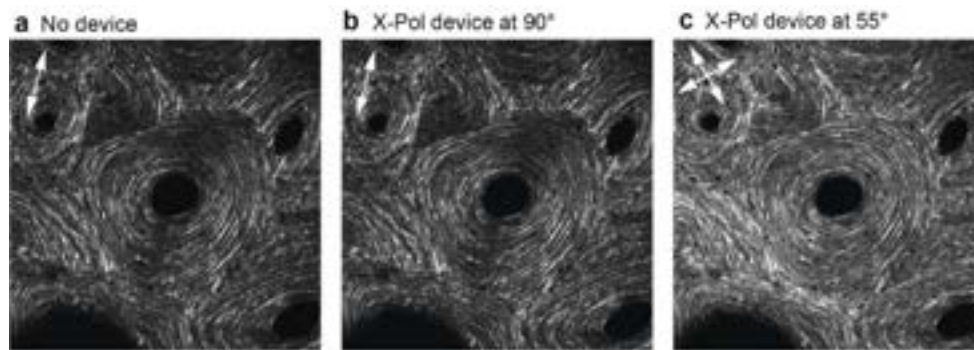
Fig. 6. Second harmonic generation in a bone section at 1020 nm excitation. (a) Image of an osteon shows dark sectors where collagen fibers are oriented orthogonal to the polarization direction of the IR laser. (b) Insertion of X-Pol device into the beam path in veritcal position (90°) has little effect on the second harmonic image. (c) Turning the device to 55° results in orthogonally polarized sub-beams. Note the absence of dark sectors.

predicted from theory, see Fig. 4(e)), most likely because the orientation of collagen fibrils is not parallel to the imaging plane, but at oblique angles to it [18]. In addition, a high-NA objective produces polarization components that are not aligned with the optical axis, reducing the anisotropy in the images [19].

Osteons provide a convenient test sample as their lamellar collagen organization is known to be rotationally symmetric. The strong polarization dependence of SHG images is even more problematic in tissues that have not the same degree of crystalline organization (e.g. skin and tissue), as the absence of signal in such images can be mistakenly interpreted as absence of collagen. Mamillary tumors, for example, are characterized by an increased collagen density, and two-photon SHG imaging has been successfully used to visualize such malignancies [20,21]. As we show, orthogonal polarization excitation makes SHG images easier to interpret, which could be helpful for the investigation and diagnosis of cancer. Analogous polarization-dependent artifacts appear in other kinds of microscopy techniques, e.g. coherent anti-Stokes Raman scattering (CARS) microscopy [22]. Orthogonal polarization could be used to create a hardware implementation of software-based methods designed to mitigate this artifact.

4. Discussion

We report unexpectedly strong effects of polarized excitation in two-photon microscopy of a particular type of GFP-labeled membrane proteins, namely GPCR-based neurotransmitter sensors. No polarization dependence was observed for the soluble red fluorescent protein tdimer2. Similarly, flexible, single-ended tethering, as in GPI-anchored GFP and iGluSnFR, did not result in measurable anisotropy. If the fluorophore can rotate in a cone, its dipole orientation relative to the direction of polarization is randomized. To obtain polarization-sensitive probes with single-ended tether, the linker has to form a continuous α-helix to prevent angular movements [23].

In GPCR-based neurotransmitter sensors, the GFP barrel is inserted into the third intracellular loop and thus tethered at both ends (Fig. 7). This architecture orients the GFP barrel more or less parallel to the cell membrane, depending on the length of the linkers [24]. Based on available structural information [23,25–27], we propose that in highly anisotropic sensors, the dipole moment of cpGFP is oriented normal to the membrane plane (Fig. 7). Interestingly, we could not detect significant polarization dependence of the norepinephrine sensor $GRAB_{NE1h}$. It has been pointed out that in these kind of GRAB sensors, large parts of the third intracellular

loop are retained and provide a flexible link to the GFP barrel [24]. Thus, subtle differences in sensor design can have profound effects on the sensitivity to polarization. The effects of adding single or multiple lipid anchors to GFP were previously explored [27,28] and the resulting linear dichroism was most clearly detected using two-photon exaction. In the development of sensors intended for *in vivo* imaging, typically performed with two-photon microscopes using polarized excitation, isotropic fluorescence should indeed be a selection criterion.
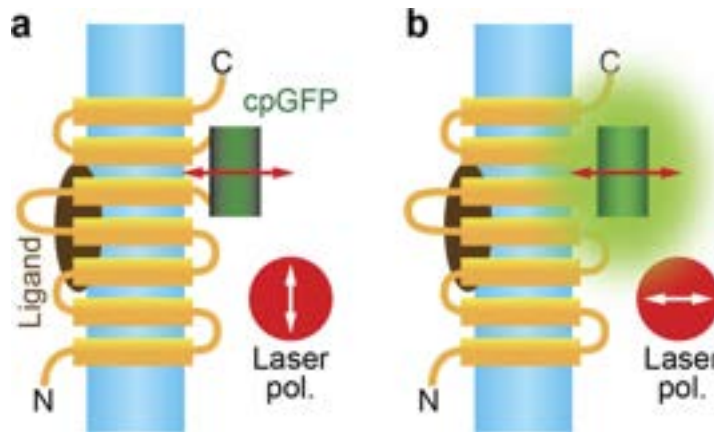

Fig. 7. Proposed dipole orientation in polarization-sensitive GPCR sensors. (a) Laser polarization parallel to the dendritic membrane (blue) does not excite cpGFP. (b) Laser polarization must be aligned with the dipole of cpGFP (red arrow) to excite fluorescence. Note that rotation of the molecule in the membrane plane does not affect dipole orientation.

For quantitative neurotransmitter measurements deep in in brain tissue, we propose a simple solution, to alternate pulses of orthogonal polarization. We show that the X-Pol device significantly reduces direction bias in neurons. For specific applications, fluorescence-detected linear dichroism could also be exploited, e.g. to investigate lipid domains or physical interactions between subunits of G proteins [28,29]. However, this works best in spherical cells and requires an active device to rapidly switch laser polarization. For the class of GPCR-based neurotransmitter sensors, the goal is to precisely measure extracellular neurotransmitter concentrations on the entire surface of the neuron. As we demonstrate, this goal is put in jeopardy if linear polarized excitation is used.

In most confocal microscopes, lasers are coupled by conventional single mode optical fibers that do not preserve the polarization state of the light propagating along the fiber. As the sample is excited at arbitrary polarization that also fluctuates over time, we would not expect systematic polarization artifacts in confocal images. Confocal polarizing microscopes have been built for special purposes [28,30,31], but are not in general use for neuroscience applications.

Our prototype X-Pol device was assembled from off-the-shelf components and is therefore inexpensive to reproduce. We would like to point out, however, that precise alignment of the optical components inside the device is important to ensure complete overlap of the two point-spread functions generated by the sub-beams. If the mirror prisms are not well adjusted, loss of resolution or even double images may occur. Aligning the device to the center of the beam is less critical as long as beam clipping is avoided. The added dispersion of 20 mm N-BK7 glass ($GVD = 70$ fs^2/mm) was readily compensated by pre-chirping (MaiTai DeepSee, SpectraPhysics). Flint glass (N-SF1), which is typically used for beam splitting cubes, induces more GVD (247 fs^2/mm). To further reduce GVD, broadband thin plate beam splitters could be arranged at Brewster's angle in a chevron design, again mounted with axial tilt to achieve 50/50 splitting [32]. Instead of rotating the X-Pol device, the polarization of the incoming beam could be tilted

with a half-wave plate. However, adding an achromatic half-wave plate roughly doubles the cost of the device without obvious benefits. It is also possible to generate orthogonal polarization by a birefringent crystal, e.g. yttrium vanadate (YVO_4), but this creates a lateral displacement of the two output beams.

The X-Pol device doubles the pulse repetition rate while cutting the energy of individual pulses in half. This effect should require an increase in average power (by $2^{0.5}$) to achieve the same image intensity. On the other hand, more fluorophores can be excited when using orthogonal pulse trains, increasing the effective concentration of fluorescent proteins. Examining the red fluorescence of tdimer2, we found that these two effects were in balance, and no increase in average power was required when imaging with the X-Pol device at 55°. Green fluorescence was independent of dendritic orientation with the X-Pol device, but less bright than in optimally oriented dendrites excited with linear polarized light. This was expected, as the weaker excitation by the split pulses was not compensated by recruitment of additional green fluorophores. Increased repetition rates have been reported to reduce bleaching in biological preparations [33–35] but require higher average power, which can affect cellular physiology by local heating [36]. Some of the beneficial effects shown by Ji et al. [33], using a more complex pulse splitter design, may have been due to orthogonally polarized output pulses and in consequence, recruitment of additional fluorophores.

An intuitive solution to overcome linear polarization artifacts is to use circularly-polarized light by employing an achromatic quarter-wave plate. This solution would indeed work for one-photon illumination, however it is not effective for two-photon excitation. For efficient two-photon absorption, the sum of angular momenta of the absorbed photons is required to be zero [37,38].

In addition to optical measurements of neurotransmitter concentration with GPCR-based sensors, excitation with orthogonal polarization could also be advantageous for two-photon excitation of channelrhodopsin as well as opsin-derived sensors of membrane voltage [39]. Indeed, polarization-dependence of genetically encoded voltage sensors has recently been reported [40]. In membranes, cytoskeletal labeling and in fixed tissue, where the rotation of fluorophores is slowed down or locked, conventional linearly polarized two-photon microscopes continuously excite the same subset of fluorophores, leading to anisotropic photobleaching [41]. Orthogonally polarized pulse trains double the number of excitable fluorophores, increasing brightness (compared to excitation pulses of the same energy and repetition frequency polarized in one direction) or reducing bleaching when imaging with adapted laser power. Based on our experience, we predict that two-photon microscopy will follow the lead of confocal microscopy and use mixed polarization as default imaging mode.

Disclosures. MP (P), TGO (P).

Data availability. Data underlying the results presented in this paper are not publicly available at this time but may be obtained from the authors upon reasonable request.

References

1. S. T. Hess, E. D. Sheets, A. Wagenknecht-Wiesner, and A. A. Heikal, "Quantitative analysis of the fluorescence properties of intrinsically fluorescent proteins in living cells," Biophys. J. **85**(4), 2566–2580 (2003).
2. A. H. A. Clayton, Q. S. Hanley, D. J. Arndt-Jovin, V. Subramaniam, and T. M. Jovin, "Dynamic fluorescence anisotropy imaging microscopy in the frequency domain (rFLIM)," Biophys. J. **83**(3), 1631–1649 (2002).
3. G. de Vito, P. Ricci, L. Turrini, V. Gavryusev, C. Müllenbroich, N. Tiso, F. Vanzi, L. Silvestri, and F. S. Pavone, "Effects of excitation light polarization on fluorescence emission in two-photon light-sheet microscopy," Biomed. Opt. Express **11**(8), 4651 (2020).

4. T. Patriarchi, J. R. Cho, K. Merten, M. W. Howe, A. Marley, W.-H. Xiong, R. W. Folk, G. J. Broussard, R. Liang, M. J. Jang, H. Zhong, D. Dombeck, M. von Zastrow, A. Nimmerjahn, V. Gradinaru, J. T. Williams, and L. Tian, "Ultrafast neuronal imaging of dopamine dynamics with designed genetically encoded sensors," Science **360**(6396), eaat4422 (2018).

5. F. Sun, J. Zeng, M. Jing, J. Zhou, J. Feng, S. F. Owen, Y. Luo, F. Li, H. Wang, T. Yamaguchi, Z. Yong, Y. Gao, W. Peng, L. Wang, S. Zhang, J. Du, D. Lin, M. Xu, A. C. Kreitzer, G. Cui, and Y. Li, "A genetically encoded fluorescent sensor enables rapid and specific detection of dopamine in flies, fish, and mice," Cell **174**(2), 481–496.e19 (2018).

6. M. Jing, Y. Li, J. Zeng, P. Huang, M. Skirzewski, O. Kljakic, W. Peng, T. Qian, K. Tan, J. Zou, S. Trinh, R. Wu, S. Zhang, S. Pan, S. A. Hires, M. Xu, H. Li, L. M. Saksida, V. F. Prado, T. J. Bussey, M. A. M. Prado, L. Chen, H. Cheng, and Y. Li, "An optimized acetylcholine sensor for monitoring in vivo cholinergic activity," Nat. Methods **17**(11), 1139–1146 (2020).

7. J. Feng, C. Zhang, J. E. Lischinsky, M. Jing, J. Zhou, H. Wang, Y. Zhang, A. Dong, Z. Wu, H. Wu, W. Chen, P. Zhang, J. Zou, S. A. Hires, J. J. Zhu, G. Cui, D. Lin, J. Du, and Y. Li, "A genetically encoded fluorescent sensor for rapid and specific in vivo detection of norepinephrine," Neuron **102**(4), 745–761.e8 (2019).

8. J. Wan, W. Peng, X. Li, T. Qian, K. Song, J. Zeng, F. Deng, S. Hao, J. Feng, P. Zhang, Y. Zhang, J. Zou, S. Pan, M. Shin, B. J. Venton, J. J. Zhu, M. Jing, M. Xu, and Y. Li, "A genetically encoded sensor for measuring serotonin dynamics," Nat. Neurosci. **24**(5), 746–752 (2021).

9. J. S. Wiegert, C. E. Gee, and T. G. Oertner, "Single-cell electroporation of neurons," Cold Spring Harb. Protoc. **2017**(2), pdb.prot094904 (2017).

10. P. Milovanovic, E. A. Zimmermann, C. Riedel, A. vom Scheidt, L. Herzog, M. Krause, D. Djonic, M. Djuric, K. Püschel, M. Amling, R. O. Ritchie, and B. Busse, "Multi-level characterization of human femoral cortices and their underlying osteocyte network reveal trends in quality of young, aged, osteoporotic and antiresorptive-treated bone," Biomaterials **45**, 46–55 (2015).

11. T. A. Pologruto, B. L. Sabatini, and K. Svoboda, "ScanImage: flexible software for operating laser scanning microscopes," Biomed Eng Online **2**(1), 13 (2003).

12. T. G. Oertner, "Functional imaging of single synapses in brain slices," Exp. Phys. **87**(6), 733–736 (2002).

13. C. E. Gee, I. Ohmert, J. S. Wiegert, and T. G. Oertner, "Preparation of slice cultures from rodent hippocampus," Cold Spring Harb. Protoc. **2017**(2), pdb.prot094888 (2017).

14. R. E. Campbell, O. Tour, A. E. Palmer, P. A. Steinbach, G. S. Baird, D. A. Zacharias, and R. Y. Tsien, "A monomeric red fluorescent protein," Proc. Natl. Acad. Sci. U. S. A. **99**(12), 7877–7882 (2002).

15. J. S. Marvin, B. Scholl, D. E. Wilson, K. Podgorski, A. Kazemipour, J. A. Müller, S. Schoch, F. J. U. Quiroz, N. Rebola, H. Bao, J. P. Little, A. N. Tkachuk, E. Cai, A. W. Hantman, S. S.-H. Wang, V. J. DePiero, B. G. Borghuis, E. R. Chapman, D. Dietrich, D. A. DiGregorio, D. Fitzpatrick, and L. L. Looger, "Stability, affinity, and chromatic variants of the glutamate sensor iGluSnFR," Nat. Methods **15**(11), 936–939 (2018).

16. G. Kondoh, X. H. Gao, Y. Nakano, H. Koike, S. Yamada, M. Okabe, and J. Takeda, "Tissue-inherent fate of GPI revealed by GPI-anchored GFP transgenesis," FEBS Lett. **458**(3), 299–303 (1999).

17. J. C. Mansfield, V. Mandalia, A. Toms, C. Peter Winlove, and S. Brasselet, "Collagen reorganization in cartilage under strain probed by polarization sensitive second harmonic generation microscopy," J. R. Soc. Interface **16**(150), 20180611 (2019).

18. K. E. Stockhausen, M. Qwamizadeh, E. M. Wölfel, H. Hemmatian, I. A. K. Fiedler, S. Flenner, E. Longo, M. Amling, I. Greving, R. O. Ritchie, F. N. Schmidt, and B. Busse, "Collagen fiber orientation is coupled with specific nano-compositional patterns in dark and bright osteons modulating their biomechanical properties," ACS Nano **15**(1), 455–467 (2021).

19. D. Axelrod, "Carbocyanine dye orientation in red cell membrane studied by microscopic fluorescence polarization," Biophys. J. **26**(3), 557–573 (1979).

20. T. Meyer, N. Bergner, C. Bielecki, C. Krafft, D. Akimov, B. F. M. Romeike, R. Reichart, R. Kalff, B. Dietzek, and J. Popp, "Nonlinear microscopy, infrared, and Raman microspectroscopy for brain tumor analysis," J. Biomed. Opt. **16**(2), 021113 (2011).

21. P. P. Provenzano, D. R. Inman, K. W. Eliceiri, J. G. Knittel, L. Yan, C. T. Rueden, J. G. White, and P. J. Keely, "Collagen density promotes mammary tumor initiation and progression," BMC Med. **6**(1), 11 (2008).

22. Y. Fu, T. B. Huff, H.-W. Wang, J.-X. Cheng, and H. Wang, "Ex vivo and in vivo imaging of myelin fibers in mouse brain by coherent anti-Stokes Raman scattering microscopy," Opt. Express **16**(24), 19396 (2008).

23. A. Sugizaki, K. Sato, K. Chiba, K. Saito, M. Kawagishi, Y. Tomabechi, S. B. Mehta, H. Ishii, N. Sakai, M. Shirouzu, T. Tani, and S. Terada, "POLArIS, a versatile probe for molecular orientation, revealed actin filaments associated with microtubule asters in early embryos," Proc. Natl. Acad. Sci. **118**(11), e2019071118 (2021).

24. L. Ravotto, L. Duffet, X. Zhou, B. Weber, and T. Patriarchi, "A Bright and Colorful Future for G-Protein Coupled Receptor Sensors," Front. Cell. Neurosci. **14**, 67 (2020).

25. F. I. Rosell and S. G. Boxer, "Polarized absorption spectra of green fluorescent protein single crystals: Transition dipole moment directions," Biochemistry **42**(1), 177–183 (2003).

26. Y. Chen, X. Song, S. Ye, L. Miao, Y. Zhu, R. G. Zhang, and G. Ji, "Structural insight into enhanced calcium indicator GCaMP3 and GCaMPJ to promote further improvement," Protein Cell **4**(4), 299–309 (2013).

27. R. D. Roorda, T. M. Hohl, R. Toledo-Crow, and G. Miesenböck, "Video-rate nonlinear microscopy of neuronal membrane dynamics with genetically encoded probes," J. Neurophysiol. **92**(1), 609–621 (2004).

28. J. Lazar, A. Bondar, S. Timr, and S. J. Firestein, "Two-photon polarization microscopy reveals protein structure and function," Nat. Methods **8**(8), 684–690 (2011).

29. A. Gasecka, T. J. Han, C. Favard, B. R. Cho, and S. Brasselet, "Quantitative imaging of molecular order in lipid membranes using two-photon fluorescence polarimetry," Biophys. J. **97**(10), 2854–2862 (2009).

30. I. I. Smalyukh, S. V. Shiyanovskii, and O. D. Lavrentovich, "Three-dimensional imaging of orientational order by fluorescence confocal polarizing microscopy," Chem. Phys. Lett. **336**(1-2), 88–96 (2001).

31. C. E. Bigelow, D. L. Conover, and T. H. Foster, "Confocal fluorescence spectroscopy and anisotropy imaging system," Opt. Lett. **28**(9), 695–697 (2003).

32. D. J. Dummer, S. G. Kaplan, L. M. Hanssen, A. S. Pine, and Y. Zong, "High-quality Brewster's angle polarizer for broadband infrared application," Appl. Opt. **37**(7), 1194 (1998).

33. N. Ji, J. C. Magee, and E. Betzig, "High-speed, low-photodamage nonlinear imaging using passive pulse splitters," Nat. Methods **5**(2), 197–202 (2008).

34. F. Niu, R. Wu, D. Wu, D. Gou, L. Feng, L. Chen, Z. Zhang, and A. Wang, "Photobleaching of ultrashort pulses with different repetition rates in two-photon excitation microscopy," Laser Phys. **29**(4), 046001 (2019).

35. J. Mütze, V. Iyer, J. J. MacKlin, J. Colonell, B. Karsh, Z. Petrášek, P. Schwille, L. L. Looger, L. D. Lavis, and T. D. Harris, "Excitation spectra and brightness optimization of two-photon excited probes," Biophys. J. **102**(4), 934–944 (2012).

36. E. Schmidt and M. Oheim, "Infrared excitation induces heating and calcium microdomain hyperactivity in cortical astrocytes," Biophys. J. **119**(11), 2153–2165 (2020).

37. K. D. Bonin and T. J. McIlrath, "Two-photon electric-dipole selection rules," J. Opt. Soc. Am. B **1**(1), 52 (1984).

38. I. Micu, C. Brideau, L. Lu, and P. K. Stys, "Effects of laser polarization on responses of the fluorescent Ca^{2+} indicator X-Rhod-1 in neurons and myelin," Neurophotonics **4**(2), 025002 (2017).

39. J. M. Kralj, A. D. Douglass, D. R. Hochbaum, D. Maclaurin, and A. E. Cohen, "Optical recording of action potentials in mammalian neurons using a microbial rhodopsin," Nat. Methods **9**(1), 90–95 (2012).

40. W. Bloxham, D. Brinks, S. Kheifets, and A. E. Cohen, "Linearly polarized excitation enhances signals from fluorescent voltage indicators," bioRxiv 2021.07.21.453006 (2021).

41. K. Sharma, D. K. Fong, and A. M. Craig, "Postsynaptic protein mobility in dendritic spines: long-term regulation by synaptic NMDA receptor activation," Mol. Cell. Neurosci. **31**(4), 702–712 (2006).